

Università degli Studi di Napoli Federico II
SCUOLA POLITECNICA E DELLE SCIENZE DI BASE

DIPARTIMENTO DI INGEGNERIA INDUSTRIALE
Corso di Dottorato in Ingegneria Industriale

Doctoral thesis
in
Industrial Engineering

**Development of a Multi-Disciplinary
Analysis and Optimization framework and
applications for innovative efficient regional
aircraft**

XXXII Cycle

Author:
Vittorio Trifari

Coordinator:
Prof. Michele Grassi

Tutor:
Prof. Fabrizio Nicolosi

March 12, 2020


Declaration of Authorship

I, Vittorio Trifari, declare that this thesis, titled “Development of a Multi-Disciplinary Analysis and Optimization framework and applications for innovative efficient regional aircraft”, and the work presented in it are my own. I confirm that:

- This work was done wholly or mainly while in candidature for research degree at this University.
- Where any part of this thesis has previously been submitted for a degree or any other qualification at this University or any other institution, this has been clearly stated.
- Where I have consulted the published work of others, this is always clearly attributed.
- Where I have quoted from the work of others, the source is always given. With the exception of such quotations, this thesis is entirely my own work.
- I have acknowledge all main source of help.
- Where the thesis is based on work done by myself jointly with others, I have made clear exactly what was done by others and what I have contributed myself.

Date: 12th Mar, 2020

Sign: _____

A handwritten signature in black ink, appearing to read 'V. Trifari', is written over a horizontal line. The signature is stylized and includes the date '12/03/20'.

ABSTRACT

An in-depth market analysis of the regional aircraft segment has revealed that world passenger traffic is expected to maintain 4.5% annual growth over the next two decades.

In a context of economical growth, oil price is expected to double in the next 20 years, regardless of temporary fluctuations. Thus, fuel price will again be a key decision factor for airlines. Furthermore, in terms of regional market, fuel price is higher in regional airports than in main airports due to higher fuel transportation costs, which translates to a worldwide average extra cost of +34%.

At the same time world air transport demand will increase 2.5 times by 2037, reaching 17 trillion **Revenue Passenger Kilometers (RPKs)** for all commercial aircraft segments.

As middle-class and consumer spending increase in many regions, the propensity to travel will develop with new emerging regional markets taking the lead. By 2037, the Middle East and Asia Pacific will be the fastest growing markets, with an annual growth rate of 5.7%, followed by Latin America with 5.2%, Africa with 4.8%. In this scenario, turboprops, as typical first movers, offer higher rewards for exploring new routes and developing regional networks.

However, being the aircraft one of the most polluting means of transport, future aircraft must also comply with the environmental issue. The climate change and the increasing lack of resources claim for a clear reduction of the aviation impact on citizens and the environment. The integration of innovative and affordable technologies in future aircraft platforms plays a key role to increase the appeal and the benefits for both customers and airlines.

The combination of all these factors results in a very challenging design process for engineers to come up with innovative aircraft configurations and technologies.

Regional aircraft are playing an increasingly role in the evolution of the airline operations. For many years, this growth has been faced by a wide adoption of regional jets. Their success can be largely attributed to their popularity with passengers, who prefer them because they are more comfortable and faster than turboprops. The regional jet market has grown to be a strong sector based on a combination of higher loads and greater profitability. Embraer foresees world demand for 8230 new jets up to 150-seat segment over the next 20 years.

However, despite the regional jets success, turboprop engines are 10-30% more efficient than jet engines in cruise conditions leading to a potential consistent reduction of the amount of fuel used per mission as well as pollutant emissions. According to ATR forecasts, assuming all short haul flights operated by regional jets today are replaced by modern turboprops, 11% of overall regional aviation CO₂ emissions could be saved.

State this, regional jets provides for faster connections with a higher payload in spite of higher fuel consumptions and pollutant emissions; while turboprop aircraft allows to reduce air transport environmental impact but with lower passengers capacity and lower speed.

Thus, the research question at the base of this thesis is: “What could be the impact, in terms of performance, that innovative high-capacity turboprop aircraft configurations can have on the current regional aircraft scenario?”

To answer this question this work will define a set of **Top-Level Aircraft Requirements (TLARs)** suitable for modern regional transport applications which will be used to design several innovative turboprop aircraft platforms. Each of them will undergo a complete **Multi-Disciplinary Analysis and Optimization (MDAO)** process to define the set of optima configurations. Finally, a comparison with the current state of the art regional jet platform, represented by the Airbus A220, will be performed.

The **MDAO** process will be carried out using the **Java toolchain of Programs for Aircraft Design (JPAD)** framework developed at the University of Naples Federico II by the **Design of Aircraft and Flight technologies (DAF)** group. The author has personally developed most of the **JPAD** modules that will be presented with particular focus on the performance and the **MDAO** modules. The first one has been completely designed using a simulation-based approach to easily perform accurate and fast flight and ground performance analyses; while the second one uses all the advantages provided by **Object-Oriented Programming (OOP)** to perform a full factorial **Design Of Experiments (DOE)** followed by a multi-objective optimizations process involving computational intelligences like **Genetic Algorithms (GA)** or **Particle Swarm Optimization (PSO)** algorithms.

The **JPAD** framework, especially in term of performance evaluation, has been widely used during the first two loops of the Clean Sky 2 European project named **IRON** from which all innovative turboprop configurations under examination have been derived. **JPAD** is the result of the efforts of the **DAF** research group which involved several PhD students in a virtuous collaboration process, including the author of this thesis work.

Because of the multidisciplinary nature of research, an added value of this thesis can be found in the combination of two complementary branches of engineering: Aerospace, in terms of Aircraft Design, and Computer Science, in terms of Software Engineering.

CONTENTS

Declaration of Authorship	iii
Abstract	v
List of Figures	xii
List of Tables	xv
List of symbols	xvii
Acronyms	xxvii
Glossary	xxxii
1 Introduction	1
1.1 Definition of the research question	1
1.2 Aircraft market scenario	3
1.3 Research context and thesis structure	7
1.3.1 Thesis structure	7
2 The IRON project	9
2.1 The first loop of design activities	10
2.2 The second loop of design activities	16
2.3 Candidate's contribution to the IRON project	42
3 A new framework for Aircraft Preliminary Design	45
3.1 Introduction	45
3.2 Aircraft Design software scenario	46
3.3 The JPAD software	48
3.3.1 Software architecture	50
3.3.2 The Core of the JPAD framework	51
3.3.3 Aircraft parameterization in JPAD	55
3.3.4 Analyses modules	66
3.3.5 Graphical User Interface (GUI) and Automatic CAD generation	107

3.3.6	Multi-Disciplinary Analyses and Optimizations	112
3.4	Candidate's contribution to the development of JPAD	118
4	Applications	121
4.1	Case study: Airbus A220-300	122
4.2	TLARs and key design aspects of innovative regional turboprop aircraft	158
4.3	High-capacity turboprop models definition and their MDAO	161
4.4	Analysis of results	169
4.5	Candidate's contribution to the applications chapter	176
5	Conclusions	177
	Acknowledgements	181
	References	183

LIST OF FIGURES

1.1	Worldwide air transport demand growth 2019-2038.	3
1.2	Oil price forecast.	4
1.3	Distribution of seats offered by single-aisle aircraft over the years.	5
1.4	Distribution of distances flown by single-aisle aircraft over the years.	5
1.5	In-service fleet share - turboprops and regional jets.	6
2.1	IRON project loops.	10
2.2	IRON aircraft model baseline.	11
2.3	IRON boarding diagram - Loop 1 ending	16
2.4	IRON boarding diagram limitations - Loop 1 ending	16
2.5	High-speed turboprop configurations derived from the DC-9 Super 80	18
2.6	IRON configurations comparison Loop 2 - Top views.	21
2.7	Example of Pareto front for the optimization of Configuration 1 - IRON Loop 2	22
2.8	Payload-Range: effects of different cruise SFC - IRON Loop 2, Configuration 2 [11].	24
2.9	DOC comparison: IRON (Configuration 2) and the reference regional jet, 1440nm [11].	26
2.10	DOC comparison: IRON (Configuration 2) and the reference regional jet, 400nm [11].	26
2.11	IRON aircraft model configuration for loop 2.	27
2.12	Systems and components center of gravity positions - IRON loop 2.	29
2.13	Wing local angle of attack deficit due to canard downwash - cruise.	30
2.14	Wing local angle of attack deficit due to canard downwash - landing.	31
2.15	Aircraft pitching moment coefficient, center of gravity effects at cruise conditions.	32
2.16	Aircraft pitching moment coefficient, center of gravity effects at climb conditions.	32
2.17	Effects of center of gravity and i_h on aircraft pitching moment coefficient.	33
2.18	IRON loop 2 - Adopted technologies (left) and considered riblet shape (right).	34
2.19	IRON loop 2 - Residual climb gradient in hot & high conditions	37
2.20	IRON loop 2 - Payload-Range diagrams	40
3.1	TIOBE programming community index, March 2020.	49
3.2	JPAD framework architecture.	50
3.3	jpad-core architecture.	52
3.4	jpad-core modules dependencies.	53
3.5	jpad-core complete analysis loop.	53

3.6	jpad-core manager-calculator pattern.	54
3.7	Fuselage nomenclature. Sideview and top view outlines [79].	58
3.8	Fuselage nomenclature. Sideview and top view of nose and tail [79].	59
3.9	Fuselage nomenclature. Cross section parameters [79].	60
3.10	Planform definitions for a two-panel wing (left) and its corresponding equivalent wing (right) [79].	61
3.11	Wing nomenclature from side view [79].	63
3.12	Planform view nomenclature of a generic plain movable surface in a lifting surface [79].	64
3.13	Nacelle parameterization	65
3.14	Typical locations of the different aircraft systems [15].	69
3.15	Example of aircraft side view with all components center of gravity position produced by JPAD	70
3.16	Example of boarding diagram produced by JPAD	71
3.17	Example of take-off rotation angle calculation produced by JPAD	72
3.18	Limitation on pitch and roll angles during take-off and landing determined by the aircraft geometry [25]	73
3.19	Example of limit ground bank angle and minimum engine clearance calculation produced by JPAD	74
3.20	Example of nose and main gear position limits calculated by JPAD	75
3.21	Example of turning radius calculation produced by JPAD	76
3.22	Qualitative representation of the angle of attack input law	80
3.23	Qualitative representation of the aircraft with one engine inoperative and with full deflected rudder to ensure constant heading	83
3.24	Certification noise measurement points	91
3.25	Example of cruise flight envelope [99].	96
3.26	Specific Air Range as function of the Mach number parameterized in aircraft weight	98
3.27	Mission profile sub-phases handled by JPAD	101
3.28	Flowchart of the mission profile analysis performed by JPAD	104
3.29	Qualitative representation of the Payload-Range chart with MZFW limitation . . .	105
3.30	FAR-25 flight envelope.	106
3.31	Input Manager perspective of the jpad-commander GUI	107
3.32	Main Input Manager perspective of the jpad-commander GUI with automatically generated CAD model	108
3.33	jpad-commander Input Manager perspective - cabin layout	109
3.34	jpad-commander Input Manager perspective - wing definition	109
3.35	jpad-commander Input Manager perspective - airfoil geometry management	110
3.36	jpad-commander Input Manager perspective - airfoil lift curve management	110
3.37	jpad-commander Input Manager perspective - airfoil drag polar curve management .	111
3.38	jpad-commander Input Manager perspective - airfoil pitching moment curve management	111
3.39	Typical DOE and optimization flowchart in JPAD	114
3.40	Example of JPAD DOE response surface	115
3.41	Example of JPAD output Pareto front in multi-objective optimizations	116

4.1	A220 family (former Bombardier CSeries) 3-views	122
4.2	Excerpt of the JPAD HBPR engine database concerning the Take-off rating.	124
4.3	A220-300 3-view and CAD model representation made by JPAD	126
4.4	Seat maps comparison between the A220-300 [116] and the JPAD parametric model.	127
4.5	Comparison between the A220-300 wing [116] and the JPAD wing.	127
4.6	Comparison between the A220-300 horizontal tail [116] and the JPAD horizontal tail.	128
4.7	Comparison between the A220-300 vertical tail [116] and the JPAD vertical tail.	128
4.8	JPAD weights breakdown of the A220-300 parametric model.	134
4.9	Boarding diagram of the A220-300 parametric model - JPAD	136
4.10	A220-300 parametric model side view with each component center of gravity - JPAD	136
4.11	Take-off rotation angle check of the A220-300 parametric model - JPAD	137
4.12	Limit ground bank angle and minimum engine clearance calculation of the A220-330 parametric model - JPAD	137
4.13	Nose and main gear position limits of the A220-300 parametric model - JPAD	138
4.14	Turning radius calculation of the A220-300 parametric model - JPAD	138
4.15	A220-300 lift curves in all operating conditions at max aft and operative CG positions - JPAD	139
4.16	A220-300 drag polar curves in all operating conditions at max aft and operative CG positions - JPAD	140
4.17	A220-300 aerodynamic efficiency curves in all operating conditions at max aft and operative CG positions - JPAD	140
4.18	A220-300 balanced field length and decision speed calculation - JPAD	142
4.19	A220-300 take-off rotation speed and take-off safety speed evolution with engine failure speed - JPAD	142
4.20	A220-300 rates of climb in AEO condition against calibrated airspeed at several altitudes - JPAD	143
4.21	A220-300 rates of climb in OEI condition against calibrated airspeed at several altitudes - JPAD	143
4.22	A220-300 climb angles in AEO condition against calibrated airspeed at several altitudes - JPAD	144
4.23	A220-300 climb angles in OEI condition against calibrated airspeed at several altitudes - JPAD	144
4.24	A220-300 climb time evolution with altitude - JPAD	145
4.25	A220-300 maximum rates of climb against altitude - JPAD	145
4.26	A220-300 cruise flight envelope - JPAD	146
4.27	A220-300 cruise grid - JPAD	146
4.28	A220-300 landing speeds time histories - JPAD	147
4.29	A220-300 landing angles time histories - JPAD	148
4.30	A220-300 landing rate of descent time histories - JPAD	148
4.31	A220-300 design mission range profile - JPAD	151
4.32	A220-300 design mission time profile - JPAD	152
4.33	A220-300 design mission fuel burnt profile - JPAD	152
4.34	A220-300 aircraft mass evolution during the design mission - JPAD	153

4.35	A220-300 Fuel flow evolution during the design mission - JPAD	153
4.36	A220-300 rate of climb evolution during the design mission - JPAD	154
4.37	A220-300 TAS and CAS evolution during the design mission - JPAD	154
4.38	A220-300 Mach number evolution during the design mission - JPAD	155
4.39	A220-300 thrust and drag evolution during the design mission - JPAD	155
4.40	Payload-Range chart calculated with JPAD compared with the A220-300 Payload-Range chart [116].	156
4.41	JPAD total D.O.C. breakdown of the A220-300 parametric model.	157
4.42	Possible landing gear installation for high-wing turboprop aircraft [1].	159
4.43	Large propeller low-wing installation issues [1].	160
4.44	MDAO of the high-wing with wing-mounted engines configuration. Constraints on the minimum SSM and cruise Mach number. [1].	166
4.45	Static thrust update process for the MDAO of each high-capacity turboprop configuration. 169	
4.46	High wing with wing-mounted engines configuration. Pareto fronts and the “optimum” point [1].	170
4.47	Low wing with rear-mounted engines configuration. Pareto fronts and the “optimum” point [1].	171
4.48	Three-lifting surfaces configuration. Pareto fronts and the “optimum” point [1]. . .	172
4.49	Final solution for each aircraft configuration [1].	173

LIST OF TABLES

2.1	IRON reference aircraft major geometric characteristics	11
2.2	IRON Loop 1 aerodynamic targets and weights assumption	12
2.3	IRON Loop1 performance targets	12
2.4	IRON Loop2 performance targets	17
2.5	Comparison between high-speed turboprop configurations and the DC-9 Super 80	19
2.6	IRON configurations comparison Loop 2	22
2.7	Design mission analysis results with different SFC	23
2.8	Economic assumptions - IRON Loop 2, Configuration 2 [11].	25
2.9	Comparison between IRON (Configuration 2) and the regional jet models – 1440nm [11].	25
2.10	Comparison between IRON (Configuration 2) and the regional jet models – 400nm [11].	25
2.11	IRON loop 2 class II weight breakdown.	28
2.12	IRON loop 2 – Modified wing twist distribution.	30
2.13	IRON loop 2 – Effect of center of gravity on C_{Lmax} in take-off and landing configurations.	33
2.14	Aerodynamic efficiency at different center of gravity position with and without riblets.	35
2.15	IRON Loop 2 - Take-off simulation results.	37
2.16	V_{MC} calculation at several weight conditions.	38
2.17	IRON Loop 2 - Climb results.	38
2.19	IRON Loop 2 - Landing simulation results.	38
2.18	IRON Loop 2 - Cruise results.	39
2.20	IRON Loop 2 - Design mission simulation results.	39
2.21	IRON Loop 2 - Typical mission simulation results.	40
2.22	IRON Loop 2 - Mission data comparison between IRON and A220-300 (1600nm)	40
2.24	IRON Loop 2 - DOC comparison between IRON and A220-300 (1600nm)	41
2.25	IRON Loop 2 - DOC comparison between IRON and A220-300 (400nm)	41
2.23	IRON Loop 2 - Mission data comparison between IRON and A220-300 (400nm)	41
3.1	Summary of aircraft parameters.	56
3.2	Summary of fuselage parameters.	59
3.3	Summary of cabin layout parameters.	60
3.4	Summary of a generic lifting surface parameters.	62
3.5	Summary of airfoil parameters.	63
3.6	Summary of engine parameters.	65

3.7	Summary of nacelle parameters.	65
3.8	Summary of landing gears parameters.	66
3.9	Component reference mass percentages with respect to the MTOW.	67
3.10	FAA airplane design group classification for geometric design for airports [91].	76
3.11	Summary of take-off simulation input parameters	83
3.12	Landing simulation touchdown types	86
3.13	Summary of landing simulation input parameters	89
3.14	Summary of take-off noise trajectories simulation input parameters	91
3.15	Summary of climb simulation input parameters	93
3.16	Summary of cruise analysis input parameters	95
3.17	Summary of descent simulation input parameters	98
3.18	Summary of mission profile simulation input parameters	100
3.19	Summary of the physical quantities collected by the mission profile calculator	100
3.20	Summary of mission phases	101
3.21	Summary of V-n diagram input parameters required by JPAD	105
3.22	Fuselage update strategies implemented inside JPAD.	113
3.23	Generic lifting surface update strategies implemented inside JPAD.	113
4.1	A220-300 main geometrical data and interior arrangements.	123
4.2	A220-300 main weights data.	123
4.3	A220-300 main engines data.	124
4.4	A220-300 TLARs.	125
4.5	Main input data concerning the analysis configuration file of JPAD.	130
4.6	Main input data concerning the operating conditions configuration file of JPAD.	130
4.7	Main input data concerning the weights analysis configuration file of JPAD.	130
4.8	Main input data concerning the balance analysis configuration file of JPAD.	130
4.9	Main input data concerning the aerodynamic and stability analysis configuration files of JPAD.	131
4.10	Main input data concerning the performance analysis configuration file of JPAD.	131
4.11	Main input data concerning the costs analysis configuration file of JPAD.	133
4.12	Main output data concerning the JPAD weights analysis of the A220-300 parametric model.	134
4.13	Main output data concerning the JPAD balance analysis of the A220-300 parametric model.	135
4.14	Main output data concerning the JPAD aerodynamic and stability analysis of the A220-300.	139
4.15	Main output data concerning the JPAD take-off simulation of the A220-300.	141
4.16	Main output data concerning the JPAD climb analysis of the A220-300.	143
4.17	Main output data concerning the JPAD cruise analysis of the A220-300.	146
4.18	Main output data concerning the JPAD landing analysis of the A220-300.	147
4.19	Main output data concerning the JPAD design mission analysis of the A220-300.	149
4.20	Main output data concerning the JPAD Payload-Range analysis of the A220-300.	156

4.21	Main output data concerning the JPAD operating costs analysis of the A220-300 related to the design mission of 3100 nm.	157
4.22	TLARs for an innovative high-capacity turboprop aircraft [1]	159
4.23	Assumptions and main configuration effects on weights, aerodynamics and longitudinal static stability concerning all high-capacity turboprop configuration under investigation.	165
4.24	MDAO problem definition for all the high.capacity turboprop configurations. . . .	168
4.25	Multi-disciplinary analysis cycle results of all optima aircraft configurations. . . .	173
4.26	Optimization results. Comparison between the three optima high-capacity turboprop configurations and the reference regional turbofan platform on a mission of 1600 nm.	174

LIST OF SYMBOLS

- $C_{L\alpha_H}$ Horizontal tail lift curve slope.
- $C_{L\alpha_V}$ Vertical tail lift curve slope.
- $C_{L\alpha}$ Aircraft trimmed lift curve slope.
- $C_{l\alpha}$ Airfoil lift curve slope.
- $C_{m\alpha}$ Airfoil pitching moment curve slope.
- \mathcal{R}_c Canard aspect ratio.
- \mathcal{R}_h Horizontal tail aspect ratio.
- \mathcal{R}_v Vertical tail aspect ratio.
- \mathcal{R}_w Wing aspect ratio.
- Δ Generic quantity variation.
- $\Delta \mathbf{R}$ Range variation.
- $\Delta \mathbf{W}_{\text{Payload}}$ Payload variation calculated during the mission profile analysis iterative loop.
- $\Delta \mathbf{X}_{\text{NCap}}$ Fuselage nose trunk cap percent extension.
- $\Delta \mathbf{X}_{\text{TCap}}$ Fuselage tail trunk cap percent extension.
- $\Delta \mathbf{f}$ Equivalent parasite area variation.
- $\Delta \mathbf{t}_{\text{Hold}}$ Time interval related to a constant pilot bar input.
- Γ Dihedral angle.
- Λ Reference lifting surface sweep angle.
- $\Lambda_{\text{LEc/4}}$ Equivalent wing sweep at quarter chord.
- Λ_{LEeq} Equivalent wing sweep at leading edge.

Λ_{LEw} Wing sweep at leading edge.

Ω Aerodynamic twist angle.

Ψ Turnover angle.

Θ Aircraft pitch angle.

Θ_{TD} Aircraft pitch angle at touchdown.

α Angle of attack.

$\alpha_{0,L}$ Wing zero-lift angle of attack.

$\alpha_{0,l}$ Airfoil zero-lift angle of attack.

α_{max} Airfoil stall angle of attack.

α^* Airfoil angle of attack of end linear trait.

α_B Aircraft angle of attack in body reference frame.

α_g Aircraft angle of attack when on the ground.

α_w Absolute wing angle of attack.

α_w Wing angle of attack.

β_n Nose gear steering angle.

δ Angle between the aircraft centerline and the line passing through the center of the nose and main gears group.

δ_r Rudder deflection angle.

$\dot{(\)}$ Time derivative of a specific quantity.

α_0 Initial value of the angle of attack time derivative during take-off rotation.

α_{red} Negative angle of attack time derivative after constant angle of attack phase.

η_v Vertical tail dynamic pressure ratio.

$\left. \frac{d\epsilon}{d\alpha} \right|_H$ Downwash gradient related to the horizontal tail plane.

γ Flight path angle.

γ_{approach} Flight path angle for the approach phase.

λ_C Fuselage cylinder trunk fineness ratio.

λ_N Fuselage overall fineness ratio.

-
- λ_N Fuselage nose trunk fineness ratio.
- λ_T Fuselage tail trunk fineness ratio.
- \mathcal{S} Switching function of the set of ODE.
- \mathcal{T} Temperature.
- \mathcal{T}_{std} Standard temperature.
- μ Wheels rolling friction coefficient.
- μ_b Wheels braking friction coefficient.
- ϕ Aircraft roll angle.
- ϕ_N Fuselage windshield angle.
- ϕ_T Fuselage upsweep angle.
- ρ Air density.
- ρ_l Fuselage lower cross-section deforming factor.
- ρ_u Fuselage upper cross-section deforming factor.
- τ_r Rudder effectiveness index.
- $\varepsilon_{g_{tip}}$ Geometric twist angle at lifting surface tip station.
- \mathbf{x} Vector of state variable.
- q_0 Initial value of the pitching angular velocity during take-off rotation.
- \mathbf{a} Fuselage lower cross-section percent thickness.
- AC** Aerodynamic Center.
- \mathbf{b} Reference lifting surface span.
- \mathbf{b}_1 Wing span up to kink station.
- \mathbf{b}_2 Wing span from kink station up to tip station.
- \mathbf{b}_h Horizontal tail span.
- \mathbf{b}_w Wing span.
- \mathbf{c}'_r Lifting surface root chord of the first panel assuming same sweep angles of the second panel.
- $\mathbf{C}_{d,i}$ Airfoil minimum drag coefficient.
- \mathbf{C}_{Dmin} Minimum drag Coefficient.

C_D Drag Coefficient.

c_{eq} Equivalent lifting surface root chord.

$C_{l,0}$ Airfoil lift coefficient at zero angle of attack.

$C_{l,i}$ Airfoil ideal lift coefficient (minimum drag).

$C_{l,max}$ Airfoil maximum lift coefficient.

C_{L0} Aircraft trimmed lift coefficient at zero angle of attack.

$C_{Lmax,Clean}$ Maximum lifting coefficient in clean configuration.

$C_{Lmax,LND}$ Landing maximum lifting coefficient.

$C_{Lmax,TO}$ Take-Off maximum lifting coefficient.

$C_{Lmax_{inv}}$ Maximum lifting coefficient in inverted flight.

C_{Lmax} Maximum lifting coefficient.

C_L Lifting Coefficient.

C_l^* Airfoil lift coefficient of end linear trait.

$C_{m,ac}$ Airfoil pitching moment coefficient with respect to the aerodynamic center.

C_{Mcg} Aircraft pitching moment coefficient with respect to the center of gravity.

$C_{N\delta_r}$ Rudder control power.

c_r Lifting surface root chord.

c_t Lifting surface tip chord.

D Drag.

d_B Fuselage equivalent cylinder section diameter.

d_{in} Nacelle inlet diameter.

d_{in} Nacelle outlet diameter.

d_{max} Nacelle maximum diameter.

dcs Drag counts.

$dt_{cutback}$ Time interval to pass from 100% to the cutback thrust setting.

$dt_{retraction}$ Landing gears retraction time interval.

E_{cr} Cruise aerodynamic efficiency.

-
- E_{\max} Maximum aerodynamic efficiency.
- e_s Main landing gears static deflection of struts and tires.
- f_{reserve} Percentage of the initial fuel to be considered as reserve.
- g Gravitational acceleration.
- h Aircraft altitude.
- $h_{\text{alternate}}$ The diversion cruise altitude for the mission profile analysis.
- h_{cg} Aircraft center of gravity height from ground.
- h_{cutback} The thrust cutback altitude.
- h_{end} Climb (or descent) phase final altitude.
- h_f Fuselage section height.
- h_g Main landing gears leg length.
- h_{holding} The holding altitude for the mission profile analysis.
- h_{in} Climb (or descent) phase initial altitude.
- $h_{\text{LND start}}$ Initial landing altitude.
- h_N Fuselage nose trunk tip height offset.
- h_{obstacle} Obstacle height for take-off and landing phases.
- h_T Fuselage tail trunk tip height offset.
- i_h Horizontal tail incidence angle.
- i_w Wing incidence angle.
- I_{xx} Inertia moment with respect to the longitudinal axis X.
- I_{xy} Inertia product in the x-y plane.
- I_{xy} Inertia product in the y-z plane.
- I_{xz} Inertia product in the x-z plane.
- I_{yy} Inertia moment with respect to the right-wing-oriented axis Y.
- I_{zz} Inertia moment with respect to vertical axis Z.
- k_α Slope of the pitching angular velocity time law for the take-off simulation.

- K_{δ_r} Interference factor due to the rudder deflection.
- k_{approach} Percentage of the stall speed defining the approach speed.
- K_b Rudder span effectiveness factor.
- $k_{CL_{\text{max}}}$ Percentage of the maximum lift coefficient (Take-off or Landing) which defines the max allowed lifting coefficient for the simulation.
- $K_{\text{CR weight}}$ Percentage of the maximum take-off weight to be used for the cruise analysis.
- $K_{\text{DESC weight}}$ Percentage of the maximum take-off weight for the descent phase simulation.
- k_{DragOEI} Drag coefficient increment due to failed engine.
- k_{Flare} Percentage of the stall speed defining the flare speed.
- K_{F_v} The ratio between the yawing moment coefficient of the fuselage-vertical tail combination to the yawing moment coefficient of the isolated vertical tail.
- k_{inlet} Nacelle outlet section center to maximum diameter ratio.
- k_{inlet} Nacelle inlet diameter to maximum diameter ratio.
- k_{inlet} Nacelle maximum diameter non-dimensional longitudinal position.
- $K_{\text{LND weight}}$ Percentage of the max take-off weight to be used for the initial approach phase.
- k_{outlet} Nacelle outlet diameter to maximum diameter ratio.
- $k_{\text{Touchdown}}$ Percentage of the stall speed defining the touchdown speed.
- $K_{\text{weight AEO}}$ Percentage of the maximum take-off weight for the AEO climb simulation.
- $K_{\text{weight OEI}}$ Percentage of the maximum take-off weight for the OEI climb simulation.
- L** Lift.
- l_B Fuselage overall length.
- l_C Fuselage cylinder trunk length.
- l_m Distance between the main landing gears group and the aircraft center of gravity.
- l_{Nac} Nacelle overall length.
- l_N Fuselage nose trunk length.
- l_n Distance between the nose landing gears group and the aircraft center of gravity.
- l_T Fuselage tail trunk length.
- l_v Distance between the aircraft center of gravity and the vertical tail aerodynamic center.

-
- M** Mach number.
- m** Aircraft mass.
- M_{alternate}** The diversion cruise Mach number for the mission profile analysis.
- M_{cr}** Cruise Mach number.
- M_D** Dive Mach number.
- m_f** Fuel mass.
- M_{holding}** The holding Mach number for the mission profile analysis.
- M_{MO}** Max Operating Mach number.
- n_{lim,neg}** Negative limit load factor.
- n_{lim,pos}** Positive limit load factor.
- N_v** Yawing moment provided by the vertical tail.
- R_{alternate}** The diversion range for the mission profile analysis.
- R_{climb}** Range covered during the climb phase.
- R_{current}** Calculated value of the range during the mission profile analysis iterative loop.
- R_{mission}** The mission range for the mission profile analysis.
- R_{target}** Target range for the mission profile analysis.
- r_{turn}** Aircraft 180° turning radius.
- RC** Rate of Climb.
- Re** Reynolds number.
- S** Reference lifting surface area.
- s** Aircraft position.
- S_B** Fuselage cylinder cross-section area.
- S_c** Canard area.
- S_h** Horizontal tail area.
- S_v** Vertical tail area.
- S_{wet}** Fuselage wetted area.
- S_w** Wing area.

SL Sea Level.

T Thrust.

t Time.

t_{climb} Instant at which the load factor becomes equal to 1 during take-off airborne phase.

t_{holding} The holding duration for the mission profile analysis.

t_{Hold} Instant related to the achievement of the maximum allowed lift coefficient in take-off.

t_{Rot} Instant related to the beginning of the take-off rotation.

t_{td} Instant related to the aircraft touchdown during the landing phase.

u Known input function of a system.

V Aircraft velocity.

V_∞ Aircraft speed.

V₁ Take-off decision speed.

V₂ Take-off safety speed.

V_{act} OEI Take-off speed related to the pilot reaction after failure.

V_A Landing approach speed.

V_{CAS} Calibrated airspeed.

V_{climb CAS} Reference calibrated airspeed for the climb phase simulation.

V_{descent CAS} Reference calibrated airspeed for the descent phase simulation.

V_D Dive speed.

V_{ef} Take-off engine failure speed.

V_{Flare} Landing flare speed.

V_{LO} Lift-off speed.

V_{MC} Minimum Control Speed.

V_{MO} Max Operating speed.

V_{MU} Minimum Unstick Speed.

V_{Rot} Take-off rotation speed.

V_{S,LND} Landing stall speed.

-
- $V_{S,TO}$ Take-off stall speed.
- V_{TAS} True airspeed.
- V_{TD} Landing touchdown speed.
- V_w Wind speed.
- W Aircraft weight.
- $W_{f,max}$ Maximum storable fuel mass.
- $W_{f,new}$ New value of the fuel mass calculated during the mission profile analysis iterative loop.
- $W_{f,used}$ Used fuel mass calculated during the mission profile analysis iterative loop.
- w_f Fuselage section width.
- $W_{payload}$ Payload mass.
- wt Aircraft wheelbase.
- wt Aircraft wheel track.
- X_{AC} Aerodynamic Center longitudinal position.
- X_{CG} Longitudinal center of gravity position.
- $X_{d,max}$ Nacelle maximum diameter longitudinal position.
- $X_{d,max}$ Nacelle outlet section center vertical position.
- X_{end} Ground distance at which the take-off noise trajectory simulation ends.
- $X_{LE,mac}$ Mean aerodynamic chord longitudinal position in local reference frame.
- $X_{LE,mac}$ Mean aerodynamic chord spanwise position in local reference frame.
- $X_{LE,mac}$ Mean aerodynamic chord vertical position in local reference frame.
- X_{LEw} Canard apex position in body reference frame.
- X_{LEw} Wing apex position in body reference frame.
- X_{LE} Lifting surface station leading edge longitudinal position in local reference frame.
- X_{LG} Main landing gears group position in body reference frame.
- X_{TE} Lifting surface station trailing edge longitudinal position in local reference frame.
- $X_{transition}$ Airfoil transition abscissa.
- Y Generic lifting surface section spanwise position.

Y_{CG} Lateral center of gravity position.

Y_e Critical engine lateral position in body reference frame.

Y_{in} Wing generic movable surface initial spanwise position.

Y_k Wing kink section spanwise position.

Y_{out} Wing generic movable surface final spanwise position.

Y_v Vertical tail side force.

Z_{CG} Vertical center of gravity position.

Z_{LE} Lifting surface station vertical position in local reference frame.

ACRONYMS

ACARE Advisory Council for Aeronautics Research in Europe.

ADORNO Aircraft Design and nOise RatiNg for regiOnal aircraft.

AEA Association of European Airlines.

AEO All Engines Operative.

AGILE Aircraft 3rd Generation MDO for Innovative Collaboration of Heterogeneous Teams of Experts.

AIAA American Institute of Aeronautics and Astronautics.

APR Auxiliary Power Reserve.

APU Auxiliary Power Unit.

ATA Air Transportation Association of America.

ATAG Air Transport Action Group.

BADA Base of Aircraft Data.

BFL Balanced Field Length.

BPR By-Pass Ratio.

BRF Body Reference Frame.

CAS Calibrated Air Speed.

CASM Cost Per Available Seat Mile.

CD Collaborative Design.

CIRA Centro Italiano Ricerche Aerospaziali.

CRD Collaborative Remote Design.

- CSALP** CSeries Aircraft Limited Partnership.
- DAF** Design of Aircraft and Flight technologies.
- DLR** Deutsches Zentrum für Luft- und Raumfahrt.
- DOC** Direct Operating Costs.
- DOE** Design Of Experiments.
- DSL** Domain Specific Language.
- EAS** Equivalent Air Speed.
- EASA** European Aviation Safety Agency.
- ECAC** European Civil Aviation Conference.
- EIA** Energy Information Agency.
- FAR** Federal Aviation Regulations.
- GA** Genetic Algorithms.
- GDP** Gross Domestic Product.
- GE** General Electric.
- GUI** Graphical User Interface.
- H2020** Horizon 2020.
- HBPR** High By-Pass Ratio.
- IADP** Innovative Aircraft Demonstrator Platform.
- IAS** Indicated Air Speed.
- IATA** International Air Transport Association.
- IRON** Innovative turbopROp cOnfigurationN.
- ISA** International Standard Atmosphere.
- ITT** Indicated Turbine Temperature.
- IVP** Initial Value Problem.
- JPAD** Java toolchain of Programs for Aircraft Design.
- LFL** Landing Field Length.

-
- LRF** Local Reference Frame.
- LTO** Landing and Take-Off.
- MAC** Mean Aerodynamic Chord.
- MD** Monolithic Design.
- MDAO** Multi-Disciplinary Analysis and Optimization.
- MEW** Manufacture Empty Weight.
- MLW** Maximum Landing Weight.
- MOEAs** Multi-Objective Evolutionary Algorithms.
- MTOW** Maximum Take-Off Weight.
- MZFW** Maximum Zero-Fuel Weight.
- ODE** Ordinary Differential Equations.
- OEI** One Engine Inoperative.
- OEW** Operating Empty Weight.
- OML** Outer Mold-Line.
- OOP** Object-Oriented Programming.
- OPEC** Organization of the Petroleum Exporting Countries.
- PSO** Particle Swarm Optimization.
- RANS** Reynolds-averaged Navier–Stokes equations.
- RPKs** Revenue Passenger Kilometers.
- SAR** Specific Air Range.
- SFC** Specific Fuel Consumption.
- SMILE** Statistical Machine Intelligence and Learning Engine.
- SSM** Static Stability Margin.
- TAS** True Air Speed.
- TLARs** Top-Level Aircraft Requirements.
- TNAC** Transport Aircraft Noise Classification.

TOFL Take-Off Field Length.

TOW Take-Off Weight.

TRL Technology Readiness Level.

VeDSC Vertical tail DESign Stability and Control tool.

ZFW Zero-Fuel Weight.

GLOSSARY

Advisory Council for Aeronautics Research in Europe More info can be obtained at the following link <https://www.acare4europe.org/about-acare>.

Aircraft 3rd Generation MDO for Innovative Collaboration of Heterogeneous Teams of Experts

The AGILE innovation project is granted by the European Commission. AGILE targets multidisciplinary optimization using distributed analysis frameworks. The project is set up to proof a speed up of 40% for solving realistic MDO problems compared to today's state-of-the-art. The use cases are realistic overall aircraft design tasks for conventional, strut-braced, box-wing and BWB configurations. The scope of development: Advanced optimization techniques and strategies; Techniques for collaboration; Knowledge-enabled information technologies. The project ran from 2015 to 2018 and was part of the Horizon 2020 program. (<https://www.agile-project.eu/>).

Aircraft Design and nOise RatiNg for regiOnal aircraft The ADORNO project focuses on the development of aircraft models for a regional aircraft engine platform. The main objective is to provide aircraft requirements (e.g. thrusts, oftakes, etc.) as well as trade factors for specific fuel consumption, engine drag and engine weight on fuel burn for both a year 2014 reference aircraft and a CS2 target aircraft. In addition, an aircraft noise method will be developed and integrated in an aircraft design chain. (<https://http://www.adorno-project.eu/>).

American Institute of Aeronautics and Astronautics The American Institute of Aeronautics and Astronautics (AIAA) is a professional society for the field of aerospace engineering. The AIAA is the U.S. representative on the International Astronautical Federation and the International Council of the Aeronautical Sciences. (<https://www.aiaa.org/>).

Centro Italiano Ricerche Aerospaziali The Italian aerospace research center.

Design of Aircraft and Flight technologies Design of Aircraft and Flight technologies research group of the University of Naples Federico II (www.daf.unina.it).

Deutsches Zentrum für Luft- und Raumfahrt German aerospace research center..

Energy Information Agency United States Energy Information Agency.

Gross Domestic Product The total value of all the goods and services produced within a country's borders. It's generally used to measure the growth of the country's economy.

Innovative turbopROp cOnfigurationN Research project that complies with the European Union topic JTI-CS2-2015-CPW02-REG-01-03 (Green and cost efficient Conceptual Aircraft Design including Innovative Turbo-Propeller Power-plant) as part of the Clean Sky 2 program for Horizon 2020.

Revenue Passenger Kilometers A measure of traffic for an airline flight, bus, or train calculated by multiplying the number of revenue-paying passengers aboard the vehicle by the distance traveled.

Reynolds-averaged Navier–Stokes equations Time-averaged equations of motion for fluid flow.

Chapter **1**

INTRODUCTION

In much of society, research means to investigate something you do not know or understand.

– Neil Armstrong

1.1 Definition of the research question

Every research work starts from an unsolved question or problem and its definition is the first fundamental milestone in the path to the PhD degree.

Being this an Industrial Engineering thesis, the research question should be addressed to the improvement of the current state of the art in one or more of its sub-fields. In this case the subject of interest is Aerospace Engineering with a focus on Preliminary Aircraft Design.

Nowadays most of the major airlines, especially in the regional aircraft segment from 20 to 150 seats, are demanding for a replacement of several hundred heritage airplanes, currently in service around the world, which are now coming to the end of their useful commercial life. Furthermore, the climate change and the increasing lack of resources claim for a clear reduction of the aviation impact on citizens and the environment. Thus, the integration of innovative and affordable technologies in future aircraft platforms will play a key role to increase the appeal and the benefits for both customers and airlines [1].

Preliminary Aircraft Design can address both these issues defining a new frontier of innovation in terms of configurations and technologies suitable for the ever-increasing demand for more green and efficient aircraft. The **International Air Transport Association (IATA)**, the **Air Transport Action Group (ATAG)** and the Clean Sky 2 Programme have defined several environmental targets as driving parameter in the research for new technologies.

As reported by **ATAG** in [2], in 2008, leaders from across the industry gathered at **ATAG's Aviation & Environment Summit** to deliver a strategic vision for aviation's sustainable development, signing the Commitment to Action on Climate Change. As part of the commitment, the **ATAG** board developed a set of environmental goals for the short, medium and long-term.

These goals were supported and reiterated by the IATA Board and the association's Annual General Meeting. They include:

- An average improvement in fuel efficiency of 1.5% per year from 2009 to 2020.
- A cap on net aviation CO₂ emissions from 2020 (carbon-neutral growth).
- A reduction in net aviation CO₂ emissions of 50% by 2050, relative to 2005 levels.

The Clean Sky 2 Programme aims to accelerate the introduction of new technology in the 2025-2035 timeframe. By 2050, 75% of the world's fleet now in service (or on order) will be replaced by aircraft that can deploy Clean Sky 2 technologies [3]. High level objectives for Clean Sky 2 can be summarized as follow:

- A reduction in CO₂, NO_x and environmental noise from -20% to -30% in the 2014-2024 timeframe.
- A reduction in CO₂ of -75% by 2050.
- A reduction in NO_x of -90% by 2050.
- A reduction in environmental noise of -60% by 2050.

If one target is to reduce aircraft environmental impact, at the same time world air transport demand will more than double by 2038, reaching almost 18 trillion RPKs for all commercial aircraft segments [4]. In addition, oil price is expected to double in the next 20 years, regardless of temporary fluctuations [5].

The combination of these factors results in a very challenging design process for engineers to come up with innovative aircraft configurations or technologies.

Regional aircraft are playing an increasingly role in the evolution of the airline operations. For many years, this growth has been faced by a wide adoption of regional jets. Their success can be largely attributed to their popularity with passengers, who prefer them because they are more comfortable and faster than turboprops.

However, despite the regional jets success, turboprop engines are 10-30% more efficient than jet engines in cruise conditions leading to a potential consistent reduction of the amount of fuel used per mission as well as pollutant emissions [1]. According to ATR forecasts, assuming all short haul flights operated by regional jets today are replaced by modern turboprops, 11% of overall regional aviation CO₂ emissions could be saved [5].

To summarize, regional jets provides for faster connections with a higher payload in spite of higher fuel consumptions and pollutant emissions; while turboprop aircraft allows to reduce air transport environmental impact but with lower passengers capacity and lower speed. Thus, the research question at the base of this thesis is: **What could be the impact, in terms of performance, that innovative high-capacity turboprop aircraft configurations can have on the current regional aircraft scenario?**

To answer this question, the first step will be to provide an in-depth market analysis of the regional aircraft segment to better highlight both the current state of the art as well as current market forecasts for the next 20 years.

1.2 Aircraft market scenario

The last decade has been marked by a series of broadly felt economic crises and negative shocks, starting with the Global Financial Crisis of 2008–2009, followed by the European Sovereign Debt Crisis of 2010–2012 and the global commodity price realignments of 2014–2016. Furthermore, 2018 introduced and reinforced several challenges to the global economy. The escalation of issues like the global trade war and Brexit brought tension to markets in every region of the globe. After a strong period of optimism (specially in US), the stock market starts to accommodate and regional economies will likely slow their pace of growth to the following years. As a result, economic forecasts carried out by Embraer estimate an annual **Gross Domestic Product (GDP)** growth rate of about 2.8% in the period 2019-2038 [4].

Air transport demand has always had a tight correlation with each country **GDP**. Consumers travel more when they have greater income, but there also appear to be spikes in demand related to deregulation of global travel by open-skies agreements, service quality improvements, and additional routes. The mature regions of North America and Europe have seen these effects over the last 10 years; the developing regions of Africa, Asia, the Middle East, and Latin America will see the largest gains over the next 10 years as they benefit from higher incomes and these other factors [6].

As middle-class and consumer spending increase in many regions, the propensity to travel will develop with new emerging regional markets taking the lead. By 2037, the Middle East and Asia Pacific will be the fastest growing markets, with an annual growth rate of 5.7%, followed by Latin America with 5.2%, Africa with 4.8% [5] as shown in Figure 1.1.

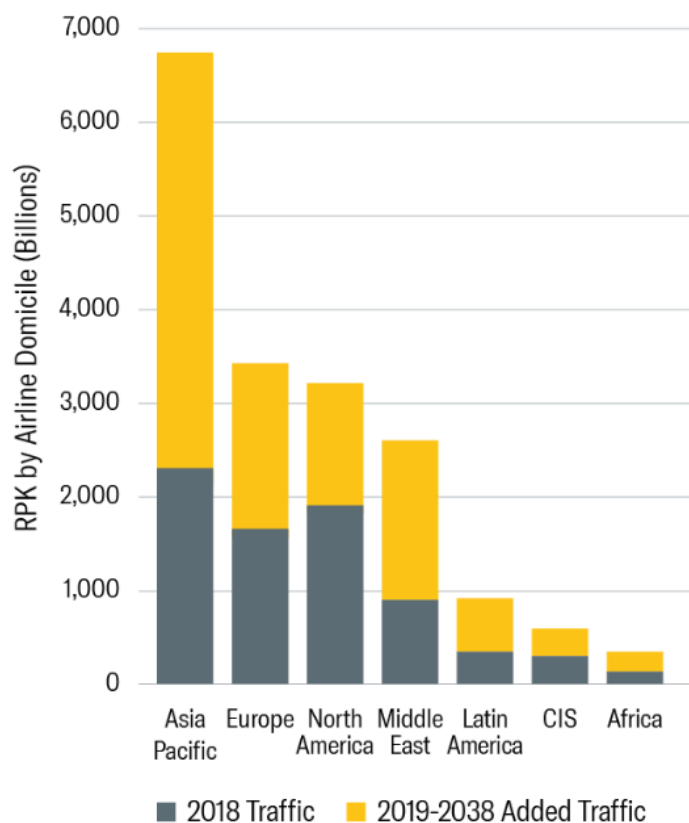


Figure 1.1 Worldwide air transport demand growth 2019-2038 [4].

An in-depth market analysis of the regional aircraft segment has revealed that world passenger traffic is expected to maintain 4.4% annual growth over the next two decades [4] [5] [7]. Although macro-economic trends forecast an economical growth over next years, oil price is expected to increase as well, remarking its role as key decision factor for every airline. As shown in Figure 1.2, Energy Information Agency (EIA), Organization of the Petroleum Exporting Countries (OPEC) and World Bank expects almost the same trend for oil price outlook which will probably double by 2037 after temporary fluctuations and a period of decrease from 2014 to 2016. Oil price will again reach a price per barrel of about 80-100US\$. Higher oil prices influence airline decisions to replace or retire less efficient aircraft types. As oil price volatility surges, the demand for more fuel-efficient and segment-optimized aircraft will increase [8]. Focusing on the regional market, the oil price increase will probably be higher in regional airports than in main airports due to higher fuel transportation costs, which translates to a worldwide average extra cost of +34% [5].

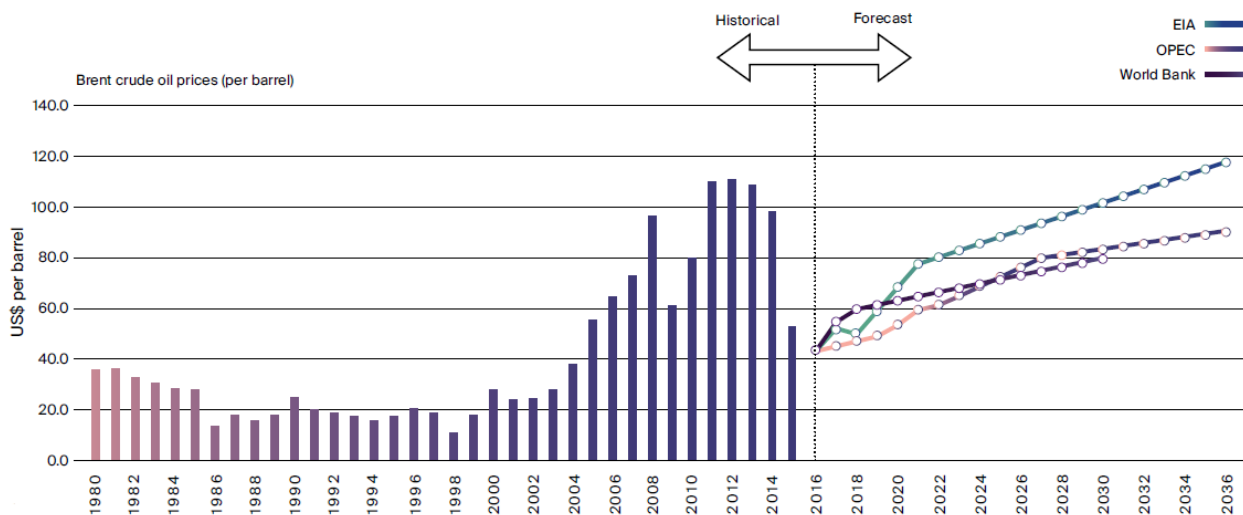


Figure 1.2 Oil price forecast - Oxford Economics, OPEC and EIA [8].

The fast growth of the regional markets, especially in emerging countries, will contribute in creating several new routes making the single-aisle aircraft segment the ideal solution to satisfy new market requirements.

The small single-aisle aircraft segment has finally been rejuvenated with a new product offering, after a long period of being served by sub-optimized and aging products. The segment has played an important role in growing regional markets and short- to medium-haul mainline markets. Since 2006, the number of routes flown by aircraft around the world in this seat segment has increased by 20%. Aircraft in this segment connect over 7,000 city pairs as an integral part of airline networks globally [8].

According to Airbus Global Market Forecast [7], taking the single-aisle fleet, both average seats and range have increased. Seats average 169 seats today, with average range 590 nm. From Figure 1.3 and Figure 1.4, it can also be seen that there is significant variation around the mean for aircraft size and particularly for range. As well as showing the wide spectrum of operations for which the airlines use these aircraft, it also demonstrates why the range capability of aircraft products is an important consideration for airlines and manufacturers alike; a capability which also equates to flexibility.

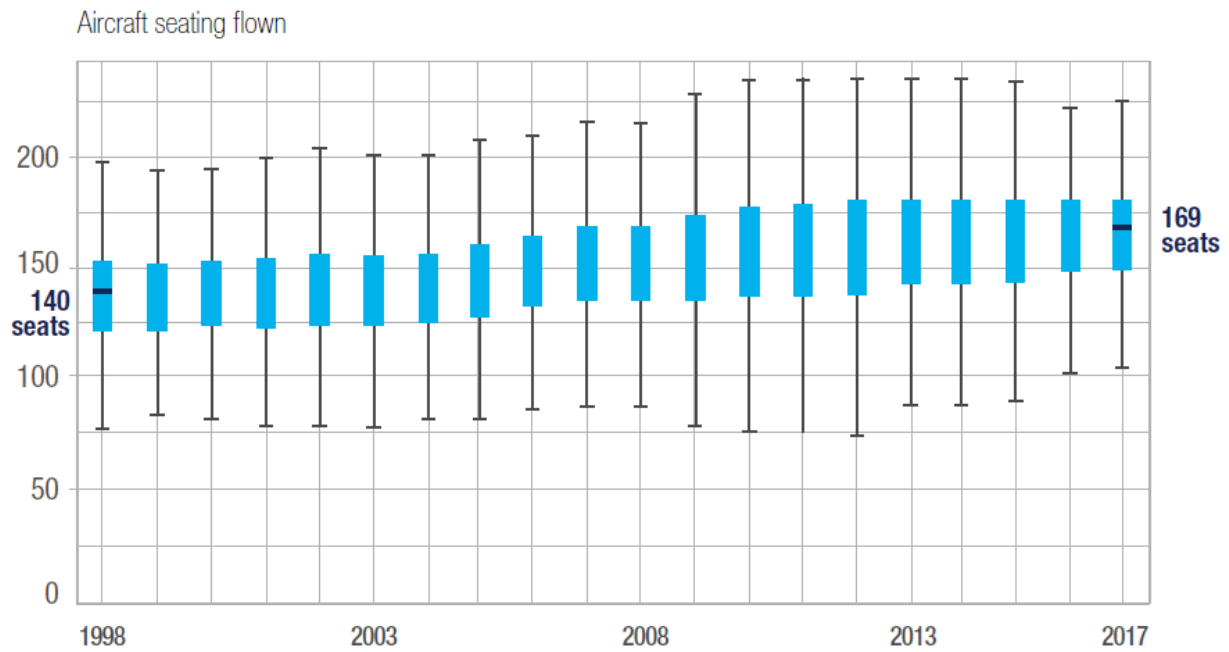


Figure 1.3 Distribution of seats offered by single-aisle aircraft over the years [7].

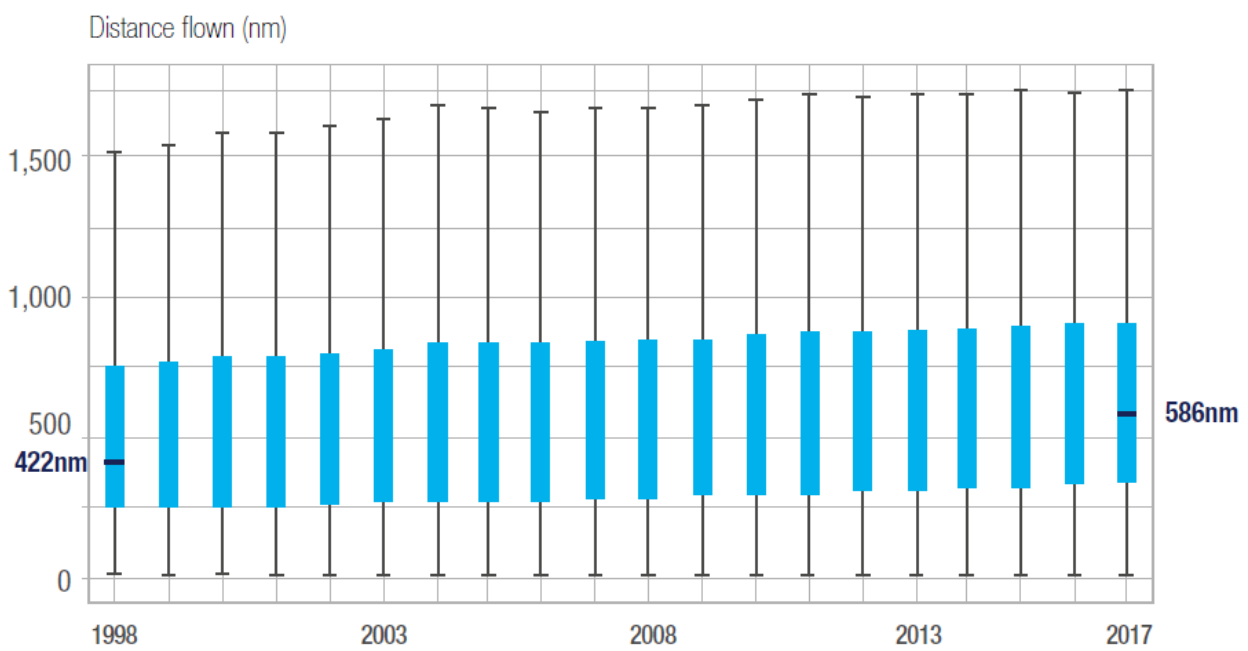


Figure 1.4 Distribution of distances flown by single-aisle aircraft over the years [7].

Most of the major player in the regional market scenario like ATR, Embraer, Bombardier and Airbus foresee great opportunity both for turboprop aircraft and regional jets. As shown in Figure 1.5, up to 2016 these two aircraft type have been sharing the regional market evenly with a slightly increasing advantage of regional jets due to a higher number of seats and longer typical mission distances with respect to the typical distance of 330nm of turboprops [5].

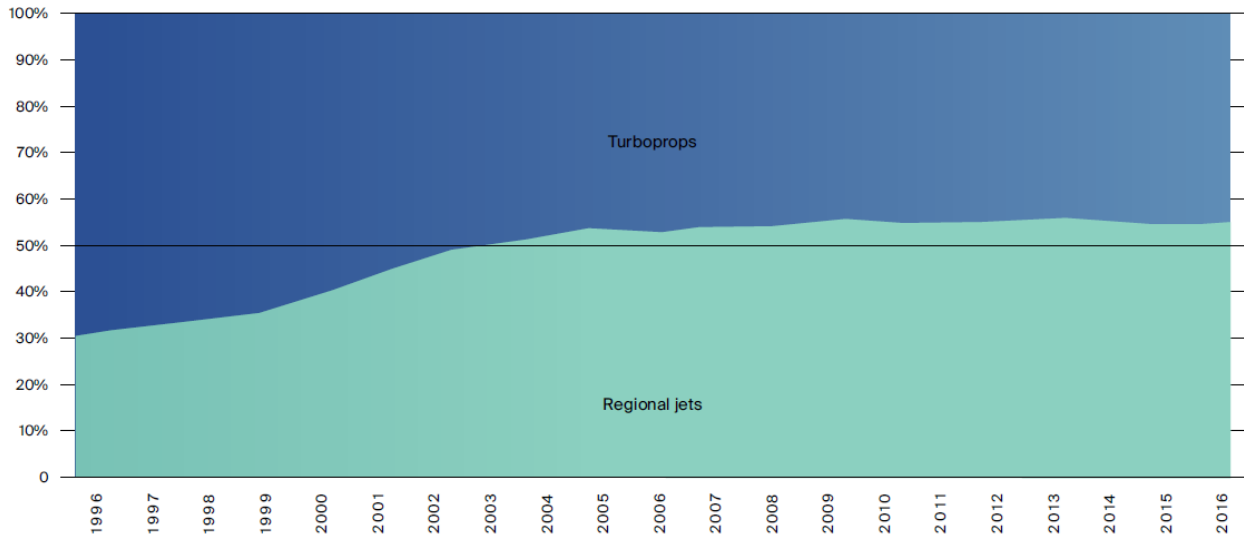


Figure 1.5 In-service fleet share (turboprops and regional jets) - Flightglobal Fleets Analyzer [8].

The great interest in the small single-aisle aircraft segment up to 150-seats is also highlighted by the most relevant manufacturers in this sector.

- Bombardier Commercial Aircraft forecasts 12550 deliveries in the 60- to 150-seat segment over the 2017-2036 time frame. The total market is valued at US\$820 billion with the small single-aisle segment responsible for around 70% of revenues [8].
- Embraer foresees world demand for 10550 new aircraft with up to 150-seats over the next 20 years representing a total market value of US\$600 billion. Of these, 8230 are regional jets up to 150-seats, while 2320 are turboprops [4].
- Airbus Global Market Forecast [7] estimates a total number of 37400 delivered aircraft in the next 20 years for a global value of US\$5.8 trillion. Of these, 28500 belongs to the small single-aisle jet segment representing 76% of all delivers and 54% of the total value.
- ATR market analysis [5] calculates that of the 2260 turboprop in service at 2017, 3020 new aircraft will be delivered of which 1120 units (40%) will be used as replacement for aged aircraft and 4060 units (60%) will represent fleet growth. Furthermore, 630 of the 3020 new turboprops will be in the 40- to 60-seats segment while 2390 aircraft will be in the 61- to 80-seats segment highlighting an increased interest toward higher passengers capacities.

1.3 Research context and thesis structure

Nowadays several research works are focused on the investigation of new regional platforms which cope with ever more stringent performance, costs and emissions requirements. Innovation, in the regional aircraft context, can come from improved power plants, innovative materials, technologies for improved aerodynamics (e.g. natural laminar flow or riblets) as well as from unconventional aircraft concepts (e.g. Box-Wing, Strut-Braced Wings, Blended Wing Body, Three-Lifting Surfaces, etc.) [1].

The main Research and Innovation programme funded by the European Union is **Horizon 2020 (H2020)**. With its €80 billion of funding over 7 years (2014-2020), this financial instrument is helping companies, research centers and universities in developing innovation in a large variety of thematic areas with the purpose of proving global competitiveness to Europe.

One of the most important sectors of **H2020** deals with Smart, Green And Integrated Transport (**H2020-EU.3.4. - SOCIETAL CHALLENGES**). The European transport industry represents 6.3% of the Union's **GDP**, employing nearly 13 million of people. Since transport accounts for 63% of global oil consumption and 29% of the world CO₂ emissions, research programmes within **H2020** have the main purpose of developing more efficient, sustainable and environmental-friendly systems [9].

Under **H2020-EU.3.4.**, the programme **Clean Sky 2 (H2020-EU.3.4.5.)** is the one related to aircraft. **Clean Sky** is the largest European research programme developing innovative technologies aimed at reducing CO₂, gas emissions and noise levels produced by aircraft. Since this thesis work deals with the regional aircraft segment, the research programme of interest is the **H2020-EU.3.4.5.2. - Innovative Aircraft Demonstrator Platform (IADP)** regional aircraft which funded a large number of research projects.

The next chapter will provide a comprehensive description of **Innovative turboprop configurationN (IRON)** project and its first two loops of design activities in which the author of this thesis has been involved during his PhD. The project is focuses on the feasibility study of an innovative regional turboprop configuration with rear engines installation which is supposed to be competitive with respect to short/medium haul regional jets.

1.3.1 Thesis structure

Current research topics have highlighted the need for more efficient and environmental-friendly aircraft which can comply with ever more demanding performance requirements coming from the previously discussed market forecasts. A new generation of aircraft is about to be born and aircraft design engineers have the fundamental task of leading this innovation.

Starting from the final performance results of the second loop of design activities of the **IRON** project, the use of an innovative high-capacity turboprop aircraft appears to be a feasible solution to reduce the overall mission fuel consumption (and so pollutant emissions) as well as **Direct Operating Costs (DOC)** without losing too much in terms of flight time. This has been the main driver which led to the definition of the research question stated at the beginning of this introduction. To fully answer this latter, a more detailed investigation of all possible design solutions must be carried out. Thus, the research question can be further specialized in the following one: **Which high-capacity turboprop configuration could be the one that maximizes potential performance advantages with respect to the state of the art of current regional jet aircraft?**

To answer this question, in this thesis work a set of **TLARs** suitable for modern regional transport applications and in line with the main aircraft manufacturer market forecast will be defined. This will be used to design several innovative turboprop aircraft concepts and for each of them a **MDAO** process will be carried out to define the set of optima configurations.

Finally, a comparison with the current state of the art regional jet platform, represented by the Airbus A220-300, will be performed as done in the **IRON** project.

Being able to carry out such complex tasks requires to use ever more efficient and reliable analysis tools suitable for multi-disciplinary analyses and optimizations at several levels of fidelity. Thus, a fundamental part of this thesis work will deal with the description of the **JPAD** framework developed at the University of Naples Federico II.

The **JPAD** framework is the result of the efforts of the **DAF** group which involved several PhD students in a virtuous collaboration process including the author of this thesis work who has personally developed most of its modules including performance and **MDAO** modules.

The first one has been completely designed using a simulation-based approach to easily perform efficient and accurate analyses of both flight and ground performance; while the second one uses all the advantages provided by **OOP** to perform a full factorial **DOE** as well as multi-objective optimizations using computational intelligences like **GA** or **PSO** algorithms.

Having an in-house software for aircraft analyses and optimizations allowed to implement all the know-how gained by the **DAF** group during the last decade of research activities within the **JPAD** framework obtaining, this way, a competitive product with respect to the current aircraft design tool scenario. Furthermore, the possibility to easily extend its capabilities could be a key feature to face future market and research challenges.

Dealing this thesis with two parallel topics (aircraft design and software engineering), this thesis work will be organized in the following chapters.

- **Chapter 2** will provide a detailed description of the **IRON** project focusing on the first two loops of design activities and their results.
- **Chapter 3** will be completely focused on the description of the **JPAD** framework. Firstly, the state of the art of the current aircraft design software will be described highlighting strengths and weaknesses of the available tools. Secondly, the main structure of **JPAD** will be explained with special focus on the input file structure, the interconnected structure of analysis modules, the **GUI**, the automatic CAD generation process and its interoperability with external commercial tools. Then the **MDAO** module will be described both in terms of sensitivity studies capabilities and response surface optimizations.
- **Chapter 4** will deal with the application of the **JPAD** framework to investigate the topic stated in the research question. The procedure will be the one discussed before. A case study concerning an aircraft model similar to the Airbus A220-300 will be presented to show the **JPAD** capabilities as well as to provide the reference aircraft model to be used in the high-capacity turboprops comparison.
- **Conclusions** will discuss all main research outcomes as well as future developments.

Chapter **2**

THE IRON PROJECT

Aviation is proof that given, the will, we have the capacity to achieve the impossible.

– Eddie Rickenbacker

In response to the European Union topic JTI-CS2-2015-CPW02-REG-01-03 (Green and cost efficient Conceptual Aircraft Design including Innovative Turbo-Propeller Power-plant) of the second call for partners within the Clean Sky 2 programme the project **IRON** was created and approved with a scheduled duration of 6 years (2016-2022).

Centro Italiano Ricerche Aerospaziali (CIRA) is coordinator of this project, while the topic leader is Leonardo Company. Several European core-partners will work in the project as well like the engine manufacturer Avio Aero, part of the **General Electric (GE)** group. The **DAF** group of the University of Naples Federico II is a core partner of the project and the leader of the aerodynamic and performance work-package which main activities deal with the aerodynamic assessment and the performance evaluation of the innovative aircraft platform.

The project focuses on the feasibility study of an innovative regional turboprop configuration with rear engines installation which is supposed to be competitive with respect to short/medium haul regional jets. This can lead to a cleaner wing with possibilities to achieve laminar flow extension. Furthermore, a wing without engine nacelles and free of propeller interference effects will be characterized by more efficient high-lift systems resulting in a potential increment in maximum lift coefficient positively affecting ground performances.

The analysis of this kind of innovative configuration is characterized by several aerodynamic, performance and propulsion features that must be predicted with high accuracy and deep comprehension of involved phenomena to highlight possible improvements with respect to classical high-wing layout with wing-mounted engines.

The **IRON** project will also address this classical turboprop configuration. In this case one of the key elements is the reduction of the perceived propeller noise emissions.

A low-noise propeller system will be designed after exploring emerging technologies. This achievement will be attained while preserving the propulsion efficiency providing possible positive impacts on economic, environmental and social issues.

The research, addressed the analysis and design of the innovative regional aircraft configuration with rear-mounted engines, is scheduled to be carried out through 3 different loops of design with increasing level of complexity as shown in Figure 2.1 where the red dashed rectangle highlights the completed activities as well as the one still ongoing at the moment of writing. The IRON project aim is to complete the design process through numerical simulations and experimental validations reaching a Technology Readiness Level (TRL) of 4.

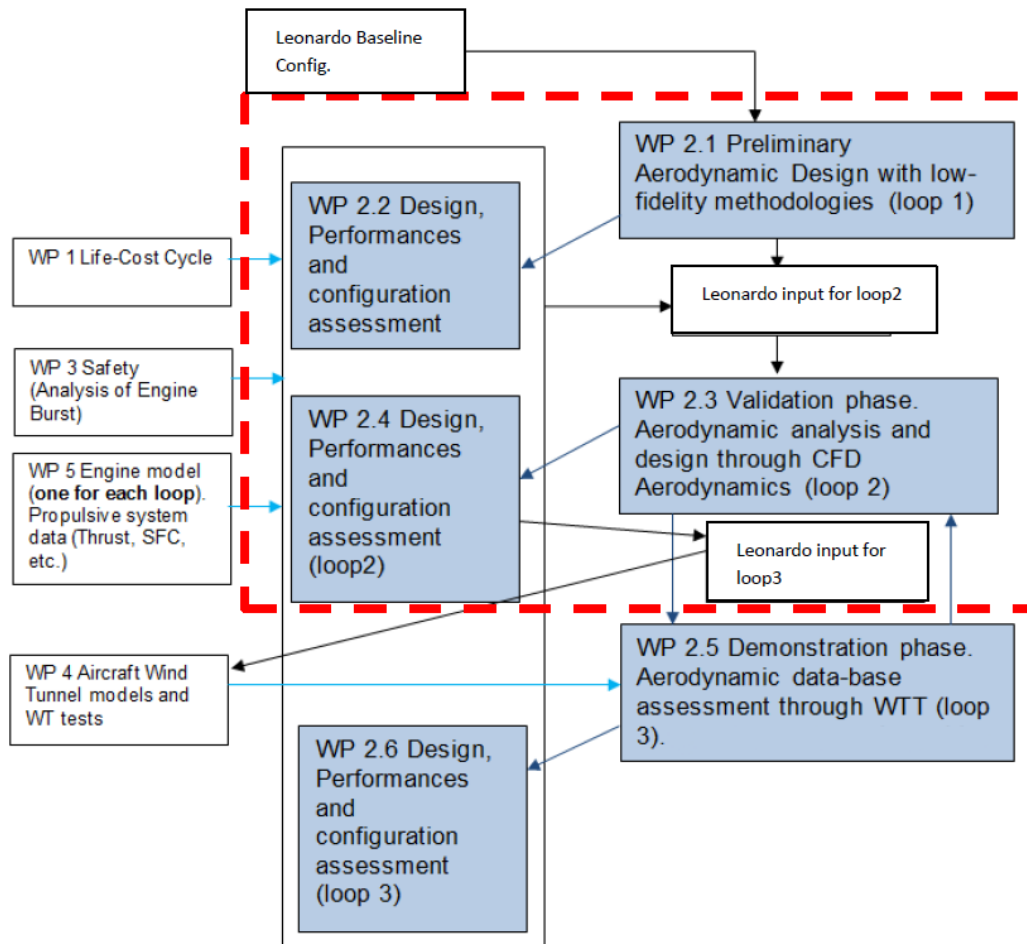


Figure 2.1 IRON project loops.

2.1 The first loop of design activities

The loop 1 analysis started in July 2016 from a baseline configuration provided by Leonardo Company (Figure 2.2) and ended in January 2017. TLARs have been issued by Leonardo company, which also provided the aircraft maximum takeoff weight and wing area.

These were very challenging, requiring a cruise Mach number of 0.62 at 30000 feet, with a moderately high lift coefficient and low drag to achieve a value of 18 in cruise aerodynamic efficiency, a maximum lift coefficient of 1.6 in clean conditions and 3.0 in landing conditions. Moreover, it is expected that the wing inner airfoils have a 18% relative thickness to allow landing gear to be stored within. Details are reported in Tables 2.1 to 2.3. All data have been assessed by Leonardo company.

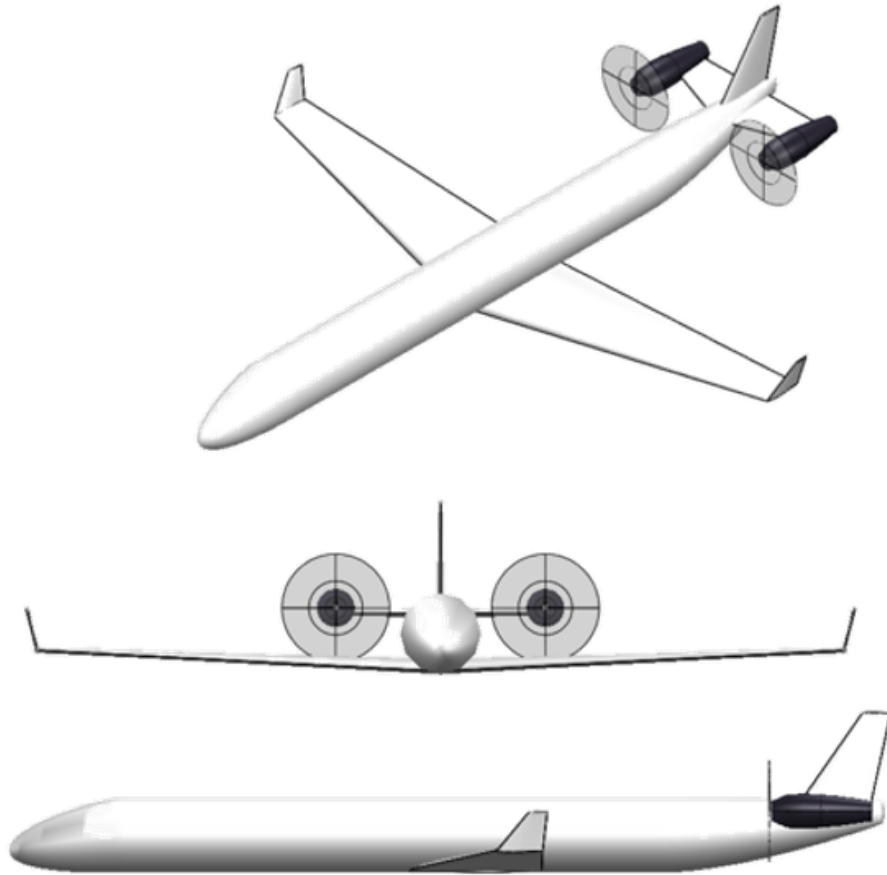


Figure 2.2 IRON aircraft model baseline.

Fuselage	Height/width	3.55 m
	Length	38.04 m
Wing	Area	105 m ²
	Aspect ratio	12
	Leading edge sweep angle	10.00°
	Taper ratio	0.40
Horizontal tail	Area	32.94 m ²
	Aspect ratio	2.5
	Leading edge sweep angle	10.38°
	Taper ratio	0.65
Vertical tail	Area	24.50 m ²
	Aspect ratio	1.36
	Leading edge sweep angle	45°
	Taper ratio	0.64

Table 2.1 IRON reference aircraft major geometric characteristics

As illustrated in the flowchart of Figure 2.1, the first activity that has been carried out during the first loop was focused on the preliminary aerodynamic design. This has been performed through the following steps as explained in [10], [11] and [12].

Aerodynamic targets	Values
Cruise efficiency	18.0
C_{Lmax} clean	1.6
C_{Lmax} take-off	2.4
C_{Lmax} landing	3.0
Weights assumptions	Values
Maximum Take-Off Weight (MTOW)	53610 kg
Maximum Zero-Fuel Weight (MZFW)	49345 kg
Maximum Landing Weight (MLW)	52000 kg
Operating Empty Weight (OEW)	33550 kg
Design Payload	13585 kg

Table 2.2 IRON Loop 1 aerodynamic targets and weights assumption

Design parameters	Values
Passengers capacity	130 at 32" seat pitch
Design range	1600 nm with 130 passengers at 104.5 kg 30' holding at 1500 ft 100 nm alternate at 15000ft 5% fuel reserve
Cruise speed	M = 0.62 at 30 kft and 97%MTOW
Time to climb	<= 13' from 1500 ft to 25 kft
One Engine Inoperative (OEI) ceiling	>= 16500 ft with 97%MTOW (ISA+10°C)
Take-Off Field Length (TOFL)	<= 1400 m with MTOW (ISA-SL)
Landing Field Length (LFL)	<= 1300 m with MLW (ISA-SL)

Table 2.3 IRON Loop1 performance targets

- **Airfoil design:** After an intensive preliminary design and optimization activity, wing airfoils have been analyzed with high-fidelity tools like MSES [13] and accurate RANS solvers. Very low drag with an extended laminar flow region on the upper and lower wing surface have been achieved. Two different airfoils have been designed for wing root and wing tip (this latter with reduced thickness ratio). Airfoils have also been designed to achieve high values of the maximum lift coefficient.
- **High-Lift design:** The flap shape and its best positioning at a specific deflection has been chosen to place the expansion peak of the pressure coefficient almost at the exit of the slot; this way it is possible to maximize the flow acceleration avoiding the flow separation on the flap. Once the right positioning of the flap has been fixed the flap geometry has been exported in terms of Cartesian coordinates and has been analyzed by means of both MSES and Reynolds-averaged Navier–Stokes equations (RANS) solver. To reach the target maximum lift coefficient of 3.0 in landing condition, the use of a single slot fowler flap was not enough. Thus, a leading edge high-lift device has been considered. However, to preserve the wing laminar flow, a morphing droop nose has been chosen.

- **3D wing aerodynamic assessment:** 3D isolated wing CFD analyses have been performed to assess the wing maximum lift capabilities.
- **Winglets design:** Winglets have been specifically designed to reduce the induced drag improving mainly the climb performance. Those have been designed and analyzed by means of 3D panel code available at the **DAF** research group of the University of Naples Federico II. This MATLAB code allows to generate a winglet shape starting from a reference wing geometry and assigning several design parameters (such as cant angle, toe angle, winglet height, winglet airfoil, etc.). Then an automated procedure performs aerodynamic calculations by means of 3D panel code.
- **Fuselage aerodynamic assessment:** Analyses have been performed by means of several approaches: the semi-empirical method suggested by Perkins [14], the strip theory method [15] [16], CFD **RANS** calculations and the FusDes method developed by the **DAF** research group [17]. Among these CFD results have been selected to for the following steps.
- **3D isolated tail planes aerodynamic assessment:** Horizontal tail aerodynamics has been estimated coupling the integrated aerodynamic characteristics of tail sections with the semi-empirical 3D lift dependent drag contribution [18].
- **Nacelles aerodynamic assessment (propellers off):** Nacelle aerodynamic analyses have been carried out by means of the semi-empirical approach proposed by Perkins [14].
- **Non-linear downwash estimation:** The methodologies used for the wing downwash calculation is the one proposed by Slingerland in his doctoral thesis [19]. This has been extended inside the UNINA **JPAD** framework considering a variable distance between the vortex plane and the horizontal tail position with the aircraft angle of attack resulting in a non-linear estimation of both downwash gradient and downwash angle.
- **Longitudinal static stability and control:** The assessment of the longitudinal static stability and control has been carried out using the Java framework named **JPAD**, which will be deeply analyzed in the next chapter, taking also into account for several non-linear effects like pendular stability, non-linear downwash and non-linear lift curve trait for all lifting surfaces.
- **3D aircraft aerodynamic assessment:** The complete aerodynamic assessment has been performed summing up all the previous contributions together with other effects due to miscellaneous, excrescences, interferences and gaps which have been calculated by means of classical semi-empirical approaches [18]. Trim drag contribution has also been considered according to the longitudinal static stability and control analyses.

At this point, trimmed drag polar and lift curves have been used to feed the **JPAD** framework performance module in charge of the ground and flight performance assessment. In addition to the aerodynamic dataset, the second required input has been the complete engine deck provided by the engine manufacturer GE Avio Aero, partner of the project. This has been developed according to power plant **TLARs** proposed by Leonardo.

The provided engine architecture is GE's unducted single fan engine, which is an unducted class engine, featuring a rotating propeller stage followed by a stator vanes stage both with variable pitch. This engine class architecture is conceived to provide higher propulsive efficiency than comparable turboprop engines at similar propeller sizes, at a lower noise, weight and complexity than other open rotor concepts.

The complete performance assessment has been carried out considering the following analyses:

- **Take-off**

- TOFL at MTOW, SL and International Standard Atmosphere (ISA) conditions.
- TOFL and second segment climb at a Take-Off Weight (TOW) related to the typical mission of 400nm with 130 passengers. Hot & high conditions (5400 ft and ISA+30°C).

- **Climb**

- Rate of climb, climb angle and climb gradient as function of the True Air Speed (TAS) in both All Engines Operative (AEO) and OEI conditions at different altitudes.
- Maximum rate of climb and maximum climb angle at different altitudes in both AEO and OEI conditions.
- Absolute and service ceilings in both AEO and OEI conditions.
- Time to climb from 1500ft to 25000ft in AEO condition using the both maximum rate of climb speed and the assigned speed of 190 knots of Calibrated Air Speed (CAS).
- Climb performance comparison with and without winglets.

- **Cruise**

- Evaluation of the cruise flight envelope as function of TAS, CAS and the Mach number.
- Evaluation of the cruise grid chart with the definition of the best range and long-range Mach numbers.
- Cruise performance comparison with and without winglets.

- **Landing**

- LFL at MLW, SL and ISA conditions with dry runway.

- **Mission profile**

- Simulation of both the design mission (1600nm) and the typical mission (400nm).
- Simulation results comparison with and without winglets.

- **Payload-Range**

- **Stall speed, minimum unstick speed (V_{MU}) and minimum control speed (V_{MC})**

Although most of the main performance did match the **TLARs**, some issues were identified. First of all, a maximum cruise Mach number of 0.60 was achieved with the most forward center of gravity position (the operative condition for this kind of aircraft configuration) instead of the value of 0.62 prescribed by the **TLARs**. This was mainly due to a lower value of the cruise aerodynamic efficiency, with this center of gravity position, compared to the **TLARs** value of 18.0 .

Engine static thrust did ensure a very good value of the **TOFL** (lower than the required value of 1400m), however the environmental noise generated by the sum of engine noise and airframe noise was too high requiring a review of both aerodynamics and engine thrusts.

A **LFL** bigger than 1300m was estimated leading to a sensitivity analysis of this performance with respect to the wing area and the $C_{L_{max}}$ in landing configuration. Since the achieved trimmed $C_{L_{max}}$ was already above the required value of 3.0, thanks to an excellent high-lift aerodynamic design, the result of the study showed that the aircraft could require an increased wing area.

The V_{MU} was moderately high requiring a longer **TOFL**. Thus, an increased horizontal tail area of about 20% was necessary.

The minimum climb gradient of 2.4% during the second segment of climb in hot and high conditions was not matched highlighting a lack of thrust compared to the **TOW** for the typical mission of 400nm.

The **MTOW** of 53610kg did not allow to store the adequate amount of fuel to fly the 1600nm design mission with the assigned **OEW** and payload. In particular three alternative solutions were proposed: to reduce the design payload about 15 passengers, to increase design fuel mass, leading to an increment in **MTOW** of about 2.5%, or to reduce the engine **Specific Fuel Consumption (SFC)** about 15%.

At the end of the first loop of design activities, the innovative aircraft configuration appeared to be not well harmonized in all its parts. Reviews of weights, balance, wing area and engines were necessary to solve all above-mentioned issues.

An in-depth weight and balance analysis carried out by Leonardo Company at the end of this loop, taking also into account on-board systems weights and positions, highlighted a larger center of gravity excursion, with respect to first assumption, passing from a 15-33% to a 4-52% of the mean aerodynamic chord as illustrated in Figure 2.3. This mainly due to the rear-mounted engines configuration and systems positions. This resulted in three critical issues:

- The aircraft was not stable with the most rearward center of gravity position (52% of the mean aerodynamic chord).
- The trimmed $C_{L_{max}}$ in landing configuration was lower than the prescribed value of 3.0 resulting in an even longer **LFL** which was already above the required value of 1300m.
- The revision of the neutral point position (27% of the mean aerodynamic chord) together with the new center of gravity excursion provided a large region where the aircraft cannot be operated.

The operative envelope illustrated in Figure 2.4 highlighted a drastic reduction of the minimum payload at which the aircraft can be used requiring different systems positions or a ballast in the forward part of the fuselage to solve the issue.

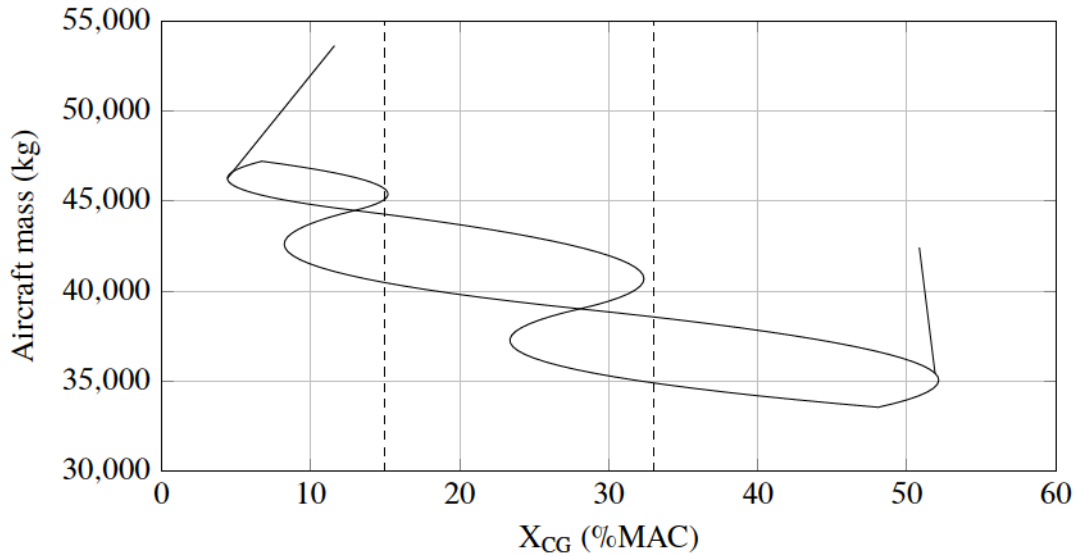


Figure 2.3 IRON boarding diagram - Loop 1 ending

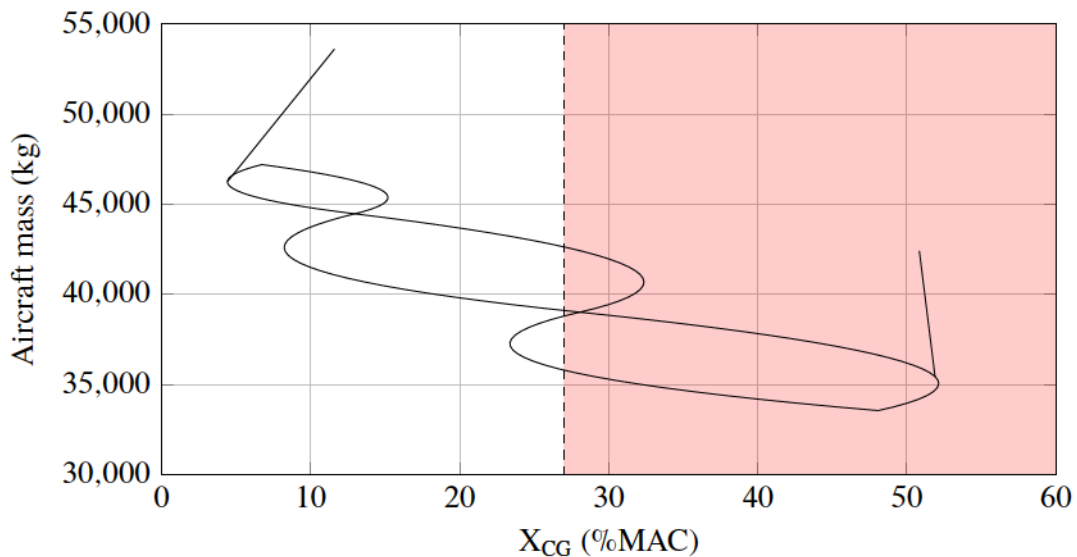


Figure 2.4 IRON boarding diagram limitations - Loop 1 ending

2.2 The second loop of design activities

The second loop of design activities started in the second half of 2017 and was deeply focused, in its starting phase, on an intensive preliminary design campaign to solve all issues that emerged from the first loop. Furthermore, the second loop of the IRON project saw a change in some of the main TLARs according to a market analysis carried out by the topic leader Leonardo Company.

As shown in Table 2.4, the cruise Mach number was increased up to 0.64 while the climb time was relaxed at 16 minutes. In addition, to take into account for future passengers needs, the single passenger weight has been increased from 104.5 kg to 108 kg resulting in a design payload of 14040 kg, 3.35% higher than loop 1.

Design parameters	Values
Passengers capacity	130 at 32" seat pitch
Design range	1600 nm with 130 passengers at 108 kg 30' holding at 1500 ft 100 nm alternate at 15000ft 5% fuel reserve
Cruise speed	M = 0.64 at 30 kft and 97%MTOW
Time to climb	<= 16' from 1500 ft to 25 kft
OEI ceiling	>= 16500 ft with 97%MTOW (ISA+10°C)
TOFL	<= 1400 m with MTOW (ISA-SL)
LFL	<= 1300 m with MLW (ISA-SL)

Table 2.4 IRON Loop2 performance targets

The **DAF** research group of the University of Naples Federico II played a fundamental role in this preliminary design phase by carrying out intense research activities aimed at identifying the best design solution for the innovative configuration.

The starting point of these design activities has been an in-depth literature review of all possible design solutions. The main reference research work has been the one developed by NASA together with McDonnell Douglas Corporation in 1981 [20]. In this work, three possible high-speed turboprop/propfan configurations appeared to be feasible to compete with the reference aircraft platform assumed as the DC-9 Super 80.

The selection of those was made after a first qualitative comparison between many different possible layouts, followed by a multi-disciplinary quantitative analysis of the following three selected configurations shown in Figure 2.5.

- Upper-wing mounted propfan (Configuration 1)
- T-Tail configuration with aft fuselage mounted propfan (Configuration 2)
- Horizontal tail mounted propfan (Configuration 3)

As shown in Table 2.5, the first and the third layouts have been identified as the best two solutions providing the highest improvements in terms of performance and **DOC**. All modifications to the baseline aircraft have been made keeping constant both wing area and **MTOW**.

As can be seen from Table 2.5, rear-mounted engines installation provides a much larger center of gravity excursion, higher horizontal tail weight as well as higher values of the equivalent parasite area. However, if the T-Tail configuration leads to lower performance and **DOC** enhancements than the wing mounted engines model, the horizontal tail mounted engines layout can mitigate the above-mentioned negative effects allowing to reach similar, or even better, performance and **DOC** improvement if compared with the classical wing-mounted engine configuration.

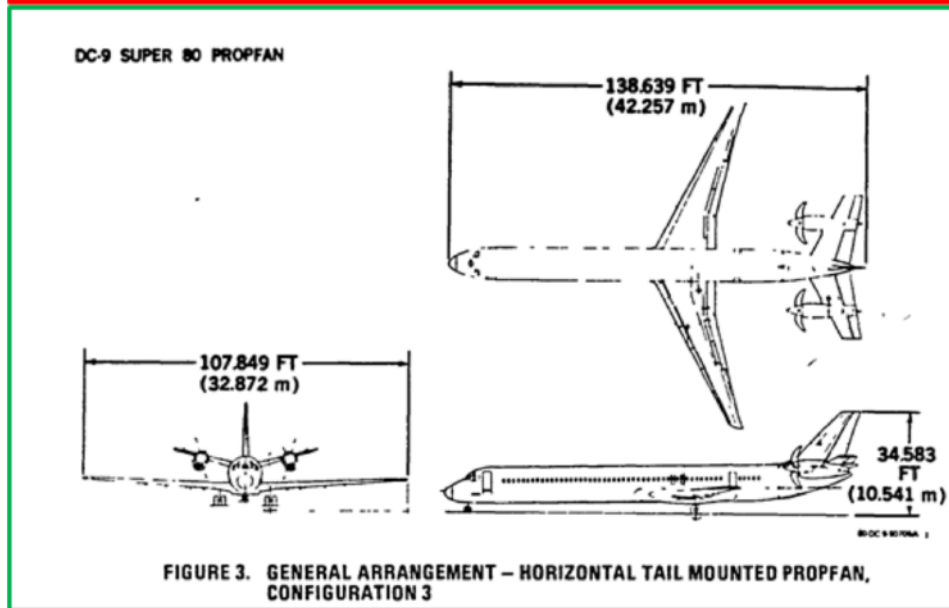
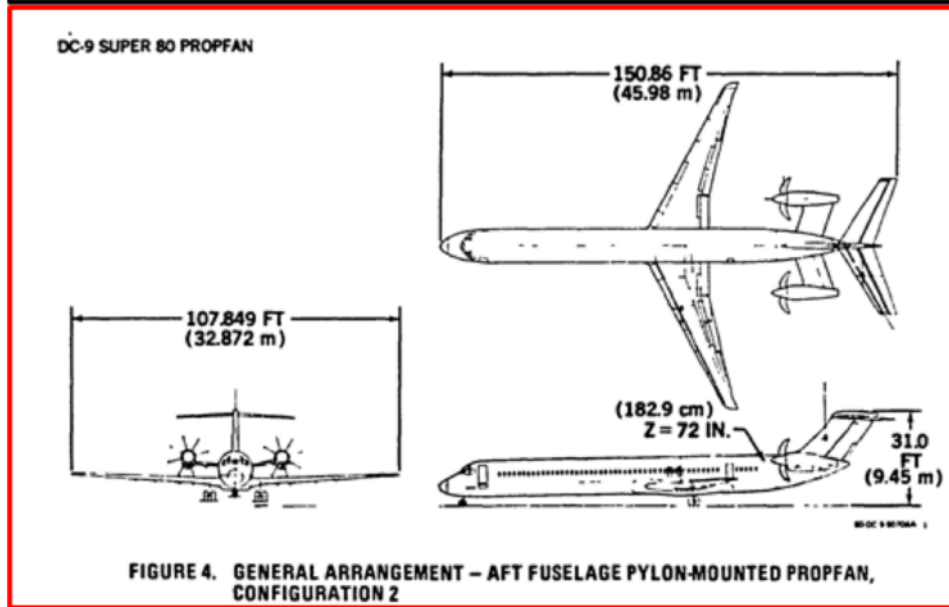
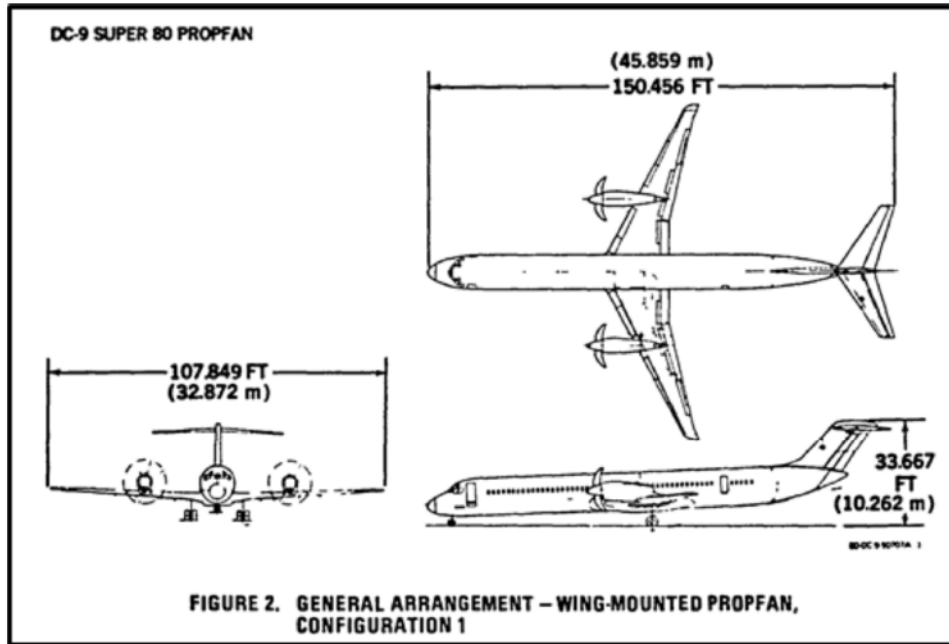


Figure 2.5 High-speed turboprop configurations derived from the DC-9 Super 80 [20].

	DC 9-80	Config. 1	Config. 2	Config. 3
Geometry				
S_w (m ²)	112	112	112	112
S_h (m ²)	29	33	36	47
S_h/S_w	0.26	0.29	0.32	0.42
S_v (m ²)	15	18	20	21
S_v/S_w	0.13	0.16	0.18	0.19
Number of propeller blades	0	8	8	8
Propeller diameter (m)	0	4.41	4.41	4.38
Weights (kg)				
Wing	6948	7026	6973	6984
Horizontal tail	870	880	1116	1301
Vertical tail	543	701	695	566
Fuselage	7381	7477	7575	7601
Landing gears	2424	2489	2470	2470
Nacelles and pylons	966	1145	2085	1032
Propulsion and engines systems	4736	5625	5623	5522
Fuel systems	330	311	619	357
Flight controls and hydraulics	1042	1135	1245	1337
Auxiliary Power Unit (APU)	381	381	381	381
Instruments	418	418	418	418
Air conditioning and pneumatics	879	1003	1133	992
Electrical and lighting system	1150	1159	1154	1157
Avionics and auto-flight controls	612	612	612	612
Furnishings	5041	5410	5086	5041
Anti-ice	269	274	271	281
Auxiliary gears	40	40	40	40
Manufacture Empty Weight (MEW)	34030	36087	37451	36091
Operator items weight	1652	1652	1652	1652
OEW	35682	37739	39103	37743
Max Payload	17842	18785	14393	15880
MTOW	63503	63503	63503	63503
Balance				
X_{CG} excursion (%MAC)	–	27%	60%	54%
Aerodynamics				
Δf nacelle and pylons (m ²)	0.0	-0.054	+0.119	-0.050
Δf wing scrubbing (m ²)	0.0	+0.036	0.0	0.0
Δf horizontal tail (m ²)	0.0	+0.046	+0.074	+0.109
Δf vertical tail (m ²)	0.0	+0.028	+0.041	+0.051
Δf total (m ²)	0.0	+0.057	+0.234	+0.110
Performance and DOC (% of baseline)				
Range variation	0.0%	+14.1%	+14.2%	+14.7%
Fuel burned variation	0.0%	-13.0%	-12.4%	-13.1%
Mean ΔDOC	0.0%	-6.0%	-5.8%	-7.9%

Table 2.5 Comparison between high-speed turboprop configurations and the DC-9 Super 80 [20].

Results of this research did prove that the initial **IRON** configuration of the first loop was indeed a good solution, however some adjustments were necessary. Following the path of the NASA work, three possible solutions were proposed to solve the first loop issues.

- Preserve the original configuration and shift back the wing while increasing the horizontal tail area and its aspect ratio.
- Change the configuration moving to a T-Tail layout.
- Change the configuration to a three-lifting surfaces layout.

Qualitative analyses have been carried out on each configuration leading to the following considerations.

In the first case, an increased horizontal tail area and a more aft wing position would have made the aircraft longitudinally stable but with cruise efficiency and high-lift performance below the required values.

The T-Tail configuration would have ensured longitudinal static stability, as well as cruise aerodynamic efficiency, while providing poor high-lift capabilities and balance issues due to a very rearward mass concentration. Thus, this configuration has been discarded since the first stage of design.

Finally, the three-lifting surfaces layout would have granted the longitudinal stability (although with a lower static stability margin) potentially increasing, at the same time, both aerodynamic efficiency and high-lift capabilities. Adding a third lifting surface could result in the possibility to reduce the tail download required to trim the aircraft. Thus, the trimmed $C_{L_{max}}$ could have been increased while the trim drag contribution could have been reduced, resulting in a higher value of the cruise aerodynamic efficiency. The potential increment of the $C_{L_{max}}$ could have also led to a reduced wing area providing an additional benefit on cruise aerodynamic efficiency as well as a reduction in aircraft weight (unless the third lifting surface would have been heavier than the wing weight reduction). Furthermore, the third lifting surface could have allowed to shift forward the aircraft neutral point position as well as giving the possibility to optimize both the center of gravity excursion and the neutral point position, at fixed static stability margin, by changing wing, horizontal tail and canard sizes and positions. After this qualitative comparison, the first and the third solutions were considered. For each of them a multi-disciplinary quantitative analysis has been performed to define the best configuration to be used as baseline for the second loop of design.

As described in [10], three different aircraft configurations have been considered assuming for each of them the horizontal tail mounted engines layout. Top views of each of these configurations can be found in Figure 2.6.

- Configuration 1: classical two lifting surfaces
- Configuration 2: classical two lifting surfaces with boarding diagram limitations (smaller horizontal tail)
- Configuration 3: three-lifting surfaces

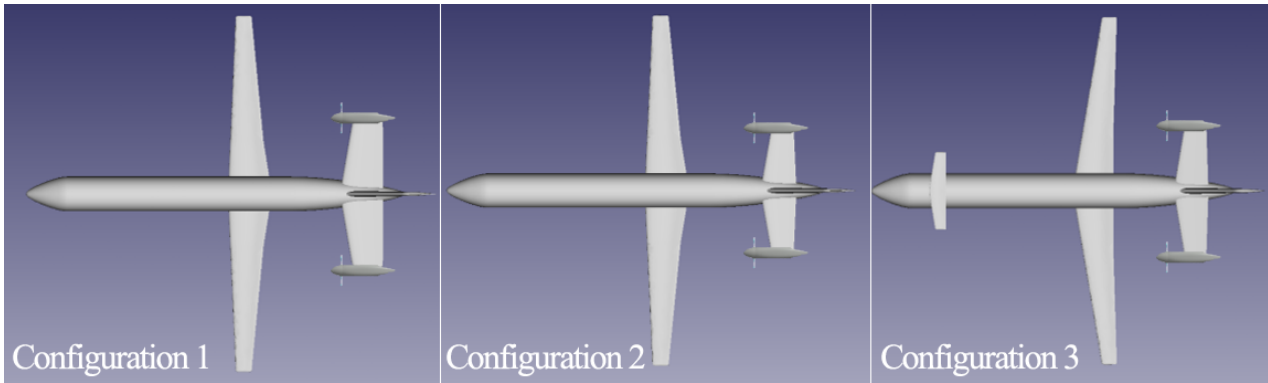


Figure 2.6 IRON configuration comparison Loop 2 - Top views.

All configurations have been designed following the same procedure: i) semi-empirical methodologies implemented in the **JPAD** framework have been used, together with some high-fidelity aerodynamic results coming from the first loop concerning airfoils, high-lift devices, winglets and fuselage, to analyze a large number of configurations generated by varying several design parameters (wing position, wing area, wing sweep angle, horizontal tail area, horizontal tail aspect ratio, and so on); ii) results of those analyses have been used to build up response surfaces useful for an optimization process and iii) configuration optimization.

The multi-objective optimization process has been carried out to identify optima configurations for each of the above-mentioned case. This has been accomplished by means of the **JPAD** framework available at **DAF** research group which implements the MOEA Framework [21], a free and open source Java library for developing and experimenting with **Multi-Objective Evolutionary Algorithms (MOEAs)** and other general-purpose computational intelligence. To accomplish the optimization process, the ε -NSGA-II and OMOPSO algorithms have been used.

ε -NSGA-II is an extension of NSGA-II that uses an ε -dominance archive and randomized restart to enhance search and find a diverse set of Pareto optimal solutions. Full details of this algorithm are given in [22].

OMOPSO is a multi-objective particle swarm optimization algorithm that includes an ε -dominance archive to discover a diverse set of Pareto optimal solutions. OMOPSO was originally introduced by Sierra and Coello Coello in [23].

According to the chosen number of design parameters, more than 7000 different combinations (each combination representing an aircraft) have been generated and analyzed to define the response surface on which to perform the optimization process. The Pareto front, in this particular problem was a multidimensional frontier, according to the chosen design parameters. Targets of the optimization process have been the cruise parameter W/E_{cruise} as well as the take-off and landing factors $W/S_w \cdot C_{L_{\text{max}}}$. To ensure the aircraft stability, a static stability margin of 5% has been assigned as constraint.

An example of two objectives Pareto front for the optimization of the Configuration 1 is shown in Figure 2.7. A comparison between the three optimized configurations is illustrated in Figure 2.6 while all the major results are summarized in Table 2.6.

The selection of each optimum configuration from their related Pareto front has been led by the cruise parameter W/E_{cruise} while take-off and landing factors have been selected to ensure **TOFL** and **LFL** values complying with **TLARs**.

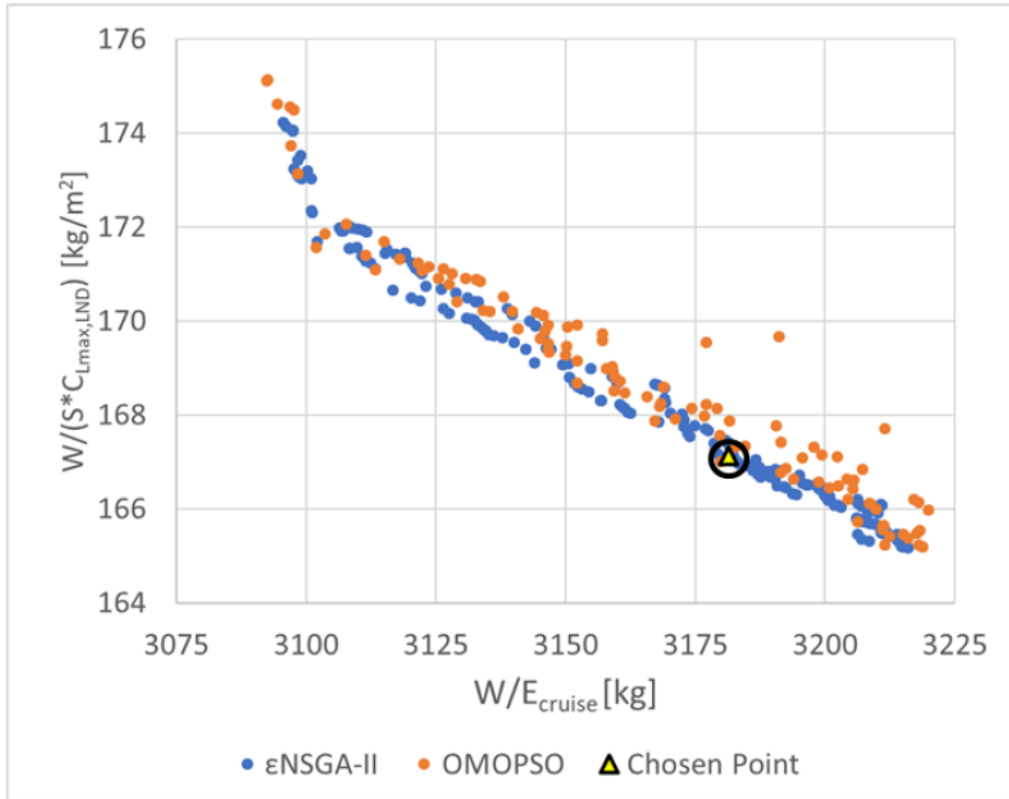


Figure 2.7 Example of Pareto front for the optimization of Configuration 1 - IRON Loop 2

	Configuration 1	Configuration 2	Configuration 3
S_w (m ²)	103.0	105.0	98.6
\mathcal{R}_w	12.2	12.0	12.1
X_{LEw} (m)	20.29	19.9	20.5
Δ_{LEw} (deg)	2.5	2.5	10.0
S_h (m ²)	56.0	37.0	38.4
S_h/S_w	0.54	0.35	0.39
\mathcal{R}_h	3.48	4.23	4.40
S_c (m ²)	–	–	11.7
S_c/S_w	–	–	0.12
\mathcal{R}_c	–	–	5.47
X_{LEc} (m)	–	–	6.0
X_{CG} range (%cMAC)	9-53%	11-40%	-35-0%
MTOW (kg)	54976	54105	54849
Cruise efficiency	17.3	17.7	18.4
C_{Lmax} Clean	1.70	1.70	1.91
C_{Lmax} Take-Off	2.63	2.63	2.90
C_{Lmax} Landing	3.19	3.09	3.40
Max cruise Mach number	0.63	0.64	0.66

Table 2.6 IRON configurations comparison Loop 2

Configuration 1 was characterized by a very large horizontal tail area (S_h of 56m^2) about 54% of the wing area. This provides an increment of both the maximum take-off weight and induced drag leading to the lowest cruise efficiency among the three solutions.

To avoid a large horizontal tail area, a limitation on the center of gravity range has been imposed leading to the Configuration 2. This aircraft must operate within the imposed X_{CG} variation of 11-40% allowing to reach a higher cruise efficiency with respect to the first configuration, a lower maximum take-off weight and a slightly reduced maximum lift coefficient in landing. However, the first two configurations did not match the required cruise aerodynamic efficiency of 18.0.

The three-lifting surfaces configuration (Configuration 3) was characterized by a reduced wing area and back-shifted wing position which led to a center of gravity excursion ahead of the mean aerodynamic chord leading edge. In this case the trimmed conditions in cruise could be achieved with a reduced download on the horizontal tail, resulting in a lower trim drag contribution. This provided a higher cruise efficiency (18.4 with respect to 17.7 of the Configuration 2). In addition, the maximum achievable lift coefficient was increased thanks to the third lifting surface lift contribution.

The definition of the three-lifting surfaces model (Configuration 3) came later during the preliminary design activities of the second design loop of the **IRON** project. In the meanwhile, Configuration 2 was used as reference model to better understand possible operative advantages coming from the use of such an innovative turboprop configuration.

The conference paper presented at the 2018 AIAA Aviation Technology, Integration, and Operations Conference [11], provides a detailed review of the analyses carried out on the Configuration 2 aircraft model. Here, due to a lower cruise aerodynamic efficiency with respect to the required value of 18.0 as well as an increased aircraft weight with respect to first loop assumptions (see Table 2.2), the mission profile analysis highlighted the impossibility to cover the required range of 1600nm with the design payload of Table 2.4 and the reference **SFC** coming from the engine deck provided by GE Avio Aero.

Similar to the first loop a sensitivity analysis has been carried out to estimate the reduction in **SFC** needed to comply with **TLARs**. Instead of a reduction of 15%, foreseen during the first loop, this configuration required only a -10% as reported in Table 2.7.

Assuming the reference **SFC** condition in Table 2.7, the maximum range that the aircraft can operate with the design payload is 1440nm as shown in Figure 2.8.

	Reference SFC	SFC-10%	SFC-15%
Mission range + 100nm alternate cruise (nm)	1700	1700	1700
Total mission duration (min)	322	322	322
Block time (min)	266	266	266
Aircraft weight at mission start (kg)	54105	54105	53800
Initial fuel weight (kg)	7294	6708	6400
Block fuel (kg)	5777	5295	5043
Fuel reserve (% of the initial fuel)	5%	5%	5%
Design passengers number	130	130	130
Allowed passengers number	125	130	130

Table 2.7 Design mission analysis results with different **SFC** - IRON Loop 2, Configuration 2 [11].

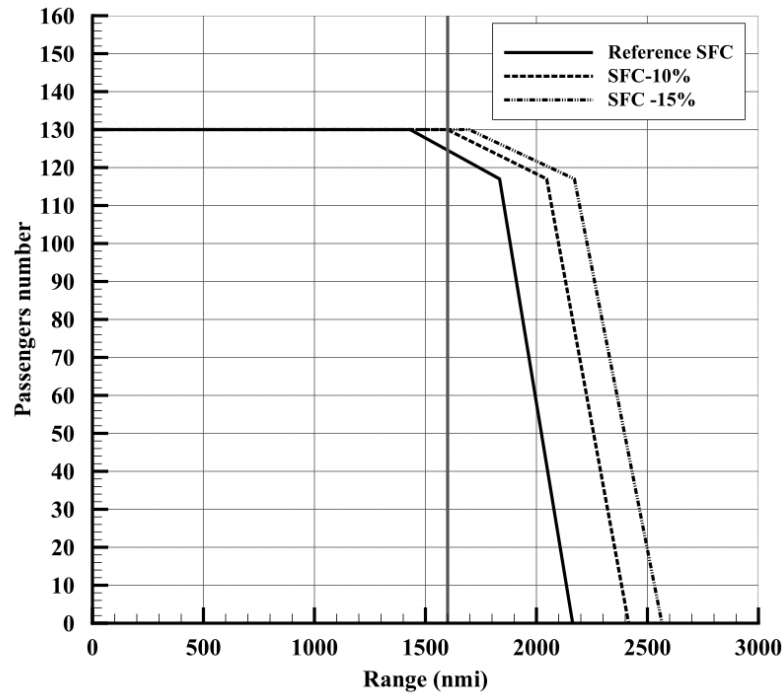


Figure 2.8 Payload-Range: effects of different cruise SFC - IRON Loop 2, Configuration 2 [11].

Since the main scope of the Clean Sky 2 project deals with the design of an aircraft with reduced emissions (thus less fuel burned per mission) a comparison between the IRON platform and a similar regional jet, like the Airbus A220 (previously known as Bombardier CS300), has been performed.

This reference regional jet has been chosen because it has TLARs very similar to the innovative aircraft platform under investigation. Not knowing the precise aerodynamic database of this regional jet, in the first instance some assumptions have been made to perform comparisons between this latter and the IRON aircraft.

A more refined assessment of the reference regional jet platform has been performed during the second loop of design by means of the JPAD framework.

As described in [11], in the preliminary design phase, the aerodynamic database of the reference regional jet aircraft model has been obtained adding about 20 drag counts to the parasite drag coefficient of the IRON airfoils. The engine model has been derived from [24] assuming a typical value of the SFC (≈ 0.57 lb/lb-h) in line with a modern geared turbofan engine with high By-Pass Ratio (BPR). The increased airfoil parasite drag coefficient has been assumed to account for the lack of wing laminar flow due to under-wing engines installation and the adoption of conventional leading edge high lift devices. The 20 drag counts value has been estimated during the first loop as the benefit coming from wing natural laminar flow on a clean wing.

The comparison between the IRON aircraft and the reference regional jet has been performed in terms of performance and DOC as described in [11]. Concerning DOC, the estimation has been carried out by means of the JPAD framework taking into account for the following costs contributions as well as the assumptions of Table 2.8. More information concerning the applied methodologies will be provided in the next chapter.

- **Capital DOC:** depreciation, interest and insurance.
- **Fuel DOC.**
- **Charges DOC:** landing, navigation and ground handling.
- **Crew DOC:** flight and cabin crews.
- **Direct maintenance DOC:** airframe and engine.
- **Total DOC:** sum of all contributions.
- **Cash DOC:** Total DOC less the capital DOC contribution.

Life span	16 years
Residual value	10% of the total investment
Number of seats	130
Estimated aircraft price	67.3 Mil.\$
Estimated single engine price	7.0 Mil.\$
Airframe relative spares	10% of the total airframe cost
Engine relative spares	30% of the total engine cost
Total investment	76.8 Mil.\$
Interests	5.4% of the total investment
Insurance	0.5% of airframe and engine costs
Fuel price	59.2\$ per barrel

Table 2.8 Economic assumptions - IRON Loop 2, Configuration 2 [11].

	IRON - Configuration 2	Reference Regional Jet	Difference (%)
Mean SAR (nm/lb)	0.141	0.093	+51.60%
Block fuel (kg)	5234	6904	-24.20%
Block time (min)	241	200	+19.90%
Total DOC (¢/seat-nm)	13.5	14.2	-4.94%
Cash DOC (¢/seat-nm)	7.5	7.9	-5.06%

Table 2.9 Comparison between IRON (Configuration 2) and the regional jet models – 1440nm [11].

	IRON - Configuration 2	Reference Regional Jet	Difference (%)
Mean SAR (nm/lb)	0.136	0.096	+41.67%
Block fuel (kg)	1619	2070	-21.79%
Block time (min)	74	62	+19.35%
Total DOC (¢/seat-nm)	21.4	23.1	-7.36%
Cash DOC (¢/seat-nm)	12.5	13.2	-5.30%

Table 2.10 Comparison between IRON (Configuration 2) and the regional jet models – 400nm [11].

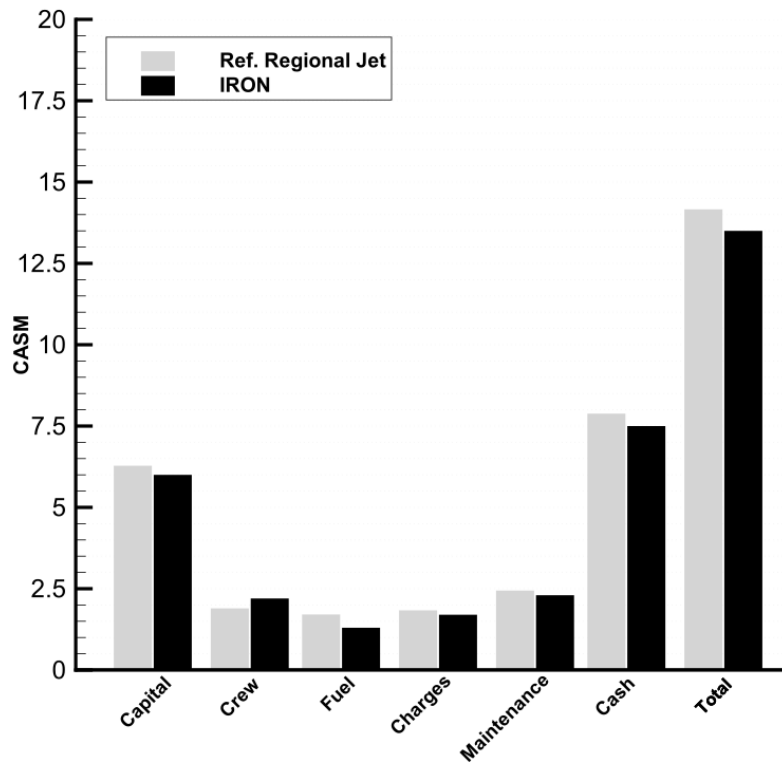


Figure 2.9 DOC comparison between IRON (Configuration 2) and the regional jet models – 1440nm [11].

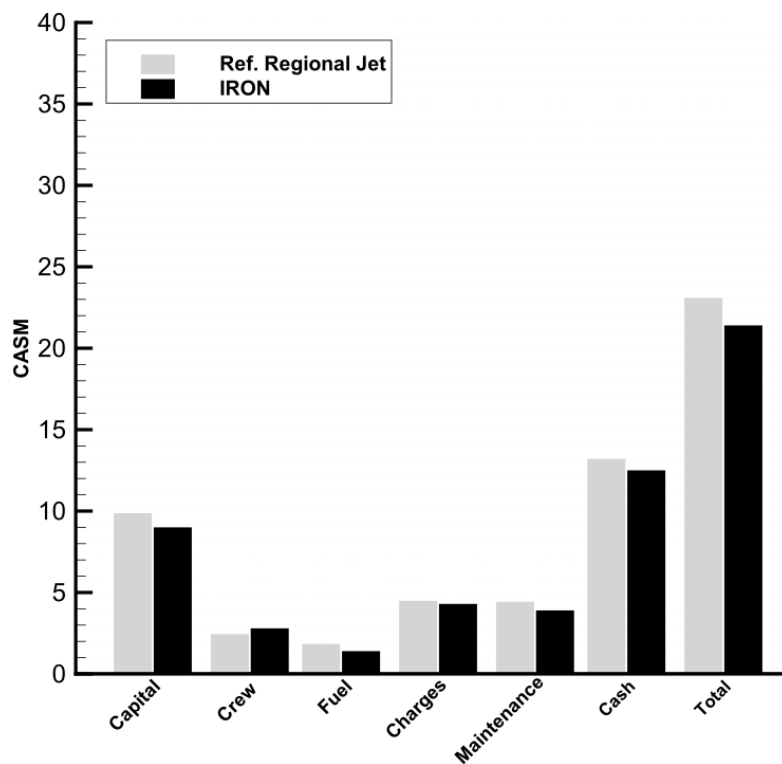


Figure 2.10 DOC comparison between IRON (Configuration 2) and the regional jet models – 400nm [11].

From the results shown in Table 2.9 and Table 2.10, the **IRON** aircraft model has a higher **Specific Air Range (SAR)** in cruise which leads to a reduction of the cruise fuel consumption. Thus, the **IRON** reduction in block fuel decrease on shorter missions due to a shorter cruise phase.

Since the regional jet model operates at higher cruise speed ($M=0.78$ instead of $M=0.64$), the block time of the regional jet will always be lower than the one related to the **IRON** aircraft.

Although the number of crew members and the crew **DOC** per hour are the same for both the aircraft, the different block times lead to a higher cost contribution for the **IRON** platform. Concerning the cash **DOC** (see Figure 2.9 and Figure 2.10), this is lower for **IRON** because of the block fuel saving. Maintenance and charges contributions also provide minor benefits due to the different aircraft weights. **IRON** total **DOC** is lower than the reference regional jet for both the design and the typical missions under investigation (see Figure 2.9 and Figure 2.10).

The benefit derives from different value of airframe and engine costs (affecting capital **DOC**). This benefit must be added to the cash **DOC** advantage. In particular, with respect to the data reported in Table 2.8, a total cost of 82 Mil.\$ for the reference regional jet aircraft and an engine price of 10 Mil.\$ have been assumed. Furthermore, as shown in Table 2.9 and Table 2.10, the total **DOC** advantage of the **IRON** aircraft is reduced on longer missions due to the effect of the capital **DOC** which mitigates the benefit provided by the lower amount of block fuel.

As a result of this comparison, Configuration 2 has already shown the possibility to provide positive effects both on the amount of fuel used per mission and the **DOC** with respect to the reference regional jet aircraft. However, several issues still have remained unsolved especially in terms of cruise aerodynamic efficiency and design range. Thus, the adoption of different innovative configuration, aimed at reducing the trim drag and to increase the aerodynamic efficiency, could provide even better improvements with respect to the reference regional jet platform, complying at the same time with assigned **TLARs**. These considerations, together with preliminary results coming from the comparison of the three loop 2 configurations (see Table 2.6), led to the selection of the three-lifting surfaces as the reference aircraft to be used for loop 2 in-depth analyses. A detailed representation of this configuration is provided in Figure 2.11.

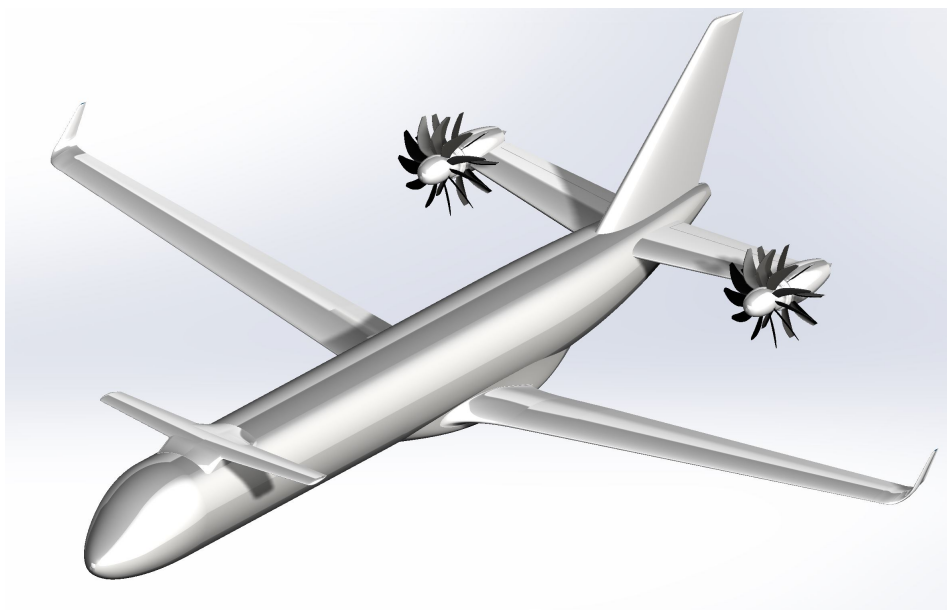


Figure 2.11 IRON aircraft model configuration for loop 2.

Structural weight = 19690 kg	
Wing	6048 kg
Fuselage	7860 kg
Horizontal tail	1800 kg
Vertical tail	658 kg
Canard	300 kg
Undercarriage	2170 kg
Control surfaces	855 kg
Systems = 6070 kg	
Air conditioning	750 kg
APU	372 kg
Electrical systems	900 kg
Batteries	385 kg
Furnishings and equipments	2322 kg
Instruments and navigation system	812 kg
Electrical actuators	529 kg
MEW = 31800 kg	
Systems overall	6070 kg
Power plant (Nacelles + Engines)	6040 kg
Structural weight	19690 kg
OEW = 34167 kg	
MZFW = 50600 kg	
OEW	34167 kg
Maximum structural payload	16430 kg
MTOW = 55174 kg	
OEW	34167 kg
Assumed design mission fuel weight	6964 kg
Design payload	14040 kg

Table 2.11 IRON loop 2 class II weight breakdown.

Once the configuration for the second loop of design has been selected, some design refinements have been performed. Starting from optima design variables coming from the optimization process, all geometrical parameters of this configuration have been fixed. These have been used to assess a class II weight estimation which provided the weight breakdown illustrated in Table 2.11. In particular, the horizontal tail plane weight has been increased with respect to the class II weight estimation methodologies to take into account for the tip mounted engine installation. The estimated weight, based on the horizontal tail area, was about 1000kg which has been increased to 1800kg according to structural considerations coming from Leonardo Company suggestions. Thus, a slight increment of the **MTOW** has been obtained.

To enhance the center of gravity excursion estimation, a preliminary aircraft systems architecture has been assumed together with Leonardo Company taking also into account for classical systems

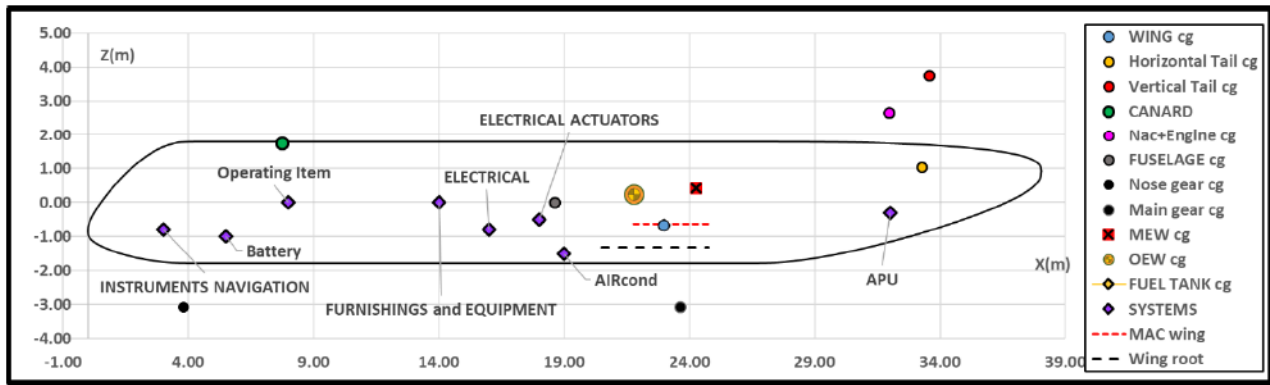


Figure 2.12 Systems and components center of gravity positions - IRON loop 2.

positions as suggested by Torenbeek [25]. Positions of each systems and airframe components are shown in Figure 2.12. It has to be highlighted that distributed systems center of gravity (electrical systems, actuators, furnishing and equipment) have been placed around the fuselage cabin trunk center.

After all design refinements have been completed and the configuration has been finally fixed, aerodynamic design activities of the second loop started in the first half of 2018 involving the re-design and optimization of wing airfoils, new winglets and wing-fuselage fillet design, wing natural laminar flow assessment and a new design of high-lift devices as described in the conference paper presented by the DAF group at the 2019 AIAA Aviation Technology, Integration, and Operations Conference [26].

As reported in this work, one of main challenges of this loop has been the assessment of the canard downwash on the wing which was completely neglected during the preliminary optimization process. As described in [26], the downwash field behind a wing, and methods for accounting for the effects on a wing in that field, are documented in several references. These include linear methods (such as Roskam [27], Silverstein [28] [29], the DATCOM [30] and non-linear method [19]). However, these references emphasize the case where an aft tail has a much smaller span than the main wing. The influence of the wing on the tail is calculated by first estimating the downwash gradient in the plane of symmetry at the longitudinal and vertical location of the tail, and then correcting for the spanwise variation across the tail. However, the data in Roskam [27] and Silverstein [28] [29] are limited to a span ratio, $b_h/b_w = 0.4$, and where the downwash gradient spanwise variation is relatively small, leading to a unique value for downwash derivative on a conventional tail plane.

In case of a canard configuration, where the forward wing has a smaller span than the aft wing, previous methods do not properly work and the spanwise variation of downwash gradient becomes quite significant, in particular in landing configuration with both wing and canard flaps fully deployed.

A first attempt to provide a method evaluating the downwash for a canard configuration is proposed by Philips [31] [32]. He evaluated downwash in the plane of symmetry for an elliptical loaded wing and then calculated the integral downwash gradient effect. This method approximated a generic wing as an elliptical one and does not account for real wing geometrical parameters. Moreover, Philips' method did not account for wing span loading distribution, avoiding any design indication for lifting surfaces twist angle distributions. A systematic method was subsequently proposed by Levy [33], where a vortex lattice approach was used to build a simplified methodology to account

for both downwash in the symmetry plane and spanwise attenuation factor. Main drawbacks of this method are the geometrical parameters range of variation and the absence of a global effect on the aerodynamic derivatives. Moreover, this approach does not cover the case of flap (or other movable surfaces) deflected. For this reason, a 3D panel code method has been used at preliminary stage to well understand the downwash behavior and to improve wing lift capabilities by modifying the wing twist distribution. The use of a 3D panel code aims at reducing the computational costs required to perform several analyses of different wing geometries and conditions.

Charts of Figure 2.13 and Figure 2.14 highlight that to reach the same local lift coefficient (at a specific angle of attack) of the configuration without the canard, an additional twist of about 1.5° and 3° for cruise and landing respectively was required.

To recover some of the lift lost due of the canard downwash, the local incidence angle of wing sections affected by this effect has been increased. On the other hand, to reduce the upwash effects due to the canard tip vortex (avoiding the tip stall), the twist has been increased in negative sign. Thus, taking into account for both cruise and landing conditions, an average value of twist incidence distribution has been chosen as reported in Table 2.12.

	Loop 1 twist	Loop 2 twist	Δ twist
Root section	$+1^\circ$	$+3^\circ$	$+2^\circ$
Kink section	$+1^\circ$	$+1^\circ$	0°
Tip section	-1°	-3°	-2°

Table 2.12 IRON loop 2 – Modified wing twist distribution.

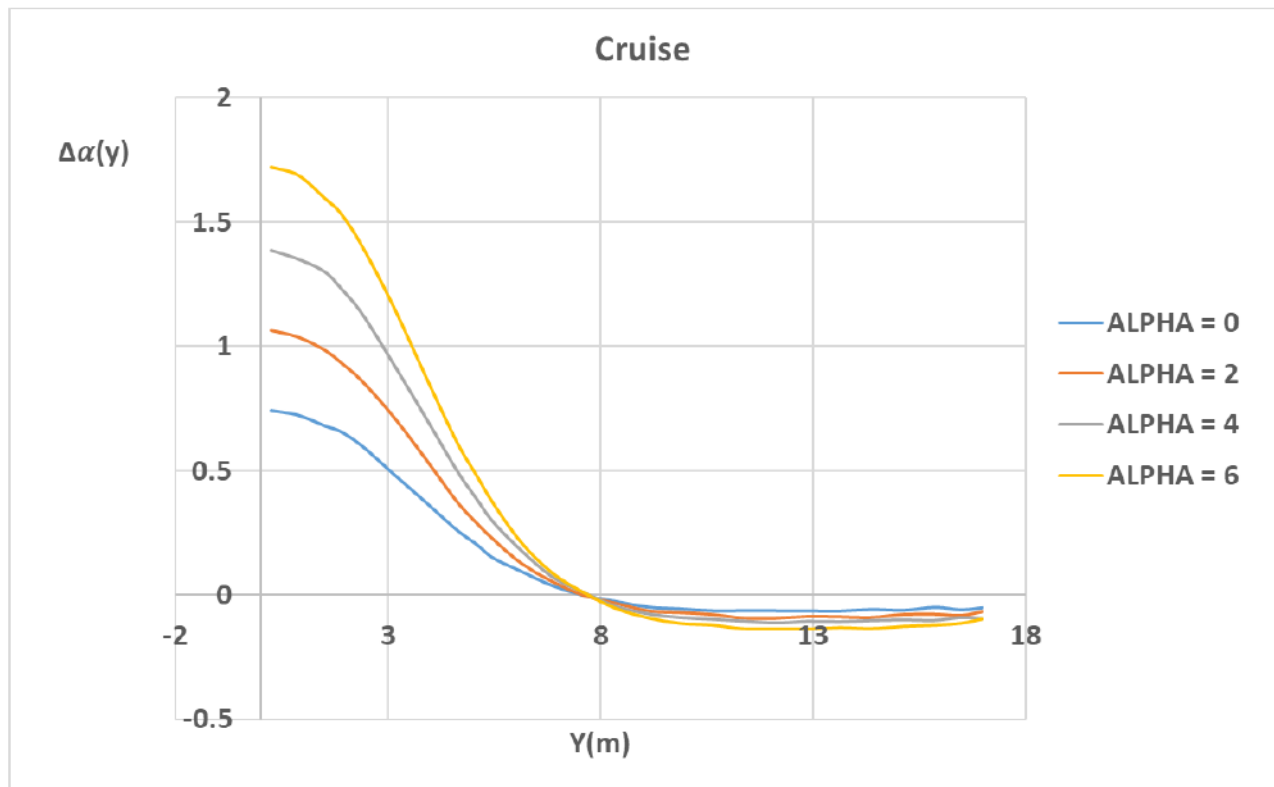


Figure 2.13 Wing local angle of attack deficit due to canard downwash in cruise condition (panel code).

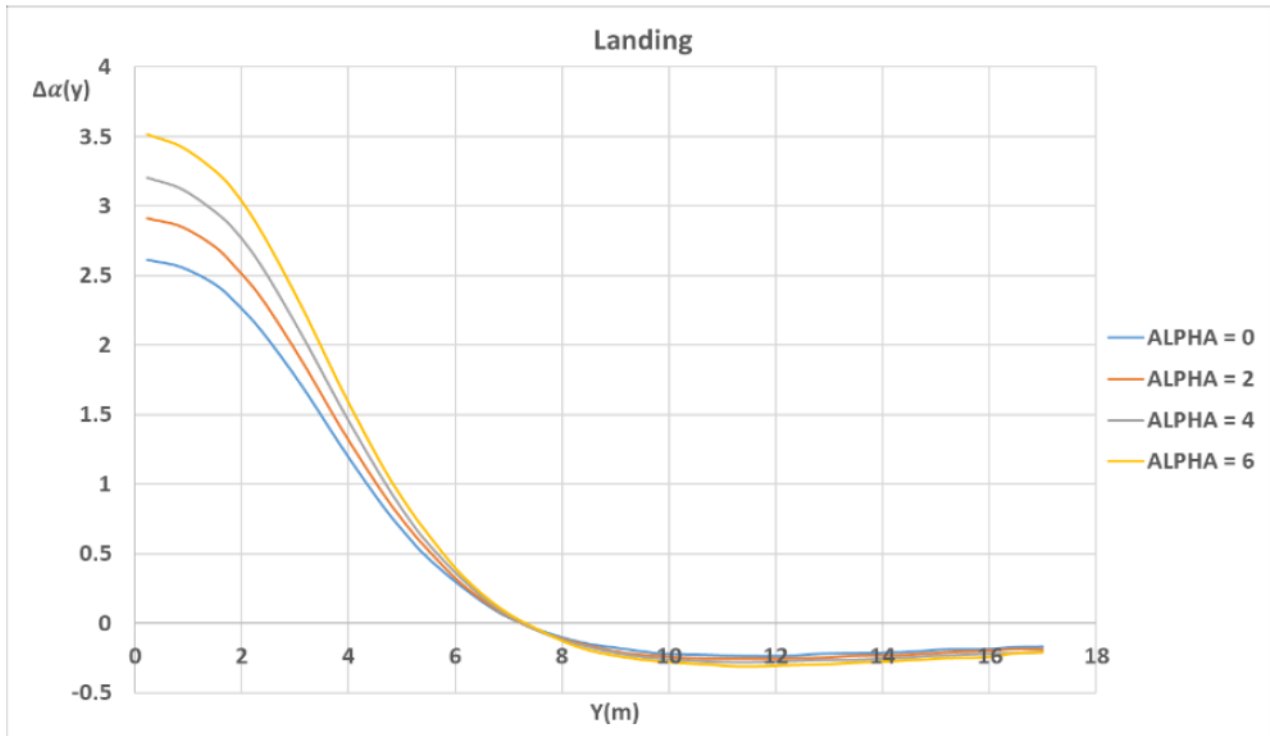


Figure 2.14 Wing local angle of attack deficit due to canard downwash in landing condition (panel code).

Once the lifting surfaces geometries have been well assessed, CFD-RANS aerodynamic analyses have been performed. Firstly, the panel code analysis has been compared with a CFD-RANS calculation, then the maximum achievable lift coefficient has been computed for the Wing-Body and Wing-Body-Canard configurations. Finally, the complete aircraft in landing configuration has been investigated to highlight how the canard wake, in full-flap condition, affects and modifies the incidence angles in the tail region, despite the large horizontal stagger.

A more detailed description of the work performed for the aerodynamic assessment, mainly focused on high-lift analyses of the three-lifting surfaces configuration, can be found in [26].

In terms of longitudinal static stability, CFD-RANS analyses have been carried out in clean configuration to assess if a static stability margin of about 5% could be granted as reported in [26].

In cruise condition the static stability margin is about 4.2% of the Mean Aerodynamic Chord (MAC) and in climb this value is about 7.8%. Thus, the aircraft provides for a large enough stability also at the most afterward center of gravity position (which has been estimated to be at 0% of the MAC). The effect of the center of gravity variation is shown in Figure 2.15 and Figure 2.16 (cruise and climb) where aircraft stability increases drastically on the whole operative center of gravity range resulting in a trim drag increment. Cruise and climb analyses have been useful also to evaluate if the combined downwash coming from both canard and wing lifting surfaces will affect the horizontal tail plane lifting capabilities. The result is the introduction of a large induced angle of attack on the horizontal tail. Despite this, the tail lift capabilities were high enough to grant a static stability margin near to the required value of 5%. However, to trim the aircraft by paying the minimum trim drag, the horizontal tail plane incidence angle has been corrected from the initial value of -2° to a final value of $+2^\circ$ to reduce the tail download. The same interaction between the canard and the wing downwash with the horizontal tail has also been analyzed in take-off and landing configurations. The interaction was still very high leading to a large negative induced angle of attack on the horizontal tail.

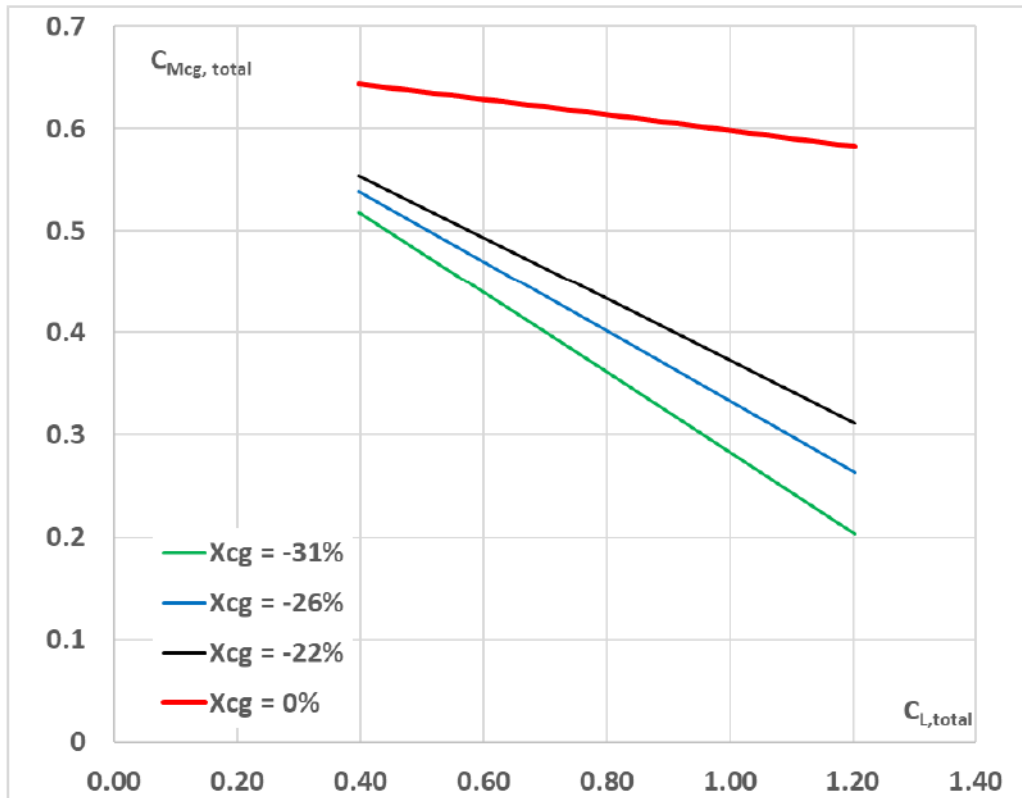


Figure 2.15 Aircraft pitching moment coefficient, center of gravity effects at cruise conditions [26].

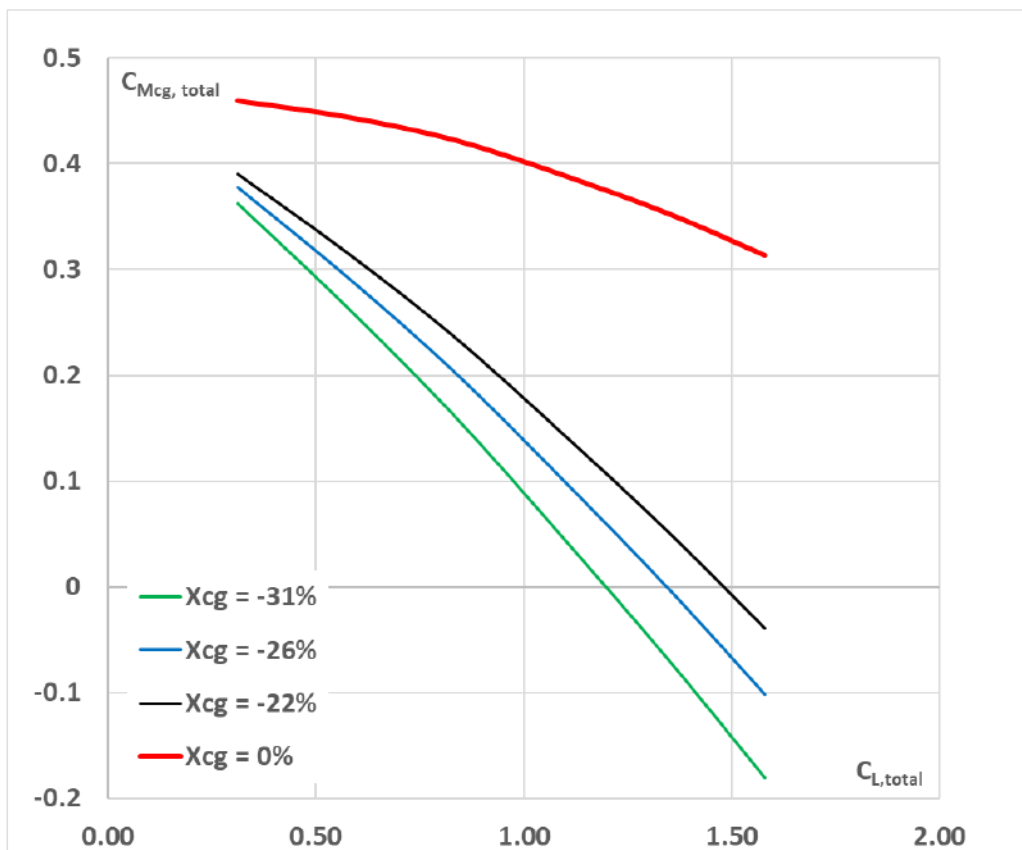


Figure 2.16 Aircraft pitching moment coefficient, center of gravity effects at climb conditions [26].

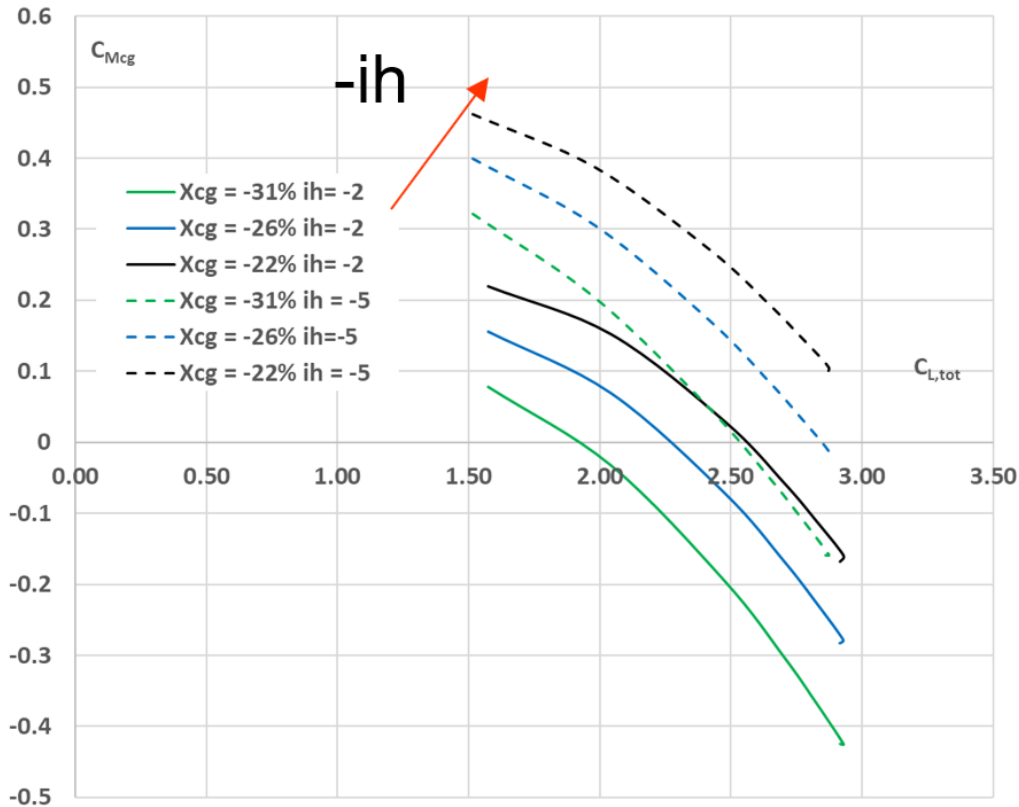


Figure 2.17 Effects of center of gravity and i_h on aircraft pitching moment coefficient [26].

As can be seen from Figure 2.17, the center of gravity effect on the pitching moment was very high also in landing configuration with a center of gravity position, at typical landing weight (about 90% of the MTOW), of about -26 to -31% of the MAC. To let the aircraft to be trimmed with reasonable elevator deflections, the horizontal tail incidence angle has been revised according to results shown in Figure 2.17 selecting a value of i_h of -5° . The same analysis has been carried out also for the take-off condition leading to a required value of the horizontal tail incidence angle of -2° . Thus, a trimmable horizontal tail has been considered for this type of aircraft. In this case the reference center of gravity position has been estimated at -22% of the MAC (related to the MTOW).

To improve the maximum lift capabilities, a leading-edge high lift device has been introduced in the form of a morphable droop nose as shown in Figure 2.18. Results coming from the first loop of design together with available indications deriving from the work by Kintscher et al. [34] have been used estimating an increment of the C_{Lmax} of about 0.2 and an increase of the stall angle of 2° .

A summary of the achievable maximum trimmed lifting coefficients in both landing and take-off conditions is reported in Table 2.13. Here, considered center of gravity positions are the one related to typical weight conditions operated in these mission phases.

X_{CG} (%MAC)	C_{Lmax} take-off (no drooped nose)	C_{Lmax} landing
-22%	2.89	-
-26%	2.85	3.19
-31%	-	3.15

Table 2.13 IRON loop 2 – Effect of center of gravity on C_{Lmax} in take-off and landing configurations.

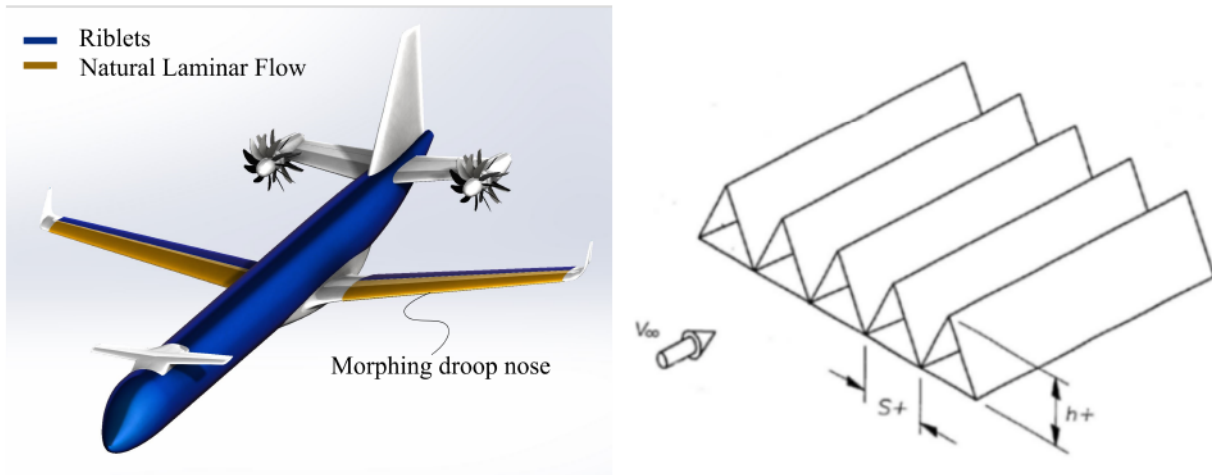


Figure 2.18 IRON loop 2 - IRON loop 2 - Adopted technologies (left) and considered riblet shape, 3M riblets $h=s$ (right).

To further increase the cruise aerodynamic efficiency, an additional technology, in the form of riblets, has been considered to reduce the aircraft drag [35] [36]. As described in the work by Mele et al. [37], riblets have been used in combination with the wing natural laminar flow to provide an important contribution to the reduction of the overall aircraft drag. In particular, as shown in Figure 2.18, riblets have been considered to be installed on the whole fuselage as well as in the turbulent part of the wing.

For sake of clarity, natural laminar flow is a passive drag reduction technique linked to a particular wing section shaping process focused on the stabilization of boundary-layer disturbances and instabilities due to pressure gradient [38]. Although very useful, successful cases of natural laminar flow have been limited to the case of unswept wing, because of the well known cross-flow instability [37].

On the other hand, riblets are small surface protrusions aligned with the direction of flow, which confer an anisotropic roughness to a surface. They are one of the few techniques that have been successfully applied to the reduction of the skin friction in turbulent boundary layers, both in the laboratory and in full aerodynamic configurations [35].

CFD-RANS simulations on IRON wing-body configuration have been carried out adopting the flow solver FLOWer developed at Deutsches Zentrum für Luft- und Raumfahrt (DLR) and modified by the University of Naples Federico II for riblet simulations. The code solves the compressible three-dimensional steady and unsteady RANS equations on block-structured meshes around complex aerodynamic configurations [37].

The spatial discretization adopted was a central finite volume formulation with explicit blended 2nd and 4th order artificial dissipation. Time integration is carried out by an explicit hybrid multistage Runge-Kutta scheme. The $k-\omega$ SST turbulence model, modified for considering riblets was adopted [39] [40] [41]. The chosen riblet shape is shown in Figure 2.18. It is a classical triangular riblet with equal height and spacing.

The main aerodynamic effect provided by riblets is a reduction of the skin friction drag, which is substantially constant with the angle of attack, resulting in an increment of the aerodynamic efficiency in all center of gravity conditions. Effects of riblets at different center of gravity position related to the cruise phase are reported in Table 2.14.

X_{CG} (%MAC)	C_L	Efficiency (riblets on)	Efficiency (riblets off)	Difference (%)
-22%	0.62	19.14	18.51	+3.40%
-26%	0.59	18.59	17.96	+3.51%
-31%	0.54	17.82	17.20	+3.60%

Table 2.14 Aerodynamic efficiency at different center of gravity position with and without riblets.

As can be seen, the large center of gravity excursion provided by this aircraft configuration leads to a consistent reduction of the aerodynamic efficiency during the cruise phase. In fact, due to the fuel consumption, the aircraft weight reduces during the cruise making the center of gravity position shift forward.

It has to be highlighted that, in case of riblets installation, the required cruise aerodynamic efficiency of 18.0 is substantially matched while, in case of no riblets installation, the aerodynamic efficiency can decrease up to 17.20. An averaged effect of riblets can be estimated in a +3.5% increment in aerodynamic efficiency for each operative cruise center of gravity positions.

As in the first loop of design, once the aerodynamic assessment has been completed, lift curves and trimmed drag polar curves (with and without riblets effects) have been used to feed the performance module of the **JPAD** framework to estimate flight and ground performance of this innovative configuration.

Parallel to the aerodynamic dataset definition, one of the loop 2 activities branch have been dedicated to the refinement of the engine deck used during the first loop of design. The combined efforts of the **DAF** group and the engine manufacturer GE Avio Aero resulted in an improved engine model with lower values of both noise emissions and **SFC**.

Sensitivity analyses, with respect to first loop data, have been carried out by the **DAF** group to investigate the effects of engine weight and **SFC** on the block fuel of both the design mission and the typical mission. Furthermore, new engine thrust requirements for each rating have been defined by the **DAF** group assuming a linear scaling of the first loop thrust data until the required performance were matched. These new requirements as well as the estimated trend curves have been used by the engine manufacturer to develop a new engine deck for the second loop of design. One of the most important result has been a reduction in cruise **SFC** of about 5.2%, with respect to the first loop engine, assuming the cruise conditions reported in Table 2.4.

The complete performance assessment has been carried out by performing the following analyses. Both cases of installed riblets and no riblets have been investigated to evaluate the effect of this technology at overall aircraft performance level.

- **Take-off**

- **TOFL** at **MTOW**, **SL** and **ISA** conditions.
- Calculation of the minimum control speed (V_{MC}) at different weight conditions.
- Residual climb gradient during the second segment of take-off climb assuming a **TOW** related to the typical mission of 400nm with 130 passengers and in hot & high conditions (5400 ft and **ISA+30°C**).

- **Climb**

- Rate of climb, climb angle and climb gradient as function of the **TAS** in both **AEO** and **OEI** conditions at different altitudes.
- Maximum rate of climb and maximum climb angle at different altitudes in **OEI** conditions.
- Absolute and service ceilings in **OEI** conditions (**ISA+10°C**).
- Time to climb from 1500ft to 25000ft in **AEO** condition using the assigned speed of 190 knots of **CAS**.

- **Cruise**

- Evaluation of the cruise flight envelope as function of **TAS**, **CAS** and the Mach number with and without natural laminar flow effects (off-design condition).
- Cruise efficiency curves as function of the cruise Mach number with and without natural laminar flow effects.

- **Landing**

- **LFL** at **MLW**, **SL** and **ISA** conditions with dry runway.

- **Mission profile and DOC**

- Simulation of both the design mission (1600nm) and the typical mission (400nm) with and without natural laminar flow effects.
- Evaluation of the **DOC** breakdown for both the design mission and the typical mission.
- Comparisons with the reference regional jet model (similar to the A220-300).

- **Payload-Range**

- Comparison of Payload-Range charts with and without natural laminar flow effects.

To take into account for aerodynamic features variation with the center of gravity excursion (see Table 2.14), the aerodynamic dataset have been interpolated at different X_{CG} positions allowing to retrieve the proper value of the aerodynamic efficiency during the mission simulation.

Starting from the take-off analysis, Table 2.15 highlights the main simulation results. As can be seen the **TOFL** requirements has been satisfied with a **TOFL**, calculated as the longest between the FAR-25 take-off field length and the balanced field length, lower than 1400m.

Concerning the results of the second climb segment simulation, those have been carried out using a take-off weight coming from the analysis of the typical mission profile (400nm) shown in Table 2.21. As shown in Figure 2.19, the residual climb gradient is above the prescribed value of 2.4% both with and without riblets.

A sensitivity analysis of the V_{MC} has been carried to investigate the effect of take-off weight on this parameter. Results are shown in Table 2.16 highlighting values in line with FAR-25 regulation which impose a maximum value of the $V_{MC}/V_{S,TO}$ of 1.13. For each weight condition the related center of gravity position has been considered.

	Riblets off	Riblets on
Ground roll distance (m)	733	719
Rotation distance (m)	127	128
Airborne distance (m)	218	217
AEO take-off distance (m)	1078	1064
FAR-25 take-off field length (m)	1240	1224
Balanced field length (m)	1356	1327

Table 2.15 IRON Loop 2 - Take-off simulation results.

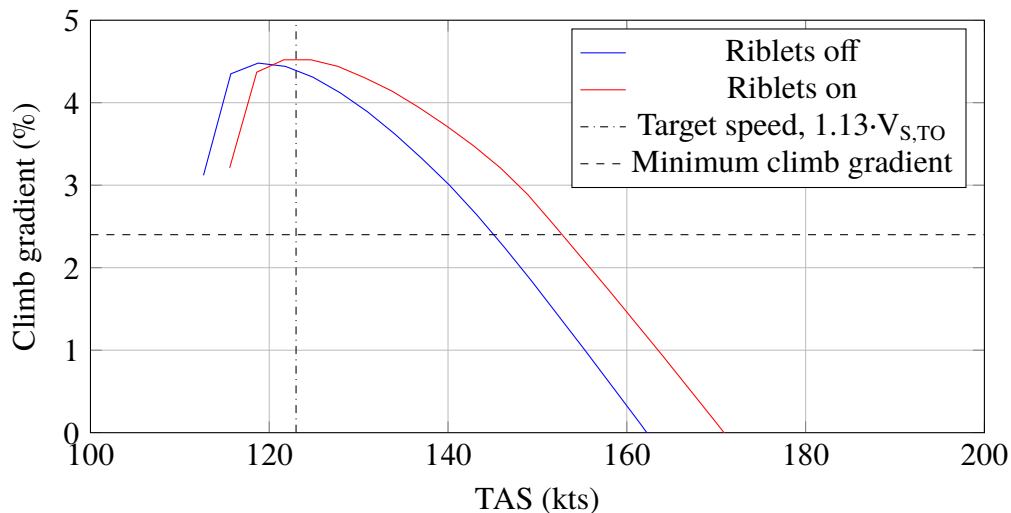


Figure 2.19 IRON loop 2 - Residual climb gradient in hot & high conditions

The analysis of results, reported in Table 2.17, related to the climb segment, highlight the aircraft capability to match both the **OEI** ceiling requirement of 16500ft and the time to climb of 16 minutes at 190 kts of **CAS**. The use of riblets allows to improve both absolute and service ceilings increasing their values of about 5.5% and 2.0% respectively.

The cruise phase analysis has been carried out investigating the effects of both natural laminar flow and riblets. The weight condition in this case has been assumed to be 97% of the **MTOW** which is related to a center of gravity position of -24% of the mean aerodynamic chord. As can be seen from Table 2.18 the aircraft can always be operated at the required altitude of 30000ft with a Mach number of 0.64 except for the case of no riblets in off-design conditions (no laminar flow). Riblets installation provides a beneficial effect on aerodynamic efficiency allowing to reach the required Mach number also in off-design condition.

Concerning the landing simulation, the estimated **LFL**, reported in Table 2.19, resulted to be higher than the required value of 1300m. This effect has been the result of a maximum take-off weight increment with respect to the first loop, a reduction of the wing area from 105m² to 98.6m² and an aerodynamic effect caused by the canard downwash which has reduced the maximum landing trimmed lifting coefficient (about 3.1 instead of the expected preliminary value of 3.4). A solution to this problem could be represented by the use of spoilers during the simulation since those devices provides two beneficial effects: an increased drag coefficient and a reduction of the wing lift, increasing this way the wheels friction force. In this case riblets has provided for a very little neglectable effect.

	100%MTOW $X_{CG} = -22\%MAC$	95%MTOW $X_{CG} = -26\%MAC$	90%MTOW $X_{CG} = -29\%MAC$
$V_{S,TO}$ (m/s)	57.5	56.0	54.5
V_{MC} (m/s)	60.9	60.6	60.4
$V_{MC}/V_{S,TO}$	1.06	1.08	1.11

Table 2.16 V_{MC} calculation at several weight conditions.

	Riblets off	Riblets on
OEI absolute ceiling, ISA+10°C (ft)	20807	21986
OEI service ceiling, ISA+10°C (ft)	18504	18880
Time to climb (1500ft-25000ft) (min)	14	14

Table 2.17 IRON Loop 2 - Climb results.

Ground roll distance	546 m
Rotation distance	93 m
Airborne distance	244 m
Landing distance	884 m
FAR-25 landing field length	1473 m

Table 2.19 IRON Loop 2 - Landing simulation results.

The most important analysis of the second loop performance assessment regarded the mission simulation. As for the cruise analysis, both design mission and typical mission have been simulated with and without riblets or natural laminar flow effects. The effect of the center of gravity excursion due to the fuel consumption has also been considered interpolating the aerodynamic dataset.

Simulation results for the design mission results of 1600nm are shown in Table 2.20. Here, the worst case is the one in off-design conditions without riblets. In this case the prescribed maximum take-off weight is not enough to cover the mission distance with the design number of passengers (a reduction of about 4 passengers is needed). This condition is also related to a maximum cruise Mach number of 0.62 which increases also the flight time with major drawback on aircraft **DOC**. To solve this, riblets installation appears to be a good solution. Major benefits are provided by the natural laminar flow which, coupled with riblets effects, allows to reach the lowest value of block fuel with a constant amount of flight time (cruise Mach number fixed at 0.64).

These results are confirmed also by the Payload-Range chart in Figure 2.20 in which all simulation conditions are represented. As can be seen, the case natural laminar flow which, coupled with riblets effects, allows to reach the longest design range.

Similar to the design mission, also for the typical mission of 400nm the worst case is the one in off-design conditions without riblets installation. The design payload is always matched, due to a take-off weight lower than the **MTOW**, and the cruise Mach number is quite close to the one specified by **TLARs** (between 0.63 and 0.64).

The same benefits provided by laminar flow and riblets can also be found for the typical mission.

	Riblets off Off-design	Riblets off Laminar flow	Riblets on Off-design	Riblets on Laminar flow
Max. Mach number	0.62	0.65	0.64	0.66
Cruise efficiency	16.87	18.33	17.64	18.95

Table 2.18 IRON Loop 2 - Cruise results.

	Riblets off Off-design	Riblets off Laminar flow	Riblets on Off-design	Riblets on Laminar flow
Mission distance (nm)	1600	1600	1600	1600
Block time (min)	270	265	265	265
Total mission time (min)	325	321	321	321
Aircraft mass at mission start (kg)	55174	55174	55174	55060
Block fuel (kg)	6055	5688	5821	5557
Total mission fuel (kg)	7043	6669	6785	6510
Residual fuel reserve	5%	5%	5%	5%
Design pax. number	130	130	130	130
Allowed pax. number	126	130	130	130

Table 2.20 IRON Loop 2 - Design mission simulation results.

However, the reduction in block fuel is lower due to a reduced influence of the cruise segment on the entire mission.

The final step of the performance assessment has been the comparison of the innovative IRON configuration with the reference regional jet aircraft model based on the Airbus A220-300. Differently from the end of the first loop of design, in this case the A220-300 model has been defined using the JPAD framework using semiempirical methodologies concerning weights and aerodynamics. The turbofan engine model has been the same used for the comparison made at the end of the first of loop.

The comparison between the IRON aircraft model and the reference regional jet has been carried out assuming the same mission profile for both the design mission and the typical mission. It must be noted that, although both aircraft have similar values of the maximum aerodynamic efficiency, the cruise aerodynamic efficiency of the A220-300 model is lower than the one of calculated for the IRON aircraft model. Thus, IRON will benefit of both a reduced SFC (coming from the engine) and a higher aerodynamic efficiency.

Block fuel and block time are compared in Table 2.22 and Table 2.23 for the design mission and the typical mission respectively.

All percentages are referred to the A220-300 aircraft model showing that the combination of both laminar flow and riblets allows to reach a reduction in block fuel of about -25.0% on the typical mission with only 12 minutes of block time increment. Concerning the typical mission, lower reductions in block fuel with respect to the design mission are achieved due to a lower impact of the cruise segment on the entire mission.

	Riblets off Off-design	Riblets off Laminar flow	Riblets on Off-design	Riblets on Laminar flow
Mission distance (nm)	400	400	400	400
Block time (min)	74	74	74	74
Total mission time (min)	129	129	129	129
Aircraft mass at mission start (kg)	51011	50940	50916	50860
Block fuel (kg)	1664	1606	1609	1568
Total mission fuel (kg)	2664	2596	2573	2520
Residual fuel reserve	5%	5%	5%	5%
Design pax. number	130	130	130	130
Allowed pax. number	130	130	130	130

Table 2.21 IRON Loop 2 - Typical mission simulation results.

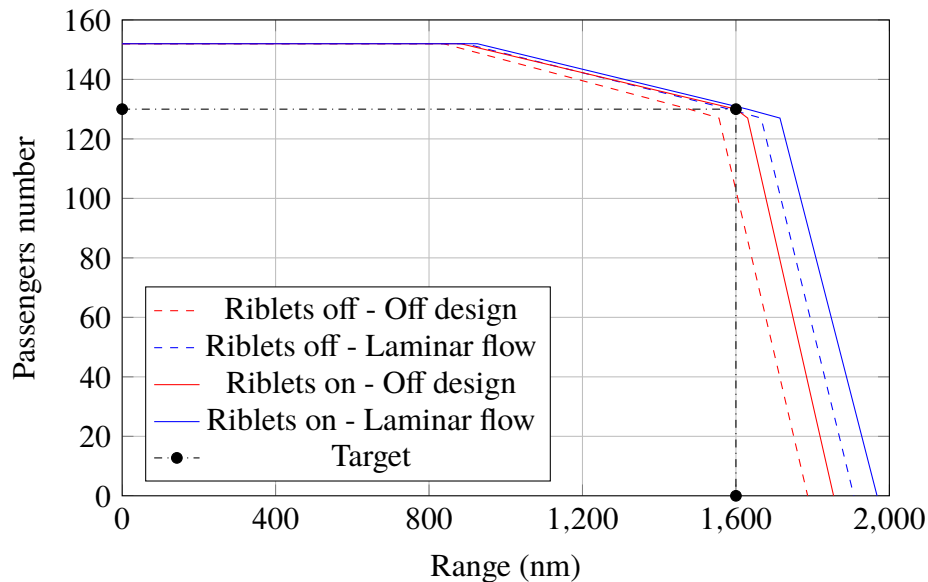


Figure 2.20 IRON loop 2 - Payload-Range diagrams

	Riblets off Off-design	Riblets off Laminar flow	Riblets on Off-design	Riblets on Laminar flow	Reference Regional Jet
Block Time (min)	270 (+22.73%)	265 (+20.45%)	265 (+20.45%)	265 (+20.45%)	220
Block fuel (kg)	6055 (-23.89%)	5688 (-26.84%)	5821 (-28.51%)	5557 (-30.15%)	7956
Design pax. number	130	130	130	130	130
Allowed pax. number	126	130	130	130	130

Table 2.22 IRON Loop 2 - Mission data comparison between IRON and A220-300 (1600nm)

	Riblets off Off-design	Riblets off Laminar flow	Riblets on Off-design	Riblets on Laminar flow	Reference Regional Jet
Total DOC (¢/seat·nm)	13.53 (-2.24%)	13.31 (-3.86%)	13.36 (-3.49%)	13.27 (-4.10%)	13.84
Cash DOC (¢/seat·nm)	7.44 (-3.36%)	7.32 (-5.25%)	7.35 (-4.79%)	7.28 (-5.64%)	7.72

Table 2.24 IRON Loop 2 - DOC comparison between IRON and A220-300 (1600nm)

	Riblets off Off-design	Riblets off Laminar flow	Riblets on Off-design	Riblets on Laminar flow	Reference Regional Jet
Total DOC (¢/seat·nm)	21.63 (-6.28%)	21.52 (-6.75%)	21.58 (-6.50%)	21.47 (-6.99%)	23.08
Cash DOC (¢/seat·nm)	12.44 (-5.83%)	12.36 (-6.42%)	12.39 (-6.21%)	12.32 (-6.75%)	13.21

Table 2.25 IRON Loop 2 - DOC comparison between IRON and A220-300 (400nm)

	Riblets off Off-design	Riblets off Laminar flow	Riblets on Off-design	Riblets on Laminar flow	Reference Regional Jet
Block Time (min)	74 (+19.35%)	74 (+19.35%)	74 (+19.35%)	74 (+19.35%)	62
Block fuel (kg)	1664 (-19.61%)	1606 (-22.27%)	1609 (-22.40%)	1568 (-24.27%)	2070
Design pax. number	130	130	130	130	130
Allowed pax. number	130	130	130	130	130

Table 2.23 IRON Loop 2 - Mission data comparison between IRON and A220-300 (400nm)

In terms of **DOC**, economic assumptions in Table 2.8 have been used for the **IRON** aircraft model while, for the reference regional jet, different values of aircraft price, engine price and total investment have been considered. These latter amounts equal to 82 Mil.\$, 10 Mil.\$ and 94.2 Mil.\$ respectively. As for mission simulations, all analyses have been carried out using the **DOC** module of the **JPAD** framework. The take-off weight of the A220-300 model has not been assumed equal to the declared **MTOW** being both the design and the typical missions under investigation shorter than the A220-300 design mission range. Take-off weight values of 60487kg, for the 1600nm mission, and 54354kg, for the 400nm mission, have been estimated by the **JPAD** performance module (still higher than the **IRON** aircraft model).

Results of this comparison are shown in Table 2.24 for the design mission and in Table 2.25 for the typical mission.

Although the increase in flight time due to different values of cruise Mach numbers, the beneficial effect provided by the block fuel reduction leads to a reduction also of the **DOC** passing from the A220-300 model to **IRON**. This difference increases when dealing with the short mission due to a reduced flight time difference.

2.3 Candidate's contribution to the IRON project

The design team of the University of Naples Federico II, involved in the activities described in this chapter, includes several members of the **DAF** research group. The group is coordinated by Fabrizio Nicolosi, associate professor at the University of Naples Federico II and professor of Aircraft Design and Flight Mechanics.

To carry out the activities scheduled for the **IRON** project, the **DAF** group has worked in collaboration with other project partners like Leonardo company, the Italian aerospace research center CIRA and the engine manufacturer GE AVIO.

Below the reader can find an overview of the team as well as a detailed description of the contribution provided by the author of this thesis to the design activities of the **IRON** project.

- **Fabrizio Nicolosi** - Associate professor at the University of Naples Federico II and professor of Aircraft Design and Flight Mechanics. Professor Nicolosi has been the coordinator of all the design activities carried out by the **DAF** research group within the **IRON** project.
- **Salvatore Corcione** - Research fellow and member of the **DAF** research group. Salvatore Corcione has been involved in most of the technical activities related to the first two loops of the **IRON** project with major focus on the aerodynamic assessment of both loop 1 and loop 2 configurations as well as on the preliminary design activities between the first two loops.
- **Manuela Ruocco** - PhD student and member of the **DAF** research group. She has collaborated with Salvatore Corcione to carry out the aerodynamic assessment of both loop 1 and loop 2 configurations.
- **Vincenzo Cusati** - PhD student and member of the **DAF** research group. His contribution to the **IRON** project has been mainly focused on numerical and experimental analyses related to the loop 2 configuration as well as on nacelles and canard positioning aimed at reducing aerodynamic interferences and solving longitudinal static stability issues. He has also performed a **DOC** estimation of the “Configuration 2” aircraft model reported in Figure 2.6.
- **Vittorio Trifari** - PhD student, author of this thesis and member of the **DAF** research group. A detailed description of his contribution to the **IRON** project can be summarized in the following key points:
 - Preliminary estimation of high-lift devices effects related to the first loop configuration.
 - Complete performance assessment of the first loop aircraft configuration.
 - Preliminary design activities related to the **MDAO** of the three aircraft configurations in Figure 2.6 and the downselection of the best one to be used for the second loop.
 - Performance evaluation of “Configuration 2” aircraft model (see Figure 2.6) and comparison with the reference regional jet.
 - Complete performance and **DOC** assessment of the three-lifting surfaces aircraft configuration and comparison with the reference regional jet.

List of publications involving the candidate and his contribution

- Nicolosi F., Corcione S., Della Vecchia P., **Trifari V.**, Ruocco M., and De Marco A. «Design and aerodynamic analysis of a regional turboprop innovative configuration». In: *6th CEAS Air and Space Conference (CEAS 2017)*. Elsevier Procedia, 2017. ISBN: 9781510858794.
 - Candidate's contribution is related to the preliminary estimation of high-lift devices effects.
- Nicolosi F., Corcione S., **Trifari V.**, Cusati V., Ruocco M., and Della Vecchia P. «Performance evaluation and DOC estimation of an innovative turboprop configuration». In: *2018 Aviation Technology, Integration, and Operations Conference*. American Institute of Aeronautics and Astronautics (AIAA), 2018. DOI: <https://doi.org/10.2514/6.2018-3662>.
 - Candidate's contribution is related to the **MDAO** of the rear-mounted engines configuration as well as to the complete performance assessment of the optimized aircraft model and its comparison with the reference regional jet platform.
- Nicolosi F., Corcione S., Della Vecchia P., **Trifari V.**, and Ruocco M. «Aerodynamic design and analysis of an innovative regional turboprop configuration». In: *31st Congress of the International Council of the Aeronautical Sciences, ICAS 2018*. International Council of the Aeronautical Sciences, 2018. ISBN: 9783932182884.
 - Candidate's contribution is related to the **MDAO** of the three aircraft configurations in Figure 2.6 and the downselection of the best one to be used for the second design loop.
- Corcione S., **Trifari V.**, Nicolosi F., Cusati V., Ciliberti D., and Della Vecchia P. «Feasibility study of innovative regional turboprop: an overview of the European project IRON». In: *9th EASN International Conference on "Innovation in Aviation & Space"*. 2019. DOI: <https://doi.org/10.1051/mateconf/201930403014>.
 - Candidate's contribution is related to the **MDAO** of the three aircraft configurations in Figure 2.6 and the downselection of the best one to be used for the second design loop. Furthermore, the candidate has carried out the complete performance evaluation of the three-lifting surface making also a comparison with the reference regional jet platform.

Chapter **3**

A NEW FRAMEWORK FOR AIRCRAFT PRELIMINARY DESIGN

A good programmer is someone who always looks both ways before crossing a one-way street.

– Doug Linder

3.1 Introduction

Being the research, by its nature, multidisciplinary, an added value provided by the author during his PhD lies in the combination of two different, although complementary, branches of engineering: Aerospace, in terms of Aircraft Design, and Computer Science, in terms of Software Engineering.

This chapter presents a Java framework, named **JPAD**, developed at the University of Naples Federico II by the **DAF** research group to perform multi-disciplinary analyses and optimizations of civil transport aircraft. As stated at the end of the previous chapter, the **JPAD** framework is the result of the efforts of the **DAF** group which involved several PhD students in a virtuous collaboration process, including the author of this thesis who has personally developed most of its modules.

Nowadays a key word in all branches of engineering is “teamwork”. Both researches and industrial applications cannot be undertaken by a single person, so the development of an efficient, versatile, multi-disciplinary and reliable framework for aircraft preliminary design cannot derive from the work of a single PhD student or researcher. Part of the PhD journey deals with the development of soft skills capable of making the candidate a fundamental resource both in the University and in every industry, and teamwork has surely been one of them for the author of this thesis.

Before describing the **JPAD** framework architecture and its features, a comprehensive overview of the state of the art of current aircraft preliminary design software will be provided to highlight their strengths and weaknesses. This phase has guided the development of the framework through the years allowing to combine several architectural features, methodologies and software technologies.

After that, the chapter will be focused on the main **JPAD** characteristics, especially the **MDAO** module, providing also two validation case studies concerning a turboprop aircraft model similar to the well-known ATR-72 and a turbofan regional jet similar to the A220-300.

3.2 Aircraft Design software scenario

Nowadays the preliminary design phase of an aircraft has become very challenging due to ever more demanding requirements. The goal of first design stages is to search for the configuration that best fit all requirements, among the results of a great number of multi-disciplinary analyses, as fast as possible, and with a certain grade of accuracy. The continuous improvement of computer calculation capabilities over years has allowed the growth of a large family of software dedicated to aircraft preliminary design activities concerning also multi-disciplinary analyses and optimizations [42]. Some remarkable examples can be found in the following software.

- **Pacelab**. A commercial software suite, written in C#, developed by the German company Pace, part of the Italian TXT Group [43]. This software has rapidly become a leader on the aircraft preliminary design market due to its user-friendliness and its robust and efficient software architecture. The suite is made up of several interconnected modules each of which adding very important features to the base version (i.e. on-board systems architecture or detailed cabin layout definition). However, some methodologies and database lack for the required scientific know-how that only research centers or Universities can provide.
- **SUAVE**. An open-source software, written in Python, developed at the University of Stanford [44]. It comes with lots of interesting features, among which the possibility to analyze unconventional configurations (i.e. blended-wing body) with different levels of fidelity or the possibility to take-into account for different sources of energy (i.e. solar power). However, it has poor visualization features and no dedicated input files lowering its user-friendliness.
- **FLIGHT**. Developed in 2006 at the University of Manchester by leading aeronautical authority Dr Antonio Filippone, FLIGHT is state-of-the-art software for the prediction and modelling of fixed wing aircraft performance. Through analyzing the performance of airborne vehicles and any sub-systems using the latest academic research, FLIGHT can accurately map aircraft operation under all flight conditions, allowing for numerous logistical variations. A unique benefit of the software is the ability to calculate the impact of noise and **Landing and Take-Off (LTO)** emissions, both within and around an airport [45] [46].
- **ADAS**. A software for the conceptual/preliminary design of transport aircraft (Transport Jet, regional Turboprops, business jet) and light aircraft developed at the University of Naples Federico II by prof. Fabrizio Nicolosi and Eng. Giuseppe Paduano [47]. The software, which development started in 2005, is completely written in Visual Basic and comes with a dedicated graphic user interface to enhance user-friendliness. Its architecture provides for independent design module, however it was not conceived for **MDAO** applications.

- **CEASIOM**. A conceptual aircraft design Python framework developed within the frame of the SimSAC (Simulating Aircraft Stability And Control Characteristics for Use in Conceptual Design) Specific Targeted Research Project (STREP) approved for funding by the European Commission 6th Framework Programme on Research, Technological Development and Demonstration. CEASIOM is meant to support engineers in the conceptual design process of the aircraft, with emphasis on the improved prediction of stability and control properties achieved by higher-fidelity methods than found in contemporary aircraft design tools. Moreover, CEASIOM integrates into one application the main design disciplines, aerodynamics, structures, and flight dynamics, impacting on the aircraft performance. However, the framework does not carry out the entire conceptual design process, thus it requires as input an initial layout as the baseline configuration that it then refines and outputs as the revised layout [48]. For this reason, the framework has been used in combination with the abovementioned ADAS software [49].
- **Piano**. A professional tool for the analysis of commercial aircraft commercialized since 1990. It is used in preliminary design, competitor evaluation, performance studies, environmental emissions assessments and other developmental tasks by airframe and engine manufacturers, aviation research establishments and governmental or decision-making institutions throughout the world [50].
- **ADS (Aircraft Design Software)**. A commercial software developed by OAD (Optimal Aircraft Design) after six years of development which has become a standard for the conceptual design of the modern generation of light aircraft. The tool is suitable for several kind of customers among which aircraft designers, amateur builders, universities and research institutes [51].
- **AAA (Advanced Aircraft Analysis)**. A commercial software developed by DARCorporation widely used by industries and Universities. The tool is suitable for conceptual and preliminary design phases of both conventional and unconventional fixed wings aircraft configurations. The software allows for multi-fidelity analyses, combining classical and fast semi-empirical methodologies with physics-based methods. In addition, a graphic user interface provides for the required user-friendliness [52].
- **RDS^{win}**. Developed by the design and consulting company (Conceptual Research Corporation) of Daniel P. Raymer, this commercial software is conceived to support industries, governments and Universities during preliminary aircraft design activities. It performs **MDAO**, as well as trade studies, and comes with a graphic user interface to enhance user-friendliness. The tool is suitable both for commercial transport aircraft and military fighters, giving to users the possibility to experiment also with unconventional configurations [53].

A key feature that most of these software provide, is the possibility to parametrically define both aircraft components and complete aircraft configuration leading to a very fast and intuitive definition process of a generic aircraft model. With software and computer hardware currently available in aerospace industry, the design process has become very effective and employs, a very sophisticated and highly optimized chain of calculation tools [42].

A modern preliminary aircraft design tool should be characterized by a certain level of accuracy and reliability, the capability to perform multidisciplinary analyses and optimizations, and reasonably

short computational times for a complete analysis process. Because of the relevance of aircraft performance, noise and emissions levels, maintenance and operative costs in the commercial success of a transport aircraft, a modern software framework must be developed aiming at a multidisciplinary approach. Another important feature lies in the user-friendliness of the software allowing users to interact with the framework in an easy, fast, and efficient way. To ensure longevity and to enrich future exploitation capabilities, the possibility to include in the software multiple fidelity analysis methodologies or to easily implement new semi-empirical models, is of primary importance. One remarkable example is given by the possibility to easily generate and export the aircraft configuration CAD model in one or more standard formats and to execute high-fidelity analyses with external tools (i.e. Computational Fluid Dynamics or Finite Element Method solvers) [42].

DAF research group members have been users of most of the abovementioned software, and they have reached a mature vision of which features one must expect from a modern MDAO software. This vision has driven the development of JPAD as a modular framework, gathering all the lessons learned in the last few decades of tool development for aircraft design [54].

In recent years, the DAF group has gained knowledge and experience in developing, testing and validating several approaches and methodologies concerning aircraft design field of application. For instance, an improved approach regarding the vertical tail plane design and sizing was accomplished by means of numerical and experimental analyses [55] [56] [57]. This methodology was also applied to size the vertical tail plane of a new twin-engine commuter aircraft [58], then was validated through wind tunnel tests [59]. Past research activities have, also, focused on aerodynamic derivatives estimation on light and General Aviation aircraft [60]. Another methodology, regarding the design of the fuselage and the prediction of its aerodynamic characteristics, was developed through CFD-RANS calculations performed on several fuselage geometries suited for regional transport aircraft [17]. The research group have developed a deep experience as far as aircraft design [61] [62] [63] is concerned also for innovative technologies [64], such as for design and aerodynamic analysis of airfoil and high lift devices [65] and performance estimation of light aircraft with morphing devices [66]. Most of these knowledges have been included in the JPAD library using dedicated external databases [42].

3.3 The JPAD software

The idea of JPAD derived from the experience gained by the DAF research group in the design of general aviation and turboprop aircraft [67] [58] [59].

Gathering the best practices coming from the current aircraft design software scenario, JPAD offers the following features: It is modular and easily extendable; is based on advanced features of Java (Java 8+ and JavaFX [68]) and is designed using object-oriented and functional criteria; it is portable; the inputs and the outputs are fully configurable with a flexible XML-based set of files; it can automatically generate CAD outputs via the OpenCASCADE modelling library [69]; its analysis sub-models are based both on semi-empirical formulations combined with more refined simulation-based methods, offering a multi-fidelity analysis approach; it is designed to allow interface with any other external calculation tool.

These features make the JPAD framework a modern tool in “continuous” development, according to professional software maintenance criteria [54].

JPAD is completely written in Java, a well-known general-purpose, concurrent, class based and **OOP** language. One design goal of the Java language is the portability, which means that programs written for the Java platform must run similarly on any combination of hardware and operating system with adequate runtime support [42].

As described in the work of Mohamed Fayad and Douglas Schmidt [70], object-oriented application frameworks are a promising technology for reifying proven software designs and implementations in order to reduce the cost and improve the quality of software.

OOP deals with the minimum of three software engineering goals; namely reusability, extensibility and flexibility. Reusability is very beneficial in two ways for any developer. Firstly, the time for producing a code is reduced; once developed it becomes easy and efficient to reuse it many times. Secondly, the reliability of the code increases as we are using the previously existing code for our development. Extensibility can be related to the concept of inheritance in **OOP**. The attribute or behavior that is set for the base class will be extended to its derived class automatically and hence the same attribute can be used to refer the derived class variables. **OOP** is very flexible in terms of software development. Its flexibility can be understood by polymorphism, where we can add more variations and do modifications using the same function name but with different variables [71].

A wide selection of possible **OOP** languages is available in the programming languages scenario and among them Java has been the most used one since July 2015 according to the TIOBE programming community index shown in Figure 3.1. The TIOBE Programming Community index is an indicator of the popularity of programming languages updated each month by the software quality company TIOBE [72].

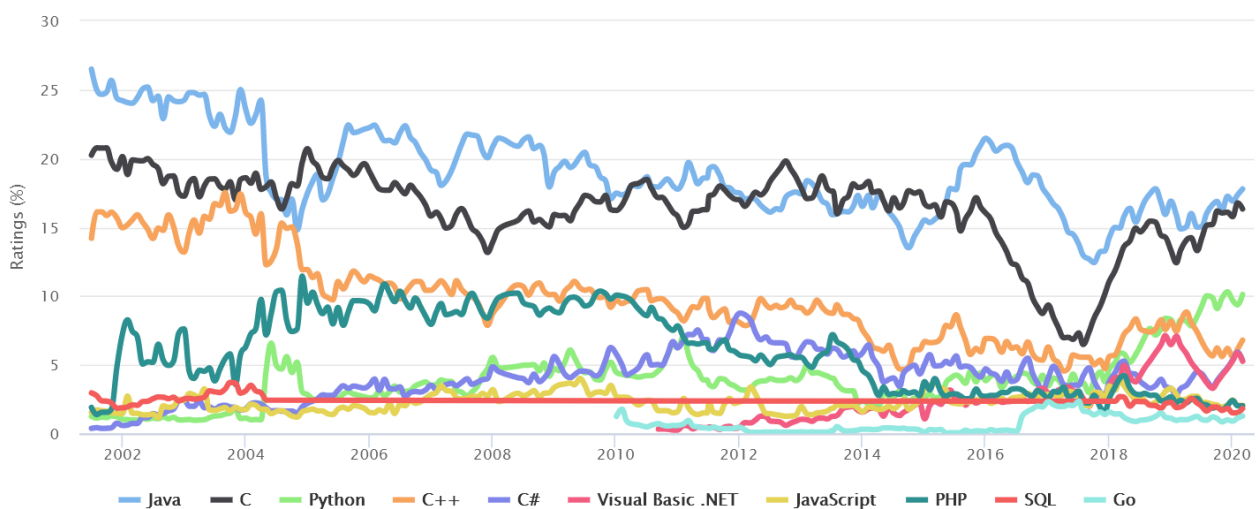


Figure 3.1 TIOBE programming community index, March 2020 (www.tiobe.com).

Beside its popularity, the choice of Java has been made due to the following key points: The language is widely supported by Oracle and a huge community of developers so that the problem of having an obsolete library due to aging is avoided. The Java language promotes the use of open source libraries which provide a very simple management of input and output tasks as well as complex mathematical operations. Finally, the language promotes modularity so that it is easier to work with an ever-changing team [73].

The **JPAD** library represents a powerful alternative to a plethora of similar software, both freeware and commercial. Most of these tools have an important history, and many of them have been in use for decades. However, some of them were conceived with poor software design criteria, have a rigid textual input, and come with no visualization features. One notable example is Digital DATCOM [74], a very well-known computer program that implements a variety of semi-empirical formulations derived from several years of aerodynamic investigations, mainly in the United States. This software solution was developed in the 1970s and lacks many of the usability features typically expected in modern applications [54]. For this reason, the **JPAD** framework has been provided with a dedicated **GUI** to easily manage aircraft generation, analyses and results visualization. This **GUI**, named **JPADCommander**, has been completely designed using the JavaFX [68] library together with a JavaFX-based development tool, named SceneBuilder [75], which allowed to create an efficient and modern user interface.

3.3.1 Software architecture

To define an efficient, intuitive and extensible software architecture requires a relevant amount of experience and knowledge about current software development technologies. As previously stated, modularity is a fundamental feature for a modern and robust software environment. Thus, the **JPAD** framework has been organized as an interconnected ecosystem of software modules each one related to a specific task. The main root at the base of the framework is the **jpad-core** module which allows to manage the parametric aircraft model generation and to perform all available analyses. On top of that, as shown in Figure 3.2, several other modules provide other important features as listed below. Each of this module will be further described in the following subsections.

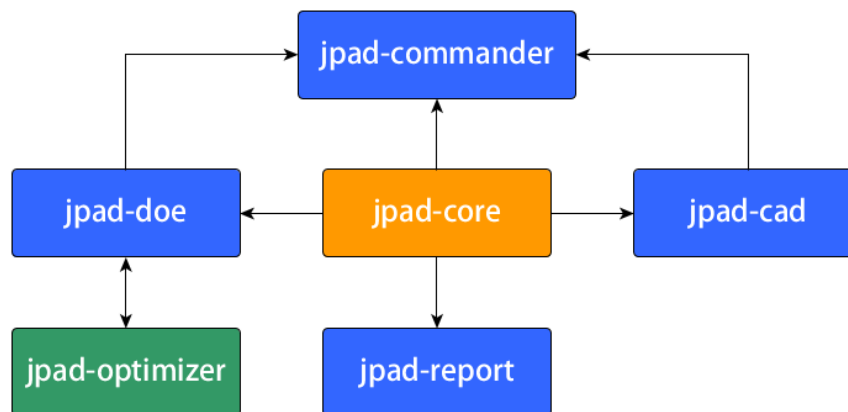


Figure 3.2 JPAD framework architecture.

- **jpad-cad** - This module is in charge of the automatic CAD model generation based on the aircraft parameterization made in the **jpad-core** module.
- **jpad-commander** - The dedicated **GUI** of the **JPAD** framework. Completely written using JavaFX combined with SceneBuilder, this powerful tool allows user to easily define an Aircraft model, to generate its CAD, to run a set of analyses and to visualize their results.

- **jpad-doe** - Module conceived to perform sensitivity studies by changing geometrical or analysis-related design parameters. It uses the **jpad-core** module to run each aircraft analysis performing a full-factorial design of experiments. The result is a response surface suitable for built-in optimizations or other external optimization tools. Thanks to a recent collaboration on a bachelor's thesis work between the **DAF** group and the Computer Engineering department of the University of Naples Federico II, this module has been enhanced with the possibility to use an adaptive multi-threading approach to reduce the total computational time.
- **jpad-optimizer** - This standalone module can be used to perform single-objective as well as multi-objectives optimizations using the state of the art of metaheuristic optimization algorithms based on computational intelligence like **GA** or **PSO** algorithms. Being standalone, this module can be used also outside the **JPAD** framework in combination with other analysis tool like the abovementioned Pacelab APD.
- **jpad-report** - Conceived for a fast and efficient output visualization, this module allows to automatically generate a complete aircraft report mixing text, figures and tables both in Microsoft Word and PDF file formats.

The framework architecture shown in Figure 3.2 provides for the required flexibility needed to easily extend framework functionalities in the near future. New modules can be inserted in the **JPAD** framework with very little effort to face incoming research challenges dealing with aircraft preliminary design, as the hybrid-electric distributed propulsion.

In terms of Software Engineering, handling such a complex software structure is not a simple task and a smart developer must use the right tool to overcome this problem. Nowadays, a very large set of powerful open-source technologies are available to help developers during their work and, dealing with a multi-project software structure, the use of Gradle revealed to be a successful choice.

Gradle is an open-source build automation tool focused on flexibility and performance. Built using a Groovy [76] or Kotlin [77] **Domain Specific Language (DSL)** [78], Gradle is conceived for large multi-project builds. It uses incremental builds recognizing which part of the code are already updated and allowing to avoid the execution of those parts.

Gradle is also a fundamental resource when dealing with dependencies. It allows to keep tidy and updated the whole external libraries tree by automatically download them from dedicated online repositories. Thus, avoiding the need to manually add JAR files to the specific project.

3.3.2 The Core of the JPAD framework

The **JPAD** framework has been conceived to be used in an industrial environment across conceptual and preliminary design phases. In these phases a lot of different configurations should be analyzed, so the software has been developed to provide results in a short period of time, thus the need to use simple but reliable semi-empirical methods. A comprehensive study of the methods available in literature has been firstly carried out to improve results accuracy: each method (produced in-house or drawn from literature) has been tested against experimental data so that statistical quantities (e.g., standard deviation) could be estimated either to find the best method currently available or to make a merger of different methods.

In Figure 3.3 the entire structure of **jpad-core** is illustrated. It is possible to clearly note that there are two main blocks: input and core.

The input block is defined by two main parts: aircraft and analyses definitions. The first one defines a parametric aircraft model using a main file (**aircraft.xml**) which collects all the components positions and the related xml file name (i.e. **fuselage.xml**, **vtail.xml**, and so on) which contains all geometrical data. Starting from the aircraft parameterization provided by these files, the **jpad-cad** module can automatically generate the CAD model as shown in Figure 3.3. This structure allows also to generate different aircraft, or different configurations of the same model, by simply combining different components allowing to easily perform comparisons between these latter. The second part of the input block defines all data required by each analysis inside the Core module. As for the aircraft definition, the user has the possibility to setup each specific discipline analysis via a dedicated xml file (**analysis_weights.xml**, **analysis_balance.xml** and so on). Each of those is used in the main analysis configuration file, named **analysis.xml**, in which the user selects the analyses to be carried out and specifies the related xml file name and path. In addition to the main two blocks, a third configuration file, named **operating_conditions.xml**, is used to specify additional operational data concerning angle of attack, altitude, engine throttle setting and, when needed, high-lift devices deflection, related to the four flight conditions taken into account by the framework (Take-off, Climb, Cruise and Landing).

The Core block collects all analysis managers related to the five disciplines considered, at the moment of writing, by the **JPAD** framework: Weights, Balance, Aerodynamic and Stability, Performance and Costs. As illustrated in Figure 3.3, each of those can be further divided in several sub-modules related to a specific discipline calculation.

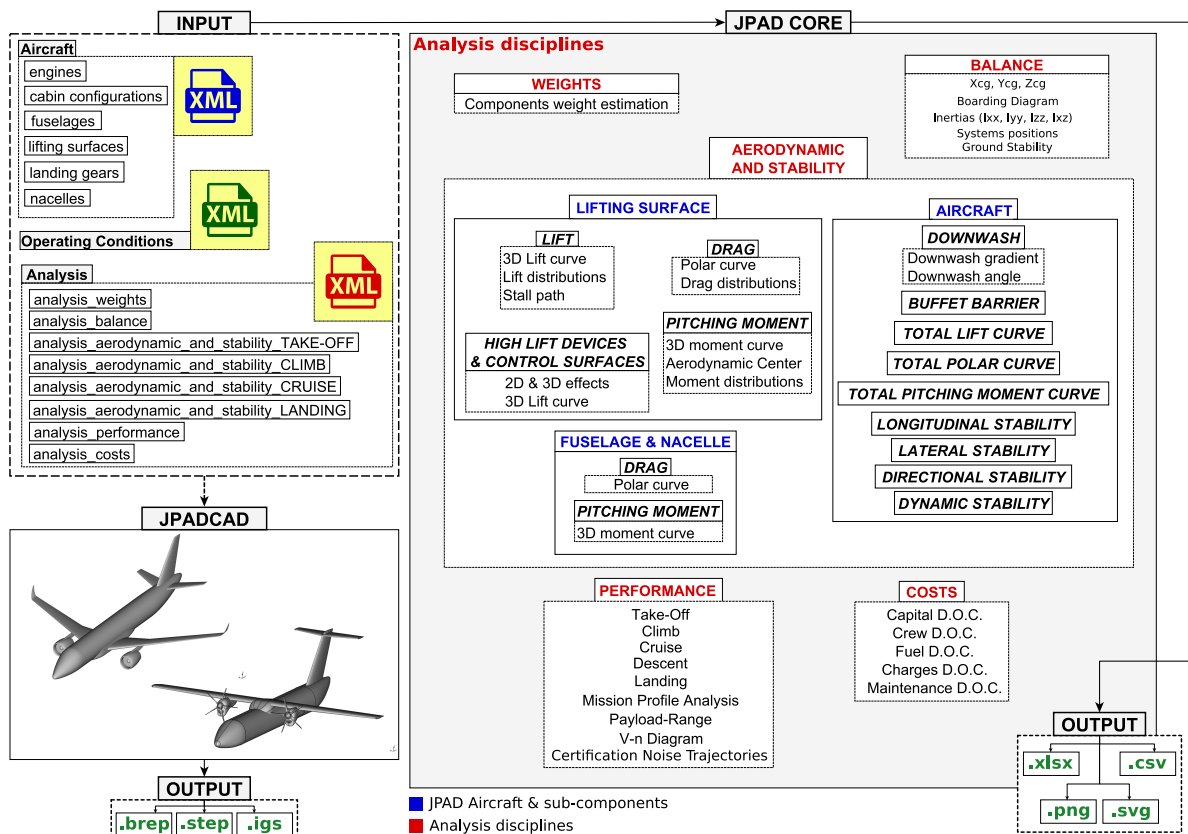


Figure 3.3 jpad-core architecture.

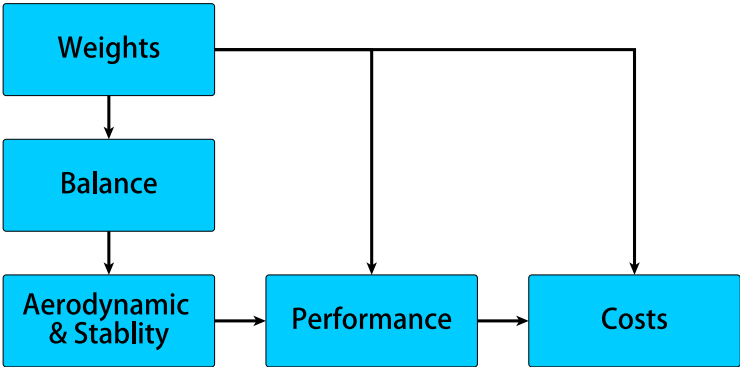


Figure 3.4 jpad-core modules dependencies.

To enhance the framework flexibility, the framework has been conceived to allow both a complete analysis loop involving all disciplines, both standalone analyses using one or more calculation modules.

As explained in [42], in case the user wants to carry out a complete analysis cycle, the JPAD framework uses a combination of its analysis modules as shown in Figure 3.4.

The flowchart of Figure 3.5 describes the behavior of the multi-disciplinary analysis loop in which the starting point is the first estimation of the amount of fuel needed for the specified mission. Then a balance analysis is carried out to determine the center of gravity excursion.

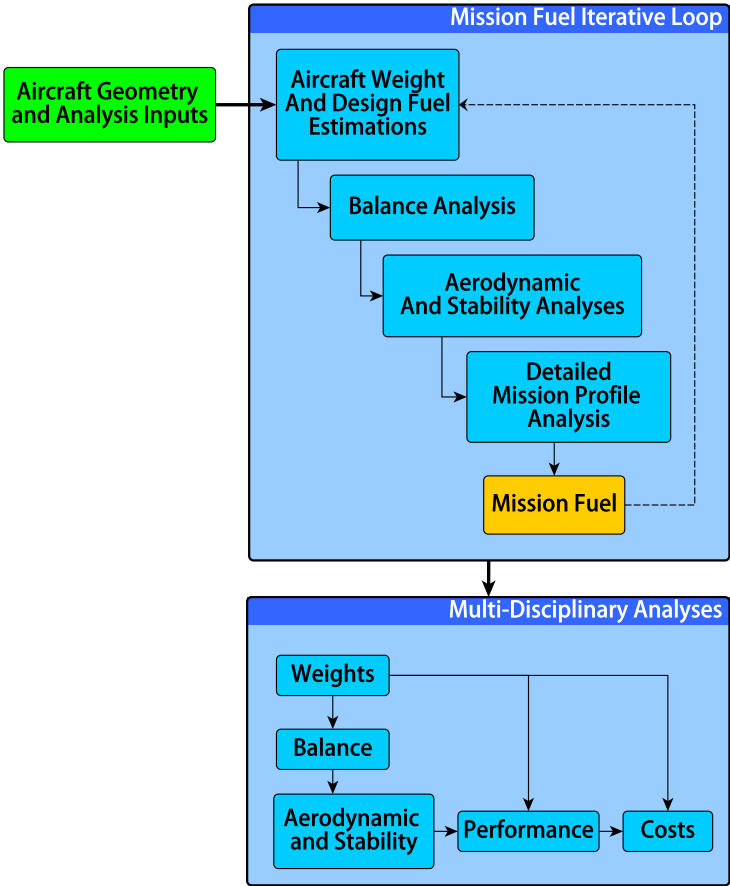


Figure 3.5 jpad-core complete analysis loop.

For each center of gravity, the aerodynamic and stability module estimates the trimmed drag polar in all the following flight condition: take-off, climb, cruise and landing. Finally, the performance module uses these data to make a detailed simulation of the initial mission profile estimating a new amount of fuel needed to cover the mission. Thus, an iterative process is carried out until the first estimated fuel mass is equal to the one calculated by the mission profile analysis. Once the preliminary iterative loop has converged, the **JPAD** library reads from file all the analysis that the user wants to perform and invokes only the required analysis modules [42].

On the other hand, if the user wants to carry out only a single analysis module, **JPAD** allows to perform standalone analyses using a customized software design pattern dedicated to this task. The idea is to link **manager** classes to **calculator** classes defining, this way, a **manager-calculator** pattern.

Managers are Java classes developed to read, write and dispatch requests. On the other side, Calculators are Java classes designed as containers for a dedicated set of static methods in charge to perform simple specific calculations related to a particular discipline sub-module. To clarify the behavior of this pattern, Figure 3.6 shows an example of use in which the user wants to perform only the take-off run simulation.

Starting from the analysis input file (**analysis.xml**), the first entity to be called is the overall analysis manager named **ACAnalysisManager**. This class reads the **analysis.xml** file and fills the list of analyses to be carried out. Depending on which discipline the user wants to carry out, this class calls for the specific discipline manager (in this case **ACPerformanceManager**). Each discipline manager can handle different analyses type as shown in Figure 3.3. To do this, they firstly read their dedicated input file defined by **analysis.xml**. Then, they fill the list of tasks to be carried out and use dedicated Java inner classes, nested inside their body, to implement the call for the particular calculator needed to fulfill the user request.

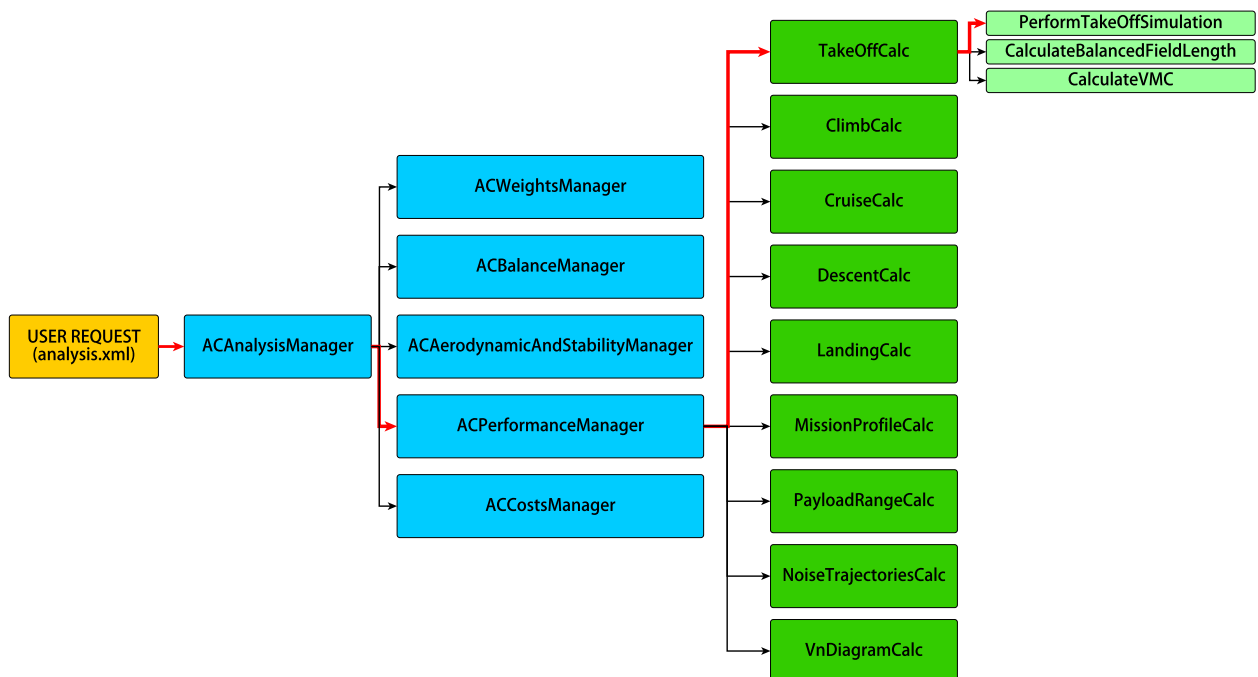


Figure 3.6 jpad-core manager-calculator pattern.

3.3.3 Aircraft parameterization in JPAD

In this section a comprehensive overview about the definition, inside **JPAD**, of a complete parametric aircraft geometry will be provided taking parts of the work reported in [79], developed by the author of this thesis together the **DAF** research group of the University of Naples Federico II. In addition, more details will be provided concerning several subcomponents main input and derived parameters as well as the description of nacelles, engines and landing gears parametric models.

The aircraft shape is the natural starting point for **MDAO** applications, both in the conceptual and preliminary design phases. Geometry management is an essential component of any **MDAO** environment, particularly if high-fidelity analysis tools are employed, i.e. when the design has passed the initial conceptual stage.

Traditionally, aircraft conceptual design performs mission analysis, sizing, and configuration down-select of candidate designs via empirical or low-fidelity physics analyses [80] [81]. During conceptual design the resultant geometry may be simple (or nonexistent), being the focus of this process to roughly define the main characteristics of the aircraft that better meet **TLARs**. In practice, the geometry parameters at this stage can define the overall shape or even the **Outer Mold-Line (OML)** of the aircraft to a degree sufficient for low-order aerodynamic analyses such as Vortex-Lattice or Panel Methods, or for simple structural analyses such as Simple Bending/Torsion Beam Theory [82]. It is in the successive preliminary design stage that the selected configurations are tweaked by means of higher fidelity analyses [25]. These refinements are constrained to fit the overall geometric parameters that guarantee **TLARs** and aim at remodelling the geometry until the aircraft that is going to be manufactured achieves a ‘frozen’ optimal configuration.

The modelling capability of the **JPAD** framework is completely based on a parametric approach and make advantage of all beneficial effects coming from **OOP**. Thus, the associative definition of all aircraft subcomponents is managed by means of ‘configuration directives’ and parametric data inputs.

Dealing with a parametric model means that all changes in a baseline configuration can be driven by changing one or more parameters which are significant to the designer. In this respect, an important challenge is to overcome the complications that tend to arise whenever the geometry definition is scattered over many different analysis methods, which can span different disciplines as well as different fidelity levels within a discipline [82]. The difficulty originates from the fact that geometry adjustments from redesign, based on one method, are likely to be inconsistent with the other geometry definitions, which ultimately must be resolved by human intervention in some typically ad-hoc manner.

An object-oriented strategy for geometric modelling proves to be advantageous to establish definitions and rules that maximize the level of automation of design cycles. Such a bottom-up approach is particularly suited for the management of multiple levels of fidelity and, ultimately, facilitates the exploration of the design space.

High-fidelity geometric modelling of a complete aircraft configuration requires the definition of hundreds of parameters and poses several challenges to the designer. The effective implementation of software data structures necessary to manage those parameters and their variations is an even more difficult task. The problem achieves the highest grade of difficulty if one wants to extend the set of variables that define a traditional fixed-wing architecture to take into account all feasible cases of non-conventional configurations.

Main inputs	Derived parameters
Aircraft type (Jet, Turboprop, etc.)	Exposed wing
Aircraft reference regulations (FAR-23, FAR-25)	Wing AC to Horizontal tail AC distance
Cabin configuration input file path	Wing AC to Vertical tail AC distance
Fuselage input file path	Horizontal tail volumetric ratio
Fuselage X position (assumed as 0.0)	Vertical tail volumetric ratio
Fuselage Y position (assumed as 0.0)	Wing AC to Canard AC distance
Fuselage Z position (assumed as 0.0)	Canard volumetric ratio
Wing input file path	Excrescences factor
Wing apex X position	Total wetted area
Wing apex Y position	
Wing apex Z position	
Horizontal tail input file path	
Horizontal tail apex X position	
Horizontal tail apex Y position	
Horizontal tail apex Z position	
Vertical tail input file path	
Vertical tail apex X position	
Vertical tail apex Y position	
Vertical tail apex Z position	
Canard input file path (if present)	
Canard apex X position (if present)	
Canard apex Y position (if present)	
Canard apex Z position (if present)	
Engine input file path (single engine)	
Engine position (Wing, H-tail or Fuselage) (single engine)	
Engine inlet X position ref. to attachment (single engine)	
Engine inlet Y position ref. to attachment (single engine)	
Engine inlet Z position ref. to attachment (single engine)	
Engine tilt angle (single engine)	
Engine nacelle input file path (single engine)	
Landing gears input file path	
Landing gears position (Wing, Nacelle or Fuselage)	
Nose gear ΔX (% of Fuselage length)	
Main gear ΔX (% of M.A.C., Nacelle or Fuselage length)	
On-board systems electrical type (AC or DC)	

Table 3.1 Summary of aircraft parameters. All positions are in Body Reference Frame (BRF)

A conventional commercial transport aircraft configuration is made up of a set of clearly identified subcomponents. The main element is the fuselage, a symmetrical, non-lifting, slender body designed to carry the payload. The most important aerodynamic subcomponent is the wing, which is the main symmetrical lifting surface that most significantly determines vehicle's performance characteristics. Commercial transport configurations exhibit invariably at least two engine nacelles, that serve as streamlined power plant housings, conceptually modelled as smaller, symmetrically disposed non-lifting bodies. Finally, conventional configurations include the horizontal empennage, a rear-mounted smaller symmetrical lifting surface (but conceptually similar to the main one), and the vertical tail, a non-mirrored lifting surface. These latter necessary for the required airplane's stability and control.

Several variants are possible, for instance the way engine nacelles are attached to the rest of the configuration, or the presence of extra empennages such as canards, and several more circumstances. Nevertheless, as far as geometric modelling is concerned (and to some extent aerodynamic modelling as well), the main conceptual effort is the definition of a parametrized template shape and of a related set of parameters that make the geometric representation as comprehensive as possible.

Beside conventional configurations, **JPAD** modelling capabilities allows user to generate also unconventional configurations by simply change few component files data or to change the combination of subcomponents files. For example, a multi-panel wing and horizontal tail combination, with appropriate dihedral angles, can lead to a boxed-wing configuration or an horizontal tail with high dihedral angle defines a V-Tail configuration. Furthermore, combining any number of engine file allows to take into account for distributed propulsion.

However, it must be noted that, for these unconventional configurations, classical semi-empirical analysis approaches are not feasible and higher-fidelity methodologies are requires. Thus, the possibility to interface the **JPAD** framework with external high-fidelity analysis tool.

Starting from the top, the parameterization of the aircraft component pass through the definition of the number and type of subcomponents, their positions and rotations in the **BRF** as well as the file path related to each component configuration file. A summary of these data is provided in Table 3.1.

Concerning the fuselage parameterization, a set of parameters defining the side view and top view is shown in Figure 3.7. The body of the fuselage is decomposed in a number of adjacent subparts: a central cylindrical trunk, being the portion where payload is allotted, and, as shown in detail in Figure 3.8, a frontal streamlined nose and a tail cone.

Along the whole-body length, the generic fuselage cross-section is modelled as the union of two parametrized Bezier curves, see Figure 3.9. These definitions, with an appropriate treatment of nose tip and tail tip ‘cap’ surfaces, allow the construction of a ‘water-tight’ (closed) surface. From this parameterization, a set of input parameters has been marked as independent, while all other parameters can be derived from them. This set of input data, along with the derived parameters is reported in Table 3.2.

The main fuselage sub-component is the cabin. Its layout parameterization is of extreme importance since it allows to estimate the center of gravity excursion during boarding operations as well as to assess whether or not the required design passengers number can be stored inside the fuselage. Moreover, the possibility to take into account for different classes (Economy, Business and First) allows for comfort and economic studies.

Starting from the number of passengers, **JPAD** performs also the estimation of the number, the type and the width of emergency exists according to regulations. To enhance the flexibility of this parameterization saving its consistency, the cabin definition may be carried out using different approaches. Thus, the user can provide all data reported in Table 3.3 or can estimate some of them (seat pitches, seat widths, passengers percentage per class type) according to statistical data.

It must be noted that if the user specifies the number of rows and the design passengers number, **JPAD** is able to define a seat map with missing seats to best fit the required number of passengers. The number of rows can be also estimated from passengers percentages for each class type.

After reading all inputs, the framework generates all derived data reported in Table 3.3 and performs consistency checks to asses if the cabin fits fuselage dimensions.

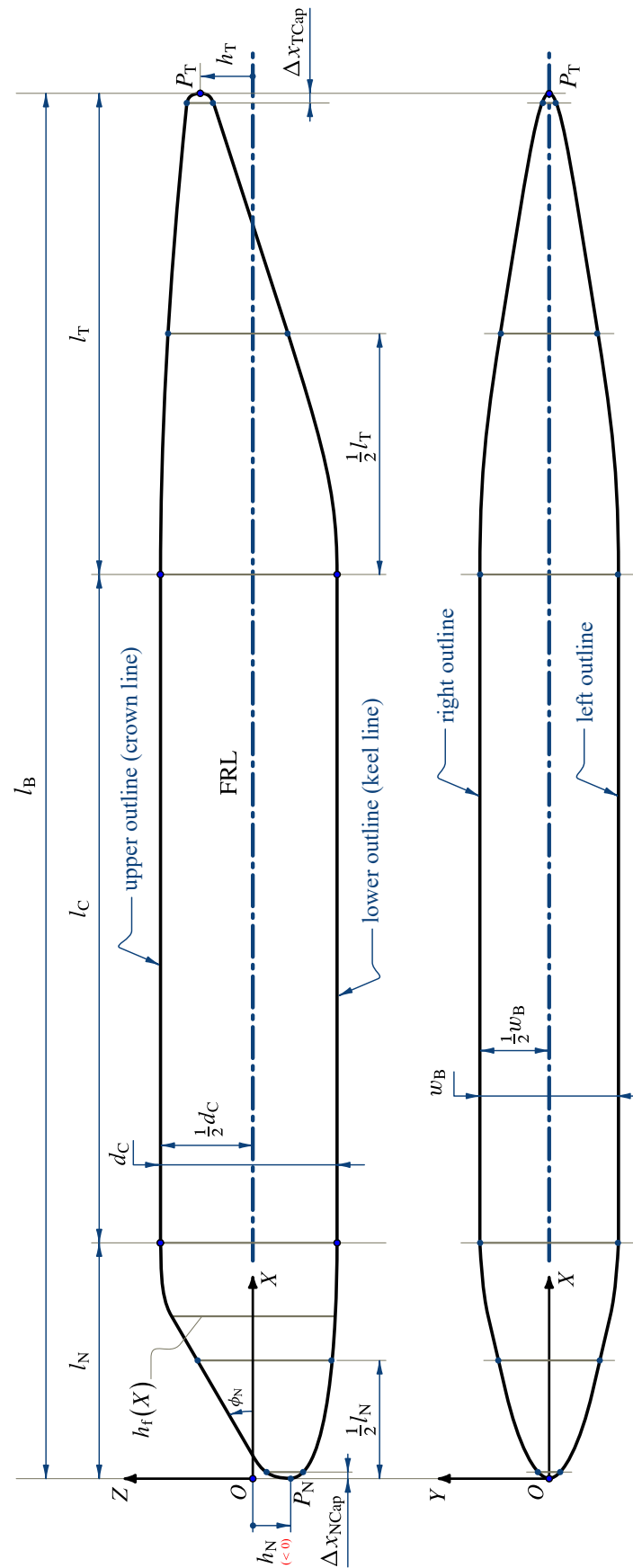


Figure 3.7 Fuselage nomenclature. Sideview and top view outlines [79].

Main inputs	Derived parameters
Overall length (l_B)	Nose trunk length (l_N)
Nose trunk length ratio (% of overall length)	Cylinder trunk length (l_C)
Nose tip height offset (h_N)	Tail trunk length (l_T)
Nose tip cap extension (% of nose trunk length)	Equivalent cylinder section diameter (d_B)
Windshield type	Nose trunk fineness ratio (λ_N)
Windshield width	Cylinder trunk fineness ratio (λ_C)
Windshield height	Tail trunk fineness ratio (λ_T)
Nose lower section percent thickness (a)	Fuselage fineness ratio (λ_B)
Nose upper section deforming factor (ρ_u)	Nose cap extension (ΔX_{NCap})
Nose lower section deforming factor (ρ_l)	Tail cap extension (ΔX_{TCap})
Cylinder trunk length ratio (% of overall length)	Windshield area
Cylinder section height	Cylinder section area (S_B)
Cylinder section width	Wetted area (S_{wet})
Cylinder lower section percent thickness (a)	Form factor
Cylinder upper section deforming factor (ρ_u)	Upsweep angle (ϕ_T)
Cylinder lower section deforming factor (ρ_l)	Windshield angle (ϕ_N)
Tail tip height offset (h_T)	Fuselage outline curves
Tail tip cap extension (% of tail trunk length)	
Tail lower section percent thickness (a)	
Tail upper section deforming factor (ρ_u)	
Tail lower section deforming factor (ρ_l)	

Table 3.2 Summary of fuselage parameters (See Figure 3.7, Figure 3.8 and Figure 3.9).

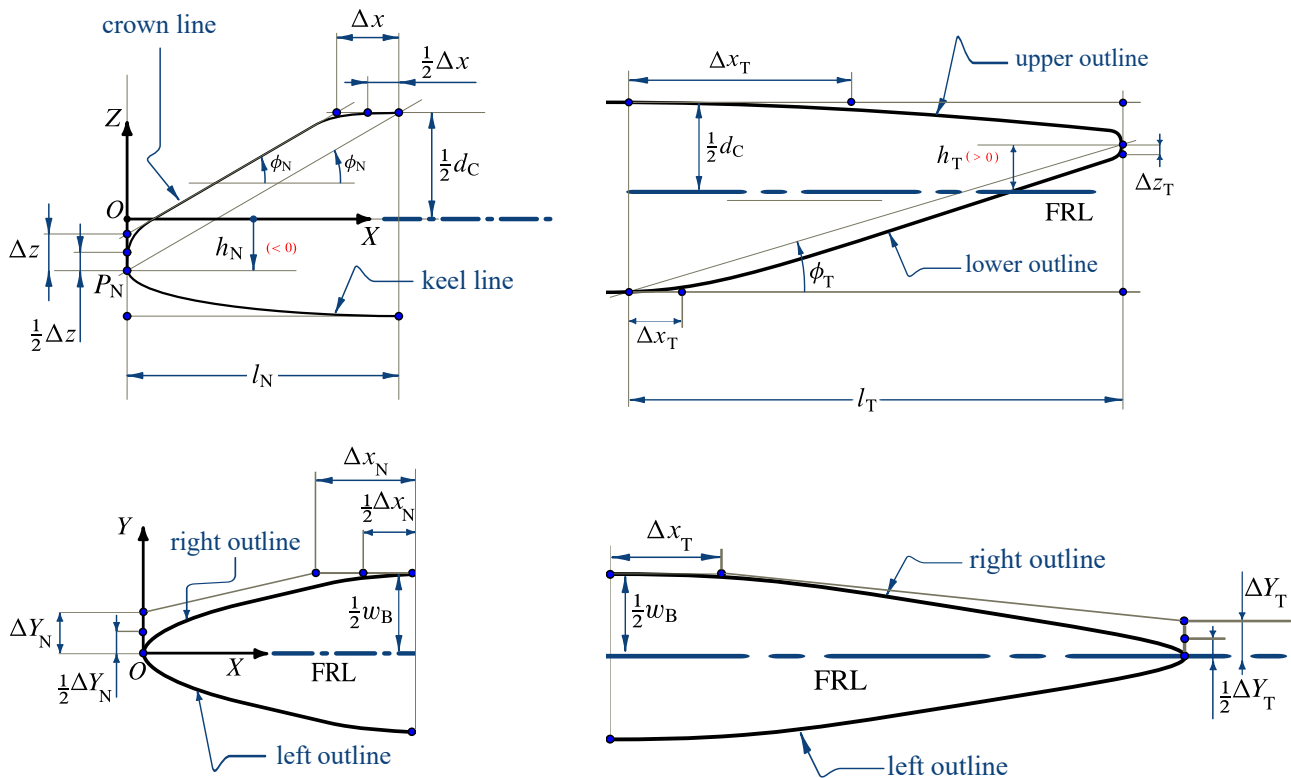


Figure 3.8 Fuselage nomenclature. Sideview and top view of nose and tail [79].

Main inputs	Derived parameters
Design pax. number	Seat blocks
Flight crew number	Cabin crew number
Classes types	Total crew number
Cabin start X offset (% fuselage length)	number of pax. Economy class
Cabin forward space (% fuselage length)	number of pax. Business class
Cabin afterward space (% fuselage length)	number of pax. First class
Economy class abreast (if present)	Number of aisles
Business class abreast (if present)	Aisles widths
Economy class abreast (if present)	Seat map
Percentage of Economy class pax. (if present)	Number of emergency exits
Percentage of Business class pax. (if present)	Type of emergency exists
Percentage of First class pax. (if present)	Emergency exists width
Seat pitch Economy class (if present)	
Seat pitch Business class (if present)	
Seat pitch First class (if present)	
Seat width Economy class (if present)	
Seat width Business class (if present)	
Seat width First class (if present)	
External seat distance from wall Economy class (if present)	
External seat distance from wall Business class (if present)	
External seat distance from wall First class (if present)	

Table 3.3 Summary of cabin layout parameters.

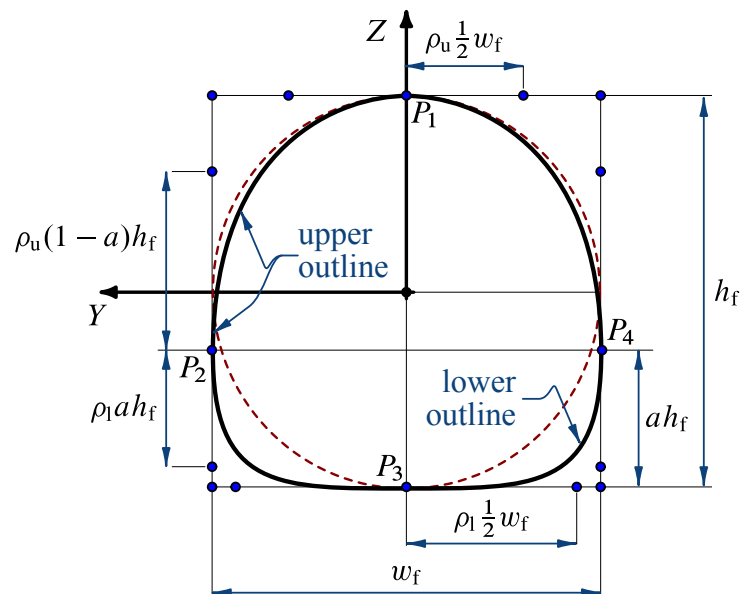


Figure 3.9 Fuselage nomenclature. Cross section parameters defining a generic section made up of two bezier curves (upper and lower) [79].

Dealing with lifting surfaces, the JPAD framework makes use of the abstraction feature of the OOP to define a single class able to parameterize wings, horizontal tails, vertical tails and canards. Each lifting surface can be modelled as an interconnection of smaller entities, named panels, which main parameters are summarized in Table 3.4 together with movable surfaces and derived geometrical data. As an example, planform parameters of a two-panel wing are reported in Figure 3.10, where also the ‘equivalent wing’ is shown. The ‘equivalent wing’ is a single-panel lifting surface representative of the real wing used by designers for layout initialization and for low-fidelity early estimations. It has the same area, the same span and the same tip chord of the real wing but with different values of both root chord and sweep angle. The generation of the ‘equivalent wing’ concerns also multi-paneled wings, horizontal tails, vertical tails and canard as well.

For a lifting surface a local reference frame of coordinates is so defined that the X axis coincides with the root section chord, originates at the chord leading edge and goes from leading to trailing edge. The Z -axis is in root section plane and points from airfoil’s lower side to upper side. Consequently, the positively oriented Y -axis completes the right-handed frame, which is pilot’s right in case of a symmetric wing.

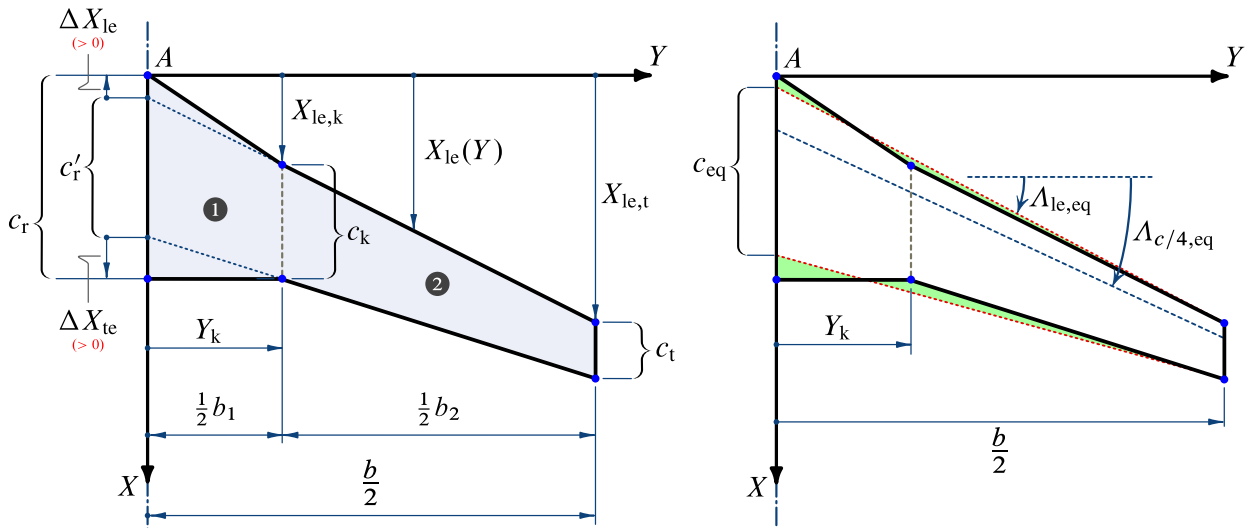


Figure 3.10 Planform definitions for a two-panel wing (left) and its corresponding equivalent wing (right) [79].

Geometrical details of a generic lifting surface panel side view are shown in Figure 3.11. Airfoils geometries and related local two-dimensional aerodynamic properties are considered as inputs to the model. These include quantities like zero-lift angle of attack, lift curve slope, aerodynamic polar, chordwise aerodynamic center position, pitching moment coefficient with respect to aerodynamic center.

Most of the airfoil aerodynamic data can be both assigned manually, both calculated via an internal dataset based on Abbott and Von Doenhoff airfoil data concerning NACA family [83]. Input data concerning airfoil geometry and aerodynamics is provided in Table 3.5

Lifting surfaces can also be equipped with one or more movable hinged aerosurfaces, including flaps, slats and ailerons (wings), elevators, rudders and control surfaces (tail planes and canards). The schematic of a wing top view with a generic movable surface is shown in Figure 3.12. In addition, in case of spoilers, also the chordwise position of the movables must be taken into account, being this aerosurface not on the trailing edge of the lifting surface.

Main inputs	Derived parameters
Main spar position	Panel area (each panel)
Secondary spar position	Panel aspect ratio (each panel)
Main spar position	Panel sweep at half chord (each panel)
Surface roughness	Panel sweep at quarter chord (each panel)
Winglet height (only wings)	Panel sweep at trailing edge (each panel)
i-th panel span	Panel taper ratio (each panel)
i-th panel dihedral	Overall area
i-th panel sweep at leading edge	Overall aspect ratio
i-th panel span	Overall span
i-th panel inner chord	Overall wetted area
i-th panel inner airfoil data	Equivalent wing
i-th panel inner twist angle	Mean aerodynamic chord
i-th panel outer chord	$X_{LE,mac}$
i-th panel outer airfoil data	$Y_{LE,mac}$
i-th panel outer twist angle	$Z_{LE,mac}$
i-th symmetric flap type	Mean thickness ratio
i-th symmetric flap inner spanwise position	Form factor
i-th symmetric flap outer spanwise position	Chord distribution
i-th symmetric flap inner chord ratio	Twist distribution
i-th symmetric flap outer chord ratio	Dihedral angle distribution
i-th symmetric flap minimum deflection	X_{LE} distribution
i-th symmetric flap maximum deflection	Z_{LE} distribution
i-th asymmetric flap type (only wings)	Y stations distributions
i-th asymmetric flap inner spanwise position (only wings)	Airfoil data distributions
i-th asymmetric flap outer spanwise position (only wings)	Symmetric flaps area
i-th asymmetric flap inner chord ratio (only wings)	Asymmetric flaps area
i-th asymmetric flap outer chord ratio (only wings)	Slats area
i-th asymmetric flap minimum deflection (only wings)	Spoilers area
i-th asymmetric flap maximum deflection (only wings)	Total aerosurfaces area
i-th slat inner spanwise position (only wings)	
i-th slat outer spanwise position (only wings)	
i-th slat inner chord ratio (only wings)	
i-th slat outer chord ratio (only wings)	
i-th slat extension ratio (only wings)	
i-th slat minimum deflection (only wings)	
i-th slat maximum deflection (only wings)	
i-th spoiler inner spanwise position (only wings)	
i-th spoiler outer spanwise position (only wings)	
i-th spoiler inner chordwise position (only wings)	
i-th spoiler outer chordwise position (only wings)	
i-th spoiler inner chord ratio (only wings)	
i-th spoiler outer chord ratio (only wings)	
i-th spoiler minimum deflection (only wings)	
i-th spoiler maximum deflection (only wings)	

Table 3.4 Summary of a generic lifting surface parameters.

Geometric parameters	Aerodynamic parameters
Max thickness ratio	$\alpha_{0,l}$
Normalized radius at leading edge	α^*
X coordinates	α^*
Z coordinates	α_{\max}
Airfoil family	$C_{l\alpha}$
Airfoil type	$C_{l,0}$
	C_l^*
	$C_{l,\max}$
	$C_{d,i}$
	$C_{l,i}$
	Laminar bucket semi-extension
	Laminar bucket depth
	Drag polar shape factor
	$C_{m\alpha}$
	$C_{m,ac}$
	$C_{m,ac}$ at stall
	Aerodynamic center (X_{ac})
	Critical Mach number
	$X_{\text{transition}}$ upper side
	$X_{\text{transition}}$ lower side

Table 3.5 Summary of airfoil parameters.

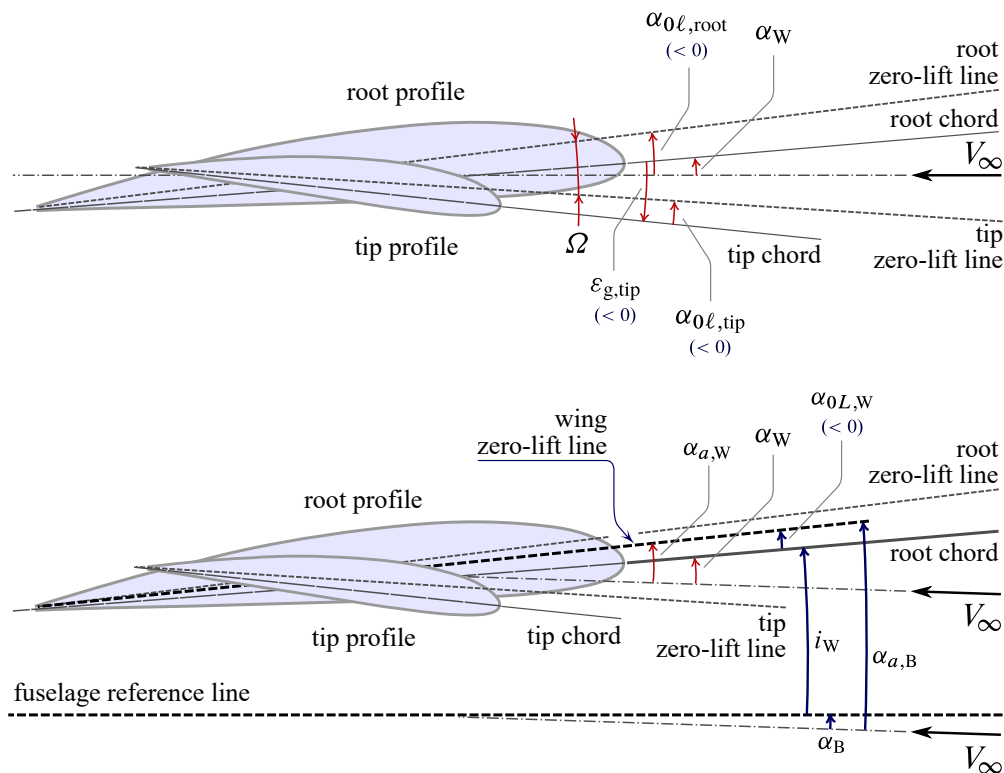


Figure 3.11 Wing nomenclature from side view [79].

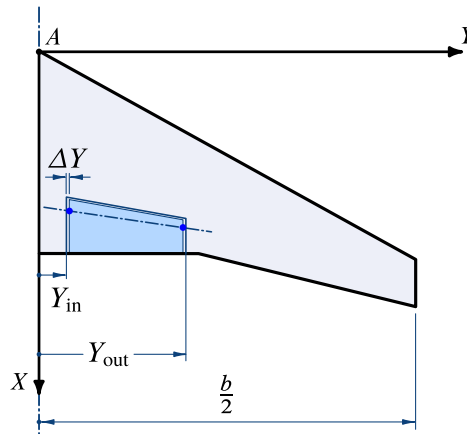


Figure 3.12 Planform view nomenclature of a generic plain movable surface in a lifting surface [79].

Another very important component to be modelled is the power plant due to its crucial impact on aircraft performance calculation. In the proposed parameterization, the power plant is considered to be divided in one or more nacelle components associated with an equal number of engine components.

For each of these abstract objects a different parameterization has been used. In particular, the nacelle has been linked to a specific engine file to allow the inheritance of its main dimension data.

Starting from the engine, its definition is strictly related to its type. **JPAD** allows to choose between turboprop, turbofan, turbojet and piston engines. According to the selected category, a specific set of parameters is used to represent the engine as shown in Table 3.6. In particular, engine length and dry mass can be both assigned by the user, or calculated using dedicated statistical database created by the **DAF** group starting from existing public engine data and statistics.

However, the most important engine input is its database file path. The database is a non-dimensional rubberized engine deck built up as an Excel file which collects thrust ratios, **SFCs** and pollutant emission indexes at different altitudes, Mach numbers, ISA deviations and throttle settings for each rating among the following ones: Max. Take-Off, **Auxiliary Power Reserve (APR)**, Max. Climb, Max. Continuous, Max. Cruise, Flight Idle and Ground Idle. **JPAD** provides the user with the possibility to either manually define a custom database or to use one of the default engine decks created by the **DAF** group during recent research projects related to turboprop and turbofan engines.

Concerning the nacelle, its shape has been modelled with a variable diameter rotating solid as shown in Figure 3.13. The two main parameters which define the overall dimension of the nacelle are its length and the maximum diameter. The length is derived from the nacelle-related engine while the maximum diameter can be either assigned by the user or calculated as described for the engine. From the maximum diameter and the overall length, four parameters are used to model the final shape defining inlet diameter ratio, outlet diameter ratio, outlet section center vertical position and maximum diameter longitudinal position. A summary of all main and derived input data is shown in Table 3.7.

Finally, the last component to be modelled is the landing gears group which consists of the nose and the main gears. The user can define whether or not landing gears are retractable as well as the number of frontal and rear wheels together with tires parameters like diameter and width. In terms of positions, the aircraft input file defines the wheelbase while wheel track is considered as an input of the landing gears configuration file.

Turbofan and Turbojets	Turboprop and Piston
Engine type	Engine type
Database file path	Database file path
Overall length	Overall length
Dry mass	Dry mass
Static thrust	Static power
By-pass ratio	Propeller diameter
	Number of blades
	Propeller efficiency

Table 3.6 Summary of engine parameters.

Main inputs	Derived inputs
Engine file path	Outline curves
Max diameter	Overall length
Inlet diameter to maximum diameter ratio	Inlet diameter
Outlet diameter to maximum diameter ratio	Outlet diameter
Max diameter non-dimensional longitudinal position	Max diameter position
Outlet section center position to max diameter ratio	Outlet section center position
	Wetted surface (S_{wet})

Table 3.7 Summary of nacelle parameters.

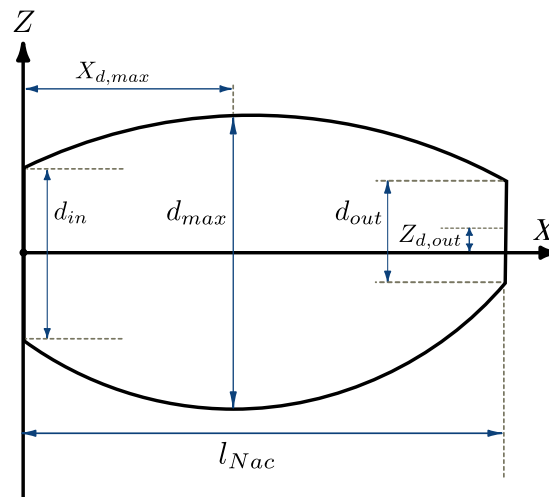


Figure 3.13 Nacelle parameterization

The nose gear leg length is not user-defined since it will be calculated as a function of the assigned frontal wheels tire diameter and of the main gear leg length. This can be either assigned by the user or calculated using an additional input data related to the desired rotation angle (by default assumed as the fuselage upsweep angle). Furthermore, the user can specify the main gear compression factor (as a percentage of the total uncompressed leg length) to account for landing gear leg compression due to the aircraft weight when on the ground.

Moreover, to perform the ground maneuverability check, the user can also define the nose wheel steering angle (by default equal to 60 degrees). A summary of the landing gears configuration file input data is provided in Table 3.8.

Main inputs	Derived inputs
Retractable boolean flag	Wheelbase
Main gear compression factor (% of main leg length)	Nose gear leg length
Main gear leg length (may be also calculated)	Main gear leg length
Wheel track	
Nose wheel steering angle	
Number of frontal wheels	
Number of rear wheels	
Frontal wheels tires diameter	
Frontal wheels tires width	
Rear wheels tires diameter	
Rear wheels tires width	

Table 3.8 Summary of landing gears parameters.

3.3.4 Analyses modules

The Core of the **JPAD** framework, as previously shown in Figure 3.3, can handle five disciplines in its multi-disciplinary workflow. This section will give an overview of each discipline-related analysis manager with major focus on those, developed by the author of this thesis, dealing with **Weights**, **Balance** and **Ground Stability**, **Performance**.

Weights

The weights manager is in charge of performing a Class-II weight estimation in order to define all aircraft weights starting from a detailed mass breakdown of all aircraft components.

Each component mass is calculated using several semi-empirical equations retrieved from the literature [15] [25] [84] [85] [86] [87] [88]. The user is allowed to choose whether to use a specific calculation method or a mean value of all component-related methods. The last strategy usually provides better results and can also take into account for different effects (e.g. mass relief effects of wing-mounted engines, fuselage mass increment due to podded landing gears, etc.) coming from different literature formulas.

In addition to this, the analysis manager is also provided with the possibility to manually calibrate each component weight by means of a dedicated set calibration factors. Those can also be used in a parametric study to simulate technological trends.

The weight estimation starts with a user-defined first guess **MTOW** which is used to assess first guess values for **MEW**, **MZFW** and **MLW** respectively assumed as 50%, 75% and 90% of the **MTOW**. Then payload and crew masses are calculated from the related cabin configuration input data assuming a user-defined mass for the generic passenger and a constant value of 86.2 kg for the generic crew member mass.

Starting from the design passengers number, also the operating items mass is estimated checking if the user-defined reference mission range is higher or lower than 2000 nautical miles.

At this point a reference value for each component mass is estimated as a fraction of the **MTOW** according to the statistical percentages reported in Table 3.9. These values will be used to estimate each component calculation method percentage relative error.

Component	Mass percentage (w.r.t. MTOW)
Fuselage	10.00%
Wing	10.60%
Horizontal tail	1.15%
Vertical tail	1.15%
Canard (if present)	1.00%
Power plant	8.30%
Nacelles	1.90%
Landing gears	4.1%
Overall systems	13.60%

Table 3.9 Component reference mass percentages with respect to the **MTOW**.

The weights analysis is carried out using an iterative process which monitors the **MTOW** variation over each loop reaching convergence when this variation is lower than 1% across two consecutive loops. The iterative loop workflow can be summarized as follows.

1. **Fuel mass estimation.** The design mission fuel mass is estimated using the fuel fraction method given that the user has assigned values for range, **SFC**, efficiency, altitude and Mach number for cruise, diversion and holding phases. However, if the user knows a reference mission fuel mass value, he can assign it directly avoiding the fuel fraction method to be invoked for each iteration.
2. **Systems and power plant masses estimation.** Each engine overall mass is estimated starting from the known value of the dry mass. In addition, the systems mass breakdown is calculated taking into account for the following groups: **APU**, Air conditioning and anti-icing system, Instruments and navigation system, Hydraulic and pneumatic systems, Electrical systems, Control surfaces, Furnishings and equipments.
3. **Structural mass estimation.** Wing, fuselage, horizontal tail, vertical tail, canard (if present), nacelles and landing gears masses are calculated using one or all available calculation methods. Control surfaces masses are considered part of structural mass as well.
4. **MEW estimation.** The structural mass is summed up with each system mass, as well as the overall power plant mass.
5. **Basic empty mass estimation.** The **MEW** is summed up with standard items mass (furnishings and equipment mass group).
6. **OEW estimation.** The basic empty mass is summed up with the operating items mass, crew mass and trapped fuel and oil mass.

7. **MZFW estimation.** The operating empty mass is summed up with the user-defined maximum payload mass. Furthermore, the **Zero-Fuel Weight (ZFW)** is calculated in the same way but using the design payload mass.
8. **MTOW estimation.** The **ZFW** is summed up with the previously calculated (or assigned) design mission fuel mass.
9. **MLW estimation.** The **MTOW** is reduced according to a user-defined percentage coming from the weights analysis XML input file.

Balance and Ground Stability

The **JPAD** balance manager allows to calculate the aircraft center of gravity position at different weight conditions, the boarding diagram and the center of gravity position of each component. In addition, it manages the calculation of aircraft inertia moments and inertias products as well as all ground stability checks needed to comply with regulations. Those checks are used also to assess whether or not the landing gear sizing has been carried out correctly.

Unlike the weights manager, the balance manager requires overall aircraft and components weights to be already estimated before starting with its calculations. This can be done in two different ways. As explained before, **JPAD** allows to carry out both a complete multi-disciplinary analysis loop, both one or more standalone analysis. In this particular case, the user can call for the outputs of the weights manager, or he can manually assign all required data needed to continue with the analysis.

A semi-empirical approach has been implemented in this case too using literature formulas proposed in [15] [25] for each component. Moreover, as for the weights manager, results can be manually calibrated by the user via a dedicated set of calibration factors which will move the generic center of gravity position by a given offset in its **Local Reference Frame (LRF)**.

A special remark concerns the estimation of the different systems groups center of gravity positions. Since no equations could be found in literature, those positions can be managed in three different ways:

- Neglected
- Assigned manually by the user giving as input X and Z positions in **BRF**
- Automatically estimated starting from typical positions shown in Figure 3.14. A summary of the assumed positions is reported below.
 - **APU:** X_{CG} position is assumed to be at 50% of the fuselage tail trunk length, while Z_{CG} position is at 0.0m in **BRF**.
 - **Air conditioning and anti-icing system:** X_{CG} position is assumed to be at 25% of the wing root chord, while Z_{CG} position is equal to the wing apex Z position in **BRF**.
 - **Hydraulic and pneumatic systems:** X_{CG} position is assumed to be calculated as the weighted average, based on the mass, of 50% root chord position of each lifting surface in **BRF**. Z_{CG} position is calculated in the same way but using each lifting surface apex Z position on **BRF**.

- **Electrical systems:** X_{CG} position is assumed to be at 25% of the wing root chord, while Z_{CG} position is calculated as the mean value between the wing apex Z position in **BRF** and the 25% of the fuselage cabin height, starting from the bottom edge.
- **Instruments and navigation systems:** X_{CG} position is assumed to be at 50% of the fuselage nose trunk length, while Z_{CG} position is equal to the fuselage apex Z position in **BRF**.
- **Control surfaces:** X_{CG} position is assumed to be calculated as the weighted average, based on the mass, of 70% mean aerodynamic chord position of each lifting surface in **BRF**. Z_{CG} position is calculated in the same way but using each lifting surface apex Z position on **BRF**.
- **Furnishings and equipments:** X_{CG} position is assumed to be at 50% of the fuselage cylinder trunk length, while Z_{CG} position is equal to the 75% of the fuselage cabin height, starting from the bottom edge. The same position has been used to assess a typical position of the operating items group.

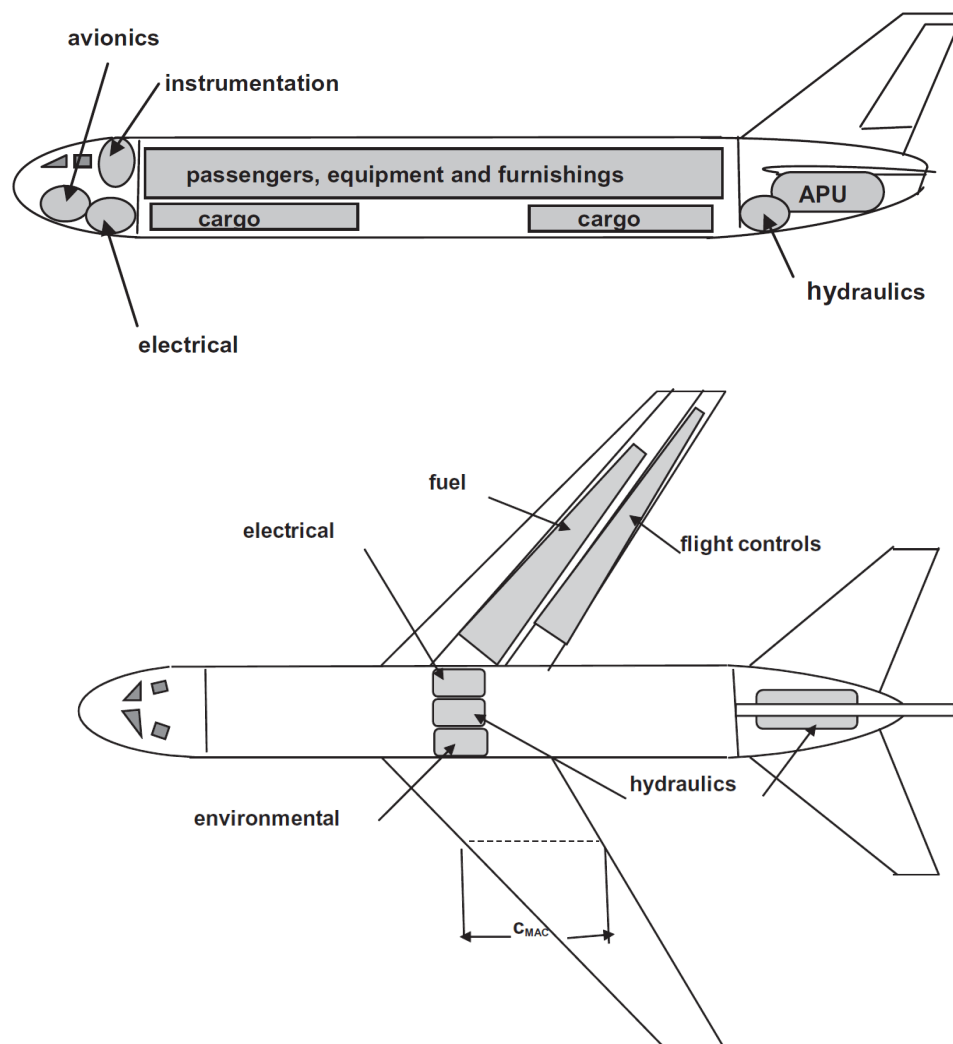


Figure 3.14 Typical locations of the different aircraft systems [15].

The complete balance analysis is carried out using the procedure reported below. As a result, the user will have access to all components center of gravity positions in **BRF**, **LRF** and as a percentage of the **MAC**. The same for the overall aircraft at all weight conditions. In addition, the module produces a visual representation of each component center of gravity position as shown in Figure 3.15.

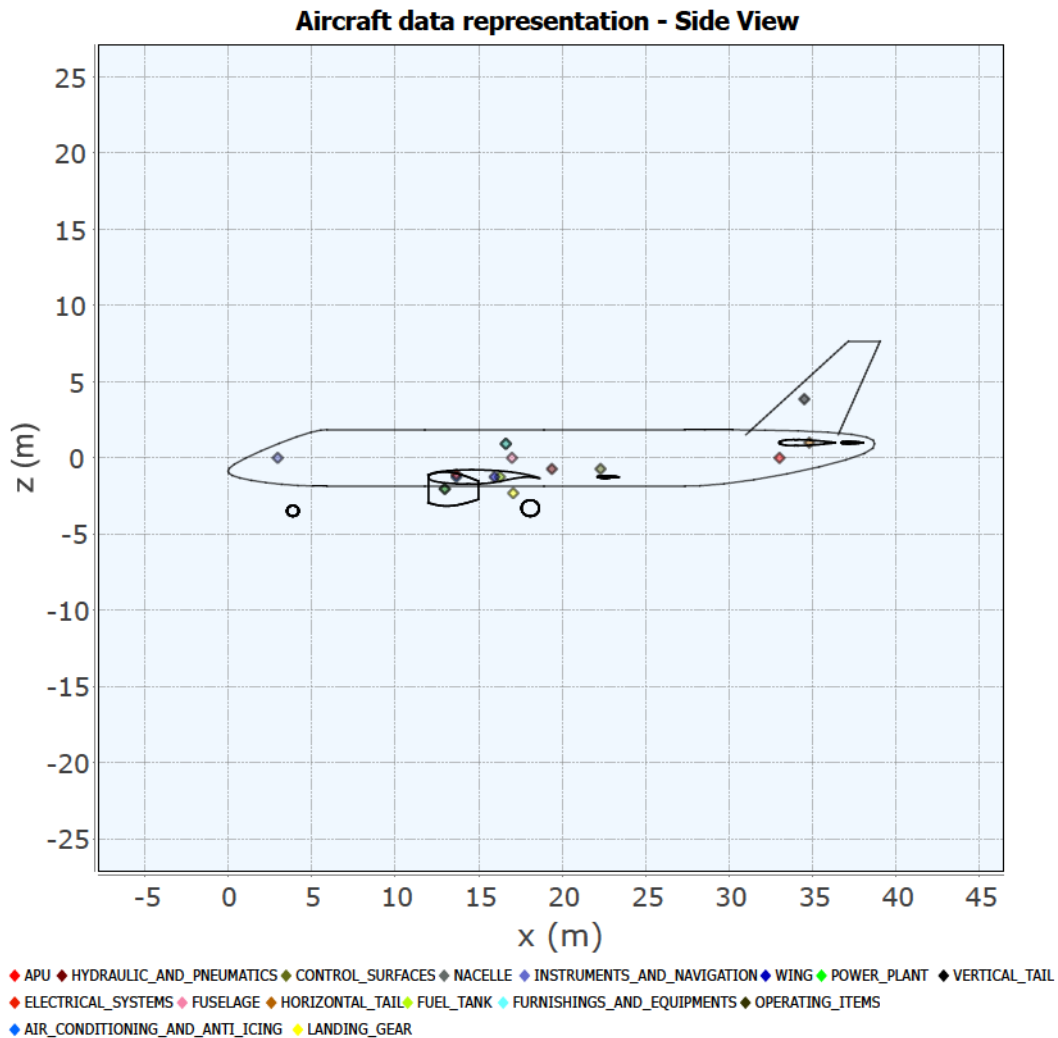


Figure 3.15 Example of aircraft side view with all components center of gravity position produced by JPAD

From the center of gravity positions envelope, the balance manager builds the boarding diagram from which the maximum forward, the maximum afterward and the operative center of gravity position are estimated. This latter assumed to be equal to the one at maximum take-off weight condition. An example is shown in Figure 3.16.

1. **Components center of gravity estimation.** Fuselage, wing, fuel tank, horizontal tail, vertical tail, canard (if present), landing gears, power plant and nacelles balance analysis is carried out collecting their center of gravity positions in **BRF**, **LRF** and as a percentage of the **MAC**.
2. **Systems center of gravity position estimation.** Systems groups center of gravity positions are calculated, taken from input data or considered equal to zero, depending on the user choice in the balance configuration file.

3. **Structural mass center of gravity position estimation.** The structural mass center of gravity position is calculated as the weighted average, based on the mass, of fuselage, wing, horizontal tail, vertical tail, canard (if present), landing gears and nacelles center of gravity positions.
4. **Structural mass (plus engines) center of gravity estimation.** From the structural mass center of gravity position, the effect of engines masses is taken into account using engines positions from the aircraft input file.
5. **MEW center of gravity estimation.** From the structural mass center of gravity position, considering also engines masses, the effects of systems masses is taken into account using the previously estimated positions (without considering the furnishings and equipment group).
6. **OEW center of gravity estimation.** From the **MEW** center of gravity position, operating items, as well as the furnishings and equipment group, are taken into account in terms of masses and positions neglecting the effects of the crew mass and the trapped fuel and oil mass on the final center of gravity location. The location of the center of gravity of the furnishings and equipment group position has been already discussed. The latter has been also used as reference position for the operating items group.
7. **Maximum zero fuel mass center of gravity estimation.** Here the passengers boarding analysis is carried out to calculate the related shift in center of gravity position.
8. **Maximum take-off mass estimation.** From the maximum zero-fuel mass center of gravity position, the effect of the design fuel mass is taken into account using previously calculated fuel tank center of gravity position.

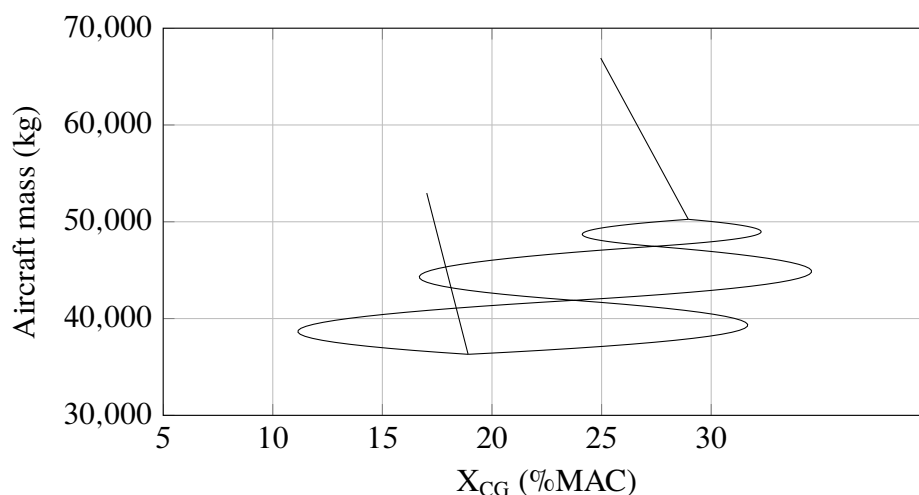


Figure 3.16 Example of boarding diagram produced by JPAD

Knowing each component mass and center of gravity position in **BRF** as well as the overall aircraft center of gravity position at a specific weight condition, the Balance module performs the calculation of all inertia moments (I_{xx} , I_{yy} , I_{zz}) and products (I_{xy} , I_{yz} , I_{xz}) according to the well-known formulas from the rigid body physics. In particular, being the aircraft symmetrical with respect to the longitudinal axis, both the inertia products I_{xy} and I_{yz} are equal to zero.

The last analysis carried out by the Balance module concerns the aircraft ground stability. Starting from a given aircraft parametric model, several checks are performed to ensure the following required features. In addition, those analysis define a set of constraints useful to assess the feasibility of the user-defined landing gears positioning.

- The possibility to safely rotate in take-off or landing
- The minimum required engine clearance from ground
- Aircraft stability at touchdown and during taxiing
- The possibility to safely perform ground operations

The first check performed by **JPAD** deals with the aircraft rotation during take-off, which is usually the most demanding one between take-off and landing phases due to higher required rotation angles. Since the main gear leg length is sized on this condition, assuming a user-defined rotation angle (or the fuselage upsweep angle) in the landing gear parametric model definition, this analysis is just a double check of the landing gear design performed by **JPAD** (see Figure 3.17). In particular, the required rotation angle is calculated assuming a main gear leg length without the static deflection of the shock strut and tire (value assigned during the definition of the landing gear parametric model as reported in Table 3.8). In addition, this analysis performs also a check to monitor the possibility of tail tipping during rotation. This phenomenon occurs when the aircraft center of gravity rotates over and aft of the location of the main gear during rotation providing an unstable behavior.

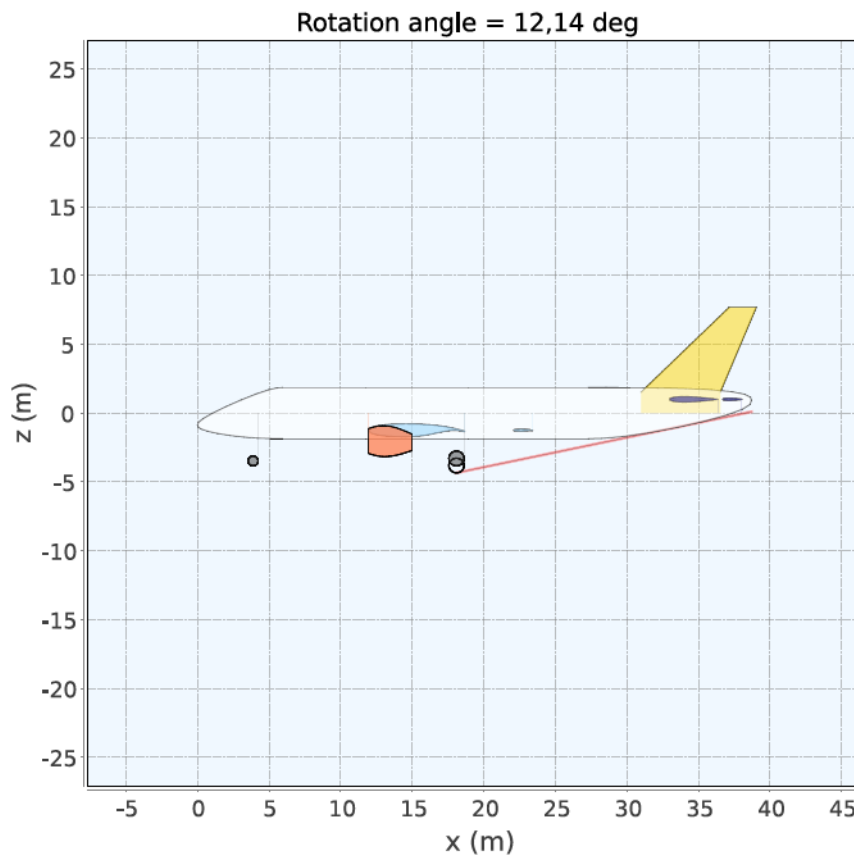


Figure 3.17 Example of take-off rotation angle calculation produced by **JPAD**

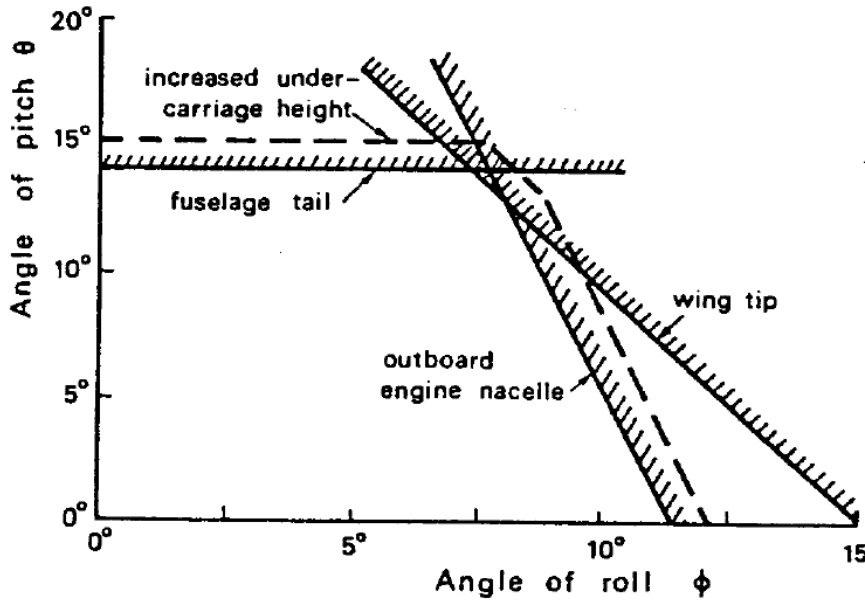


Figure 3.18 Limitation on pitch and roll angles during take-off and landing determined by the aircraft geometry [25]

As proposed in [25], the rotation angle in take-off or landing is tightly linked to the aircraft roll angle. In particular, the landing gear legs should be sufficiently long to allow any combination pitch and roll angle in the envelope shown in Figure 3.18 without the risk that any part of the aircraft touches the ground. Assuming that the pitch angle is imposed, the limit roll angle can be calculated from Figure 3.18.

Then, for a given main gear leg length, JPAD calculates the roll angle at which the wing tip touches the ground using Equation 3.5 proposed in the book by Torenbeek [25]. Here Γ is taken as the wing dihedral angle, b is the wingspan, wt is the wheel track, and Λ is the wing sweep angle.

$$\tan \phi = \tan \Gamma + \frac{2 \cdot h_g}{b - wt} - \tan \theta \tan \Lambda \quad (3.1)$$

To ensure a safety distance of the lowest nacelle from the ground at the maximum take-off weight, landing gears legs must be sufficiently long to provide an adequate engine clearance. In case of turboprops, the minimum allowed propeller clearance is imposed by **Federal Aviation Regulations (FAR)** regulations at a value of 14 inches. The Balance module of JPAD calculates the minimum engine clearance among all installed engines and provide the user with a graphical representation of the current value together with the roll angle calculated with Equation 3.5 (see Figure 3.19).

If the engine type variable is turboprop, the clearance is calculated assuming the lowest propeller point and, in case of values below the prescribed limit of 14 inches, a warning is launched making the user aware of the need to modify the landing gear sizing.

As proposed by Torenbeek [25], static stability of an aircraft at touchdown and during taxiing can be investigated by monitoring whether or not the resultant of air and mass forces intersects the ground at a point outside the triangle formed by connecting the attachment locations of the nose and main gears. In those cases, the ground will not be able to exert a reaction force which opposes the tendency to cant over. To define this triangle, three conditions must be considered.

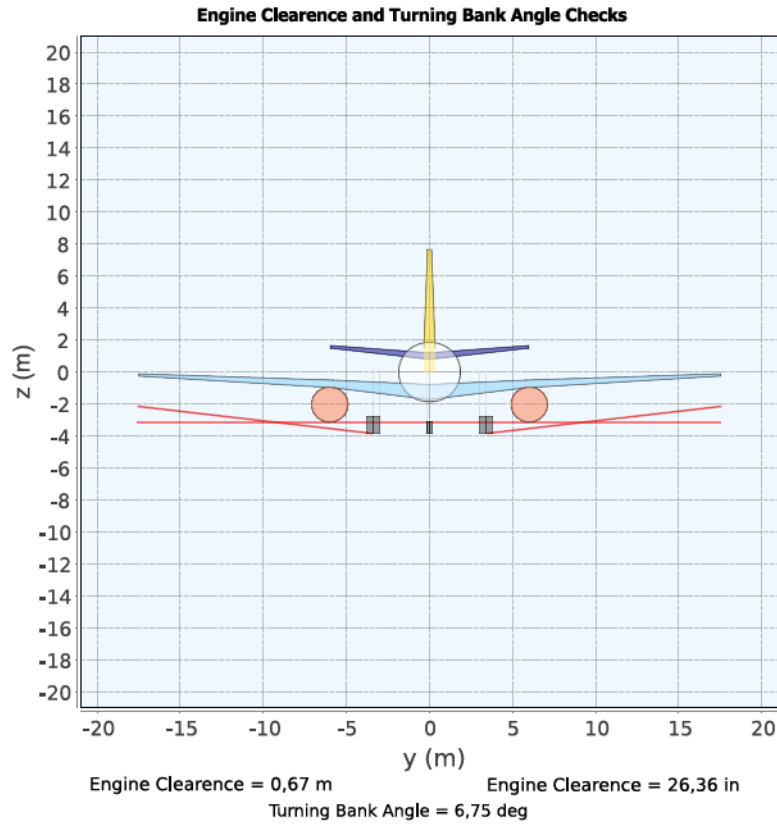


Figure 3.19 Example of limit ground bank angle and minimum engine clearance calculation produced by JPAD

- If the position of the nose gear is assumed to be fixed, the lower limit of the track of the landing gear is defined as the line tangential to the circle with a radius of 0.54 times the height of the aircraft max forward center of gravity position from the static ground line, which pass through the center of the nose gear. The constant 0.54 is based on static and dynamic instability considerations at touchdown and during taxiing.
- If the position of the main gear is assumed to be fixed, the aft limit of the nose gear position is defined as the intersection of the line, tangential to the circle described at the previous point and the aircraft centerline.
- During touchdown in landing with the max afterward center of gravity position, the main landing gear must be placed at least at a distance behind the center of gravity given by Equation 3.2, where l_m is the main gear position afterward limit e_s is the total static deflection of the shock strut and tire, h_{cg} is the height of the center of gravity with respect to the ground line and θ_{TD} is the pitch angle at touchdown. This is usually the most demanding condition. In particular, for low wing transport aircraft, the weight condition at which h_{cg} is usually calculated is at the maximum zero-fuel weight [89].

$$l_m \geq (h_{cg} + e_s) \tan \theta_{TD} \quad (3.2)$$

All those limitations are calculated by the JPAD Balance module and represented in a chart like the one reported in Figure 3.20.

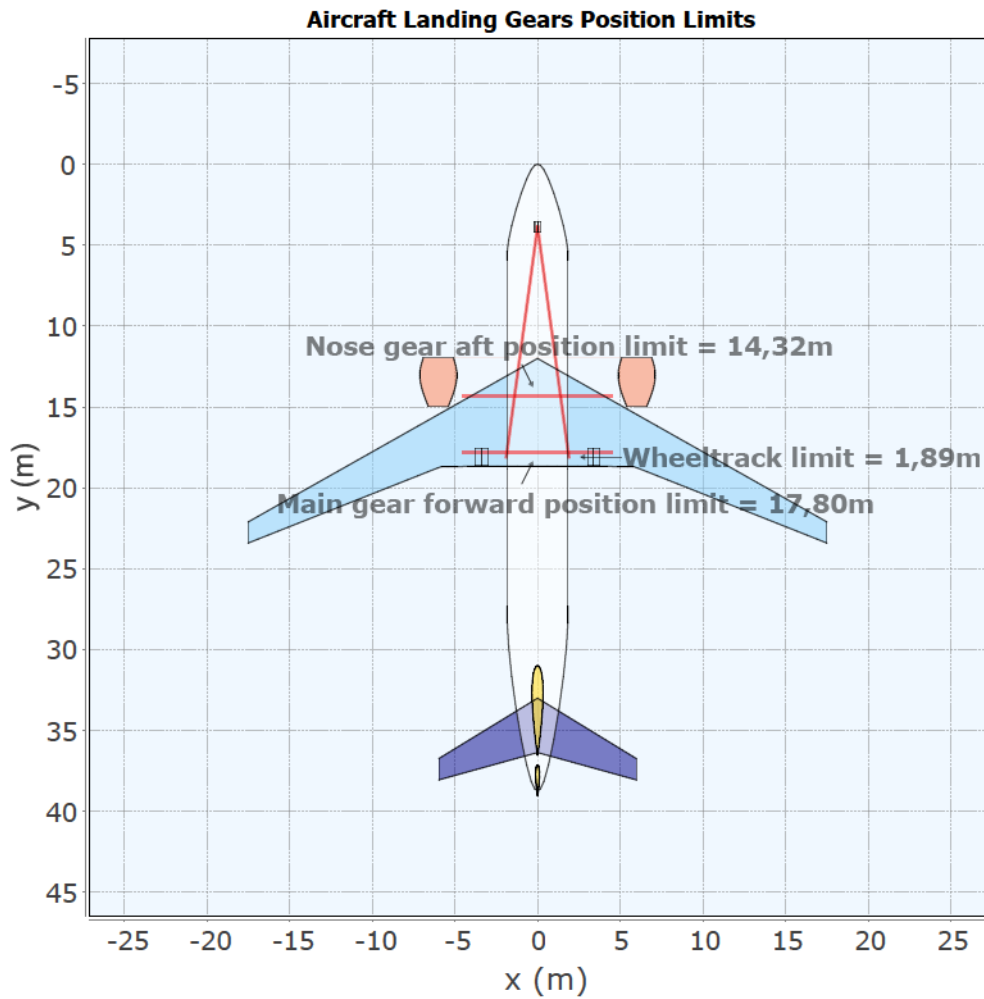


Figure 3.20 Example of nose and main gear position limits calculated by JPAD

Another important analysis to be performed in terms of ground stability concerns the sideways turnover angle. In case of crosswind conditions on the ground, forces acting in sideway direction may lead to a turnover of the aircraft. Thus, the designer should provide for the minimum turnover angle calculated according to the Equation 3.3 proposed in [89]. Here Ψ is the turnover angle, l_n is the distance between the center of gravity and the nose gear, h_{cg} is the height of the center of gravity with respect to the ground line and δ is the angle between the aircraft centerline and the line passing through the center of the nose and main gear groups. The value of δ may be derived from Equation 3.4 where t is the wheel track, l_m is the distance between the center of gravity and the main gear and l_n is the distance between the center of gravity and the nose gear.

$$\tan \Psi = \frac{h_{cg}}{l_n \cdot \sin \delta} \quad (3.3)$$

$$\tan \delta = \frac{wt}{2 \cdot (l_n + l_m)} \quad (3.4)$$

The JPAD Balance module uses the abovementioned equations to calculate the value of Ψ which is then compared with the maximum allowed angle of 63 degrees reported in [89] to evaluate whether or not the landing gear sizing has provided a sufficient wheel track.

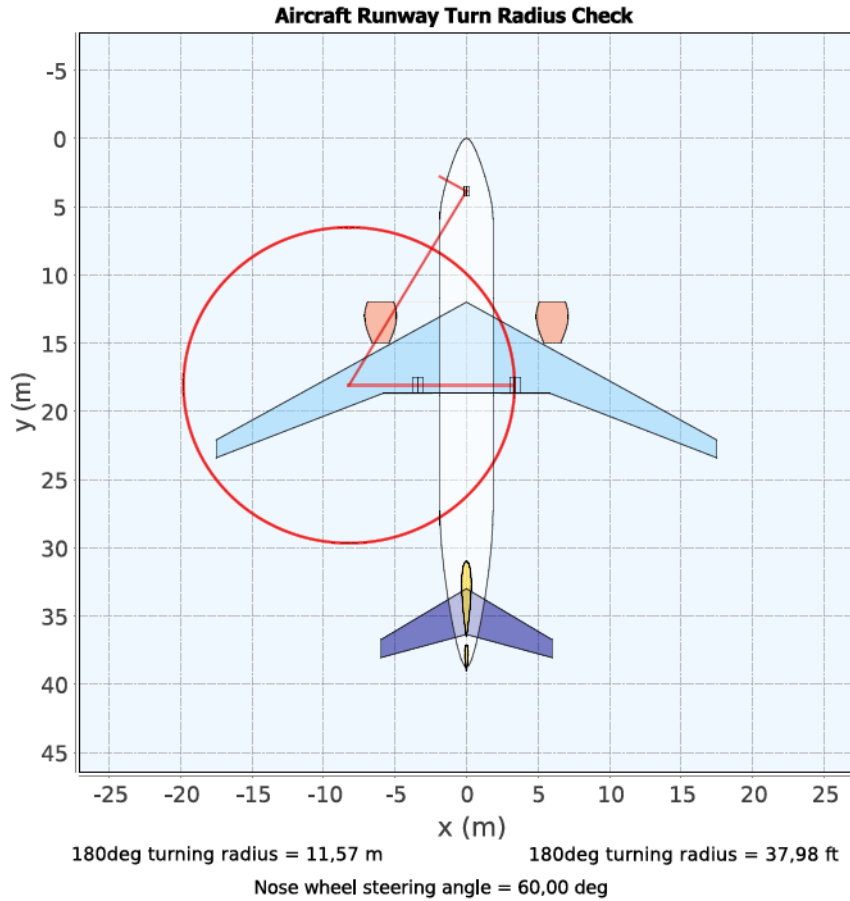


Figure 3.21 Example of turning radius calculation produced by JPAD

Besides ground stability and controllability considerations, the high costs associated with airside infrastructure improvements, e.g., runway and taxiway extensions and pavement reinforcements, have made airfield compatibility issues one of the primary considerations in the design of the landing gear [90]. Thus, aircraft must be designed to ensure maneuverability in pre-defined spaces as they move on the ground between the runway and passenger terminal. This requirement, for large aircraft, impose upper limitations on landing gears wheelbase and track. Those limitations can be derived from the comparison of the aircraft turning radius and the runway width classified by the FAA as a function of the aircraft wingspan in feet [91] (see Table 3.10). In particular, the turning radius must lower than the half of the related runway width.

Airplane design group	Wingspan (ft)	Runway width (ft)
III	[79, 118[100
IV	[118, 171[150
V	[171, 197[150
VI	[197, 262[200

Table 3.10 FAA airplane design group classification for geometric design for airports [91].

The turning radius is defined as the distances between the center of rotation and a specific part of the aircraft (e.g. the main gear location on the opposite side of the center of rotation itself).

The center of rotation is located at the intersection of the line extending from the nose gear rotated by the imposed steering angle and the y-oriented line extending from the main gears. The upper limit for the nose gear steering angle is generally set as ± 60 degrees [89]. The turning radius corresponding to a 180-degree turn is determined using Equation 3.5, where b is the wheelbase and t is the wheel track. An example of turning radius calculated by JPAD is shown in Figure 3.21.

$$r_{turn} = t \tan(90 - \beta_n) + \frac{wb}{2} \quad (3.5)$$

Aerodynamic and stability

The aerodynamics module of JPAD estimates all the aerodynamic characteristics concerning lift, drag and moments coefficients, at different operating conditions (Take-off, Climb, Cruise and Landing), both for the complete aircraft and for each component (wing, tails, fuselage and nacelles). Furthermore, the stability module gives useful data about longitudinal and lateral-directional static stability of the whole aircraft considering non-linear effects as well (i.e. pendular stability, non-linear downwash gradient, etc.).

Each analysis is carried out using one (or a mix) of the following approaches: low fidelity (e.g. semi-empirical equations from literature), medium fidelity analyses (e.g. Vortex lattice method for lifting surface loading, corrected for non-linear effects), high-fidelity surrogate model developed by the DAF group of the University of Naples Federico II [17] [63].

In terms of lifting surfaces, the starting point is the definition of all airfoils characteristics, the user may choose to manually assign each aerodynamic parameter required to model the lift curve, the drag polar and the pitching moment curve of the generic airfoil, or to assign an external set of curve (for example coming from CFD analyses) to provide for a higher analysis accuracy. A third option is to select a generic NACA airfoil from a dedicated internal database, based on the data reported in the book from Abbott and Von Doenhoff [83], by choosing the series and the thickness ratio.

In the first two cases, the user must assign all data at a low speed condition, then JPAD performs all the required Mach and Reynolds numbers corrections to scale aerodynamic data according to the specific operating condition.

As explained at the beginning of this chapter, the development of JPAD is the result of the efforts of the DAF group which involved several PhD students in a virtuous collaboration process. In particular, the module object of this section derives from the research and the development work of another DAF PhD student named Manuela Ruocco. For more information regarding methodologies and module architecture, the reader can refer to the thesis work titled “High lift and stability issues for innovative transport aircraft configurations in aerodynamic design” [92].

Performance

The performance module of the JPAD core library, has been completely developed using a simulation-based approach for each mission phase. It has been divided in several sub-modules to allow the user to perform a single performance analysis (e.g. a detailed take-off or landing simulation) or a complete mission profile analysis or a combination of them. The user can easily configure which analyses must be carried out using the analysis XML configuration file.

Among all other analysis module developed by the author during his PhD, this has been the most challenging one to design and code in order to find the right balance between flexibility, accuracy, computational time and simulation details. Although the analysis time is the most demanding one among all modules, the possibility for the user to manually enabling or disabling each analysis provides for a reduction of the effective required amount of computational efforts.

In the overall **JPAD** core dependency map, the performance module requires some weight data as well as trimmed aerodynamic data concerning polar drag curves and lift curves in every flight condition (Take-off, Climb, Cruise and Landing). The user can both assign those inputs manually (if the analysis must be carried out in standalone mode), both make the module inherit them from the related analysis manager classes. In the first case, two approaches have been conceived: working with parametrically defined parabolic drag polar curves or using external drag polar curves if the user has higher fidelity data. In any case lift curves data must be given using only the following parameters in clean, take-off and landing configurations: lift curve slope, lift coefficient at zero angle of attack and maximum lift coefficient. In addition, also the rudder effectiveness coefficient τ_r must be specified, in case of standalone mode, to allow the performance module to carry out the estimation of the minimum control speed (V_{MC}).

In terms of input data, the performance module requires also the engine database provided together with each engine. In this analysis module, the user has the possibility to define a wide set of calibration factors (set to 1.0 by default) to trim all engine related quantities (thrusts, **SFC** and emission indexes) for each engine rating (Max. Take-off, **APR**, Max. Climb, Max. Continuous, Max. Cruise, Flight Idle and Ground Idle).

At the moment of writing, the performance module allows to carry out the following analyses:

- Take-off
- Landing
- Take-off and landing noise trajectories
- Climb
- Cruise
- Descent
- Mission profile
- Payload-Range
- V-n diagram definition

The take-off calculation module computes all the take-off performance using a simulation-based approach proposed by the author of this thesis in [54]. However, due to major modifications that have been recently implemented, a review of the methodology is needed.

The analysis procedure expects to solve an appropriate set of **Ordinary Differential Equations (ODE)**, which describes the aircraft equations of motion during all the take-off phase up to the obstacle.

The strategy is to find out all the fundamentals variables of motion, which describes completely the aircraft state during this phase, and then study the dynamic system in exam in a state-space representation. These latter can be resumed in the followings:

- Aircraft position, in meters (s)
- Aircraft ground speed, in meters per seconds (V)
- Flight path, in degrees (γ)
- Center of gravity altitude from the ground (h)
- Aircraft mass (m)

The set of **ODE** that models the take-off phase may be written in the form of Equation 3.6.

$$\begin{pmatrix} \dot{s} \\ \dot{V} \\ \dot{\gamma} \\ \dot{h} \\ \dot{m} \end{pmatrix} = \begin{pmatrix} f_1(V) \\ f_2(V, \gamma, h m; \alpha) \\ f_3(V, \gamma, h m; \alpha) \\ f_4(V, \gamma) \\ f_5(V, \gamma, h) \end{pmatrix} \quad \text{with} \quad \begin{pmatrix} x_1 = s \\ x_2 = V \\ x_3 = \gamma \\ x_4 = h \\ x_5 = m \end{pmatrix} \quad \text{and} \quad u = \alpha \quad (3.6)$$

The unknown $\mathbf{x} = [x_1, x_2, x_3, x_4, x_5]^T$ is the vector of state variables. The input $u(t)$ is a given function of time that corresponds to an assumed time history of the angle of attack during take-off.

The right-hand sides of system (3.6) are defined by the following functions:

$$f_1(V) = x_2 \quad (3.7a)$$

$$f_2(V, \gamma, h m; \alpha) = \frac{g}{W} \begin{cases} T(x_2) - D(x_2, u) - \mu[W - L(x_2, u)] & \text{if } \mathcal{S}(x_2, u) < 1 \\ T(x_2) \cos u - D(x_2, u) - W \sin x_3 & \text{if } \mathcal{S}(x_2, u) \geq 1 \end{cases} \quad (3.7b)$$

$$f_3(V, \gamma, h m; \alpha) = \frac{g}{W x_2} \begin{cases} 0 & \text{if } \mathcal{S}(x_2, u) < 1 \\ L(x_2, u) + T(x_2) \sin u - W \cos x_3 & \text{if } \mathcal{S}(x_2, u) \geq 1 \end{cases} \quad (3.7c)$$

$$f_4(V, \gamma) = x_2 \sin x_3 \quad (3.7d)$$

$$f_5(V, \gamma, h) = \dot{m}_f(x_2, x_3, x_4) \quad (3.7e)$$

The total thrust $T(x_2)$ is calculated by means of the interpolating function $T_{\text{tab}}(V_a)$ based on a table lookup algorithm, where $V_{\text{TAS}} = V + V_w$ is the aircraft airspeed and V_w is the wind speed (horizontal component, negative in case of headwind).

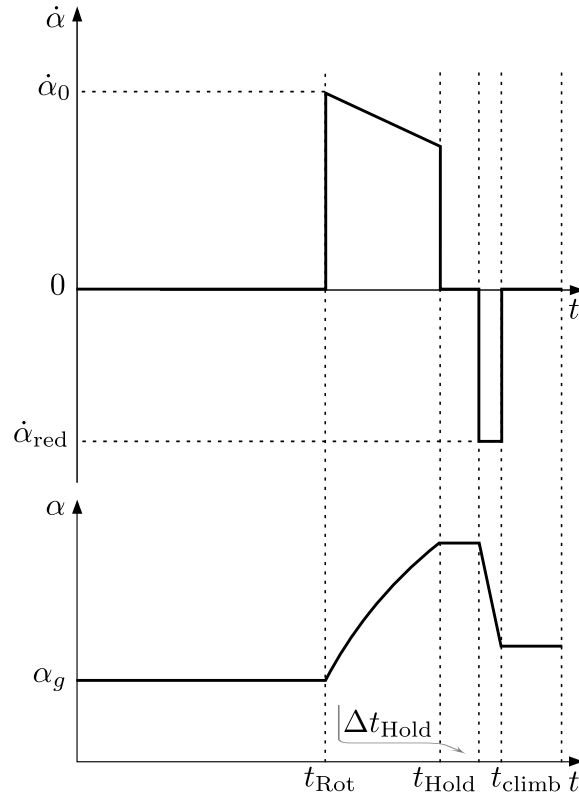


Figure 3.22 Qualitative representation of the angle of attack input law

The calculation of T is performed for each engine separately and then combined together to have the value of T . Each thrust is firstly divided in its longitudinal and transversal components according to the user defined engine tilting angle in **BRF**.

Furthermore, the fuel flow (m_f) is retrieved from the engine database Excel file described in aircraft parameterization section.

The drag D and lift L , as functions of airspeed, altitude, flight path angle, aircraft mass and angle of attack, are given by the following conventional formulas.

$$D(x_2, x_3, x_4, x_5, u) = \frac{1}{2} \rho (x_2 + V_w)^2 S C_D(x_2, x_3, x_4, x_5, u) \quad (3.7f)$$

$$L(x_2, x_3, x_4, x_5, u) = \frac{1}{2} \rho (x_2 + V_w)^2 S C_L(x_2, x_3, x_4, x_5, u) \quad (3.7g)$$

The switching function \mathcal{S} of aircraft velocity and angle of attack is defined as follows:

$$\mathcal{S}(x_2, x_3, x_4, x_5, u) = \frac{L(x_2, x_3, x_4, x_5, u)}{W \cos x_3} \quad (3.7h)$$

The formulas (3.7) make the system (3.6) a closed set of **ODE**. When the function $u(t)$ is assigned and the system is associated to a set of initial conditions, in this particular case equal to $\mathbf{x}_0 = [0, 0, 0, 0, 0]^T$, a well-posed **Initial Value Problem (IVP)** is formed, which can be solved numerically.

It has to be highlighted that the lift coefficient $C_L(x_2, x_3, x_4, x_5, u)$ is the one from the total aircraft trimmed lift curve with flaps, and eventually slats, deflected. The same applies for the drag coefficient $C_D(x_2, x_3, x_4, x_5, u)$.

However, in this case the ground effect contribution of the induced drag must be taken into account as proposed in [93].

The function $u(t)$, which represents the input law of the angle of attack as function of the time in seconds, can be constructed by picking the aircraft rotation start time t_{Rot} (when the rotation speed V_{Rot} is reached along the ground roll phase); thus, the $u(t)$ function, represented in Figure 3.22, can be defined as in Equation 3.8.

$$u(t) = \begin{cases} \alpha_g & \text{if } t < t_{Rot} \\ \alpha_1(t) & \text{if } t \geq t_{Rot} \end{cases} \quad (3.8)$$

In Equation 3.8, a constant angle of attack α_g , during the ground roll phase up to the rotation speed, and a given non-zero law $\alpha_1(t)$ for the post-rotation angle of attack time history are assumed. As can be seen from Figure 3.22, after the rotation the angle of attack changes according to an initial value of its time derivative $\dot{\alpha}_0$, which decreases with time according to the law written in Equation 3.9 as function of the angle of attack. This, until the time t_{Hold} has been reached. This particular instant is related to the achievement of the maximum admitted lift coefficient in take-off configuration, which is set at by default at 90% of the maximum achievable take-off lifting coefficient. In Equation 3.9, the k_α slope as well as the initial angle of attack time derivative $\dot{\alpha}_0$ are assigned as inputs.

$$\dot{\alpha} = \dot{\alpha}_0 (1 - k_\alpha \alpha) \quad (3.9)$$

From this point on the pilot keeps the angle of attack constant for an assigned time interval (Δt_{Hold}) during which, the acceleration decreases due to the higher induced drag. After this short time interval, the pilot must reduce the angle of attack in order to avoid the acceleration to decrease too much and so a negative time derivative $\dot{\alpha}_{red}$ is considered, the latter assumed to be constant for simplicity. Finally, since the decrease in angle of attack provides also for a reduction in lift coefficient, the time t_{climb} will be reached when the load factor is reduced to a value of 1. This means that a balance of forces, perpendicular to the flight path, has been achieved. Thus, the angle of attack time derivative returns to a value of 0.0.

During all the simulation, the maximum allowed rotation angle is constantly monitored to ensure the absence of tail strike. In case the tail touches the ground a visual warning is launched by the calculation module.

The calculation of the take-off distance in **OEI** condition is quite the same as the **AEO** case, with the difference that now there is a discontinuity in thrust, and a little drag increment, due to the failed engine. A good description of the take-off with one engine failure is proposed in [15]. Here it is explained that in the event of an engine failure during the take-off roll the pilot must decide whether to continue the take-off or, instead, abort the take-off and decelerate to a stop on the runway. Obviously, if the engine failure occurs when the aircraft is traveling very slowly, the aircraft should be kept on the ground and brought to a stop at some safe location off the runway. Conversely, if the engine failure occurs when the aircraft is close to the take-off speed the take-off should be continued. The designer must provide a means for deciding whether it is safer to abort the take-off or continue it.

The critical velocity, denoted as V_{act} , is the velocity at which action is taken, not that at which the decision to act is taken.

The time between the recognition of an engine failure, which occurs at V_{ef} , and the critical velocity V_{act} , when action is taken is required to be more than one second. Generally, this time period, which is set by the reaction time of the pilot, is taken to be about $1\text{ s} \div 2\text{ s}$. If the pilot decision is to continue the take-off with one engine inoperative, the distance to the lift-off speed V_{LO} and to the subsequent climb-out to 35 ft height above the runway, will obviously be longer than with all engines operating.

The calculation of the take-off distance in this situation is quite the same as the one explained previously, with the difference that now there is a discontinuity in thrust due to the failed engine. In particular, the thrust, $T(x_2)$, will still be read from the database but considering a number of engines reduced by one from the time t_{ef} at which the engine failure occurs.

On the other hand, in the case of the aborted take-off the pilot will apply the necessary braking procedures in order to get the maximum allowed deceleration while maintaining adequate control of the airplane motion. The portion of the aborted take-off run up to the engine failure velocity V_{ef} is calculated in the same way as that for the continued take-off, so that the distance is the same in both cases. From this point on, until the pilot reacts by activating brakes, there is only a discontinuity in thrust due to the failed engine; while, after the time interval in which the pilot decides to abort the take-off, the thrust is set to minimum (Ground Idle engine rating) and the brakes action provides an higher friction coefficient. During this phase, the Equation 3.7b changes in the following, where μ_{brakes} is bigger than μ and it is usually about 0.3 or 0.4.

$$f_2(\mathbf{x}, u) = \frac{g}{W} \{ -D(x_2, u) - \mu_{brakes} [W - L(x_2, u)] \} \quad (3.10)$$

Instead of considering the limiting cases of an aborted take-off at low V_{act} and a **OEI** take-off at high V_{act} , it is useful to determine the critical velocity at which the distance required to continue the take-off with one engine inoperative equals the distance required to safely abort it. This velocity is the decision speed V_1 , while the related distance is the **Balanced Field Length (BFL)**. The latter, in particular, plays an important role in the sizing of the runway since is the maximal distance the aircraft can cover both the **OEI** take-off and the aborted take-off.

To calculate this distance, and the related velocity, both the **OEI** take-off distance and the aborted take-off distance are estimated at different V_{act} . Each couple of speed and distance are then plotted as a function of the engine failure speed. The intersection of these two lines, at which the two distances are the same, defines the **BFL** and the V_1 .

Although **JPAD** provides for default values for most of the simulation inputs needed to perform the take-off simulation, the user has the possibility to manually assign each of them. A complete overview of the input data needed by the take-off analysis module is reported in Table 3.11. As can be seen, the user can define the desired percentage of the take-off stall speed required to calculate the rotation speed. However, according to **FAR** regulations (part 25 subpart B paragraph 25.107), the rotation speed may not be less than V_1 as well as 1.05 times the minimum control speed (V_{MC}). Furthermore, it must provide (both in **AEO** and **OEI** conditions) a minimum safety speed (V_2) at least of 1.13 times the take-off stall speed, in case of airplanes with two or three engines, or 1.08 times the take-off stall speed, in case of aircraft with more than three engines. To ensure that those conditions are satisfied, the take-off calculation module of **JPAD** firstly performs the estimation of the V_{MC} and of the **BFL**, together with the rotation speed needed to fly over the obstacle at 1.13 times the take-off stall speed in **OEI** condition, for then using those velocities to assess whether or not the

Input variables	Description
V_w	Wind speed along runway (positive in case of tailwind)
μ	Wheel rolling friction coefficient (constant value or function of speed)
μ_b	Wheel braking friction coefficient (constant value or function of speed)
dt_{Hold}	Time interval in which the pilot must hold the bar
α_g	Aircraft angle of attack on the ground
$h_{obstacle}$	Obstacle height
k_{Rot}	Percentage of the stall speed which defines the rotation speed
$\dot{\alpha}_0$	Initial value of the angle of attack time derivative
$k_{CL_{max}}$	Safety margin with respect to the max lifting coefficient
$k_{Drag_{OEI}}$	Drag increment due to failed engine
k_{α}	Slope of the angle of attack time derivative in Equation 3.9

Table 3.11 Summary of take-off simulation input parameters

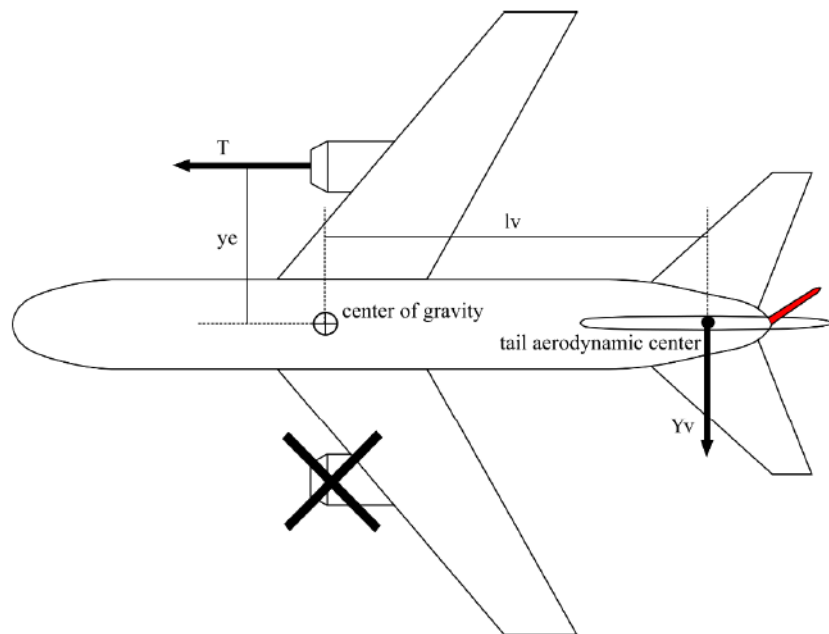


Figure 3.23 Qualitative representation of the aircraft with one engine inoperative and with full deflected rudder to ensure constant heading

desired rotation speed may be feasible. In case of an unfeasible user-defined rotation speed, the most limiting one will be chosen.

Concerning the calculation of the minimum control speed (V_{MC}), this is the calibrated airspeed below which directional or lateral control of an airplane, on the runway or in the air, can no longer be maintained by the pilot after the failure of the most critical wing-mounted engine (or while such an engine is inoperative) as long as the thrust of the opposite engine on the other wing is at the maximum (takeoff) setting.

FAR define several different V_{MC} , among which the most important one for a multi-engine airplane is the minimum control speed in air (V_{MCA}), and require engineers to size the vertical tail or stabilizer and the aerodynamic flight control surfaces of the airplane to comply with these regulations. The rudder is used to compensate the yawing moment caused by thrust asymmetry.

The minimum control speed in air (V_{MCA}) is the minimum speed at which full rudder will be necessary to fly with a constant heading and with leveled wings. In particular, the operating conditions considered are the one reported below. Figure 3.23 provides a visual representation of the problem in exam.

- One Engine Inoperative
- Take-off settings (maximum continuous thrust or APR setting)
- Maximum rudder angle deflections
- Most unfavorable center of gravity

The critical engine, which is the most distant from the center of gravity along y-axis, generates a thrust which decreases with airspeed, while the yawing moment, N_v , of the vertical tail may be expressed as reported in Equation 3.11.

$$N_v = \frac{1}{2} \rho V_{TAS}^2 S b C_{N_{\delta_r}} \delta_r \quad (3.11)$$

The most important parameters that characterize the aerodynamics of directional control are the followings.

- The vertical tail aspect ratio
- The ratio between the vertical tail span and the fuselage diameter at vertical tail aerodynamic center
- The horizontal tail position

The wing has a negligible effect, because of its distance from the asymmetric flow field induced by the rudder. The rudder control power, $C_{N_{\delta_r}}$, can be estimated from Equation 3.12 as proposed in [94].

$$C_{N_{\delta_r}} \delta_r = C_{L_{\alpha_v}} K_{\delta_r} K_b \tau_r \frac{S_V l_v}{S} \frac{l_v}{b} \eta_v \quad (3.12)$$

Here $C_{L_{\alpha_v}}$ is the isolated vertical tail lift curve slope, K_{δ_r} is the interference factor due to rudder deflection, K_b is a rudder span effectiveness factor, τ_r is the rudder effectiveness, η_v is the vertical tail dynamic pressure ratio and $\frac{S_V}{S} \cdot \frac{l_v}{b}$ is the vertical tail volumetric coefficient (l_v is the distance from the aerodynamic center of the vertical tail to the center of gravity of the airplane, as shown in Figure 3.23).

The K_b factor is function of the rudder span-wise extension as proposed in [25], while the rudder effectiveness τ_r can be obtained by assigning it (as a constant or as a function of the rudder deflection) or by calculating it using classical semi-empirical approaches from the literature. Finally, the K_{δ_r} factor is derived from Equation 3.13 where \mathcal{R}_v is the vertical tail aspect ratio and the factor K_{Fv} is defined as the ratio between the yawing moment coefficient of the fuselage-vertical tail combination to the yawing moment coefficient of the isolated vertical tail.

$$K_{\delta_r} = \begin{cases} 1.07(1 + \frac{K_{Fv}-1}{2.2}) & \text{for body mounted tail} \\ (1.33 - 0.09\mathcal{R}_v)(1 + \frac{K_{Fv}-1}{2.2}) & \text{for T-tail configuration} \end{cases} \quad (3.13)$$

The value of K_{F_v} is obtained from the **Vertical tail DESign Stability and Control tool (VeDSC)** embedded inside **JPAD**. The **VeDSC** tool is based on methods, reported in [94], developed by the UNINA **DAF** group. It is a new method to predict aircraft directional characteristics with a completely CFD-based approach. More than 300 simulations of complete and partial aircraft configurations have been performed to develop the calculation method and the related database. The innovative characteristic of **VeDSC** lies in the possibility to consider interference effects among main tail components. To take into account of particular events which can happen during the simulation, the take-off calculation module is supplied with several implementations of the Java interface **EventHandler**. The latter, through the definition of a specific function, can determine the occurrence of the wanted event by monitoring whether the sign of the function changes. In the case in exam, six events are monitored.

- **ehCkeckFailure**: It checks when the speed becomes greater than the input engine failure speed determining the instant of the engine failure occurrence.
- **ehCkeckVRot**: It checks when the speed becomes greater than the rotation speed determining the instant at which the ground roll phase ends, and the rotation phase begins.
- **ehEndConstantCL**: It checks when the time, t , becomes greater than the sum of t_{Hold} and of the given time interval Δt_{Hold} determining the instant at which the angle of attack, and the related lift coefficient, stops to be kept constant (not used in case of aborted take-off).
- **ehCheckObstacle**: It checks when the altitude becomes greater than the obstacle height of 10.7 m (35 ft) determining the instant at which the airborne phase, and so the entire take-off simulation ends (not used in case of aborted take-off).
- **ehCheckBrakes**: It checks when the time, t , becomes greater than the sum of failure time instant and of the given time interval required to the pilot to recognize the failure determining the instant at which the pilot activates the brakes (used only in case of aborted take-off).
- **ehCheckStop**: It checks when the speed becomes lower than zero determining the instant at which the aircraft has stopped (used only in case of aborted take-off).

In addition to the **EventHandler** interface, the **StepHandler** interface allows to store the state vector, the time and all the related physical quantities at every time step. This interface has the key role in managing three events, to be observed only if case of continued take-off (both **AEO** and **OEI**) that could not be handled well by the **EventHandler** interface. This are the following:

- A check upon the load factor to catch the instant at which, for the first time, it reaches a value of 1 determining the beginning of the airborne phase together with the changes in the derivatives equations.
- A check upon the lifting coefficient to determine when it reaches the threshold value defined by $K_{CL_{max}}$ (usually 90%) multiplied for the maximum take-off lifting coefficient. The related time instant is t_{Hold} .

- A second check on the load factor to define the instant at which its value is reduced to 1 after having applied a constant negative angular velocity. This instant defines t_{climb} .

Similar to the take-off, also for the landing phase a simulation-based approach, involving the resolution of an ODE system, has been implemented inside the JPAD performance module. In this case the starting point of the simulation has been assumed as the beginning of the approach phase at 1500ft above the runway.

According to the FAR regulations (part 25 subpart B paragraph 25.125), during this stabilized approach the aircraft must maintain a calibrated airspeed of not less than 1.23 times the 1-g stall speed in landing configuration down to an altitude of 50ft. Furthermore, a constant flight path angle (γ) of -3 degrees is assumed for the approach phase.

From the landing obstacle altitude (50ft) the aircraft begins the final approach down to the initial flare rotation altitude assumed to be at 20ft above the ground as suggested in [95] as averaged value for transport aircraft.

In this phase, the aircraft speed must be kept almost constant and the overall thrust is calculated using the flight idle setting for each engine rather than calculate the amount of thrust needed to ensure the 3 degrees of glide path as for the initial approach phase. As a consequence, the angle of attack begins to rise to provide for the amount of lift needed to keep the flight path angle constant.

During the flare rotation a smooth transition from a normal approach attitude to a landing attitude must be accomplished by gradually rounding out the flightpath to one that is parallel with, and within a very few inches above, the runway. During this rotation the angle of attack increases providing for higher lift as well as induced drag resulting in a deceleration of the aircraft. At the end the aircraft must touch the ground with its main landing gears and a with a reasonably low value of the vertical speed. A typical value of the descent speed at touchdown is between 2 and 3 ft/s [96]. However, as reported [96], Boeing reports that “service experience indicates that most flight crews report a hard landing when the sink rate exceeds approximately 4 ft/s”. In addition, FAR regulations (part 25 subpart C paragraph 25.473) specify a limit descent velocity of 10ft/s at the design landing weight or a limit descent velocity of 6ft/s at the design take-off weight. To allow the user to investigate different landing scenarios, the target rate of descent at touchdown can be selected as input parameter among the ones in Table 3.12.

Touchdown type	Target rate of descent
Typical	3ft/s
Perceived hard	4ft/s
Certification hard with reduced descent speed	6ft/s
Certification hard with maximum descent speed	10ft/s

Table 3.12 Landing simulation touchdown types

After the touchdown, after few seconds of wheel free-roll, the pilot must apply a breaking action of all wheels brakes, deflect all spoilers and set each engine setting to ground idle. The simulation ends when the aircraft speed reaches a value of zero.

The right-hand sides of system (3.6) changes in the following where t_{td} is the instant at which the aircraft touches the ground for the first time.

$$f_1(V) = x_2 \quad (3.14a)$$

$$f_2(V, \gamma, h m; \alpha) = \frac{g}{W} \begin{cases} T(x_2) \cos u - D(x_2, u) - W \sin x_3 & \text{if } t < t_{td} \\ T(x_2) - D(x_2, u) - \mu[W - L(x_2, u)] & \text{if } t \geq t_{td} \end{cases} \quad (3.14b)$$

$$f_3(V, \gamma, h m; \alpha) = \frac{g}{W x_2} \begin{cases} L(x_2, u) + T(x_2) \sin u - W \cos x_3 & \text{if } t < t_{td} \\ 0 & \text{if } t \geq t_{td} \end{cases} \quad (3.14c)$$

$$f_4(V, \gamma) = x_2 \sin x_3 \quad (3.14d)$$

$$f_5(V, \gamma, h) = \dot{m}_f(x_2, x_3, x_4) \quad (3.14e)$$

The aircraft drag coefficient, calculated from the input drag polar curve in landing configuration taking into account also for the ground effect, is incremented during the ground roll phase to take into account for the spoilers deflection. This additive contribution is calculated as proposed in [97], using each spoiler maximum deflection angle defined in Table 3.4. In a similar way, also the lift coefficient during the ground roll phase is affected by spoilers deflection which reduce the latter depending on each spoiler span ratio [97]. This effect provides also for an increased wheels friction force which allows to decelerate more the aircraft during this phase. This effect may also be disabled by the user from the performance input file.

The function $u(t)$, still represents the input law of the angle of attack as function of the time in seconds and can be constructed as follow.

- At the beginning of the initial approach the angle of attack is calculated from the equilibrium lifting coefficient in landing configuration associated with the initial aircraft weight and the prescribed approach speed of 1.23 times the landing stalling speed.
- During both initial and final approach phases, an iterative process for each time step is used to ensure a value of the flight path angle derivative ($\dot{x}[3]$) equal to zero. In particular, the value of the angle of attack at the previous time step is used to compute $\dot{x}[3]$ then a new value for the angle of attack is selected until the derivative reaches a value of zero (or very close to it).
- Once the aircraft has touched the ground a user-defined value of the angle of attack is considered (this latter set to 0.0 degrees by default).

The flare rotation plays a very important role in the landing simulation since it must provide for a reasonable value of the vertical speed at touchdown as well as to ensure that the aircraft effectively touches the ground with a value of the flight path angle similar to zero.

The key parameter is the angle of attack time derivative which is unknown. Thus, an iterative process has been implemented to define the best angular velocity to comply with all the required conditions.

1. Two initial attempts are made assuming the impossible case of a null angle of attack time derivative and the case of 3 deg/s of angle of attack variation during the flare rotation. Those cases are used to make a forecast of the required pitching angular velocity to match the target value of the rate of descent. The forecast is made by using linear interpolations or extrapolations.
2. In case the aircraft should surpass the user-defined limitation on the allowed maximum achievable lifting coefficient during landing rotation (by default set to 90% of the landing maximum lift coefficient) a warning is launched, and the last calculated lift coefficient is considered.
3. In case the aircraft should touch the ground with an angle of attack bigger than the fuselage upsweep angle, a tail strike warning is launched. At the same time, if the required angle of attack time derivative should provide for an angle of attack at touchdown lower than 0deg, a nose strike warning is launched. This feature provides for an important aircraft design check, monitoring if the aircraft has been designed with an adequate value of the aerodynamic efficiency in landing (too much lift capabilities lead to lower angles of attack at touchdown, while poor lift capabilities provide for higher angles of attack).
4. If the aircraft reaches the required altitude and at the same time provides for a touchdown vertical speed above the threshold, the flare simulation ends, and the ground roll phase can start.
5. If the flare rotation simulation fails, the **JPAD** performance manager switches the air distance calculation to the circular arc approach proposed in [96] before then moving on to the integration of the **ODE** set concerning only the ground phase.

The same approach used for the take-off has been used also for the landing to take into account of particular events which can happen during the simulation. Thus, the landing calculation module has been provided with the following implementations of the Java interface `EventHandler`.

- **ehCkeckObstacle**: It checks when the altitude becomes lower than the user-defined value related to the landing obstacle making the final approach phase to start.
- **ehCkeckFlareAltitude**: It checks when the altitude becomes lower than the prescribed value of 20ft above the ground making the flare rotation phase to start.
- **ehCkeckTouchdown**: It checks when the altitude becomes lower than the ground altitude identifying the instant at which the aircraft touches the ground for the first time.
- **ehCheckStop**: It checks when the speed becomes lower than zero determining the instant at which the aircraft has stopped.

Input variables	Description
Type	Touchdown type, defining the target rate of descent (see Table 3.12)
V_w	Wind speed along runway
μ	Wheel rolling friction coefficient (constant value or function of speed)
μ_b	Wheel braking friction coefficient (constant value or function of speed)
$k_{LNDweight}$	Percentage of the max take-off weight to be used for the initial approach phase
$h_{LNDstart}$	Initial landing altitude (by default set to 1500ft)
$h_{obstacle}$	Obstacle height
$\gamma_{approach}$	Flight path angle (by default set at -3deg)
k_{CLmax}	Safety margin with respect to the max lifting coefficient
$k_{Approach}$	Percentage of the stall speed defining the approach speed
k_{Flare}	Percentage of the stall speed defining the flare speed (circular arc approach)
$k_{Touchdown}$	Percentage of the stall speed defining the touchdown speed (circular arc approach)

Table 3.13 Summary of landing simulation input parameters

- **ehCheckPositiveRateOfClimb**: This EventHandler, used only before the touchdown, checks when the rate of climb becomes positive during the flare rotation. In this case the simulation error is triggered, and the performance manager switches to the semiempirical approach for the landing phase.

As for the take-off, **JPAD** provides for default values for most of the simulation inputs of the landing simulation as well. However, the user has the possibility to manually assign each of them. A complete overview of the input data needed by the landing analysis module is reported in Table 3.13.

Starting from both take-off and landing simulations, a specific performance module has been completely dedicated to the calculation of certification take-off and landing noise trajectories. In both cases, part 36, appendix A, of the **FAR** specify all conditions under which aircraft noise certification tests must be conducted.

Concerning the take-off noise trajectory, the procedure is the same as the **AEO** normal take-off with the difference that all the simulation must be carried out considering an **ISA** deviation of +10 degrees. Once the aircraft passes the obstacle at 35ft, landing gears must be retracted. This is simulated by linearly reducing the current drag coefficient, from the trimmed drag polar in take-off configuration, of a quantity equal to the overall landing gears drag coefficient. The time interval assumed to perform this reduction has been set by default to 12 seconds, however the user can change this value in the performance configuration file.

The input law of the angle of attack describes in Figure 3.22, is used to model the input variable $u(t)$ up to the obstacle altitude. From there, the instant at which the acceleration reaches a value near to zero, due to the induced drag, is monitored to estimate the aircraft speed to be maintained during all the simulation. This velocity must be in the interval $[1.13 V_{s,TO} + 10 \text{ kts}, 1.13 V_{s,TO} + 20 \text{ kts}]$. To ensure this condition, an iterative process is carried out on the rotation speed V_{rot} state that its value must also comply with all the limitation described for the normal take-off. Thus, if the calculated climb speed is lower than the lower bound of the prescribed interval, the rotation speed is increased to allow the aircraft to accelerate more during the ground roll phase. Otherwise, the rotation speed is reduced.

At this point, another iterative process (described below) is carried out during the simulation to ensure that the calculated climb speed is kept constant.

1. The last calculated angle of attack is used to predict the acceleration at the next simulation step.
2. If the acceleration is positive, the angle of attack is increased to provide for more deceleration. Otherwise its value is reduced to make the acceleration grow.

Two scenarios are considered at this point: a 100% take-off thrust simulation and another one with a thrust cutback at a specific altitude prescribed by the FAR.

The cutback altitude is selected as follows:

- 689 feet (210 meters), for airplanes with more than three engines
- 853 feet (260 meters), for airplanes with three engines
- 984 feet (300 meters), for airplanes with fewer than three engines

The cutback thrust setting must be selected according to the FAR (Appendix B to Part 36, Section B36.7). Upon reaching the cutback altitude, the aircraft thrust must not be reduced below that required to maintain either of the following, whichever is greater:

- A climb gradient of 4%
- In the case of multi-engine airplanes, level flight with one engine inoperative

In both cases (100% thrust and cutback), the simulation continues until the aircraft reaches a user-defined horizontal distance from the starting point set by default at 8000m.

The 100% thrust case is related to the identification of the lateral noise certification point which must be selected as the one related to the greatest noise level during take-off among all the measuring stations located on a line parallel to, and the specified distance from (usually 450m), the runway center line.

The cutback thrust case is related to the flyover noise certification point which is set by the FAR at 6500m from the brake-release. Ending the simulation further than 6500m ensures that the aircraft passes above the flyover certification point.

A representation of all noise certification measurement points is provided in Figure 3.24, while a complete overview of the input data needed to perform both take-off noise trajectories simulation is reported in Table 3.14.

The take-off noise trajectories module uses the following implementations of the Java EventHandler interface to monitor all simulation main events.

- **ehCkeckVRot**: It checks when the speed becomes greater than the rotation speed determining the instant at which the ground roll phase ends, and the rotation phase begins.
- **ehEndConstantCL**: It checks when the time, t , becomes greater than the sum of t_{Hold} and of the given time interval Δt_{Hold} determining the instant at which the angle of attack, and the related lift coefficient, stops to be kept constant.

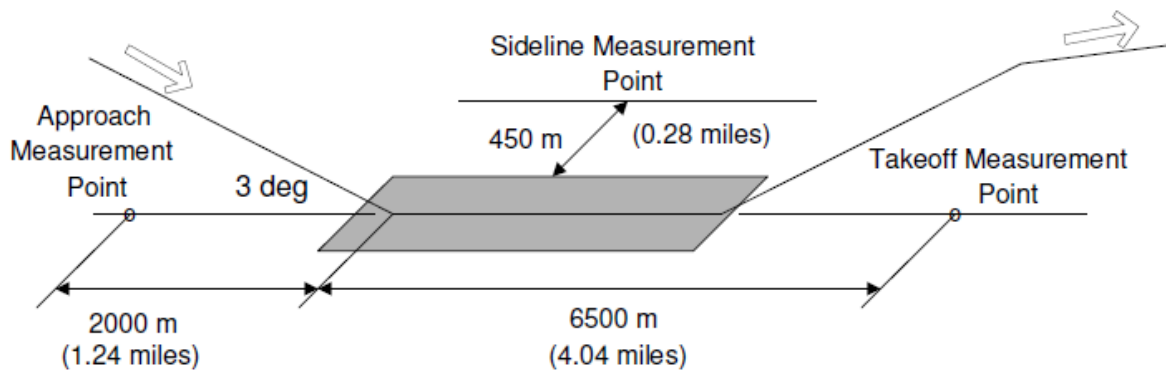


Figure 3.24 Certification noise measurement points

Input variables	Description
X_{end}	Ground distance at which the simulation ends.
$h_{cutback}$	The thrust cutback altitude.
$dt_{retraction}$	Landing gears retraction time interval.
$dt_{cutback}$	Time interval to pass from 100% to the cutback thrust setting.

Table 3.14 Summary of take-off noise trajectories simulation input parameters

- **ehCheckObstacle:** It checks when the altitude becomes greater than the obstacle height of 10.7 m (35 ft) determining the instant at which the airborne phase, and so the entire take-off simulation ends.
- **ehCheckLandingGearsRetractionStart:** It checks when the altitude becomes greater than the obstacle height of 10.7 m (35 ft) determining the instant at which the landing gears retraction must start
- **ehCheckLandingGearsRetractionEnd:** It checks when the time become greater than the sum of the initial landing gears retraction instant plus the user-defined retraction time interval, determining the instant at which the landing gears retraction must end
- **ehCheckCutbackAltitude:** It checks when the altitude becomes greater than the user-defined cutback altitude, determining the instant at which the thrust reduction must start
- **ehCheckFlyoverCertificationPoint:** It checks when the ground distance becomes greater than 6500m, determining the instant at which the aircraft passes above the flyover certification point. At this point all simulation details are saved.
- **ehCheckXEndSimulation:** It checks when the ground distance becomes greater than user-defined end simulation distance, determining the instant at which the simulation must be stopped.

In addition, to take into account for other events that cannot be monitored directly with the EventHandler interface, the Java StepHandler interface is used as for the normal take-off case.

The following events are monitored:

- A check upon the load factor to catch the instant at which, for the first time, it reaches a value of 1 determining the beginning of the airborne phase together with the changes in the derivatives equations.
- A check upon the lifting coefficient to determine when it reaches the threshold value defined by $K_{CL_{max}}$ (usually 90%) multiplied for the maximum take-off lifting coefficient. The related time instant is t_{Hold} .
- A second check on the load factor to define the instant at which its value is reduced to 1 after having applied a constant negative angular velocity. This instant defines t_{climb} .
- A check on the acceleration to define the instant at which its value is reduced to 0 for the first time after the lift-off.

The landing noise trajectory simulation is performed in the same way as the normal landing phase. However, the need to only model the trajectory up to the end of the final approach allows to completely ignore the iterative process needed to simulate the flare rotation phase. Furthermore, the number of EventHandler implementation, listed below, is reduced resulting in a reduction of computational time needed to perform the simulation.

- **ehCkeckObstacle:** It checks when the altitude becomes lower than the user-defined value related to the landing obstacle making the final approach phase to start.
- **ehCkeckFlareAltitude:** It checks when the altitude becomes lower than the prescribed value of 20ft above the ground making the flare rotation phase to start.
- **ehCheckApproachCertificationPoint:** It checks when the altitude becomes lower than 120.5m, determining the instant at which the aircraft passes above the approach certification point. At this point all simulation details are saved.

According to part 36, appendix A, of the FAR, the approach noise certification point is defined as the one at 2300m from the brake release (or 2000m from the runway start) which corresponds to an aircraft altitude above the ground of 120.5m (see Figure 3.24).

Moving to flight phases, the performance manager of JPAD allows to carry out the detailed analysis of climb, cruise and descent segments. For each of them a simulation-based approach is still used but with several modifications. Firstly, no ODE system must be solved, secondly, fewer discrete time steps are considered for the simulation. Starting from the climb segment, the analysis is carried out taking into account for both AEO and OEI conditions in order to calculate the following quantities:

- The rate of climb, the climb angle and the climb gradient as a function of true and calibrated airspeed, as well as the Mach number, at different altitudes
- The aerodynamic efficiency as a function of true and calibrated airspeed, as well as the Mach number, at different altitudes

Input variables	Description
$k_{weightAEO}$	Percentage of the max. take-off weight for the AEO simulation.
$k_{weightOEI}$	Percentage of the max. take-off weight for the OEI simulation.
h_{in}	Initial climb altitude.
h_{end}	Final climb altitude.
$V_{climbCAS}$	Reference calibrated airspeed for the climb simulation.

Table 3.15 Summary of climb simulation input parameters

- Max. rates of climb, climb angles and climb gradients envelopes at different altitudes
- Absolute and operative ceilings
- Time to climb at the maximum rate of climb speed
- Time to climb at the user-defined calibrated climb speed

An overview of the input data needed to calculate all those quantities is reported in Table 3.15.

The simulation considers 5 intermediate altitudes, from the initial one to the final one, at which all calculation must be made. This number is the result of a compromise between calculation accuracy and computational time.

The following assumptions have been made: the aircraft center of gravity is assumed to move in a plane, vertical to the surface of the earth; the aircraft is completely trimmed and no net rolling, pitching or rolling moment exist; no initial angular rates exist so that the only accelerations allowed for are those along the flight path and perpendicular to the flight path itself. For each altitude step and engine operating conditions (**AEO** and **OEI**) the following procedure is used:

1. Aircraft drag, lift and overall thrust are calculated as a function of the true airspeed.
2. The rate of climb as a function of the true airspeed as well as the maximum rate of climb and the maximum rate of climb speed are calculated using Equation 3.15 reported by Young in [96].

$$RC(t, V) = \frac{T(t, V)/W - D(t, V)/W}{1 + f_{acc}} \cdot V \quad (3.15)$$

where the acceleration factor is:

$$f_{acc} = \frac{V}{g} \frac{dV}{dH} = 0.7M^2\psi \quad (3.16)$$

The value of ψ can be obtained from Equation 3.17 depending on the climb flight speed schedule.

$$\psi = \begin{cases} \frac{[1+0.2M^2]^{3.5}-1}{0.7M^2[1+0.2M^2]^{2.5}} - \zeta & \text{for constant CAS} \\ 1 - \zeta & \text{for constant EAS} \\ \zeta & \text{for constant Mach number} \end{cases} \quad (3.17)$$

where the value of ζ , reported in Equation 3.18, depends on the current altitude as well as on the temperature ratio between standard and current conditions ($\mathcal{T}_{std}/\mathcal{T}$).

$$\zeta = \begin{cases} 0.190263(\mathcal{T}_{std}/\mathcal{T}) & \text{if altitude} \leq 15\text{km (troposphere)} \\ 0 & \text{if altitude} > 15\text{km (stratosphere)} \end{cases} \quad (3.18)$$

All quantities, except for the independent variable V , are function of the current time instant due to the change of aircraft weight during the climb. In addition, aircraft thrust and drag are function of the speed as well.

3. The climb angle and the related climb gradient are calculated as a function of the true airspeed as well as their maximum values using Equation 3.19 [96], where the acceleration factor is the one from Equation 3.16.

$$\sin \gamma(t, V) = \frac{T(t, V)/W - D(t, V)/W}{1 + f_{acc}} \quad (3.19)$$

4. From the calculated values of lift and drag, the aerodynamic efficiency is calculated.

At each altitude step, the calculation module evaluates also the amount of fuel used per step by retrieving the value of the **SFC** from the engine database at given altitude, Mach number and ambient temperature. The Max Climb engine rating is used for the **AEO** case while in **OEI** condition the engine rating is assumed to be the Max Continuous.

In terms of speed schedule, a constant **CAS** segment is assumed up to the crossover height, otherwise a constant Mach number speed schedule is used. The calculation of the crossover altitude is proposed by Young in [96].

Once all maximum rates of climb values are available, the calculation of both absolute and service ceilings can begins. The absolute ceiling of an airplane is that altitude at which the rate of climb reaches a value of zero.

Given a weight, the rate of climb depends on the airspeed and on the thrust level selected by the pilot. In this case, the thrust level is assumed to be the maximum climb thrust rating. If the engine database given as input to **JPAD** has enough data to cover a wide range of altitudes, then the calculation of the absolute ceiling is made by interpolating all altitudes as a function of the maximum rate of climb values retrieving the altitude at a value of zero. Otherwise, a linear extrapolation is made. The same applies for the service ceiling at which the reference max rate of climb value is set to 0.5ms^{-1} [98].

Finally, the climb time is evaluated (only in **AEO** condition) in both cases of the maximum rate of climb speed and the user-defined climb calibrated speed by numerically solving the well-known integral formula reported in Equation 3.20.

$$t = \int_{h_{in}}^{h_{end}} \frac{dh}{RC(h)} \quad (3.20)$$

The cruise performance plays a key role in the definition of the aircraft operational constrains. Since the aircraft is not free to fly at any altitude or speed, is crucial to understand which are the

Input variables	Description
$k_{CRweight}$	Percentage of the max. take-off weight to be used for the cruise analysis.
$altitudes$	Array of altitudes at which all cruise related quantities must be evaluated.
M_{MO}	Max operating Mach number.

Table 3.16 Summary of cruise analysis input parameters

maximum altitudes and maximum speeds that the aircraft can operate. In powered flight aircraft engines are assumed to be operating, thus only the AEO condition is considered. Depending on the amount of thrust used the aircraft can be in a steady state or in an accelerating flight condition. Cruise performance are evaluated only in a steady state, straight flight conditions assuming a symmetrical thrust as well. The cruise analysis is focused on the evaluation of the following quantities. To do this, additional input data are needed as reported in Table 3.16.

- Aircraft drag and overall thrust as a function of the true airspeed, the calibrated airspeed and the Mach number at different altitudes.
- Aircraft power needed and available as a function of the true airspeed, the calibrated airspeed and the Mach number at different altitudes.
- Aircraft drag and overall thrust as a function of the true airspeed, the calibrated airspeed and the Mach number at different weight conditions.
- Aircraft power needed and available as a function of the true airspeed, the calibrated airspeed and the Mach number at different weight conditions.
- Cruise flight envelope as a function of the Mach number.
- Aircraft aerodynamic efficiency as a function of the true airspeed, the calibrated airspeed and the Mach number at different altitudes.
- Aircraft aerodynamic efficiency as a function of the true airspeed, the calibrated airspeed and the Mach number at different weight conditions.
- Aircraft SAR at different weight conditions (cruise grid chart).

While the list of altitudes to be used for the cruise analysis is provided by the user (see Table 3.16), the list of different weight conditions is assumed to be made up of 5 values starting from the reference cruise weight (given by the maximum take-off weight times the user-defined cruise weight percentage) and ending at a value of -20% of this value.

For each altitude and weight condition, the JPAD performance module calculates the aircraft drag, the aircraft lift, the overall thrust, the power needed and the power available as a function of the true airspeed. It must be noted that overall thrust and power available are constant with the weight variation in case of weight parameterization. Then, from the calculated values of lift and drag, the aerodynamic efficiency is calculated for each condition.

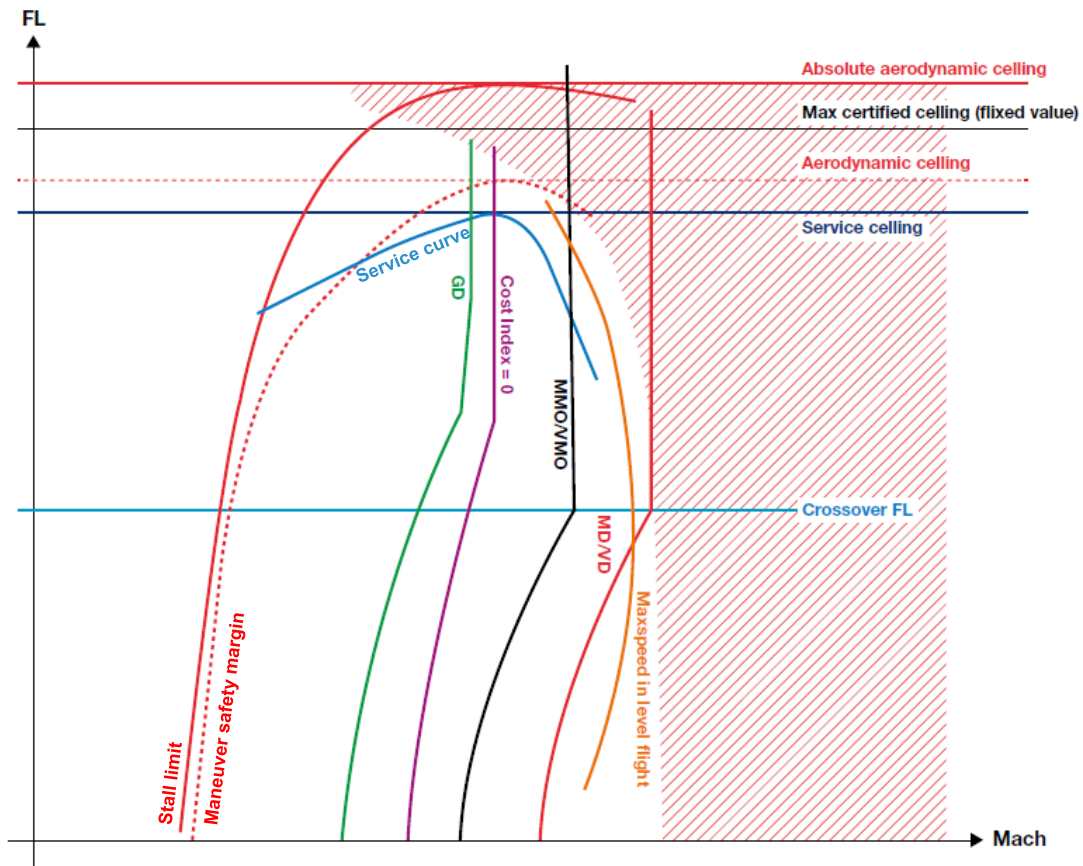


Figure 3.25 Example of cruise flight envelope [99].

One of the main objectives of the cruise analysis module is the generation of the cruise flight envelope. This chart, represented by the envelope of several limit curves, provides the maximum and minimum values of the Mach number at which the aircraft can operate in cruise for each altitude. Furthermore, it gives information about both the absolute and service ceilings in cruise as well as the structural speed limitations. To build up the chart, the following altitude-Mach relationships must be calculated as represented in Figure 3.25.

- The stall limit, given by the Mach number related to the stall speed for each altitude.
- The safety maneuver margin calculated for each altitude as the biggest between 1.23 times the 1-g stall speed and the buffet onset Mach number at 1.3g. This curve provides the aerodynamic ceiling of the aircraft in cruise. However, an accurate estimation of the buffet onset curve derives from experimental data or numerical estimations as explained in [96] [100]. A semi-empirical approach suitable for the conceptual design phase is illustrated in the work of Bérard and Isikveren [101] but the starting point is still a known and suitable buffet onset envelope related to a known seed aircraft. To overcome the absence of reliable data concerning the buffet onset curve of several type of transport aircraft, the Mach number related to the buffet onset at 1.3g have been replaced with the minimum Mach number coming from the intersection of thrust and drag curves as a function of the Mach number at a specific altitude. In case this Mach number should be lower than the one related to 1.23 times the stall speed, the latter will be used. In this way, the aerodynamic ceiling is reached at an altitude providing a thrust curve tangent to the drag curve.

- The service curve calculated for each altitude as the Mach number related to a residual rate of climb of 300ft/min. This curve provides the service ceiling of the aircraft in cruise.
- The Green Dot curve related to the speed of minimum drag at each altitude.
- The Zero Cost Index curve related to the speed providing the maximum rate of climb at each altitude.
- The maximum speed curve related to the max speed coming from the intersection of thrust and drag curves at each altitude.
- The VMO/MMO curve related to maximum operating calibrated airspeed (or Mach number) at each altitude. For altitudes above the crossover height, the MMO is considered instead of the VMO. The crossover height is the altitude at which a given value of the calibrated airspeed is equal to the related Mach number.
- The VD/MD curve related to dive calibrated airspeed (or Mach number) at each altitude. Similar to the previous case, for altitudes above the crossover height, the MD is considered instead of the VD. This limitation is related to structural issues related to the flutter phenomenon.

Finally, only in case of weight parameterization, the **SAR** is calculated as a function of the Mach number using Equation 3.21 in which the **SAR** is function of both aircraft speed and weight. Combining all possible cases of aircraft weight and cruise Mach numbers (up the maximum allowed at that altitude and weight condition) the cruise grid chart can be defined.

A qualitative example of cruise grid is shown in Figure 3.26. Here the line interconnecting all maximum values defines the best range condition, while the line interconnecting all maximum values lowered by 1% is related to the long range cruise condition. Minimum values are related to minimum operative cruise speed values while the fast cruise condition is related to the maximum allowed cruise Mach number.

Since the aircraft weight may show great variations during the cruise phase, the cruise grid chart is a very important tool for pilots because it allows to choose the right value of the cruise speed for each weight condition in order to follow some mission objectives like minimum fuel consumption or a fast cruise.

$$SAR(V, W) = \frac{V \cdot E(V, W)}{SFC(V)} \quad (3.21)$$

Concerning the descent analysis, the implemented simulation approach is similar to the climb phase. However, if the climb analysis requires only a user-defined calibrated climb speed, the descent calculation module needs two input data related to the calibrated descent speed and the required rate of descent respectively.

A description of all additional input data needed to carry out the descent simulation is reported in Table 3.17.

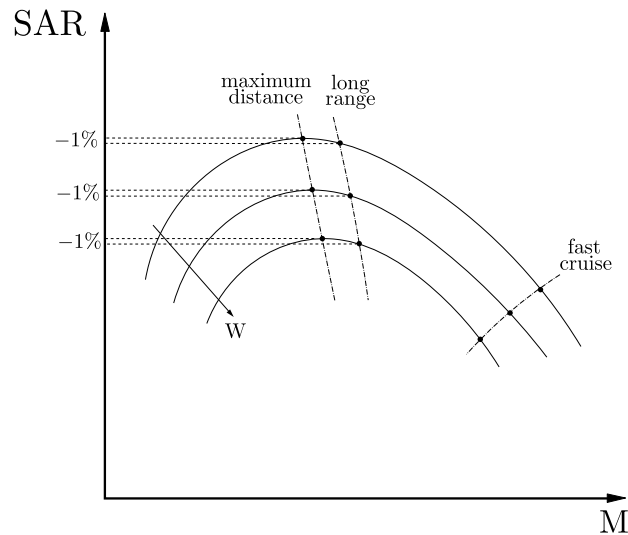


Figure 3.26 Specific Air Range as function of the Mach number parameterized in aircraft weight

Input variables	Description
$k_{DESCweight}$	Percentage of the max. take-off weight for the descent simulation.
h_{in}	Initial descent altitude.
h_{end}	Final descent altitude.
$V_{descentCAS}$	Reference calibrated airspeed for the descent simulation.
RD	Desired Rate of Descent.

Table 3.17 Summary of descent simulation input parameters

The descent path is firstly divided in 5 intermediate altitude between initial and final altitudes. For each of them the following procedure, consisting of two nested iterative loops, is applied. It must be noted that the same approach used to take into account for the acceleration factor in the calculation of both the rate of climb and the climb angle, is used also for the descent phase. In terms of flight speed schedule, a constant Mach number segment is assumed down to the crossover height (if needed), while a constant **CAS** segment is used below this altitude.

1. In case of altitude higher than the crossover height, the current value of the true airspeed is calculated using the cruise Mach number defined in the operating conditions. Otherwise, current values of the true airspeed and the Mach number are calculated from the user-defined constant descent calibrated speed and the current altitude.
2. Thrust and **SFC** values at current altitude, Mach number and **ISA** deviation are calculated both for Max Cruise and Flight Idle engine ratings.
3. A first nested iterative loop is used to ensure that the calculated rate of descent differs from the desired one less than 5%. Each iteration implements the following procedure.
 - (a) The descent angle is calculated using the current value of the true airspeed and the user-defined rate of descent. This only for the first iteration, then the calculated rate of descent is used.

- (b) From the descent angle and the true airspeed, the current value of the horizontal speed is calculated.
- (c) From the calculated descent angle and the values of altitude and aircraft mass, the value of the lift coefficient is calculated using Equation 3.22.

$$C_L = \frac{2W \cos \gamma}{\rho S V_{TAS}^2} \quad (3.22)$$

- (d) From the value of the lift coefficient, the drag coefficient and then aerodynamic efficiency are calculated by means of the input drag polar curve in clean configuration.
- (e) The aircraft drag is calculated using the current value of the drag coefficient.
- (f) A second nested iterative loop is used to define Max Cruise and Flight Idle coefficients of the related thrusts weighted average needed to ensure that the calculated rate of climb differs from the desired one less than 5%. This follows the procedure below.
 - i. Equal coefficients (0.5) are assigned to both Max Cruise and Flight Idle engine ratings to calculate a first guess averaged thrust.
 - ii. From the current values of aircraft drag, true airspeed and weight, the rate of descent is calculated.
 - iii. The ratio between the current rate of descent and the desired one is calculated to update the thrust weighted average coefficients.
 - iv. If the calculated ratio is less than 1, the Max Cruise coefficient is multiplied by the calculated ratio. Otherwise, the Flight Idle coefficient is multiplied by the reciprocal of the rate of descent ratio. In any case, the other coefficient is calculated to ensure that their sum is equal to 1.

4. Descent step length, duration and used fuel are calculated. This latter value is used to update the aircraft mass before passing to the next altitude.

In addition to the standalone analysis of a single ground or flight phase, JPAD allows the user to carry out also a complete mission profile simulation, the latter related both to a design mission, both to an off-design mission.

The mission profile analysis has the key-role of investigating the behavior of the aircraft during a specific mission by calculating and reporting time histories of the main physical quantities of interest as well as to estimate whether or not the designed aircraft is able to cover a given mission range. To perform the mission profile simulation, beside most of the input data needed by each single phase calculator, the required additional input data are reported in Table 3.18.

All most important physical quantities collected during the mission profile simulation are reported in Table 3.19.

For each mission phase, these quantities are collected step-by-step during the simulation providing their time histories. However, a summary of each phase overall data is created as well to provide the user with a more concise output representation.

To carry out the simulation, the overall mission has been firstly divided in all its sub-phases which are summarized in Table 3.20 and represented in Figure 3.27.

Input variables	Description
$R_{mission}$	The mission range
$R_{alternate}$	The diversion range
$h_{alternate}$	The diversion cruise altitude
$M_{alternate}$	The diversion cruise Mach number (can also be calculated as the best range one)
$t_{holding}$	The holding duration
$h_{holding}$	The holding altitude
$M_{holding}$	The holding Mach number (can also be calculated as the best endurance one)
$f_{reserve}$	Percentage of the initial fuel to be considered as reserve

Table 3.18 Summary of mission profile simulation input parameters

The mission profile analysis consists of three nested iterative loops, each of which involves the analysis of all phases reported in Table 3.20. The first step is to define the initial mission weight. This can be calculated using Equation 3.23 in which the initial fuel weight is unknown. Assuming a first guess value of the initial fuel weight equal to a quarter of the maximum take-off weight, the first phase to be analyzed is the take off.

$$TOW = OEW + W_{Payload} + W_{fuel} \quad (3.23)$$

The take-off phase is analyzed using the same procedure described for the standalone take-off calculation neglecting the case of engine failure during the simulation. The distance covered as well as all other needed physical quantities reported in Table 3.19 are collected during the ODE system integration.

Description	Unit
Mission range	nm
Mission duration	min
Mission used fuel	kg
Pollutant emissions (NO _x , CO, HC, Soot, CO ₂ , SO _x , H ₂ O)	kg
Aircraft weight	kg
Aircraft speed (TAS, CAS and Mach number)	kts
Aircraft overall thrust and drag	lbf
Aircraft overall fuel flow	lb/h
Aircraft overall SFC	lb/lb h
Aircraft lift and drag coefficients	
Aircraft aerodynamic efficiency	
Aircraft rate of climb	ft/min
Aircraft climb angle	deg
Aircraft climb gradient	%
Power plant required power	kW
Power plant required energy	kWh

Table 3.19 Summary of the physical quantities collected by the mission profile calculator. Pollutant emissions are calculated only if the related emission index in the engine database is given.

Phase number	Description
1	Take-off
2	Climb
3	Cruise
4	First descent down to 1500ft
5	Second climb from 1500ft up to alternate cruise altitude
6	Alternate cruise
7	Second descent down to holding altitude
8	Holding (typically at 1500ft)
9	Approach and landing (from 1500ft)

Table 3.20 Summary of mission phases

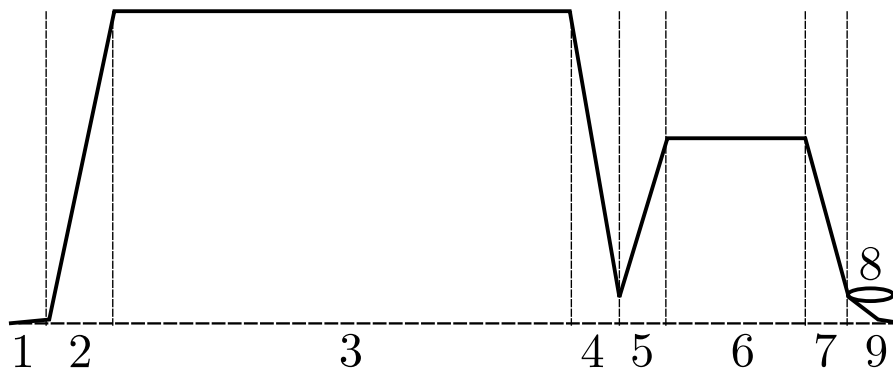


Figure 3.27 Mission profile sub-phases handled by JPAD

The same applies for the climb segment in which all mission profile related quantities are evaluated for each altitude step. In this case all calculations related to the definition of absolute and service ceiling as well as all details concerning rate of climb, climb angles and climb gradients in OEI conditions are not taken into account. Starting from AEO thrust, drag, rate of climb and aircraft weight for each step, and knowing the amount of fuel used per step, values for SFC, fuel flow and emissions can be easily derived (e.g. pollutant emissions are calculated multiplying the fuel used by the related emission index, if present). Furthermore, applying Equation 3.20 for each altitude step, the time history of the climb time using the assigned calibrated climb speed can be obtained.

Finally, from step-related values of the climb angle, the climb time and the aircraft speed the distance covered can be calculated as shown in Equation 3.24 where n is the number of altitude steps.

$$R_{climb} = \sum_{i=1}^n \int_{h_i}^{h_{i+1}} V \cos \gamma dt \quad (3.24)$$

The cruise phase influences all the remaining mission segments and since the cruise range is unknown, as well as the required time and the related amount of fuel used, an iterative process is needed to find the cruise range that fits in the overall mission distance. Starting from a first guess value (assumed equal to the total mission range), the cruise range is divided into 5 steps.

For each of them, the following procedure is used.

1. From the initial cruise aircraft weight and the known cruise altitude, aircraft drag, and overall thrust are calculated as function of the true airspeed.
2. The thrust-drag intersection is performed to estimate the maximum allowed cruise flight speed. If the user-defined operating Mach number is bigger than the one obtained from the maximum allowed speed, this latter is used.
3. Knowing the initial cruise aircraft weight, the cruise altitude and the cruise speed, the equilibrium lifting coefficient can be calculated.
4. From the value of the lift coefficient, the drag coefficient is obtained from the trimmed drag polar curve in cruise condition.
5. Current values of aircraft drag, and aerodynamic efficiency are calculated.
6. By comparing the Max Cruise thrust deliverable by the power plant and the required thrust needed to equal the aircraft drag, the throttle setting is calculated.
7. From the values of cruise altitude, Mach number, ISA deviation and throttle setting, the current value of the SFC can be calculated. This, multiplied by the estimated cruise thrust, provides for the current value of the fuel flow.
8. Knowing the length of the cruise distance step and the cruise speed, the time needed to cover that distance can be easily calculated.
9. By multiplying the calculated step duration and the fuel flow, the amount of fuel used can be obtained.
10. Pollutant emissions as well as power and energies needed to cover the current cruise step are calculated from the used fuel, the cruise step duration and the current value of the overall thrust.
11. A new aircraft weight is calculated for the next cruise range step.

The first descent phase is analyzed in the same way as the standalone descent described before. After the first descent, from the cruise altitude to an altitude of 1500 ft, a second climb up to alternate cruise altitude has been considered. This has been analyzed in the same way as the main climb.

The following segment is the alternate cruise which is analyzed following the same procedure as the main cruise but using as first guess distance a value equal to the user-defined alternate range. During this phase, if the user has decided to let JPAD calculate the alternate cruise Mach number, the best range Mach number is estimated from the cruise grid described in the cruise standalone module.

A second descent from the alternate cruise altitude down to the user-defined holding altitude is considered for then analyzing the holding phase. This is considered to last for a user-defined amount of time and is divided into 5 intermediate time intervals. The procedure used to carry out the analysis of each time step, follows the pattern of the both main and alternate cruise phases. However, if the user has decided to let JPAD to calculate the loiter Mach number, this is assumed as the one providing for the best endurance. In this case an iterative loop is used to assess the value of the Mach number related to the lowest fuel consumption per step.

Finally, approach and landing phases are analyzed by integrating the set of ODE described in the standalone landing calculation module. At this point, two checks must be performed to ensure that the simulated mission is consistent with the user requirements. Firstly, if the total alternate distance (sum of second climb, alternate cruise and second descent distances) covered with the assumed alternate cruise range is not equal to the target diversion range, a new alternate cruise range is calculated using the range variation obtained from Equation 3.25.

$$\Delta R = R_{target} - R_{current} \quad (3.25)$$

Then the same check is performed on the calculated block range (sum of take-off, climb, main cruise, first descent, approach and landing distances) to ensure that the assumed cruise range complies with the overall target block range. If those value does not match, the main cruise range variation is calculated using Equation 3.25. At the end of those iterative loops, the mission range and diversion ranges are equal to the target values. However, the assumed initial fuel weight may not guarantee the residual user-defined fuel reserve assumed in Table 3.18. In this case a new initial fuel weight is calculated using Equation 3.27.

$$W_{f,new} = \frac{W_{f,used}}{1 - f_{reserve}} \quad (3.26)$$

It has to be noted that, if the new initial fuel weight leads to a new take-off weight bigger than the maximum take-off weight is assumed as the initial mission weight and the payload is reduced by a quantity given by Equation 3.25 rounded to the closest integer value to calculate the maximum allowed passenger number for the analyzed mission.

$$\Delta W_{payload} = MTOW - TOW \quad (3.27)$$

To better understand the analysis process of the overall mission profile, a visual representation of the analysis workflow is provided in the flowchart of Figure 3.28. This is very similar to the one proposed in [96]. However, although considering a more detailed mission profile with more sub-phases, it does not take into account for the possibility of an unfeasible take-off weight occurring when the sum of the total fuel needed to cover the mission plus the OEW and the payload becomes greater than the MTOW. In this case two possibility are available: to reduce the mission distance or to reduce the payload. The latter has been selected for the mission profile analysis implemented in JPAD as previously described.

The mission profile analysis, with some minor modifications, is also the core of the Payload-Range analysis module. In fact, since each point of this diagram is related to a specific mission, the same simulation-based approach may be used to calculate all the points needed to build up the chart. A qualitative representation of the Payload-Range chart is reported in Figure 3.29. Four main couples of payload and range values must be defined:

- **Point A:** max payload, MTOW and zero range.
- **Point B:** max range with max payload and with MTOW (Harmonic Range).
- **Point C:** max range with the design payload and with MTOW (Design Range).

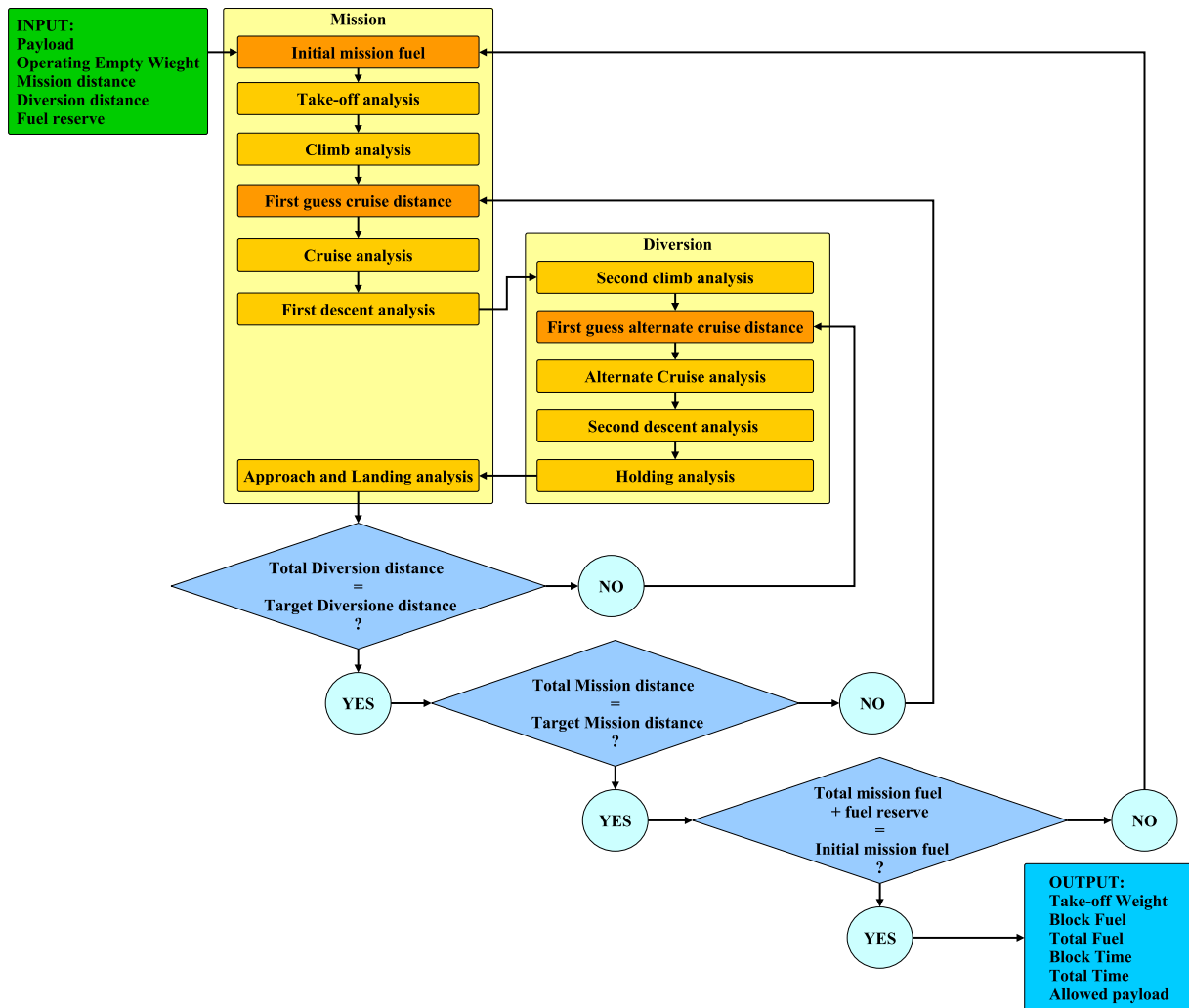


Figure 3.28 Flowchart of the mission profile analysis performed by JPAD

- **Point D:** max range at max fuel capacity.
- **Point E:** max range at zero payload.

The main objective of the Payload-Range analysis module is to calculate the payload, the range, the aircraft mass and the amount of fuel needed for each of the above-mentioned points.

Beside point A, which is very simple to obtain, to calculate points B, C, D and E the starting point is to assess their payload masses. The first two points are related to the known values of the maximum payload and the design payload respectively.

Whereas, the point D payload can be obtained by retrieving the maximum fuel tank capacity, estimated at the creation of the aircraft parametric model, and using Equation 3.28.

$$W_{payload} = MTOW - OEW - W_{fuel,max} \quad (3.28)$$

Knowing each payload, the next step is to calculate the amount of fuel related to each point. This can be easily done using Equation 3.29. In particular, points B, C and D are calculated at the maximum take-off weight, while the last one (point E) has a lower take-off weight given only by the **OEW** and the maximum allowed fuel weight.

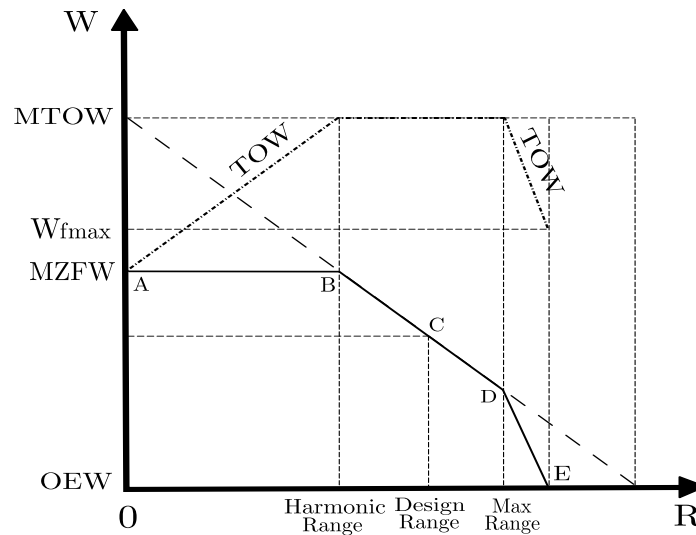


Figure 3.29 Qualitative representation of the Payload-Range chart with **MZFW** limitation

Input variables	Description
$C_{Lmax,inv}$	Inverted flight maximum lifting coefficient
$n_{lim,pos}$	Positive limit load factor
$n_{lim,neg}$	Negative limit load factor

Table 3.21 Summary of V-n diagram input parameters required by JPAD

$$W_{fuel} = MTOW - OEW - W_{payload} \quad (3.29)$$

Finally, all estimated fuel weights are used inside the mission profile calculation module to estimate the range that can be covered with that amount of fuel. In this case, the iterative loop on the block range is neglected since no assigned mission range is specified. Furthermore, the iterative loop on the initial mission fuel is modified to guarantee that the latter equals the calculated mission fuel for that specific point on the Payload-Range chart ensuring, at the same time, the user-defined fuel reserve. It must be noted that the range reported on final Payload-Range chart is related only to the block range neglecting the distance related to the diversion.

The last analysis that can be performed by the JPAD performance manager at the moment of writing concerns the generation of the flight maneuvering and gust envelope, also known as V-n diagram. This chart is used to define structural operative limitations in terms of aircraft load factor and speed. This resource is of extreme importance when dealing with aircraft certification tests (e.g. static wing test) and operations since it defines the maximum allowed load that the aircraft can tolerate at every operational speed.

The definition of each point of this chart is clearly specified by FAR part 25 (sections 25.333, 25.334, 25.335, 25.337, 25.341) concerning the definition of cruise and dive speeds as well as gust speeds, these latter assumed to be symmetrical and in vertical direction with respect to the aircraft.

Beside the envelope in flight conditions, JPAD takes into account also for take-off and landing phases producing the flight envelope chart in case of flaps deflection.

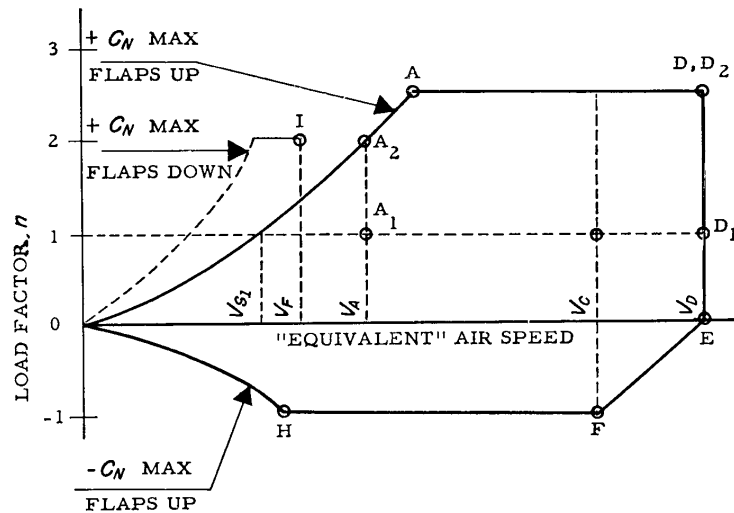


Figure 3.30 FAR-25 flight envelope.

As for the main envelope, FAR-25 provide all the details needed to define the design flap speed and its maximum load factor. A visual representation of FAR-25 flight envelopes is provided in Figure 3.30. In addition, a summary of the input data needed by the JPAD calculator is reported in Table 3.21.

Costs

The last module of JPAD is the one in charge of estimating DOC. Being able to provide an estimation of both overall aircraft DOC and its breakdown starting from the preliminary design phase is of extreme importance for an aircraft design software since it allows the designer to involve this fundamental set of parameters in an MDAO process. The estimation of the DOC breakdown concerns flight operations and consider the following items.

- **Capital costs:** depreciation, interest, and insurance.
- **Crew costs:** flight and cabin.
- **Fuel cost.**
- **Charges:** landing, navigation, ground handling, noise, emissions.
- **Direct maintenance:** airframe and engine

To estimate those cost items, the methodologies defined by Association of European Airlines (AEA) [102] for capital, fuel, a part of charges (landing, navigation and ground-handling) and crew costs has been implemented while the Air Transportation Association of America (ATA) [103] method has been used for direct maintenance costs. Noise charges are calculated by using the formulation recommended by the Transport Aircraft Noise Classification (TNAC) group within the European Civil Aviation Conference (ECAC) [104] [105]. The emissions charges are estimated using formulation prescribed by ICAO in annex 16 volume 2 [106].

As for the aerodynamic and stability analysis module, also this one has been developed by another DAF PhD student named Vincenzo Cusati. For more information regarding methodologies and module architecture, the reader can refer to the thesis work titled “Design activities for innovative turboprop aircraft with minimum economic and environmental impact” [107].

3.3.5 GUI and Automatic CAD generation

To provide for an efficient, simple and complete user experience, a new module of the JPAD framework, named `jpad-commander`, has been developed to create the GUI as shown in the software architecture flowchart of Figure 3.2.

As previously explained, the `jpad-commander` module has been completely designed using the JavaFX library [68] together with a JavaFX-based development tool named SceneBuilder [75]. The user experience to be provided via the `jpad-commander` GUI consists in a guided sequence of operations and perspectives related to all software features from aircraft parametric model generation up to its multi-disciplinary analysis and optimization.

Starting from the *Input Manager* the user can firstly define the aircraft object (or import one of the default aircraft models) for then applying all geometrical modification he wants to generate a new aircraft. This perspective, shown in Figure 3.31, allows also for the automatic creation of the aircraft CAD model as well as its visualization in a dedicated 3D scene which uses the MeshView library of JavaFX to allow for a conversion in the native JavaFX format. The generated aircraft model can be easily exported and used in most of the top commercial CAD and CFD software.

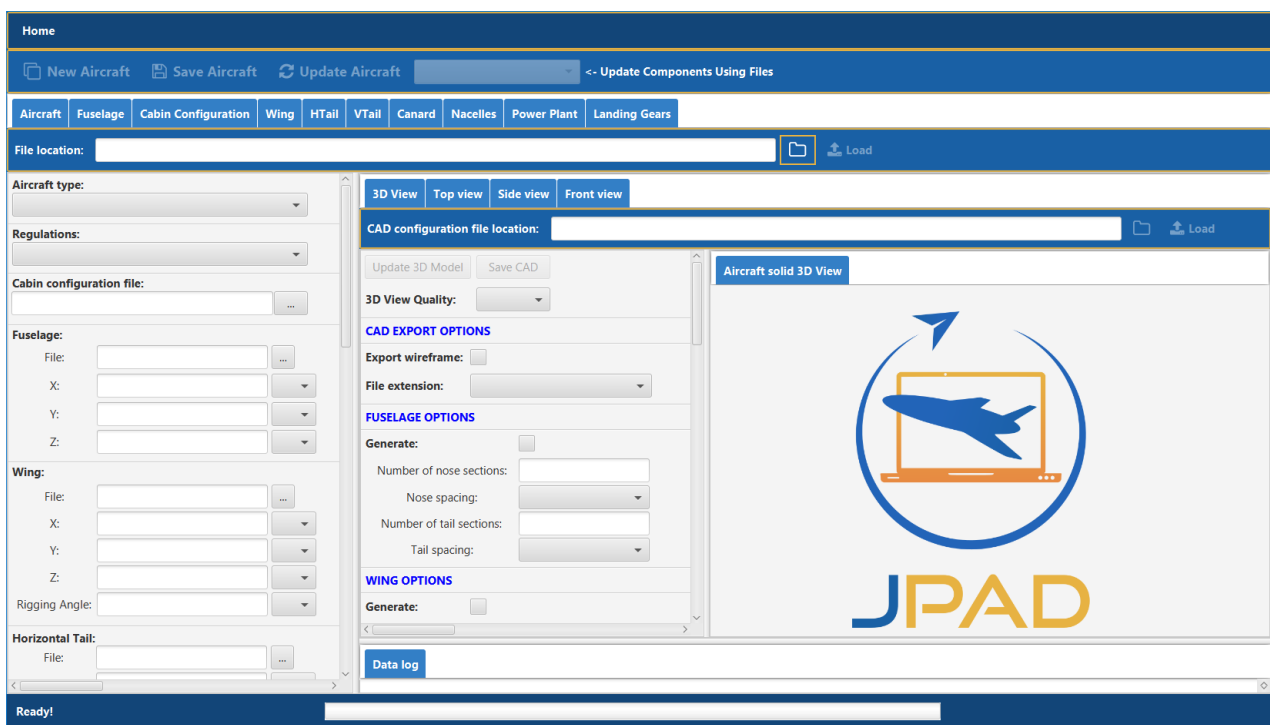


Figure 3.31 Input Manager perspective of the `jpad-commander` GUI

In addition to the possibility of generating the aircraft model, it is also possible to generate the following advanced parts making the classical CAD modelling much faster and simpler.

- Wing-fuselage junctions
- Rounded lifting surfaces tips and winglets
- Control surfaces and high-lift devices with their related housings
- Pylons, nacelles and propellers

Then the user can access the *Analysis Manager* perspective to setup the analyses workflow (one or more standalone analysis as well as a complete analysis cycle or a multi-disciplinary optimization) and all needed additional input data for each required analysis module. Finally the *Output Manager* perspective allows to visualize all analyses-related output data both via tables and charts.

Some examples of the **jpad-commander** GUI are provided from Figure 3.32 to Figure 3.34 concerning the *Input Manager*. The first one is related to complete aircraft model showing also its automatically generated CAD model, the second one concerns the cabin layout definition (extremely important in the balance analysis) while the third one deals with an example of lifting surface (the wing in this case) showing also all movable surfaces.

Since airfoil data must be defined together with their related lifting surface, a dedicated perspective has been developed inside each lifting surface GUI tab as shown from Figure 3.35 to Figure 3.38. Here the user can manage airfoil geometry and aerodynamic data concerning lift curve, drag polar curve and pitching moment curve. Furthermore, it is possible to assign each aerodynamic data or to import external curves if the user has higher fidelity data and wants to enhance the aerodynamic module calculation accuracy.

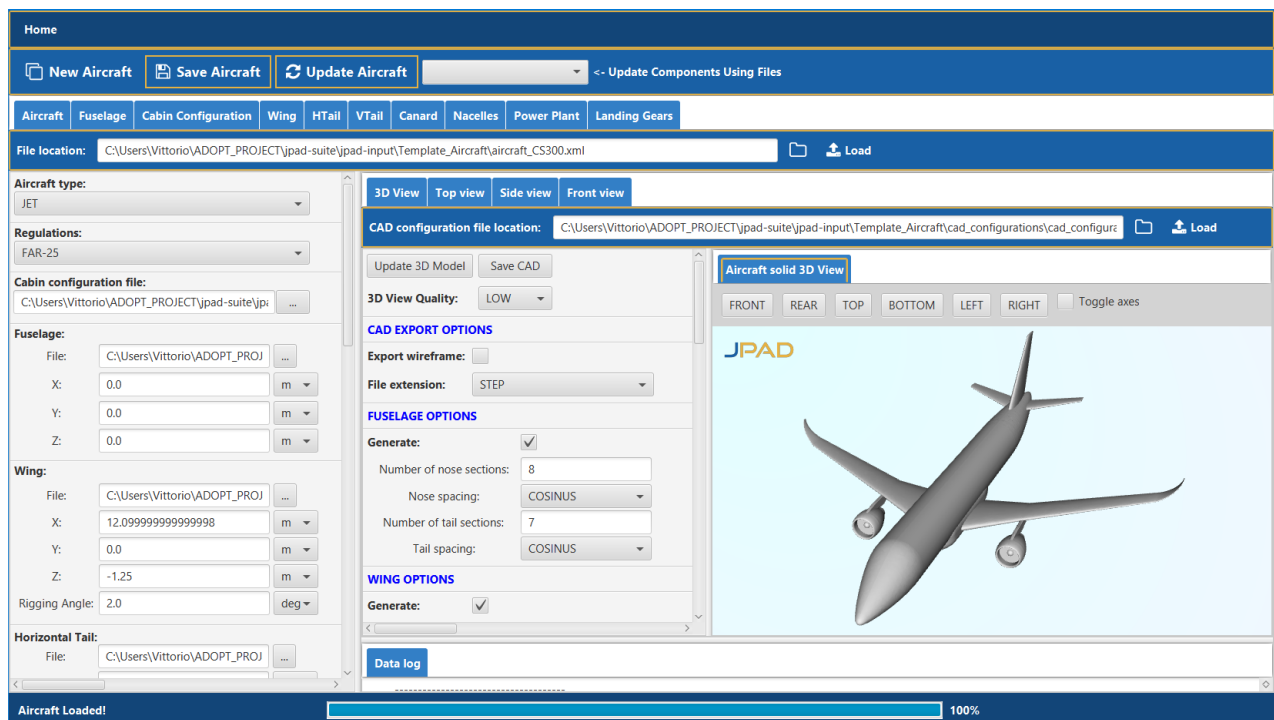


Figure 3.32 Main Input Manager perspective of the **jpad-commander** GUI with automatically generated CAD model

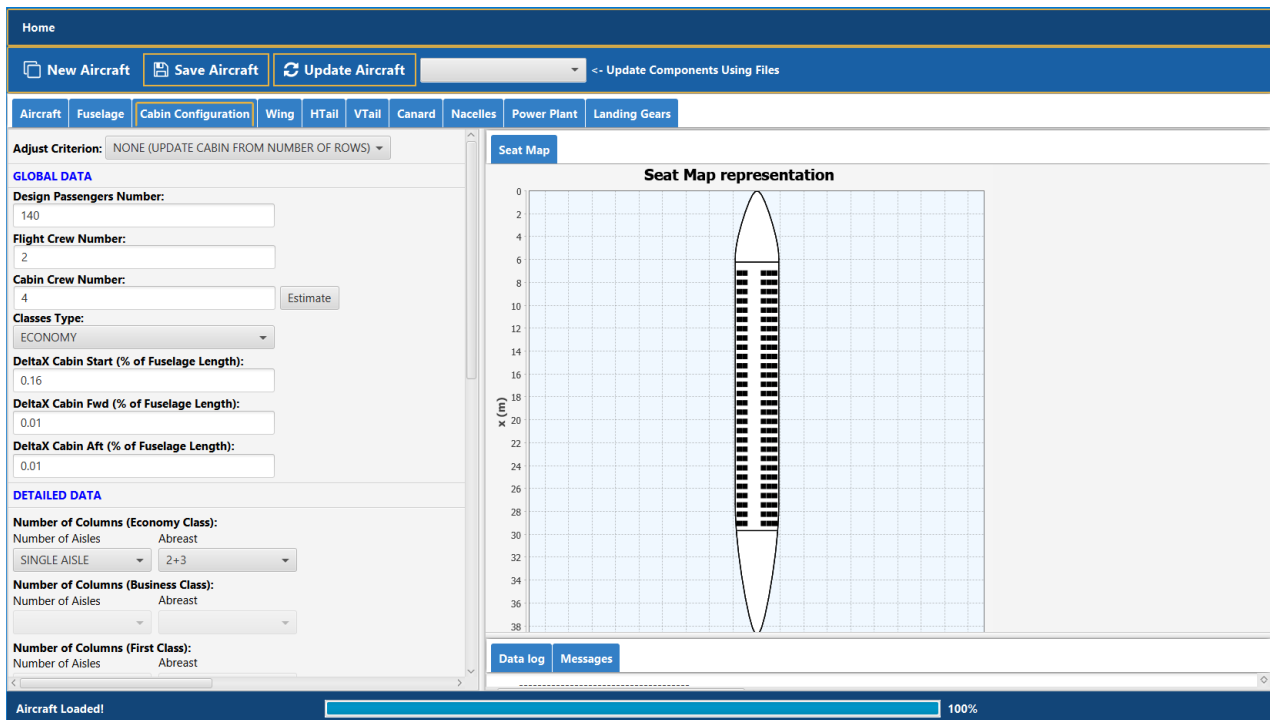


Figure 3.33 jpad-commander Input Manager perspective - cabin layout

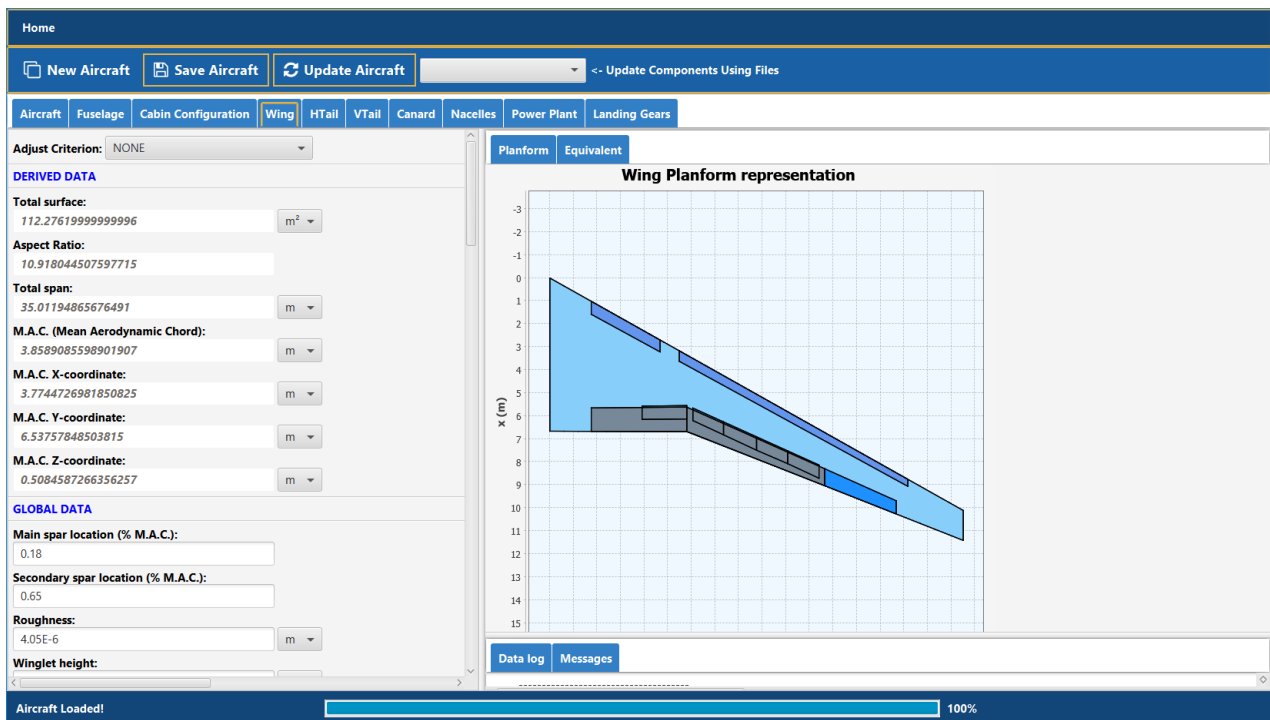


Figure 3.34 jpad-commander Input Manager perspective -wing definition

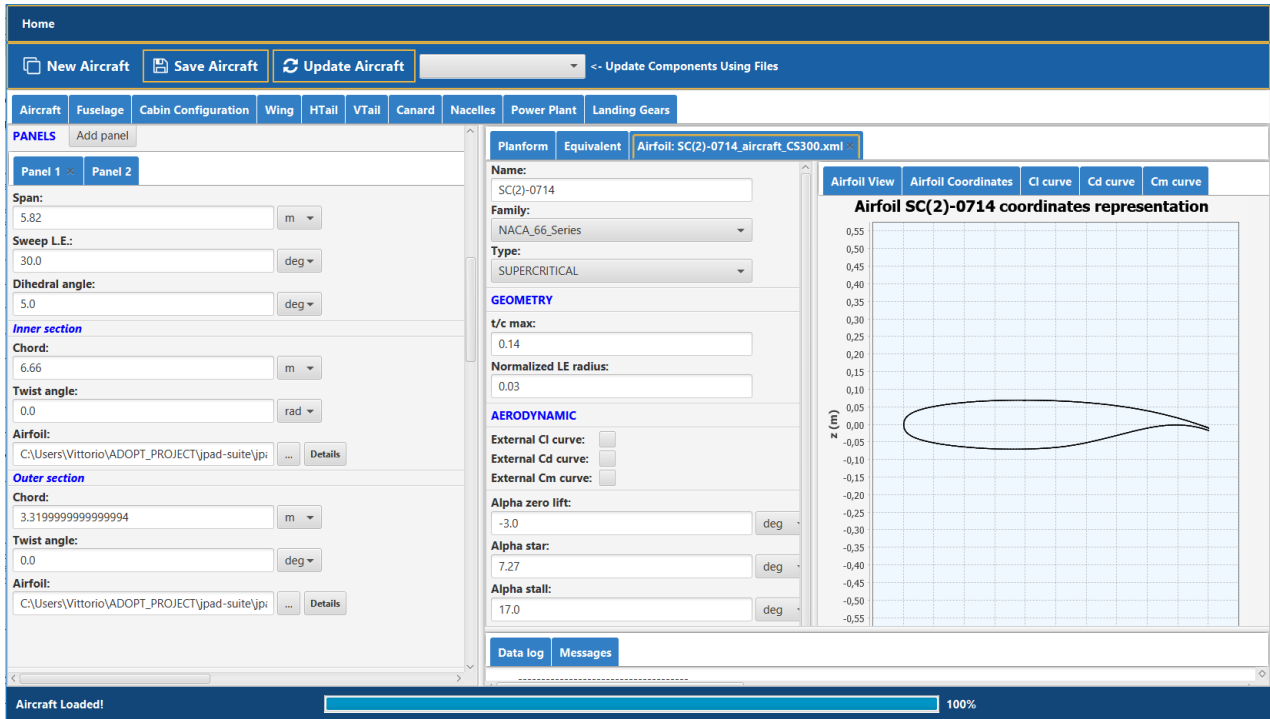


Figure 3.35 jpad-commander Input Manager perspective - airfoil geometry management

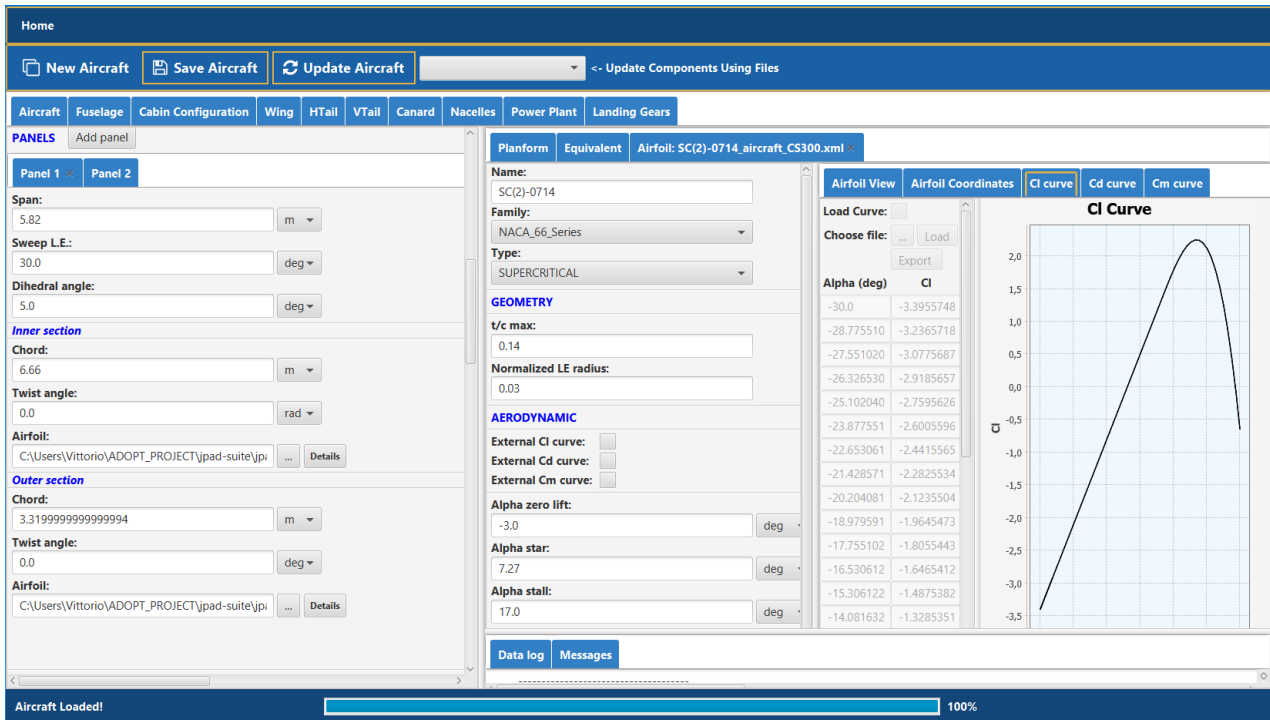


Figure 3.36 jpad-commander Input Manager perspective - airfoil lift curve management

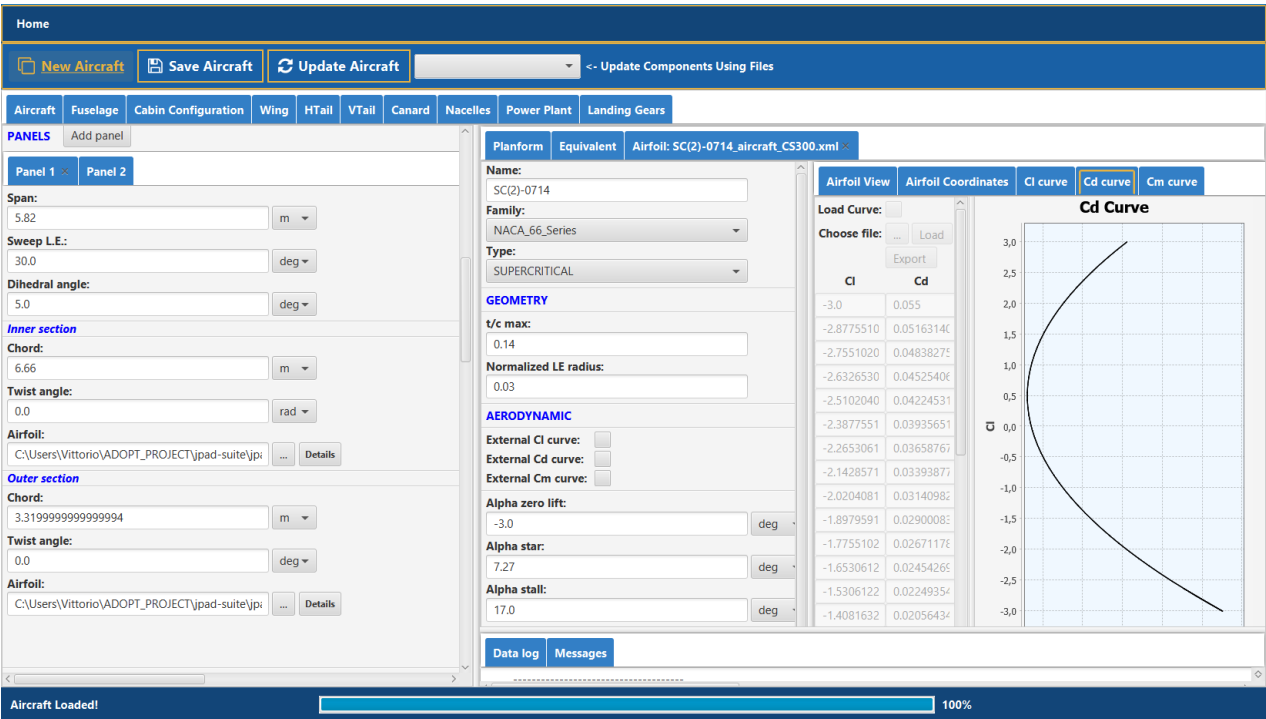


Figure 3.37 jpad-commander Input Manager perspective - airfoil drag polar curve management

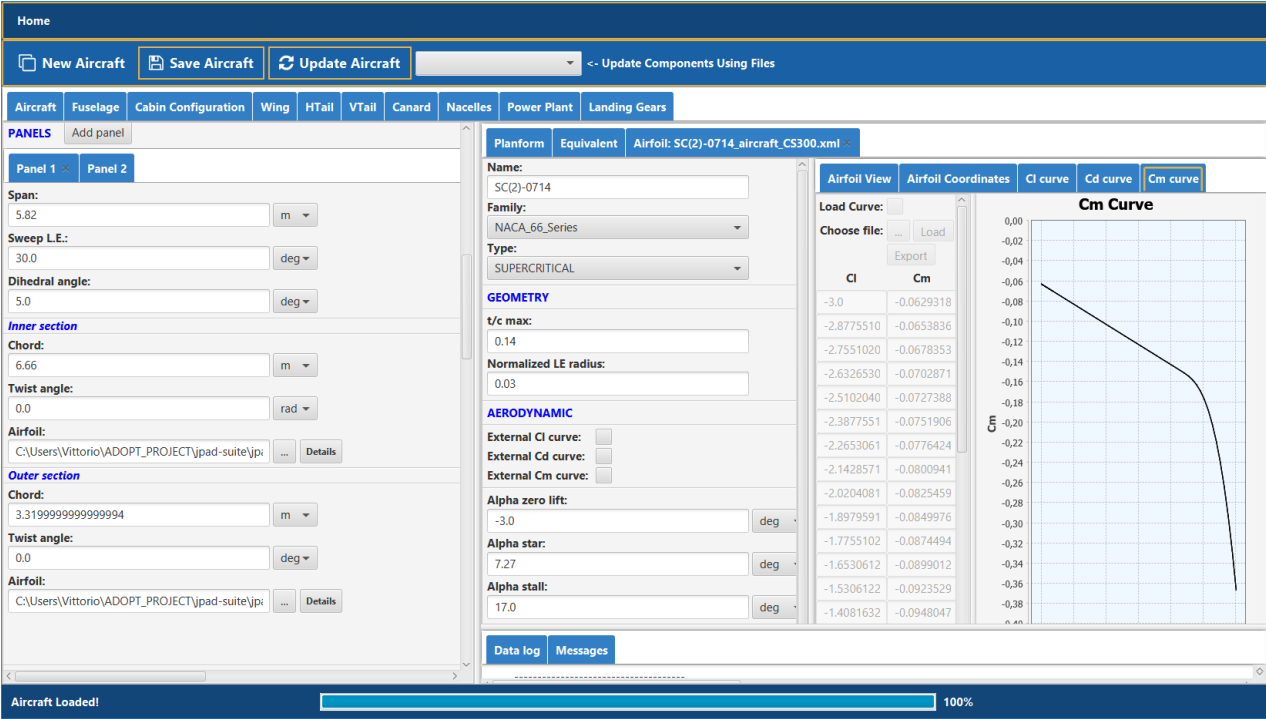


Figure 3.38 jpad-commander Input Manager perspective - airfoil pitching moment curve management

3.3.6 Multi-Disciplinary Analyses and Optimizations

The **JPAD** library is designed as an interconnection of different modules each one dedicated to a specific task. In the previous section an overview of the Core module has been provided. However, since the one of the main goals of **JPAD** is to carry out **MDAO** workflows, the focus of this section will be on two framework components: the parametric studies and **DOE** module and the single and multi-objective optimization module. These use all the Core features of the library and allow users to easily analyze a large number of different aircraft models searching for one or more optimum configurations.

Before entering the details of these modules, a brief state of the art of typical **MDAO** problems solving techniques is required. As described in [42], a first attempt to solve these problems expects to entrust all the analyses to an expert well versed in all disciplines to reduce communications and organization problems. This approach, named **Monolithic Design (MD)**, has been widely used to carry out conceptual design phases in the past and is suitable only for simple problems or when approximate results are acceptable. Nowadays a single expert is unable to monitor a complex process, like the design of a complete aircraft, and new multidisciplinary design techniques are required. To manage all disciplines, a way could be to define a process in which the aircraft is designed thanks to the collaboration of a group of different experts (one per discipline). That is the **Collaborative Design (CD)** approach. The third generation of **MDAO** approaches, core of the European Aircraft 3rd Generation **MDO for Innovative Collaboration of Heterogeneous Teams of Experts (AGILE)** project, is a direct evolution of the previous one and is called **Collaborative Remote Design (CRD)**. This involves a group of experts geographically located in different parts of the world that can communicate and exchange their own tools or results through a remote server connection. In this way is possible to take advantage of the knowledge of several aerospace research centers or companies in each certain discipline. A case study concerning the **CRD** approach is provided in [108].

Focusing on **JPAD**, the two abovementioned modules together with all the Core features, define a closed **MDAO** environment which concerns the **MD** approach. However, the possibility given by **JPAD** to be potentially interfaced with external tools and to use standalone modules makes this library suitable also for modern **MDAO** approaches like **CD** or **CRD**. In fact, the optimization module has been widely used in recent European project research activities to solve **MDAO** problems belonging both to **MD** [11] both to **CRD** [109].

The first module to be discussed is the parametric studies and **DOE** module which allows users to have access to all the possible input variable needed to define both the aircraft parametric model, both main analyses input parameters (e.g. calibration factors to simulate technological trends) giving the possibility to specify which one have to be changed and within which values range. As shown in Figure 3.39, this module creates different aircraft equal to the number of combinations of all the design parameter array elements, (full factorial combination).

To ensure the feasibility of each generated aircraft model, a consistency check is performed for each design variables values combination. This consists of a series of geometrical checks used to assess that there are no overlapped or “floating” parts (i.e. estimated cabin dimensions make the latter overcome fuselage outlines, a lifting surface isn’t attached to the fuselage, etc.). Moreover, the user can assign one or more strategies in the geometry update of each aircraft model. Those concerns usually fuselage shape, lifting surfaces planforms, tail planes positions and engines static thrust.

Strategy	Description
1	Update fuselage length at fixed nose and tail trunks length ratios and at fixed fuselage diameter.
2	Update fuselage length with fixed trunks fineness ratios.
2	Update fuselage length with fixed trunks fineness ratios and overall fineness ratio.
3	Update fuselage cylinder trunk length (stretching).
4	Update fuselage nose trunk length with fixed overall length and diameters.
5	Update fuselage nose trunk length with fixed trunks length ratios and diameters.
6	Update fuselage nose trunk length with fixed trunks fineness ratios.
7	Update fuselage tail trunk length with fixed overall length and diameters.
8	Update fuselage tail trunk length with fixed trunks length ratios and diameters.
9	Update fuselage tail trunk length with fixed trunks fineness ratios.

Table 3.22 Fuselage update strategies implemented inside JPAD.

Strategy	Description
1	Update lifting surface aspect ratio and span at fixed panels relative span and chords ratio.
2	Update lifting surface aspect ratio and panels span at fixed panels chords ratio.
3	Update lifting surface aspect ratio and area at fixed panels relative span and chords ratio.
4	Update lifting surface aspect ratio and panels chords at fixed panels span percentages.
5	Update lifting surface area and span at fixed panels relative span and chords ratio.
6	Update lifting surface area and panels spans at fixed panels chords ratio.
7	Update lifting surface span and panels chords at fixed panels relative span
8	Update lifting surface panels chords, and panels span.

Table 3.23 Generic lifting surface update strategies implemented inside JPAD.

Dealing with the fuselage, all geometry update strategies are focused on the management of nose, cylinder and tail trunks parameters as well as cylinder trunk section dimensions. A summary of the available strategies is provided in Table 3.22.

Each lifting surface planform (wing, horizontal tail, vertical tail and canard) can be modified by taking into account for overall equivalent lifting surface parameters (area, span, aspect ratio, etc.) or by managing each panel data. A summary of all possible strategies is provided in Table 3.23.

In addition to the previous strategies, concerning the case of horizontal and vertical tail planes, the user can choose if a generic tail plane must be moved or scaled to keep the volumetric ratio of the baseline constant. If the area scaling provides for an unfeasible tail position, the latter is also modified starting an iterative loop to match the target volumetric ratio. The selection of this strategy makes impossible for the user to adopt any of the rules reported in Table 3.23 for the considered tail plane.

Finally, engines static thrust can also be involved in the aircraft update process aiming at some given objectives. For example, the user may choose to fix the design point by keeping the thrust to weight ratio (T/W) constant, or to scale the overall thrust to match some target performance (i.e. take-off field length, cruise Mach number, etc.). Despite previous cases, those strategies require for an additional iterative loop within the complete analysis cycle shown in Figure 3.5 since each engine static thrust must be modified according to performance module feedbacks. It must be noted that, to take into account for the snow-ball effect provided by engine parameters modification, for each updated static thrust JPAD calculates new values of the engine dry mass, the engine overall length as

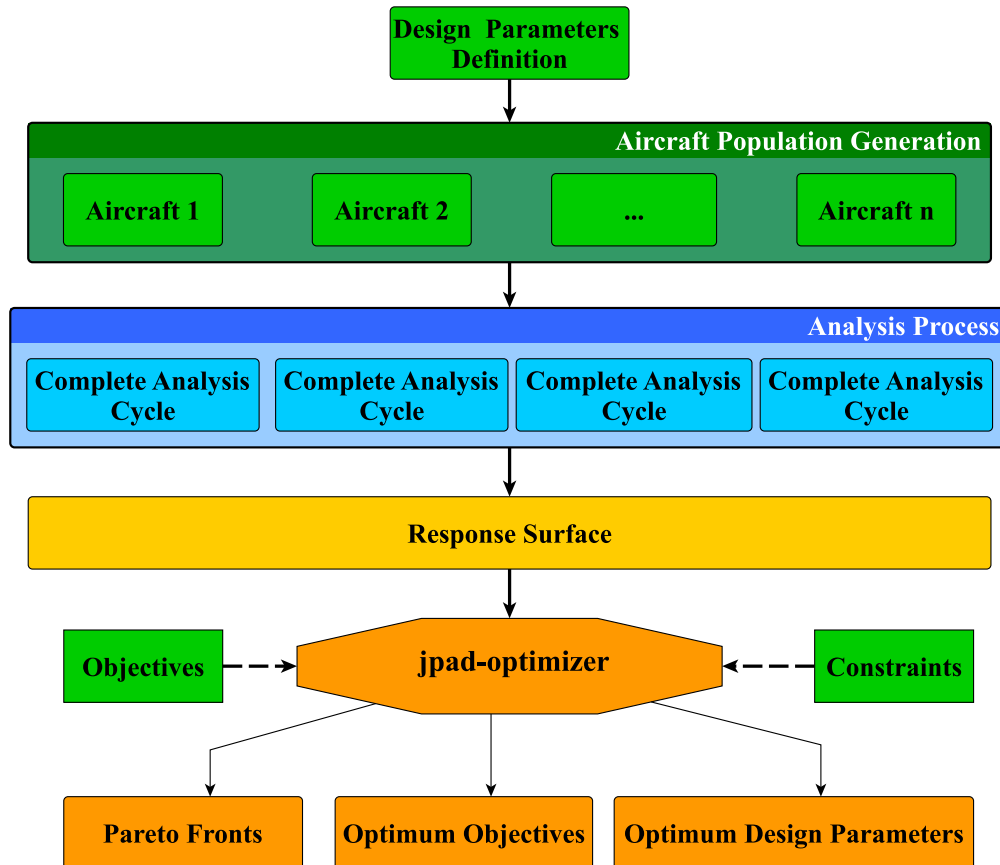


Figure 3.39 Typical DOE and optimization flowchart in JPAD

well as main nacelle dimensions (length and maximum diameter). In this way, effects of the engine update process influence not only the performance module, but also weights, balance, aerodynamics and longitudinal static stability analyses.

Each of these is then analyzed using a combination of JPAD Core modules represented in Figure 3.3. The possibility to invoke individually each analysis module, or even a single output parameter calculation method, plays a key role in reduction of the computational time required for the whole calculation process. In addition, thanks to the possibility to easily manage multiple parallel threads, the user can further reduce the amount of computational time running more than one analysis simultaneously.

To carry out a complete analysis cycle, JPAD uses a combination of its analysis modules as described in the previous sections (see Figure 3.5).

At the end of each analysis cycle JPAD stores in an external dataset all the output variable that the user has decided to monitor defining, this way, a cloud of solution points (one per aircraft) from which all possible response surfaces can be generated. An example of response surface generated by JPAD is shown in Figure 3.40. Here, an aircraft model similar to the Airbus A220-300 has been modified by changing its wing area and aspect ratio to monitor the related effects on the block fuel for a design mission of 3100 nautical miles.

As shown in Figure 3.39, all these data are then passed to the single and multi-objective optimization module. This latter, conceived as a standalone tool usable both within the JPAD framework, both externally as an independent application.

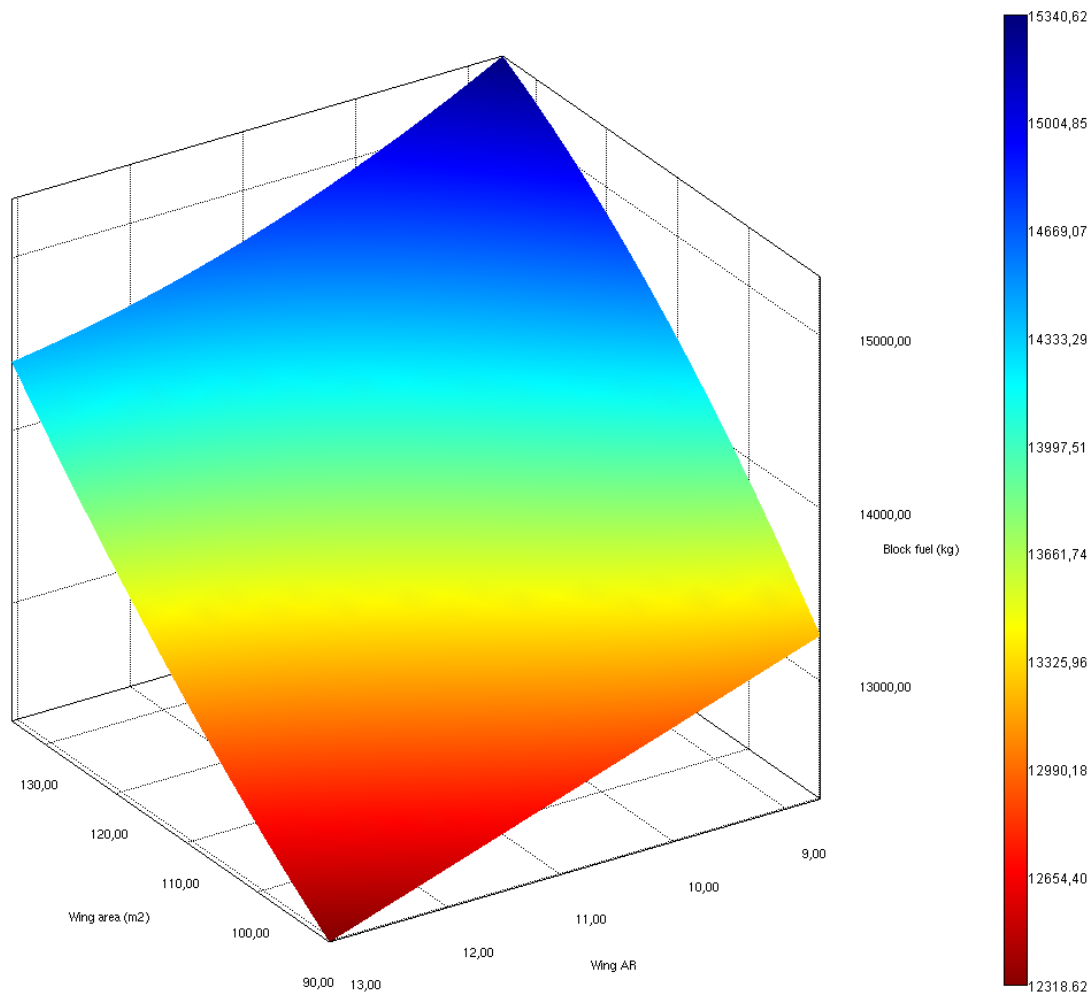


Figure 3.40 Example of JPAD DOE response surface

The core of the **JPAD** optimization module is based on well-known metaheuristics algorithms, among which the most commonly used are **GAs** and the **PSO** algorithms. The use of metaheuristics algorithms allows to easily manage complex optimization problems with a reduced amount of calculations if compared with classical deterministic algorithms (i.e. gradient based like Newton-Raphson). As explained in [110], gradient-based algorithms show some issues with discontinuous objective functions due to the use of derivatives to find the optimum solution.

On the other hand, metaheuristics algorithms do not rely on derivatives but only on objective function values, thus they can easily manage complex and even discontinuous response surfaces.

JPAD is provided with all the current state-of-the-art metaheuristic optimization algorithms thanks to the use of a dedicated external library named MOEA Framework [21]. Although the optimization module can use every algorithm provided by this library, two of them have been commonly used in recent research activities (e.g. **IRON** project) due to better results quality and computational efforts: ε -NSGAII (Non-dominated Sorting Genetic Algorithm) and OMOPSO (Optimized Multi-Objective Particle Swarm Optimization) algorithms are used.

As explained in Chapter 2, ε -NSGA-II is an extension of NSGA-II that uses an ε -dominance [111] archive and randomized restart to enhance search and find a diverse set of Pareto optimal solutions. Full details of this algorithm are given in [22].

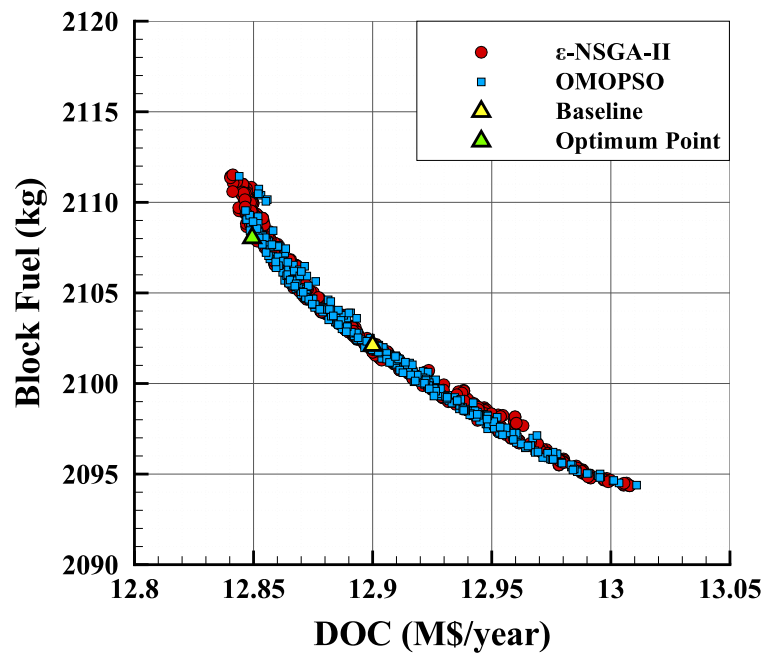


Figure 3.41 Example of JPAD output Pareto front in multi-objective optimizations [42]

OMOPSO is a multi-objective particle swarm optimization algorithm that includes an ϵ -dominance [111] archive to discover a diverse set of Pareto optimal solutions. OMOPSO was originally introduced in [23].

Using both these algorithms, the JPAD optimization module can easily solve complex MDAO problems reading all the following required instructions from a dedicated configuration file containing the following data.

- The number of design variables, objectives and constraints.
- Whether or not an objective has to be minimized or maximized.
- Upper and lower boundaries of the design variables.
- Constraints in terms of values and type of violating condition (i.e. outside an interval, bigger than a prescribed value, etc.).
- The algorithm to be used. The user can choose whichever approach he/she wants among the ones proposed in the MOEA Framework. Multiple selection is allowed to compare results.

Together with this information, the complete set of points of the response surface must be passed to the module as a .csv file. Before the optimization process, all response surface points are interpolated using radial basis function interpolation with a Gaussian radial basis function kernel and a constant shape parameter of 300 which has proven to be the best compromise in terms of interpolation accuracy [112]. The radial basis function interpolation process has been implemented by means of a dedicated Java library named **Statistical Machine Intelligence and Learning Engine (SMILE)** [113].

At the end of the process, charts of all possible combinations of Pareto fronts as well as a series of .csv files (one per algorithm) containing the complete set of optima values both for design variables and objectives are produced.

An example of Pareto front coming from the **JPAD** optimization module is shown in Figure 3.41. A detailed explanation concerning the definition of the Pareto front as well as how to approach a multi-objective optimization problem is proposed in [114].

3.4 Candidate's contribution to the development of JPAD

The **JPAD** software is the result of the efforts made in recent years by the **DAF** research group of the University of Naples Federico II. Its development involved several PhD students in a virtuous collaboration process, including the author of this thesis who has personally developed most of its modules.

Below the reader can find an overview of the development team as well as a detailed description of the contribution provided by the author of this thesis to the development of the **JPAD** software.

- **Fabrizio Nicolosi** - Associate professor at the University of Naples Federico II and professor of Aircraft Design and Flight Mechanics. Professor Nicolosi has followed the overall development of **JPAD** as coordinator of the **DAF** research group giving important feedbacks to the development team in terms of implemented methodologies and results.
- **Agostino De Marco** - Assistant professor of Flight Mechanics at University of Naples Federico II. Professor De Marco has guided the early stages of development of **JPAD** involving promising PhD students in the development team and making most of the initial choices in terms of programming language and software architecture.
- **Manuela Ruocco** - PhD student and member of the **DAF** research group. Her contribution to the **JPAD** software has been mainly focused on the development of the aerodynamic and stability module in which she implemented also some improved methodologies.
- **Vincenzo Cusati** - PhD student and member of the **DAF** research group. He has developed and implemented inside **JPAD** the **DOC** analysis module.
- **Mario Di Stasio** - PhD student and member of the **DAF** research group. His contribution to the **JPAD** software has been focused on the development of the **jpac-cad** module. Furthermore, together with the author of this thesis, he has collaborated in the development of the **jpac-commander** user interface.
- **Vittorio Trifari** - PhD student, author of this thesis and member of the **DAF** research group. Together with prof. De Marco he has guided the development of **JPAD** coordinating the work of the development team and implementing most of the software analysis modules. A detailed description of his contribution to the development of **JPAD** can be summarized in the following key points:
 - Definition, together with other development team members, of the main software architecture as well as of the input files structure.
 - Development of both **jpac-doe** and **jpac-optimizer** modules.
 - Development of the **jpac-commander** user interface.
 - Development of the following **jpac-core** modules: weights, balance and performance.
 - Enhancement of the balance analysis module related to the implementation of both aircraft inertias calculation and aircraft ground stability assessment.

List of publications involving the candidate and his contribution

- **Trifari V.**, Ruocco M., Cusati V., Nicolosi F., and De Marco A. «Java Framework for Parametric Aircraft Design – Ground Performance». In: *Aircraft Engineering and Aerospace Technology* 89.4 (2017), pp. 599–608. DOI: <http://dx.doi.org/10.1108/AEAT-11-2016-0209>.
 - Candidate's contribution is related the development of both take-off and landing calculation modules. Together with prof. De Marco, the candidate has defined the set of **ODE** used for the integration of aircraft equations of motion during the simulation. Furthermore, the candidate has personally developed the set of EventHandler needed to carry out the simulation.
- De Marco A., Cusati V., **Trifari V.**, Ruocco M., Nicolosi F., and Della Vecchia P. «A Java Toolchain of Programs for Aircraft Design». In: *6th CEAS Air and Space Conference (CEAS 2017)*. Elsevier Procedia, 2017. ISBN: 9781510858794.
 - Candidate's contribution is related to the performance assessment of the ATR-72 aircraft model shown in the case study as well as to the sensitivity analysis of the **FAR-25** take-off field length with respect to the wing loading and the thrust to weight ratio. In terms of software structure, the candidate is responsible for the development of the initial version of the **GUI** as well as of the performance analysis module. The input files structure definition is the result of the work of all authors.
- **Trifari V.**, Ruocco M., Cusati V., Nicolosi F., and De Marco A. «Multi-disciplinary analysis and optimization Java tool for aircraft design». In: *31st Congress of the International Council of the Aeronautical Sciences, ICAS 2018*. International Council of the Aeronautical Sciences, 2018. ISBN: 9783932182884.
 - Candidate's contribution is related to the development of both the parametric studies and the multi-objective optimization modules. Furthermore, the candidate has carried out the case study concerning the ATR-72 aircraft model.
- De Marco A., Di Stasio M., Della Vecchia P., **Trifari V.**, and Nicolosi F., and De Marco A. «Automatic modeling of aircraft external geometries for preliminary design workflows». In: *Aerospace Science and Technology* (2020). DOI: [10.1016/j.ast.2019.105667](https://doi.org/10.1016/j.ast.2019.105667).
 - Candidate's contribution is related to the enhancement of the **jpad-commander** and its application in order to estimate aircraft models generation times.

Chapter **4**

APPLICATIONS

Aeronautics was neither an industry nor a science. It was a miracle.

– Igor Sikorsky

In this final chapter the research question made at the beginning of this thesis work will be addressed and answered defining whether or not a modern high-capacity turboprop configuration could be a feasible solution to improve aircraft performance for regional transport applications, as well as which particular configuration will be the best for this task.

After showing the main outcomes of research activities carried out during the first two design loops of the **IRON** project, the use of a three-lifting surfaces high-capacity turboprop appears to be a good solution for reducing both block fuel and **DOC** with a little increment in flight time, however, as addressed in the thesis work developed by Vincenzo Cusati [107], more detailed numerical and experimental analyses have shown instability issues linked to the canard installation. The problem has been solved by changing the relative positions of tailplane and canard and by moving the engines at the tip of the tailplane. Furthermore, the canard position and geometry have been optimised in order to reduce the effects of its wake with respect to tailplane. Numerical analyses has also allowed to make an estimation of the canard installation effect in terms of overall downwash gradient acting on the horizontal tailplane. This has been used in the **MDAO** process of the three-lifting surfaces configuration considered in this thesis work.

In the comparison between different high-capacity turboprops and regional jets, the aircraft model assumed as reference regional jet platform has been the Airbus A220-300 (former Bombardier CS300) which represents the state-of-the-art of the current regional turbofan scenario. Differently from the reference regional jet used during the first two design loops of the **IRON** project, the concurrent development of the **JPAD** software has allowed to use, for this thesis work, a more detailed A220-300 aircraft model suitable for more reliable comparisons. In particular, from the participation of the **DAF** research group in another Clean Sky 2 project named **Aircraft Design and nOise RatiNg for regiOnal aircraft (ADORNO)**, together with the engine manufacturer MTU Aero Engines, the turbofan engine database used by the software **JPAD** has been refined by the author of this thesis, using the

GasTurb [115] software, to be as similar as possible to the real engine with a reduction of the first guess value of the **SFC** of about -6%.

To show the capabilities of the **JPAD** software as well as to provide a validation case, the next section of this chapter will be dedicated to the case study of the Airbus A220-330 aircraft model. Then, a set of **TLARs** suitable for modern high-capacity turboprop aircraft will be assessed and all generated turboprop models will be discussed. Finally, the **MDAO** process for each configuration will be described and the related results will be commented deriving, this way, the answer to research question of this thesis work.

4.1 Case study: Airbus A220-300

The Airbus A220-300 is a narrow-body, single-aisle, twin engine, medium-haul jet airliner, previously known as Bombardier CS300 which typical range values are around 3200nm [116]. It has been designed from ground-up and has been initially produced by Bombardier Aerospace but is currently operated by Airbus and built by **CSeries Aircraft Limited Partnership (CSALP)** joint venture. It belongs to the Airbus newly branded A220 family, in which the A220-100 (former Bombardier CS100) offers a smaller option. Figure 4.1 provides a 3-views representation of the A220 family.

It features 38.7m of overall length, a wingspan of 35.1m, and a total height of 11.5m. It can accommodate from 130 (in a 2-class configuration) to 160 passengers (single-class layout) with two-by-three seatings. This aircraft offers one of the highest overhead bin volume per passenger and one of the widest aisle [117].

Being a clean sheet design, the A220-300 features the latest generation flight deck, fly-by-wire, and a large use of composites (both for the fuselage and the wings, to the point that it has been nicknamed “the plastic airplane”) along with aluminum-lithium alloys, which help managing target operating weights [118].

It comes equipped with two Pratt & Whitney PurePower GTF engines, providing a static thrust (at SL, flat rated **ISA+15°C**) from 93.4kN (PW1521G) to 103.6kN (PW1524G) [119] [120].



Figure 4.1 A220 family (former Bombardier CSeries) 3-views

The use of **High By-Pass Ratio (HBPR)** geared turbofan engines, along with the aforementioned use of advanced materials and aerodynamic devices (such as winglets), allow for an improved saving on fuel (20% compared with A320neo and Boeing 737NG, according to Bombardier) and operating costs (12% with respect to the latest-generation competitors and 15% with respect to current market-leading models) [118].

A data summary concerning main geometric characteristics and the interior arrangements, maximum weights and capacities as well as details regarding installed engines characteristics have been reported from Table 4.1 to Table 4.3. These data have been retrieved from several public sources, mostly comprising technical documents provided by the manufacturer, official aircraft brochures and **European Aviation Safety Agency (EASA)** type-certificate data sheets. In particular, engine data reported in Table 4.3 have been used as starting point to model the PW1524G engine inside the GasTurb software [115].

The resulting database, in the form of an Excel file, has been made dimensionless and to comply with the data model described in the previous chapter. Each sheet of this database is related to an engine rating and provides information about the thrust ratio, the **SFC** and all available pollutant emission indexes as functions of altitude, Mach number, **ISA** deviation and throttle setting. An excerpt, taken from the **HBPR** database used for the A220-300 model, is provided in Figure 4.2 concerning the Take-off rating. Whenever a cell should be empty, a value of zero is considered.

Overall length	38.71 m
Overall height	11.5 m
Wingspan	35.1 m
Wing area	112.3 m ²
Fuselage diameter	3.7 m
Cockpit crew	2 pilots
Cabin crew	3 (minimum)
Passengers	130 (2-class) - 160 (full economy)
Seat configuration	2-3 (full economy)
Seat pitch	81.3 cm (full economy)
Seat width	47-48 cm (full economy)
Cargo volume	31.6 m ³
Cabin width	3.28 m
Cabin height	2.13 m

Table 4.1 A220-300 main geometrical data and interior arrangements [117] [116] [121].

MTOW	67585 kg
MLW	58740 kg
MZFW	55792 kg
OEW	37081 kg
Max Payload	18711 kg
Max Fuel mass	17726 kg

Table 4.2 A220-300 main weights data [116].

	PW1521G	PW1524G
Stages	1-GearBox-3-8-2-3	1-GearBox-3-8-2-3
BPR	12:1	12:1
Overall length	3.184 m	3.184 m
Diameter, fan tip	185.42 cm	185.42 cm
Dry mass	2177 kg	2177 kg
SL Static Thrust, Take-off	21970 lbf	24400 lbf
SL Static Thrust, Max Continuous	20760 lbf	23050 lbf
SL Static Thrust, Take-off Flat Rating	ISA+30°C	ISA+30°C
SL Static Thrust, Max Continuous Flat Rating	ISA+25°C	ISA+25°C
Max Permissible ITT, Take-off	1054°C	1054°C
Max Permissible ITT, Max Continuous	1006°C	1006°C
Max Permissible Low Pressure Spool Speed	10600 rpm	10600 rpm
Max Permissible High Pressure Spool Speed	24470 rpm	24470 rpm
Min Low-Pressure Spool Speed, Flight Idle	1991 rpm	1991 rpm
Min Low-Pressure Spool Speed, Ground Idle	1574 rpm	1574 rpm
Min High-Pressure Spool Speed, Flight Idle	13264 rpm	13264 rpm
Min High-Pressure Spool Speed, Ground Idle	13264 rpm	13264 rpm

Table 4.3 A220-300 main engines data [120] [122].

	A	B	C	D	E	F	G	H	I	J	K	L	M
1	Altitude	Mach	delta Temperature	Throttle Setting	T/TO	TSFC	EI NOx	EI CO	EI HC	EI soot	EI CO ₂	EI SOx	EI H ₂ O
2	ft	none	°C	none	none	lb/(lb*hr)	g/kg	g/kg	g/kg	g/kg	g/kg	g/kg	g/kg
3	0	0	0	0	1	1.000	0.244	22.409			3392.255		1250
4	0	0.1	0	0	1	0.872	0.281	22.670			3395.573		1250
5	0	0.15	0	0	1	0.820	0.301	22.901			3408.131		1250
6	0	0.2	0	0	1	0.774	0.321	23.235			3414.716		1250
7	0	0.25	0	0	1	0.735	0.342	23.357			3394.457		1250
8	1000	0	0	0	1	0.977	0.244	22.381			3411.484		1250
9	1000	0.1	0	0	1	0.853	0.281	22.466			3414.795		1250
10	1000	0.15	0	0	1	0.803	0.300	22.670			3408.959		1250
11	1000	0.2	0	0	1	0.759	0.320	22.474			3388.529		1250
12	1000	0.25	0	0	1	0.721	0.341	22.428			3359.203		1250
13	2000	0	0	0	1	0.956	0.244	21.976			3417.355		1250
14	2000	0.1	0	0	1	0.835	0.280	21.845			3396.938		1250
15	2000	0.15	0	0	1	0.786	0.300	21.905			3382.031		1250
16	2000	0.2	0	0	1	0.744	0.320	21.711			3356.946		1250
17	2000	0.25	0	0	1	0.707	0.340	21.640			3322.422		1250
18	3000	0	0	0	1	0.935	0.244	21.326			3389.433		1250
19	3000	0.1	0	0	1	0.818	0.280	21.195			3373.496		1250
20	3000	0.15	0	0	1	0.770	0.299	21.071			3353.645		1250
21	3000	0.2	0	0	1	0.729	0.319	20.880			3328.066		1250
22	3000	0.25	0	0	1	0.693	0.339	20.849			3293.373		1250
23	4000	0	0	0	1	0.912	0.244	20.448			3365.12		1250
24	4000	0.1	0	0	1	0.799	0.280	20.548			3349.315		1250
25	4000	0.15	0	0	1	0.753	0.299	20.392			3323.946		1250
26	4000	0.2	0	0	1	0.713	0.319	20.204			3298.057		1250

Figure 4.2 Excerpt of the JPAD HBPR engine database concerning the Take-off rating.

One sheet of the Excel file, the “Engine Info”, is related to two relevant parameters concerning the engine: the type of engine (turbofan, turboprop, piston, etc.) and the by-pass ratio (used only in case of turbofan engines). This latter is used as reference value when the user modifies the by-pass ratio parameter inside the engine configuration file (see Table 3.6). This allows to easily change the behavior, in terms of thrust and SFC, of a turbofan engine by means of a dedicated external database built up using thrust ratios and SFC curves (at different altitudes, Mach numbers and by-pass ratios) proposed in the book of Jenkinson [24].

Accommodation (typical)	135 pax (full economy)
Design range (typical)	3100 nm
TOFL (MTOW, ISA, SL, dry)	1890 m
LFL (MLW, ISA, SL, dry)	1509 m
BADA averaged climb speed (CAS)	271 kts
BADA averaged rate of climb	1642 ft/min
BADA maximum rate of climb	2862 ft/min
BADA averaged descent speed (CAS)	218 kts
BADA averaged rate of descent	2186 ft/min
BADA maximum rate of descent	3700 ft/min
Cruise Mach number (typical)	0.78
Cruise altitude (typical)	37000 ft
Max cruise Mach number at 37 kft	0.82
Max operating altitude	41000 ft
Alternate cruise range	200 nm
Alternate cruise altitude	20000 ft
Holding duration	30 min
Holding altitude	1500 ft
Fuel reserve	5%

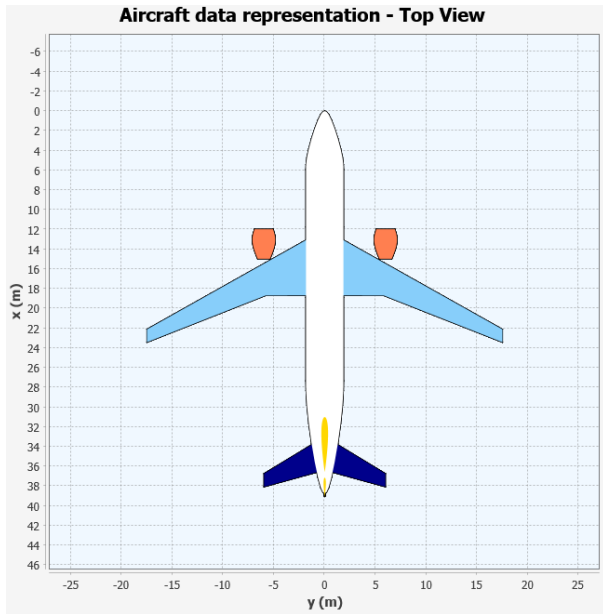
Table 4.4 A220-300 TLARs.

In addition to these data, the **Base of Aircraft Data (BADA)** database, described in [123], provides useful information to make some assumptions concerning the TLARs of the A220-300. In particular, regarding aircraft performance such as rate of climb and descent (as well as related calibrated airspeeds), BADA does not directly provide information related to the A220-300, however it redirects to the Airbus A318-112 which has been used to retrieve those unknown data. Furthermore, rates of climb (along with calibrated airspeeds) are provided at three main aircraft weight conditions (low, medium, and high) among which the high weight (68000kg) has been selected as reference condition.

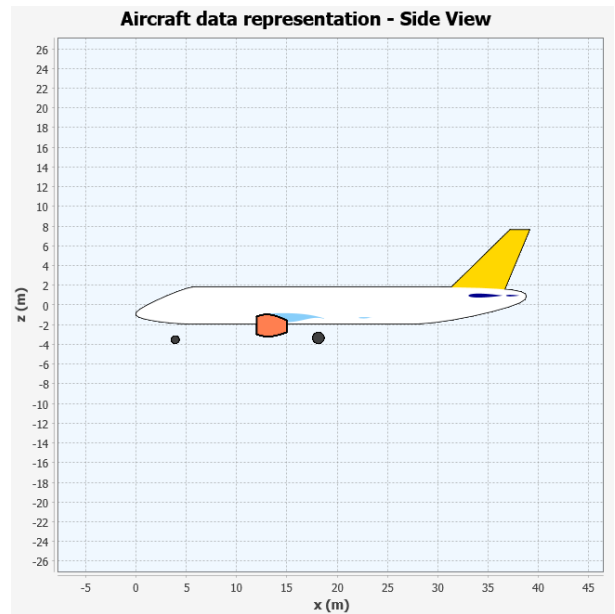
Gathering the above-mentioned information from all cited public sources, the set of TLARs reported in Table 4.4 has been produced. This, together with weights data in Table 4.2 has been used as starting point in the configuration of each JPAD analysis input file.

The first step of this case study concerns the generation of the aircraft parametric model to be used as baseline for the multi-disciplinary analysis process. Beside main geometrical data reported in Table 4.1 and engine data reported in Table 4.3, most of the parameter values, described in the previous chapter, needed to define the aircraft parametric model have been derived directly from the A220-330 3-view representation available in [116] via digitalization. The cabin layout has been modeled taking as reference the seat map presented in [116], while data concerning airfoils have been taken from [124] considering the SC(2)-0714 as root and kink stations airfoil and the SC(2)-0710 as tip airfoil.

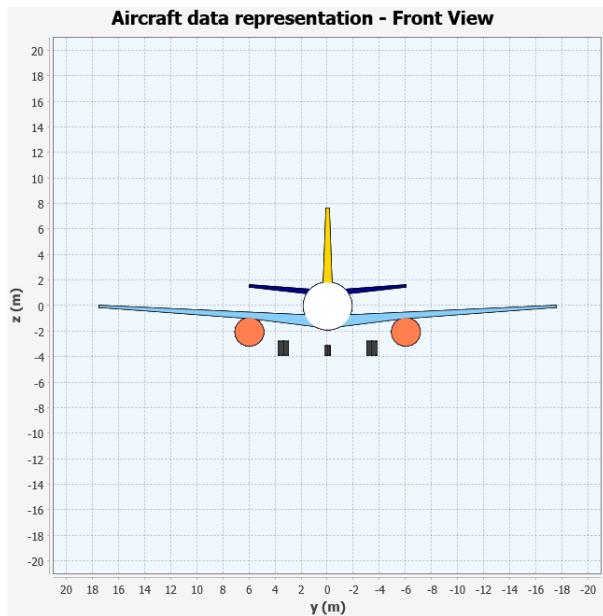
The resulting aircraft model is shown in Figure 4.3 where the 3-views, together with the related CAD model, have been collected. In addition, Figure 4.4 shows the generated seat map compared with the one reported in [116]. Finally, Figure 4.5, Figure 4.6 and Figure 4.7 provide a visual representation of each lifting surface, including its movables, compared with excerpts coming from [116].



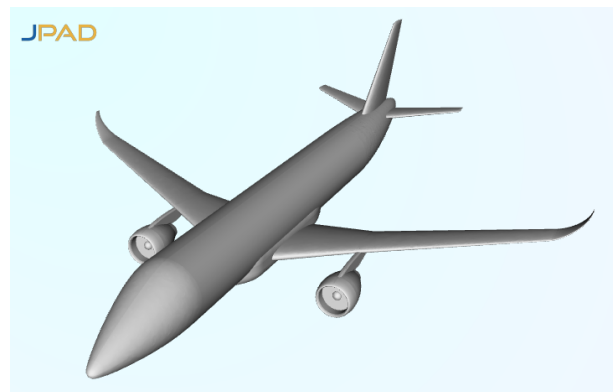
(a) Top view



(b) Side view

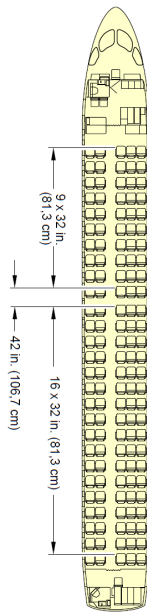


(c) Front view

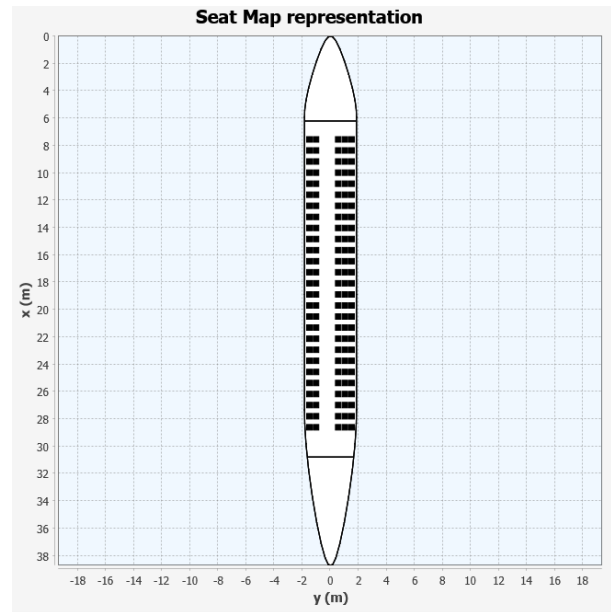


(d) CAD model

Figure 4.3 A220-300 3-view and CAD model representation made by JPAD

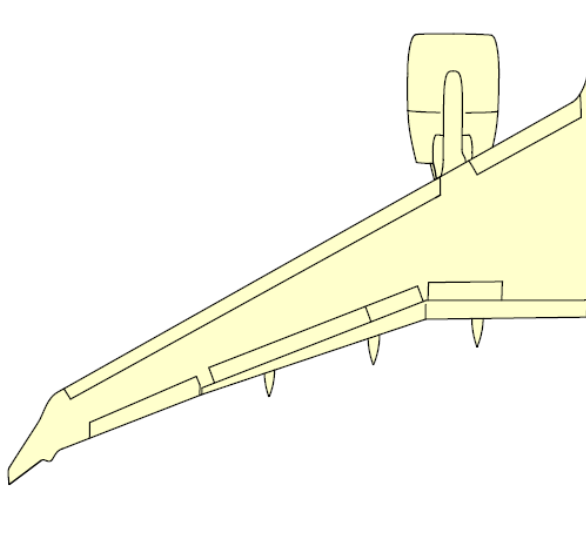


(a) A220-300 seat map [116]

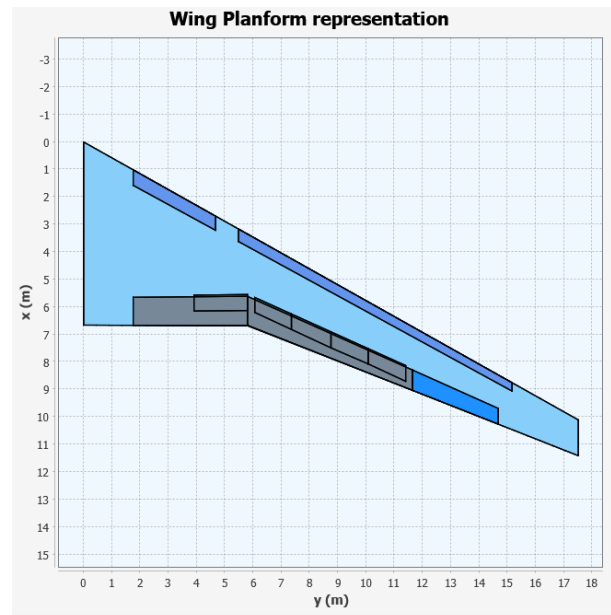


(b) A220-300 seat map - JPAD

Figure 4.4 Seat maps comparison between the A220-300 [116] and the JPAD parametric model.

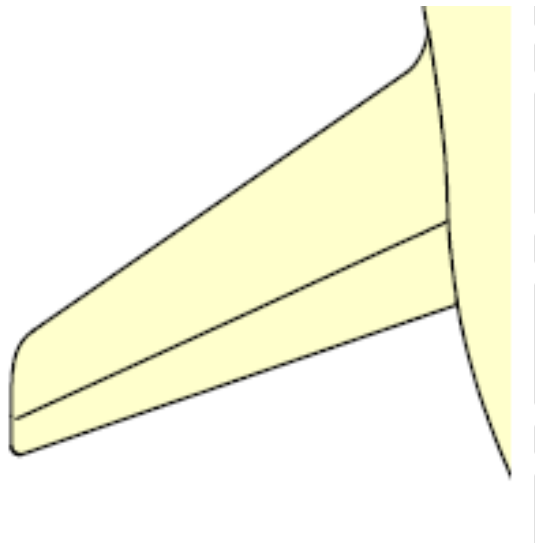


(a) A220-300 wing [116]

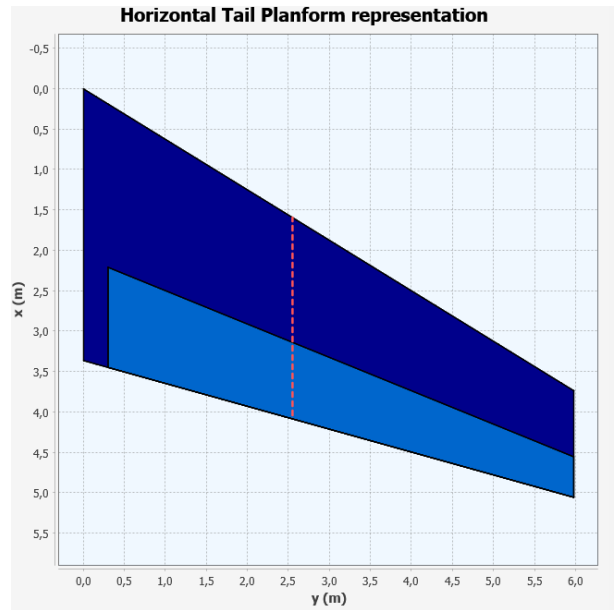


(b) A220-300 wing - JPAD

Figure 4.5 Comparison between the A220-300 wing [116] and the JPAD wing. It must be noted that JPAD does not take into account the fowler flap retraction inside the wing in terms of representation.

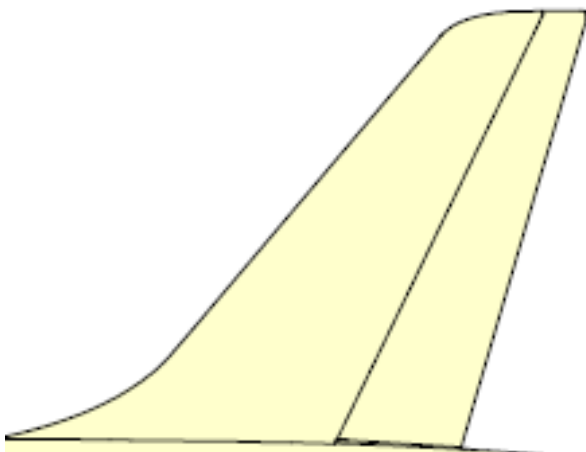


(a) A220-300 horizontal tail [116]

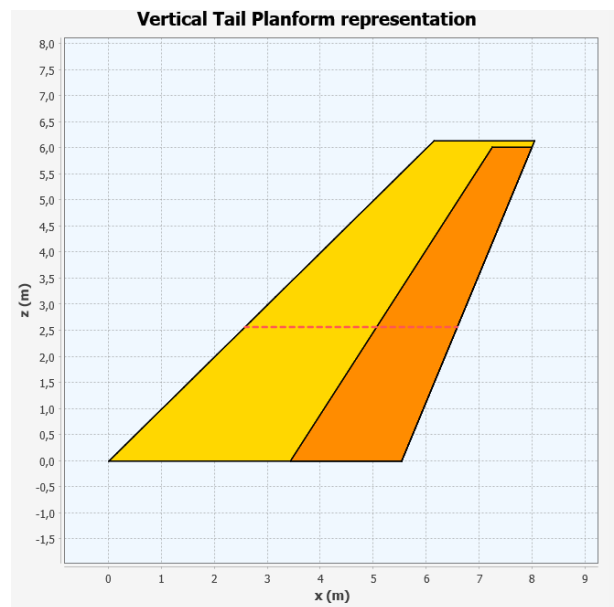


(b) A220-300 horizontal tail - JPAD

Figure 4.6 Comparison between the A220-300 horizontal tail [116] and the JPAD horizontal tail.



(a) A220-300 vertical tail [116]



(b) A220-300 vertical tail - JPAD

Figure 4.7 Comparison between the A220-300 vertical tail [116] and the JPAD vertical tail.

Once the aircraft model has been created, the second step of this case study is related to the configuration of each analysis input file needed to perform a complete multi-disciplinary analysis process involving all disciplines reported in Figure 3.5.

The main goal of this analysis is to match, as good as possible, the set of **TLARs** reported in Table 4.4. Thus, to comply with the design range of 3100nm, the iterative loop concerning the mission fuel has been activated. This has provided for slightly different values of **MTOW** and **OEW** with respect to the real ones reported in Table 4.2 with consequent little modifications in terms of balance, aerodynamics, stability and final performance.

Before commenting on some of the most important results of the multi-disciplinary analysis process, a review of all input data used to carry out this task is provided in Table 4.5 to Table 4.11.

It must be noted that the throttle setting reported in the operating condition input file (see Table 4.6) is the one related to the specific engine rating used in that particular mission phase. For example, a throttle setting of 70% in cruise makes **JPAD** to interpolate the Excel engine database at a throttle equal to the desired one (if available). However, in this case, 70% does not stand for the 70% of the maximum available thrust of the engine (static thrust) but the 70% of the maximum thrust deliverable for that particular rating (in this case cruise).

Concerning weight and balance analyses, the “Average” method stands for the mean value of all available methodologies implemented inside **JPAD** and cited in the previous chapter. No calibration factors have been used for both these analyses. Systems position, as well, have been calculated using the approach proposed in Chapter 3.

Moving on to the aerodynamic and stability analysis, the drag increment in take-off and landing due to landing gears has been estimated as proposed in the method by Torenbeek [25] which is based on frontal wheels areas of nose and main gears and takes into account for the angle of attack as a well as for the flap deflection (if the main landing gear is mounted on the wing). Furthermore, a calibration factor of 0.4 has been used to reduce the drag coefficient coming from excrescences, interferences and coolings in order to account for aerodynamic improvements of this clean-sheet aircraft with respect to old semi-empirical estimations. More details concerning the aerodynamic and stability module and the related implemented methodologies (e.g. horizontal and vertical tails dynamic pressure ratios or elevator and rudder effectiveness) can be found in the PhD thesis by Manuela Ruocco [92].

In terms of trimmed lift curves and downwash angle, the improved methodologies proposed in [92] have been used to consider the effect provided by airfoils non-linear lift curves on the overall wing lift distribution, as well as the effect provided by a non-linear downwash angle on the horizontal tail. On the other hand, the trimmed drag polar curve in each condition has been obtained using the classical parabolic approach in which the parasite drag coefficient of each component has been estimated as proposed in [24] and the Oswald factor has been calculated using the method by Scholz reported in [125]. Furthermore, the drag increment due to flap deflections has been estimated according to [126].

For the performance analysis, typical simulations parameters have been used for take-off, landing and noise trajectories analyses as well as other parameters coming from the **FAR**. Data from Table 4.4 have been used to fill most of the parameter values related to climb, descent and mission profile analyses. No calibration factors have been used for engine thrust, **SFC** and pollutant emission indexes being the engine database already adjusted and approved within the **ADORNO** project.

Finally, dealing with costs, a description of the main input parameters needed to perform the analysis, as well as a summary of all calculation methods references, is provided in the PhD thesis by Vincenzo Cusati [107] while typical values for most of these latter can be found in the books by Kundu [127], Sforza [15] and Jenkinson [24] (e.g. utilization, spare costs, typical life span, insurance, interests and typical labour rates). In addition, fuel price has been assumed according to IATA fuel price monitor [128], while aircraft price and engine unit cost have been derived from [129] and [130] respectively.

Input data	Value
Positive limit load factor	2.5
Negative limit load factor	1.0
Mission fuel iterative loop	TRUE
Components weight and center of gravity method	Average

Table 4.5 Main input data concerning the analysis configuration file of JPAD.

Input data	Take-off	Climb	Cruise	Landing
Reference altitude	0ft	37000ft	37000ft	0ft
Reference Mach number	0.2	0.4	0.78	0.172
ISA deviation	0°C	0°C	0°C	0°C
Throttle setting for database	100%	100%	100%	100%
Flaps deflection	15°	0°	0°	35°
Slats deflection	10°	0°	0°	25°

Table 4.6 Main input data concerning the operating conditions configuration file of JPAD.

Input data	Value
Reference MTOW	67585kg
MLW to MTOW ratio	0.85
Overall single passenger mass	103kg
Design cruise altitude	37000ft
Design cruise Mach number	0.78
Max payload	18711kg
Reference mission fuel mass	16700kg
Components masses calibration factors	1.0

Table 4.7 Main input data concerning the weights analysis configuration file of JPAD.

Input data	Value
Include systems and estimate systems position	TRUE
Components centers of gravity calibration factors	1.0

Table 4.8 Main input data concerning the balance analysis configuration file of JPAD.

Input data	Take-off	Climb	Cruise	Landing
Alpha body range	$-4^{\circ} \div 17^{\circ}$	$-4^{\circ} \div 17^{\circ}$	$-4^{\circ} \div 9^{\circ}$	$-4^{\circ} \div 12^{\circ}$
Beta range	$0^{\circ} \div 20^{\circ}$	$0^{\circ} \div 20^{\circ}$	$0^{\circ} \div 20^{\circ}$	$0^{\circ} \div 20^{\circ}$
Elevator deflection range	$-30^{\circ} \div 10^{\circ}$	$-30^{\circ} \div 10^{\circ}$	$-30^{\circ} \div 10^{\circ}$	$-30^{\circ} \div 10^{\circ}$
Rudder deflection range	$5^{\circ} \div 30^{\circ}$	$5^{\circ} \div 30^{\circ}$	$5^{\circ} \div 30^{\circ}$	$5^{\circ} \div 30^{\circ}$
Lifting surfaces momentum pole (% MAC)	0.25	0.25	0.25	0.25
Fuselage momentum pole (% fuselage length)	0.5	0.5	0.5	0.5
Tail planes dynamic pressure ratios	Calculated	Calculated	Calculated	Calculated
Elevator and rudder effectiveness (τ)	Calculated	Calculated	Calculated	Calculated
Trimmed lift curve α calibration factor	1.0	1.0	1.0	1.0
Trimmed lift curve C_L calibration factor	1.0	1.0	1.0	1.0
Landing gears drag increment	Calculated	Calculated	Calculated	Calculated
Landing gears drag increment calibration factor	1.0	1.0	1.0	1.0
Excrescences drag increment calibration factor	0.4	0.4	0.4	0.4
Coolings drag increment calibration factor	0.4	0.4	0.4	0.4
Interferences drag increment calibration factor	0.4	0.4	0.4	0.4
Trimmed drag polar curve C_D calibration factor	1.0	1.0	1.0	1.0
Trimmed drag polar curve C_D calibration offset	0.0	0.0	0.0	0.0

Table 4.9 Main input data concerning the aerodynamic and stability analysis configuration files of JPAD.

Table 4.10 Main input data concerning the performance analysis configuration file of JPAD.

Input data	Value
Take-off	
V_w	0 m/s
μ	0.025
μ_b	0.4
dt_{Hold}	0.5 s
α_g	0°
$h_{obstacle}$	35 ft
k_{Rot}	1.05
$\dot{\alpha}_0$	$3^{\circ}/s$
k_{CLmax}	0.8
$k_{DragOEI}$	0.0050
k_{α}	0.04
Climb	
$k_{weightAEO}$	1.0
$k_{weightOEI}$	0.97
h_{in}	1500 ft
h_{end}	37000 ft
$V_{climbCAS}$	271 kts

Continuation of Table 4.10

Input data	Value
Cruise	
$k_{CRweight}$	0.9
$altitudes$	[20 kft, 25 kft, 37 kft]
M_{MO}	0.82
Descent	
$k_{DESCweight}$	0.9
h_{in}	3700 ft
h_{end}	1500 ft
$V_{descentCAS}$	218 kts
RD	2186 ft/min
Landing	
Type	Typical
V_w	0 m/s
μ	0.025
μ_b	0.4
$k_{LNDweight}$	0.85
$h_{LNDstart}$	1500 ft
$h_{obstacle}$	50 ft
k_{Rot}	1.05
$\gamma_{approach}$	-3 °
k_{CLmax}	0.9
$k_{Approach}$	1.23
k_{Flare}	1.19
$k_{Touchdown}$	1.15
Take-off noise trajectories	
X_{end}	8000 m
$h_{cutback}$	300 m
$dt_{retraction}$	12 s
$dt_{cutback}$	4 s
Landing noise trajectories	
h_{in}	4000 ft
$\gamma_{descent}$	-3 °
Mission profile and Payload-Range	
$R_{mission}$	3100 nm
$R_{alternate}$	200 nm
$h_{alternate}$	20000 ft

Continuation of Table 4.10

Input data	Value
$M_{alternate}$	Calculated
$t_{holding}$	30 min
$h_{holding}$	1500 ft
$M_{holding}$	Calculated
$f_{reserve}$	5%
V-n diagram	
$C_{Lmax_{inv}}$	-1.0
Calibration factors	
Thrust, SFC and pollutant emission indexes calibration factors	1.0
End of Table 4.10	

Input data	Value
Utilization	Calculated [127]
Capital DOC	
Life span	16 years
Residual value (% initial value)	10%
Aircraft price	91.5 mln\$
Aircraft and engines relative spare costs	0.1
Interests (%total investments)	5.4%
Insurance (% of airframe + engine prices)	0.5%
Crew DOC	
Cabin crew labour rate	90 \$/h
Cockpit crew labour rate	360 \$/h
Fuel DOC	
Unit price	82.16 \$/barrel
Charges DOC	
Landing, navigation and ground handling charges	Calculated [127]
Maintenance DOC	
Airframe and engines labour rate	40 \$/h
Engines total price	24 mln\$

Table 4.11 Main input data concerning the costs analysis configuration file of JPAD.

The first discipline investigated by the JPAD multi-disciplinary analysis process concerns the weights. Table 4.12 reports main weights analysis output data compared with A220-300 weights coming from Table 4.2 (when available), while Figure 4.8 provides a visual representation of the component weights breakdown.

Output data	JPAD	A220-330 (Table 4.2)	Difference (%)
MTOW	66911 kg	67585 kg	-1.00%
MLW	56875 kg	58740 kg	-3.18%
Max fuel mass	17233 kg	17726 kg	-2.78%
Design mission fuel mass	16660 kg	-	-
MZFW	55017 kg	55792 kg	-1.39%
Max payload	18711 kg	18711 kg	0%
Design payload	13964 kg	-	-
OEW	36306 kg	37081	-2.09%
Trapped fuel and oil mass	335 kg	-	-
Crew mass	483 kg	-	-
Operating items mass	2021 kg	-	-
MEW	30166 kg	-	-
Structural mass	19637 kg	-	-

Table 4.12 Main output data concerning the JPAD weights analysis of the A220-300 parametric model.

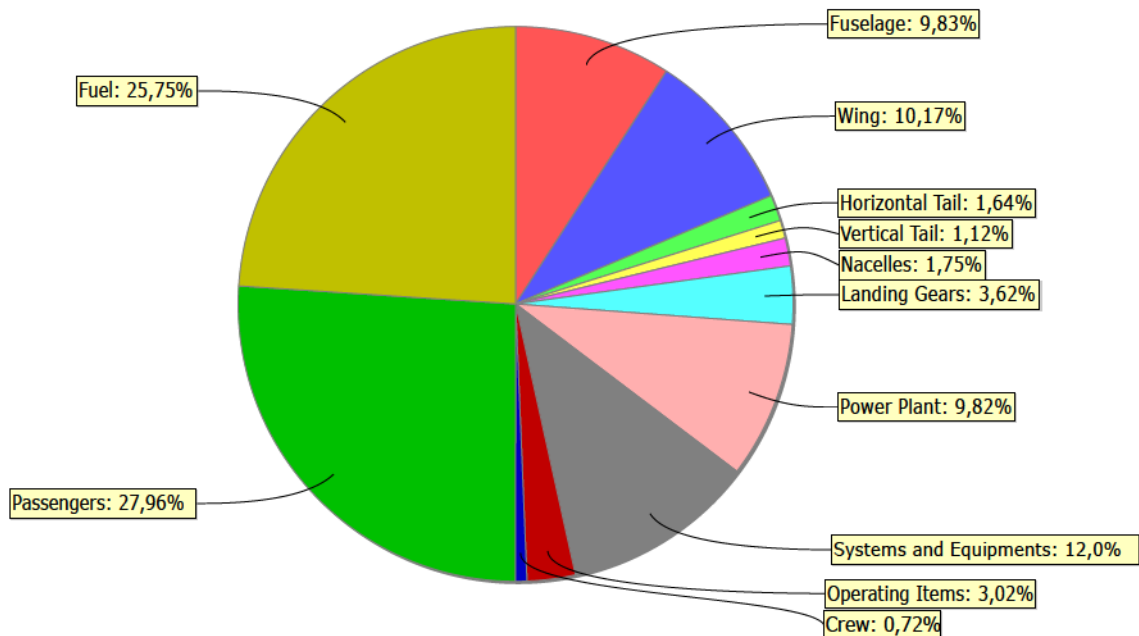


Figure 4.8 JPAD weights breakdown of the A220-300 parametric model.

Although with a tendency to underestimate aircraft weights, JPAD estimations are quite good with a maximum difference between the calculated data and the declared A220-300 data always below 5% (without using any calibration factor).

Each component weight has been used as input for the balance analysis aiming at calculating the center of gravity excursion of the parametric model under investigation as well as to ensure that all ground stability checks, described in Chapter 3, have passed. In particular, main landing gear legs lengths have been derived from a rotation angle of about 12° . Using all components masses and center of gravity positions, inertia moments and products have been calculated. A summary of the main results of the balance analysis is provided in Table 4.13, while Figure 4.9 and Figure 4.10 show the calculated boarding diagram as well as a visual representation of each component center of gravity on the side view of the A220-300 parametric model. It must be noted that the estimated center of gravity excursion ($11.15\% \div 34.57\%$ of the **MAC**) is in line with the one reported in [131] ($12.0\% \div 37.0\%$ **MAC**).

Results of all ground stability analyses are shown from Figure 4.11 to Figure 4.14 proving the good modeling of both nose and main landing gears.

Output data	Value
OEW X_{CG} (BRF)	16.5 m
OEW Y_{CG} (BRF)	0.00 m
OEW Z_{CG} (BRF)	-0.69 m
OEW X_{CG} (%MAC)	18.91%
OEW Y_{CG} (%MAC)	0.0%
OEW Z_{CG} (%MAC)	-17.81%
MZFW X_{CG} (BRF)	16.89 m
MZFW Y_{CG} (BRF)	0.00 m
MZFW Z_{CG} (BRF)	-0.50 m
MZFW X_{CG} (%MAC)	28.96%
MZFW Y_{CG} (%MAC)	0.0%
MZFW Z_{CG} (%MAC)	-12.87%
MTOW X_{CG} (BRF)	16.74 m
MTOW Y_{CG} (BRF)	0.00 m
MTOW Z_{CG} (BRF)	-0.68 m
MTOW X_{CG} (%MAC)	24.96%
MTOW Y_{CG} (%MAC)	0.0%
MTOW Z_{CG} (%MAC)	-17.73%
Max forward X_{CG} (%MAC))	11.15%
Max afterward X_{CG} (%MAC))	34.57%
Operative X_{CG} (%MAC))	24.96%
Inertia moment I_{xx}	65759 kg·m ²
Inertia moment I_{yy}	1092378 kg·m ²
Inertia moment I_{zz}	1502199 kg·m ²
Inertia product I_{xy}	0 kg·m ²
Inertia product I_{yz}	0 kg·m ²
Inertia product I_{xz}	136509 kg·m ²

Table 4.13 Main output data concerning the **JPAD** balance analysis of the A220-300 parametric model.

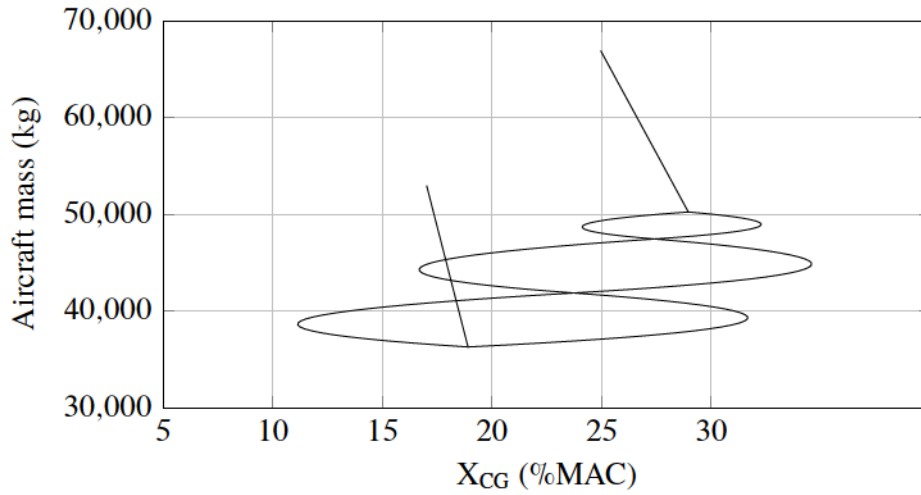


Figure 4.9 Boarding diagram of the A220-300 parametric model - JPAD. Max forward and max aftward limits are in line with the center of gravity envelope chart of the A220-300 reported in [131].

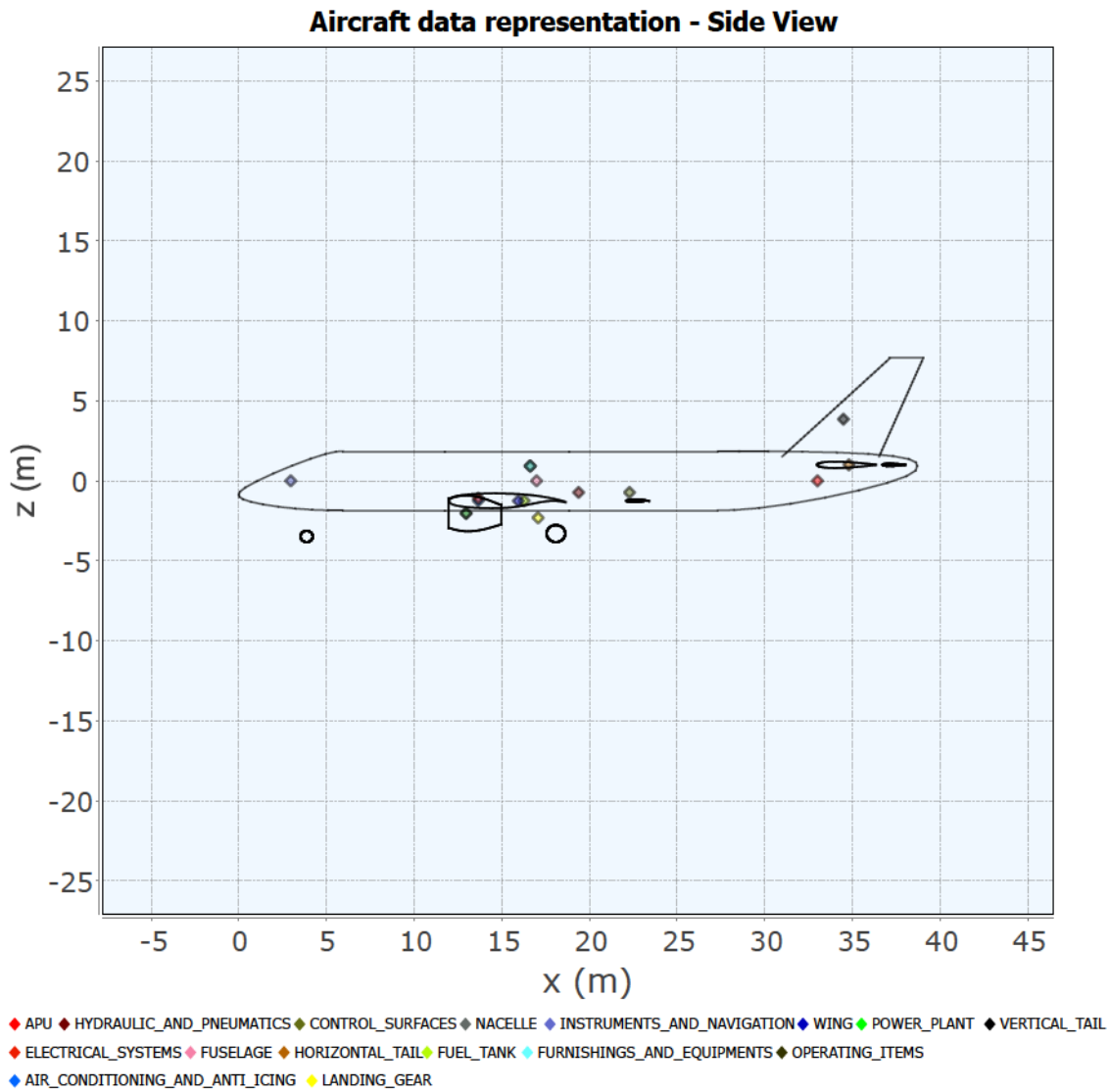


Figure 4.10 A220-300 parametric model side view with each component center of gravity - JPAD.

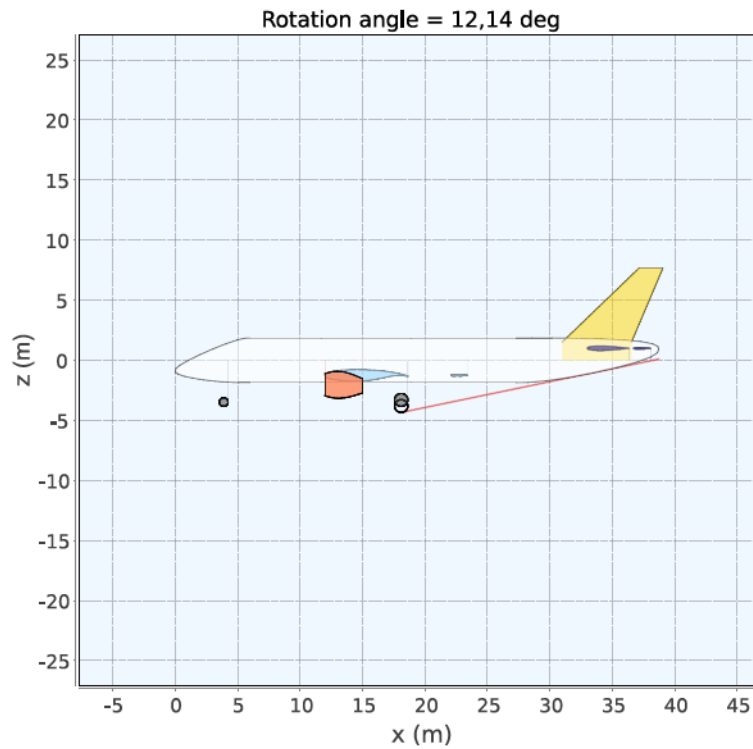


Figure 4.11 Take-off rotation angle check of the A220-300 parametric model - JPAD

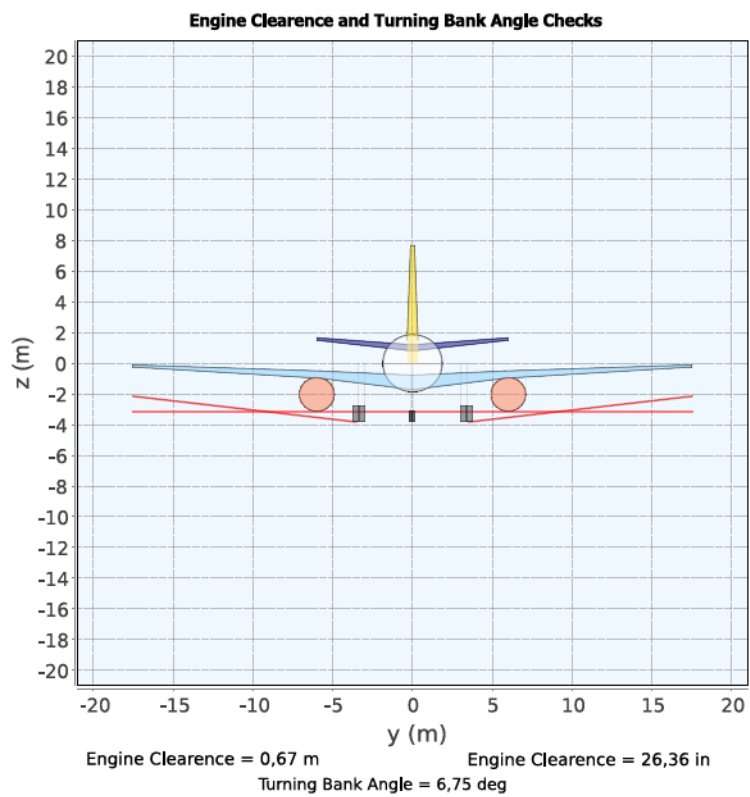


Figure 4.12 Limit ground bank angle and minimum engine clearance calculation of the A220-330 parametric model - JPAD

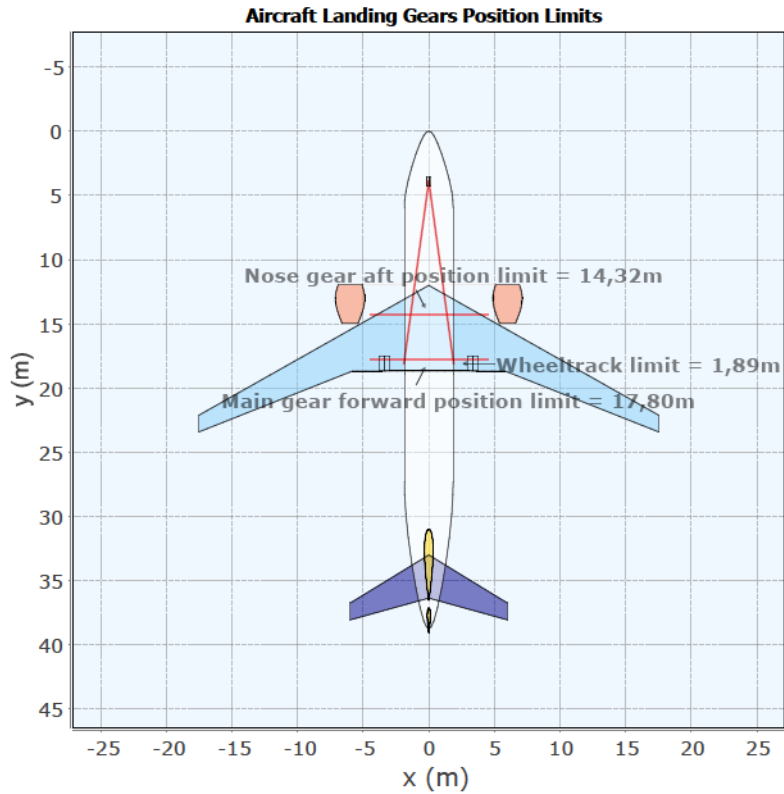


Figure 4.13 Nose and main gear position limits of the A220-300 parametric model - JPAD

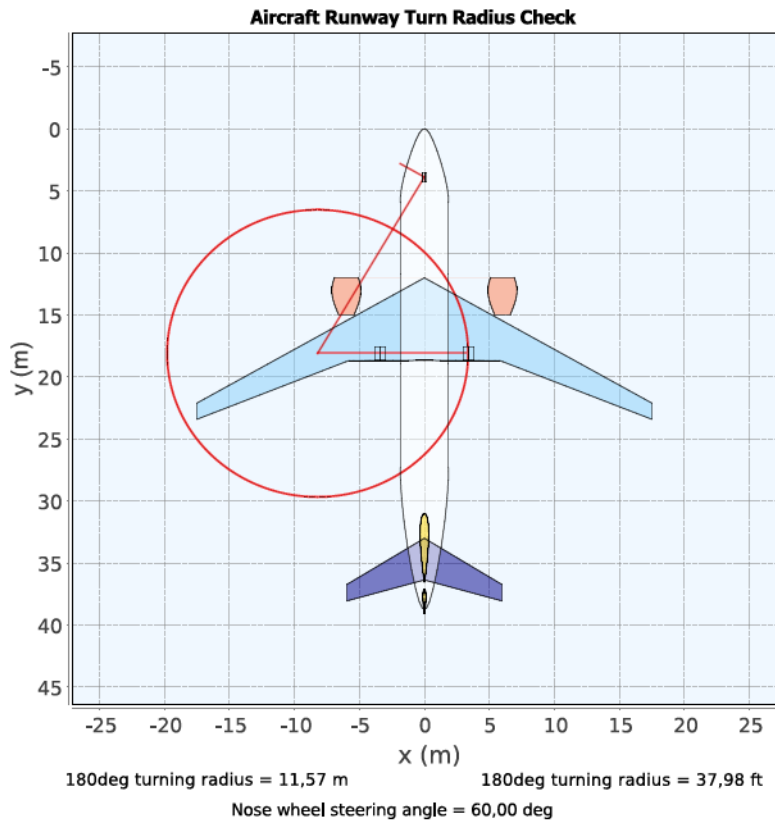


Figure 4.14 Turning radius calculation of the A220-300 parametric model - JPAD

Considering the case related to the maximum operational center of gravity position, a complete aerodynamic and stability analysis has been performed to calculate trimmed lift curves and trimmed drag polar curves needed by the performance manager of **JPAD** to carry out the overall performance assessment. A summary of the main aerodynamic and stability results is provided in Table 4.14. In addition, Table 4.14 reports also the value of the **Static Stability Margin (SSM)** at the most aft center of gravity position.

Beside numerical results, Figure 4.15, Figure 4.16 and Figure 4.17 show trimmed lift curves, trimmed drag polar curves and trimmed aerodynamic efficiency curves calculated at each operating condition reported in Table 4.6.

$X_{CG}/c = 24.96\%$				
	Take-off	Climb	Cruise	Landing
$C_{L\alpha}$ ($1/^\circ$)	0.108	0.106	0.127	0.09
C_{L0}	1.16	0.44	0.55	1.98
C_{Lmax}	2.37	1.51	1.3	2.89
C_{D0}	0.0376	0.0227	0.0204	0.0671
Neutral point (%MAC)	52.8%	58.2%	60.4%	54.2%
SSM	-27.9%	-33.2%	-35.4%	-29.3%
Max Efficiency	15.36	16.97	17.48	10.18
SSM at max aft X_{CG}	-17.2%	-22.4%	-24.6%	-18.4%

Table 4.14 Main output data concerning the **JPAD** aerodynamic and stability analysis of the A220-300.

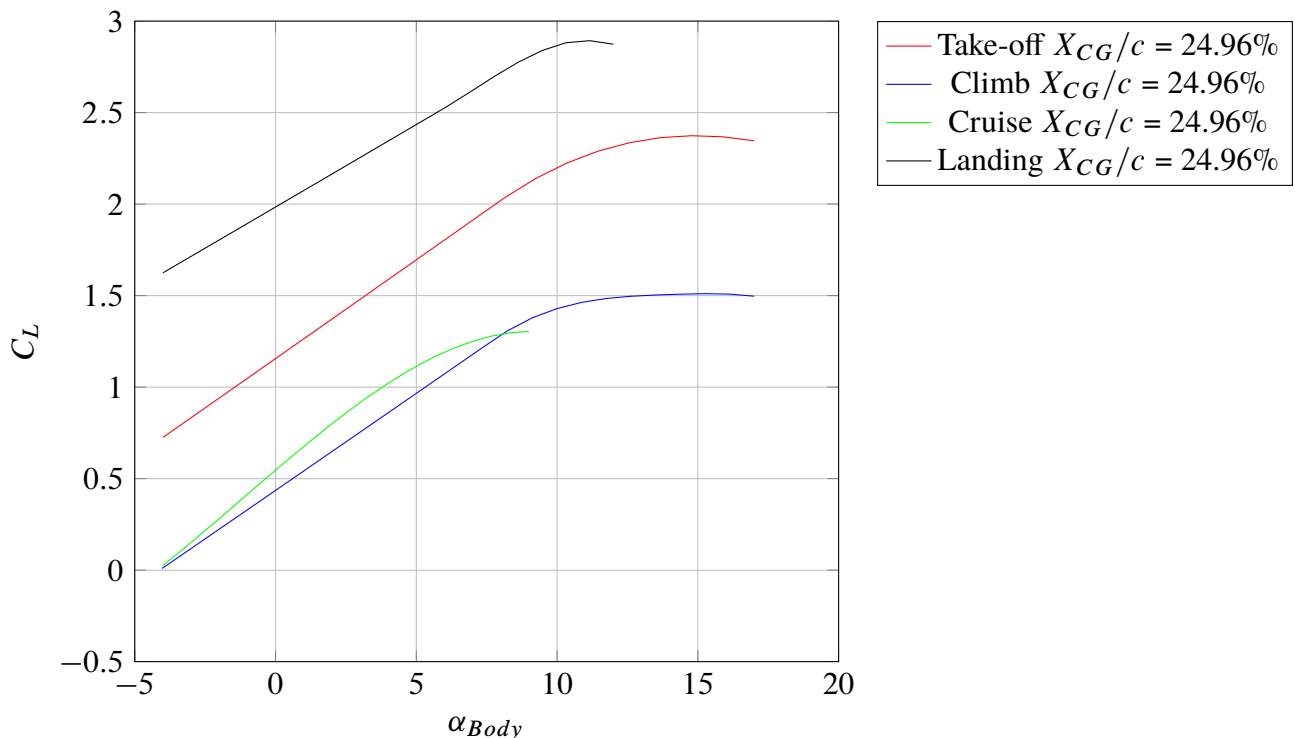


Figure 4.15 A220-300 lift curves in all operating conditions at max. aft and operative CG positions - **JPAD**

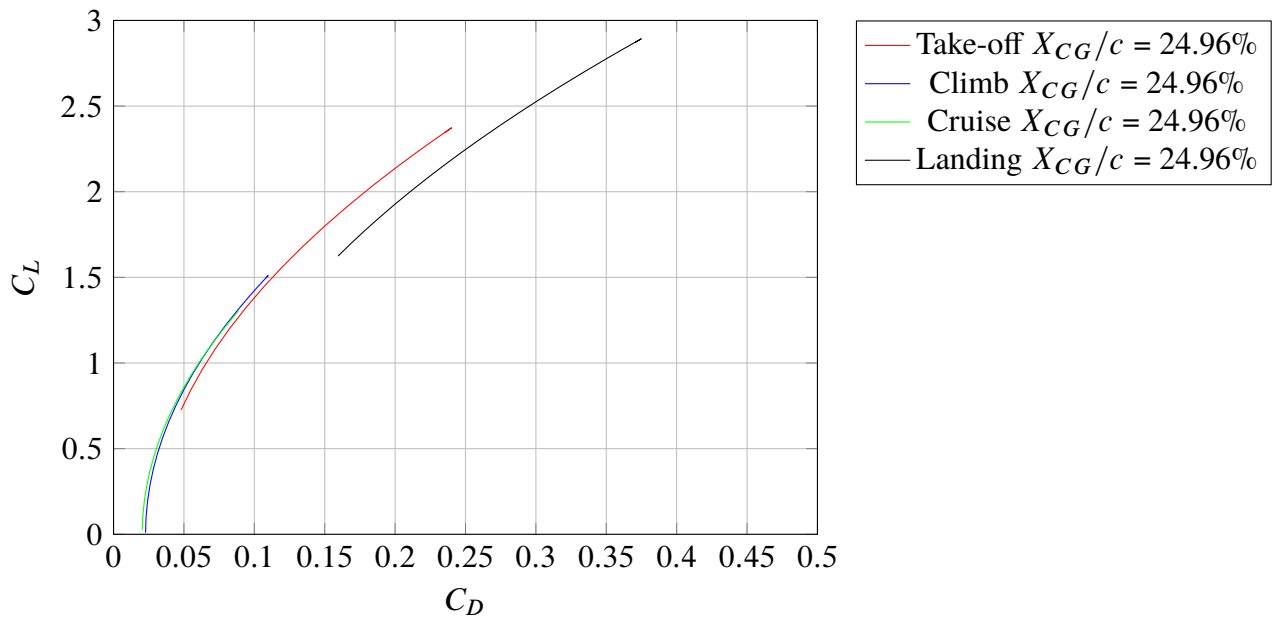


Figure 4.16 A220-300 drag polar curves in all operating conditions at max. aft and operative CG positions - JPAD

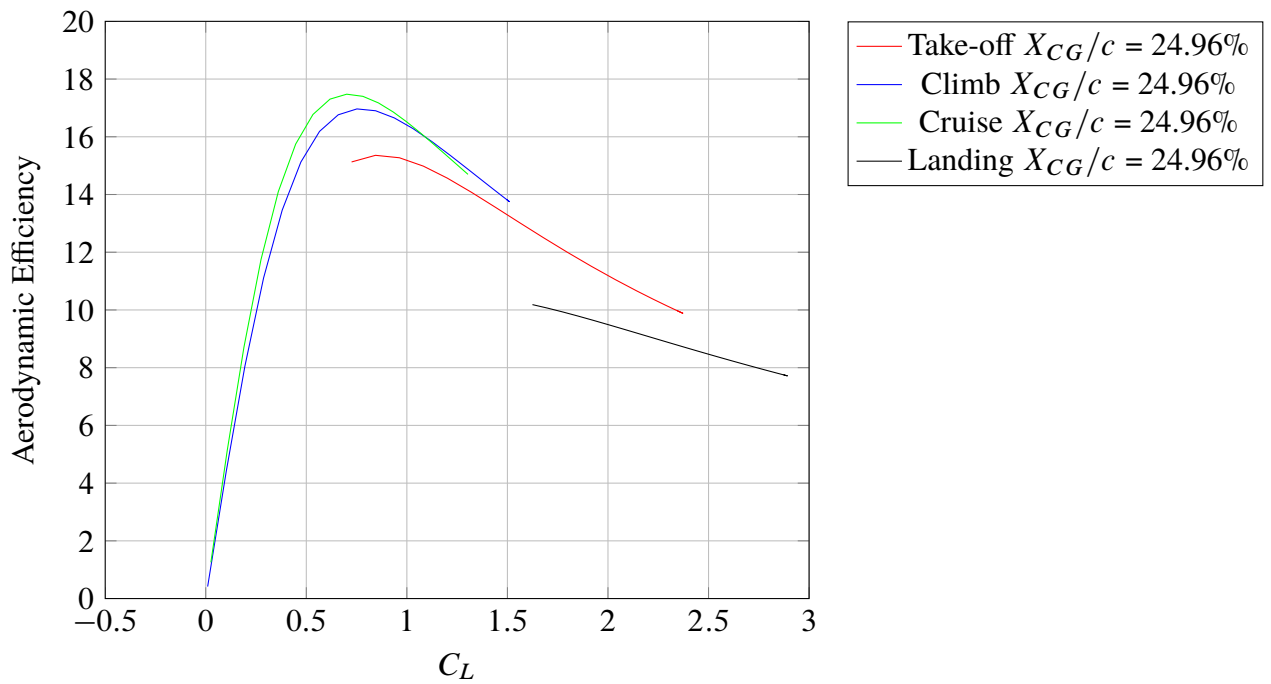


Figure 4.17 A220-300 aerodynamic efficiency curves in all operating conditions at max. aft and operative CG positions - JPAD

At this point, drag polar curves and lift curves related to the operational center of gravity position have been used as input data for the **JPAD** performance manager together with all calculated weights reported in Table 4.8 as well as the engine database described previously.

In the scope of this case study, only the most important performance results will be shown and commented in order to make a comparison with public available data concerning the A220-300. This to show the level of accuracy reached by **JPAD** for a typical transport aircraft model.

In terms of take-off, Table 4.15 reports a summary of the simulation output while Figure 4.18 illustrates the calculation of the balanced field length and the decision speed (V_1). Furthermore, Figure 4.19 shows the evolution of normalized rotation speed ($V_{Rot}/V_{s,TO}$), as well as the take-off safety speed ($V_2/V_{s,TO}$), with increasing normalized engine failure speeds ($V_{EF}/V_{s,TO}$). As can be seen, the value of $V_2/V_{s,TO}$ is always above (or equal to) the minimum value of 1.13, with respect to the take-off stall speed imposed by **FAR**.

In contrast to the input rotation speed reported in Table 4.10, a value of 1.09 times the take-off stall speed has been calculated by **JPAD** to comply with the minimum value of the $V_2/V_{s,TO}$ ratio of 1.13 in **OEI** condition.

The calculated **BFL** of 1814 m is in line with the expected value of 1890 m reported in Table 4.4 with a difference of about 4%.

Output	Value
Ground roll distance	1059 m
Rotation distance	231 m
Airborne distance	184 m
AEO take-off distance	1474 m
FAR-25 take-off distance (take-off distance times 1.15)	1695 m
BFL	1814 m
V_{MC}	53.31 m/s
$V_{s,TO}$	63.41 m/s
V_1	62.81 m/s
V_{Rot}	69.31 m/s
V_{LO}	75.01 m/s
V_2	77.65 m/s
$V_{MC}/V_{s,TO}$	0.84
$V_1/V_{s,TO}$	0.99
$V_{Rot}/V_{s,TO}$	1.09
$V_{LO}/V_{s,TO}$	1.18
$V_2/V_{s,TO}$	1.22
Take-off duration	35 s
Fuel used for take-off	50.9 kg
Take-off NO_x emissions	1.17 kg
Take-off CO_2 emissions	171.65 kg
Take-off H_2O emissions	63.07 kg

Table 4.15 Main output data concerning the **JPAD** take-off simulation of the A220-300.

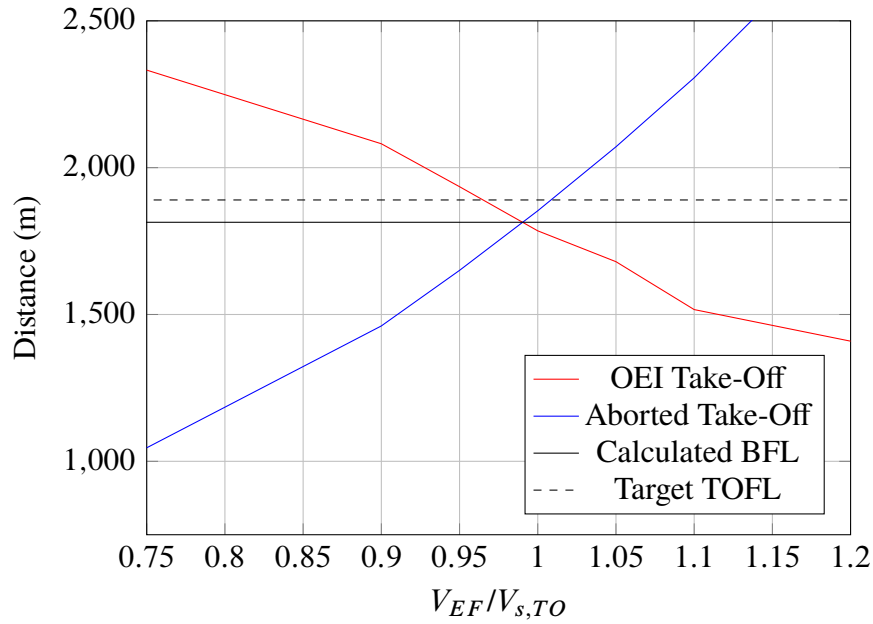


Figure 4.18 A220-300 balanced field length and decision speed calculation - JPAD

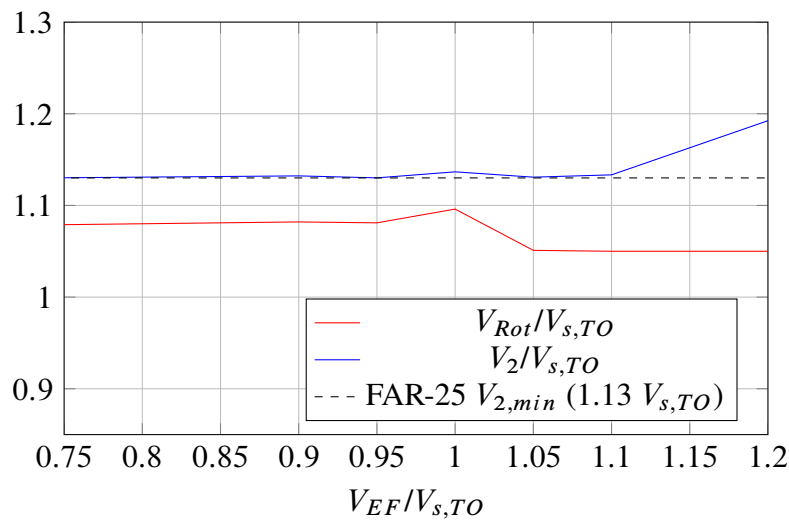


Figure 4.19 A220-300 take-off rotation speed and take-off safety speed evolution with engine failure speed - JPAD

The AEO climb analysis of the A220-300 parametric model highlights an absolute ceiling and a service ceiling of 13036 m (42768 ft) and 12808 m (42021 ft) respectively with a time to climb, up to the cruise altitude of 11278 m (37000ft), equal to: 17 minutes in case of an averaged calibrated climb speed of 271 kts; 16 minutes in case of the best rate of climb speed for each altitude. The same analysis, carried out in OEI condition, provides for values of both absolute ceiling and service ceiling of 6316 m (20721 ft) and 6196 m (20327 ft) respectively. Results of both AEO and OEI climb analyses are reported in Table 4.16, while Figure 4.20 to Figure 4.23 show the evolution, both in AEO and OEI conditions, of the rate of climb and the climb angle with aircraft calibrated airspeed at several altitudes from 1500 ft up to 37000 ft. In addition, Figure 4.25 gathers all maximum rates of climb values for each altitude, providing a way to visually estimate both absolute and service ceilings reported in Table 4.16. Finally, Figure 4.24 illustrates the evolution of the climb time with the altitude.

Output	Value
AEO absolute ceiling	13036 m (42768 ft)
AEO service ceiling	12808 m (42021 ft)
OEI absolute ceiling	6316 m (20721 ft)
OEI service ceiling	6196 m (20327 ft)
Minimum time to climb (1500ft-37000ft)	16 min
Time to climb at average climb speed (1500ft-37000ft)	17 min
Fuel used for climb	930 kg
Climb NO _x emissions	17.50 kg
Climb CO ₂ emissions	2538.50 kg
Climb H ₂ O emissions	1003.51 kg

Table 4.16 Main output data concerning the JPAD climb analysis of the A220-300.

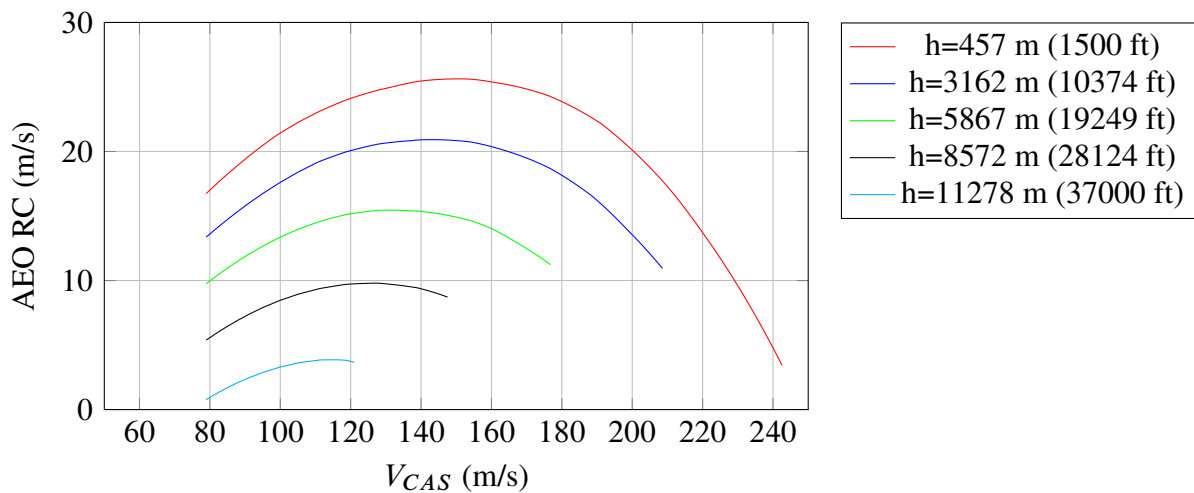


Figure 4.20 A220-300 rates of climb in AEO condition against calibrated airspeed at several altitudes - JPAD

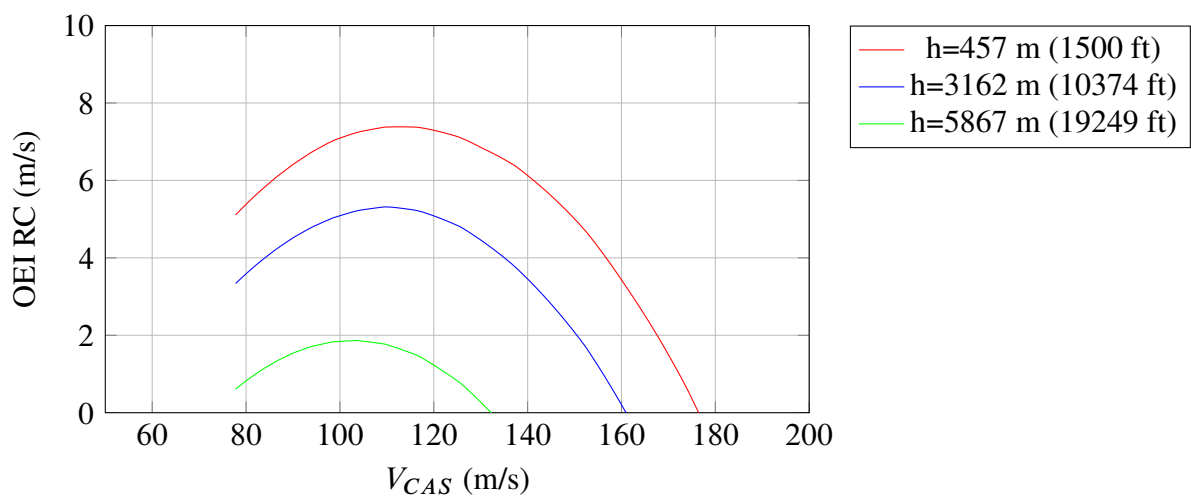


Figure 4.21 A220-300 rates of climb in OEI condition against calibrated airspeed at several altitudes - JPAD

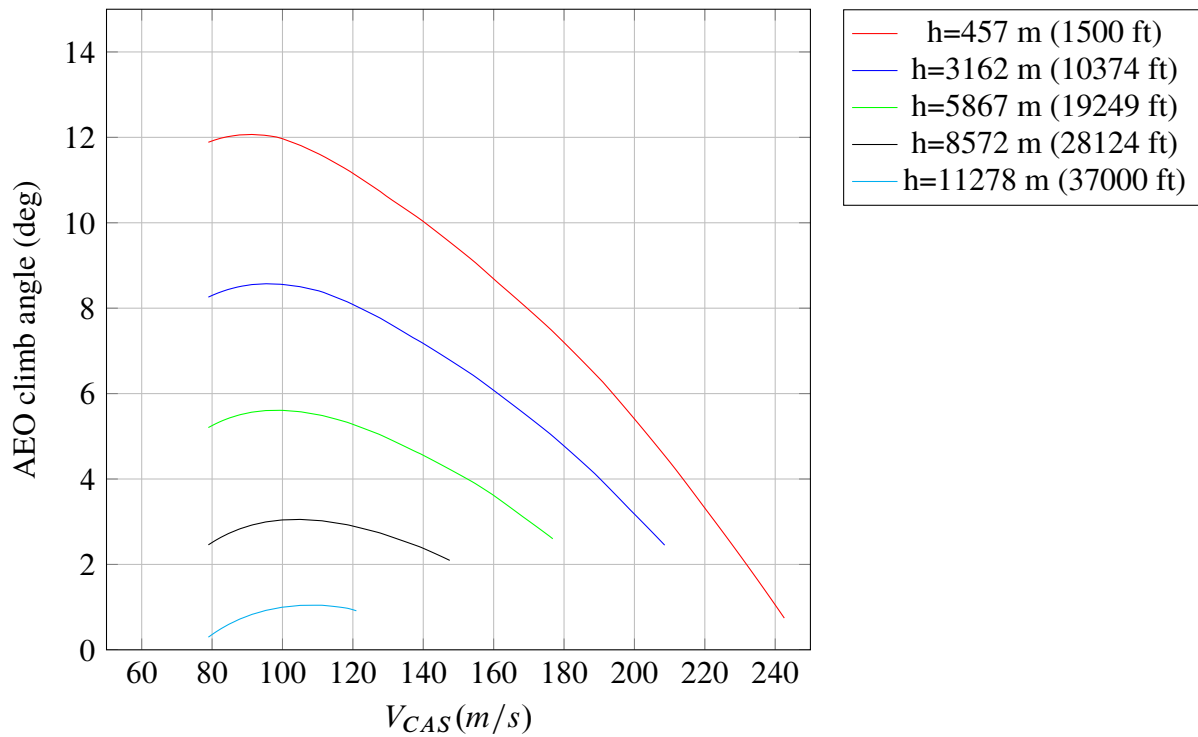


Figure 4.22 A220-300 climb angles in AEO condition against calibrated airspeed at several altitudes - JPAD

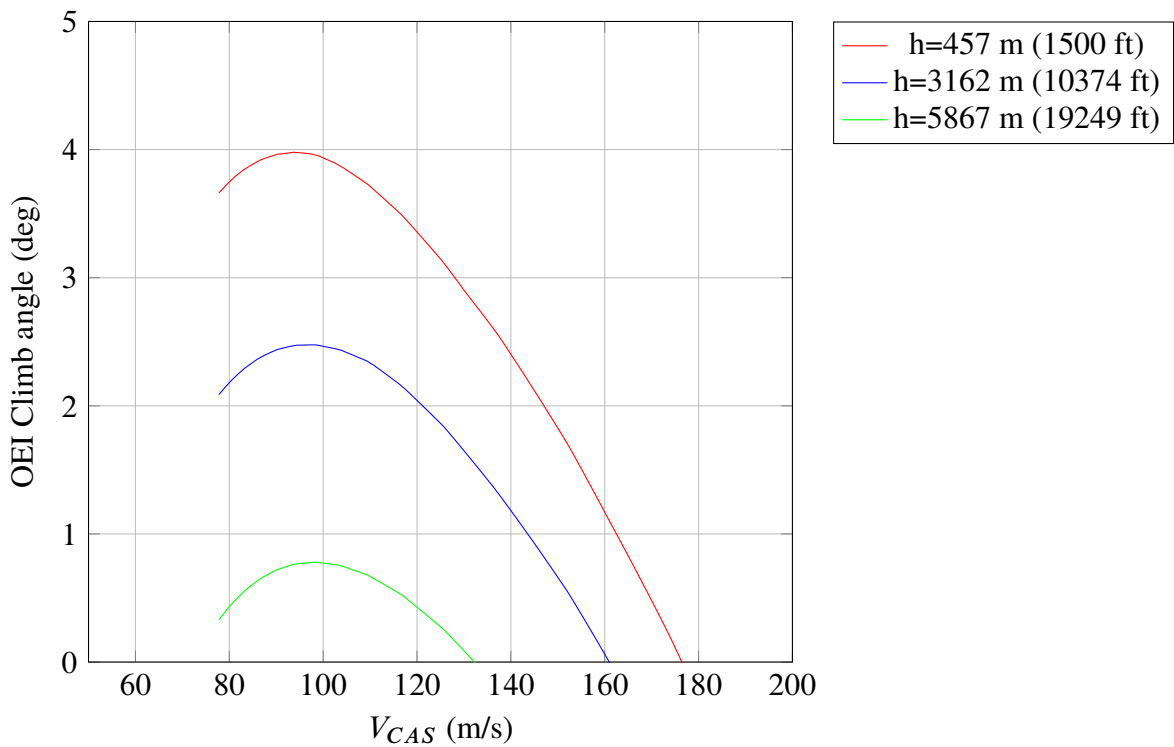


Figure 4.23 A220-300 climb angles in OEI condition against calibrated airspeed at several altitudes - JPAD

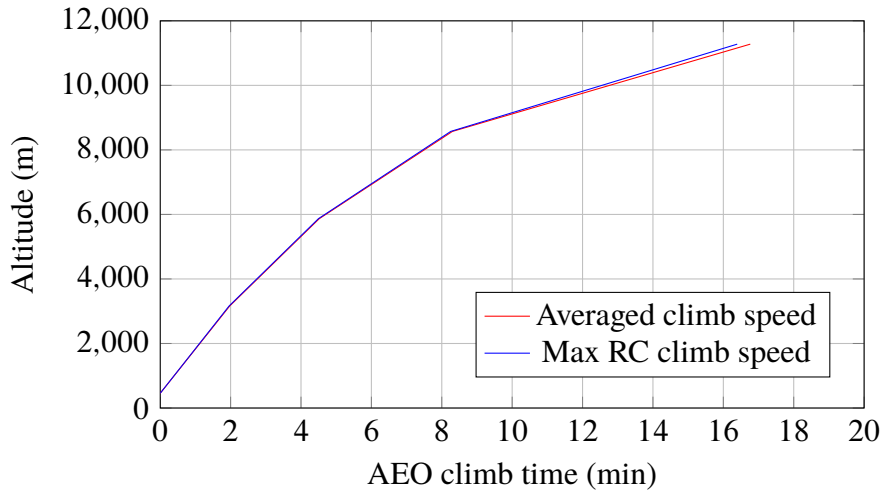


Figure 4.24 A220-300 climb time evolution with altitude - JPAD

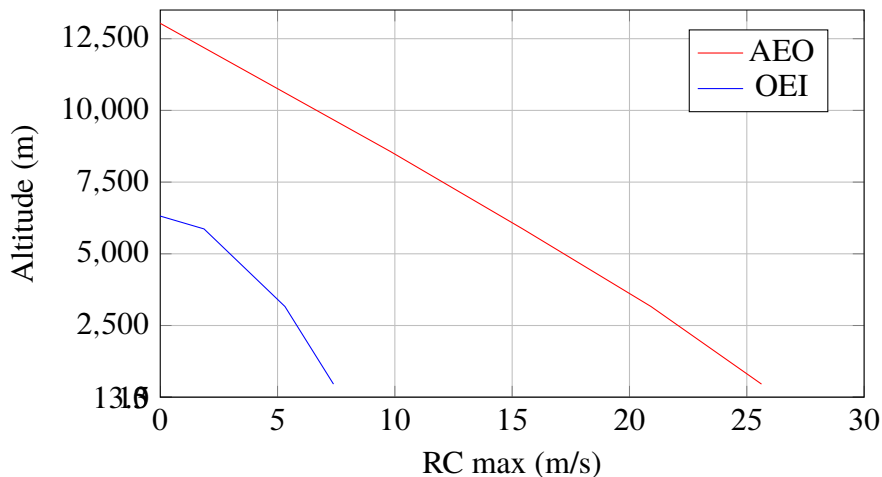


Figure 4.25 A220-300 maximum rates of climb against altitude - JPAD

Moving to the cruise analysis, the flight envelope shown in Figure 4.26 allows to define all characteristic Mach numbers at the cruise altitude of 37000ft and with an aircraft weight equal to 97% of the **MTOW**. Those are collected in Table 4.17 together with available thrust, aircraft drag and the aerodynamic efficiency, calculated at a Mach number of 0.78, at the cruise altitude. The cruise grid chart is shown in Figure 4.27 highlighting best range and long-range conditions at several aircraft weight conditions assuming a fixed value of the cruise altitude equal to 37000ft.

A maximum cruise Mach number of 0.81 has been reached at the altitude of 37000 ft with a difference of about 1.2% with the one reported in Table 4.4. Furthermore, the max operating altitude highlighted by the cruise flight envelope is equal to 13030 m, in agreement with the climb analysis, and with a difference of about 4% with respect to the max operating altitude of 12500 m (41000 ft) reported in Table 4.4.

Output	Value
Thrust available (37 kft, M=0.78)	36691 N
Drag (37 kft, M=0.78)	36691 N
Aerodynamic efficiency (37 kft, M=0.78)	16.1
Stall Mach number (37 kft)	0.51
Minimum Mach number (37 kft)	0.63
Mach number for 300ft/min of RC (37 kft)	0.73
Green dot Mach number - Minimum drag (37 kft)	0.67
Cost index=0 Mach number - Maximum RC (37 kft)	0.67
Maximum Mach number (37 kft)	0.81
Maximum operating Mach number (37 kft)	0.82
Dive Mach number (37 kft)	0.88

Table 4.17 Main output data concerning the JPAD cruise analysis of the A220-300.

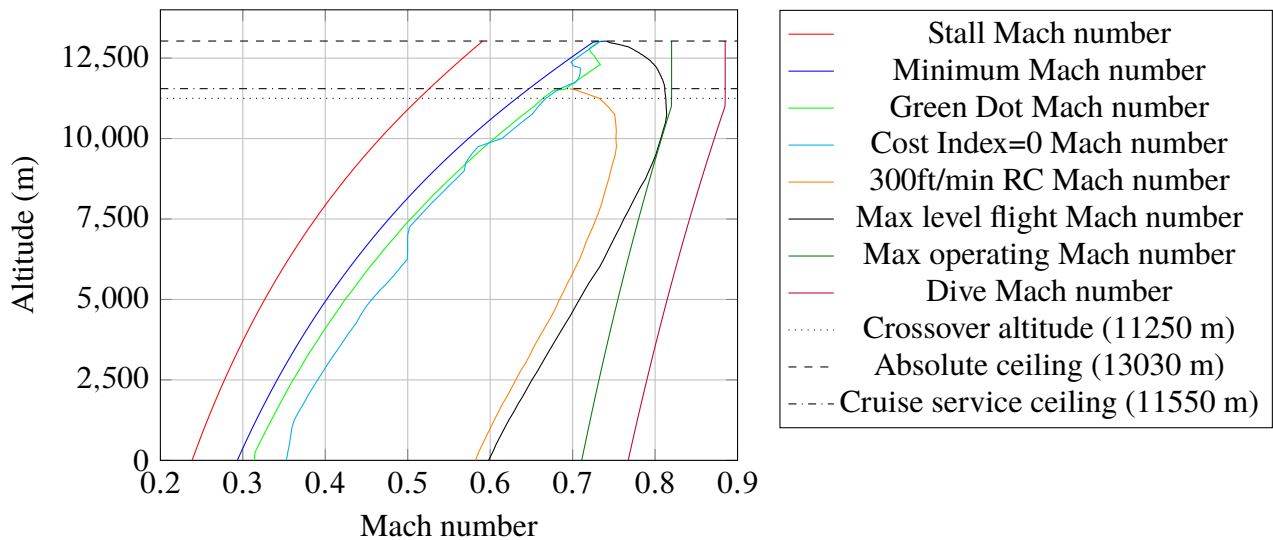


Figure 4.26 A220-300 cruise flight envelope - JPAD

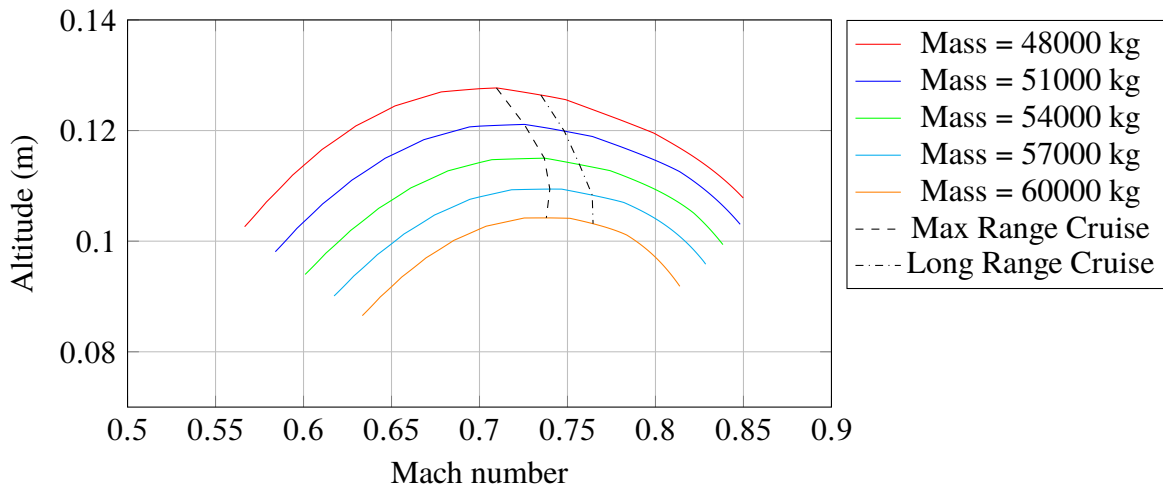


Figure 4.27 A220-300 cruise grid - JPAD

The last standalone analysis to be commented concerns the landing phase. Using input data reported in Table 4.10, a complete simulation has been carried out considering the typical case of 3 ft/s of vertical speed at touchdown. Main simulation output data are provided in Table 4.18, while Figure 4.28, Figure 4.29 and Figure 4.30 show the following time histories: aircraft velocity (both **TAS** and **CAS**); simulation angles (angle of attack, flight path angle and pitch angle) and the aircraft rate of descent. Those have been reported to prove the compliance of the simulation with the specifications coming from the **FAR**. Moreover, the calculated **LFL** of 1575 m differs from the declared A220-300 **LFL** (1509 m) reported in Table 4.4 less than 5% proving the good level of accuracy reached by the performance analysis module of **JPAD**.

Output	Value
Airborne distance	184 m
Flare rotation distance	109 m
Ground roll distance	652 m
Landing distance	945 m
FAR-25 LFL	1575 m
Total landing distance (from 1500 ft)	9587 m
$V_{s,LND}$	52.95 m/s
V_A	65.13 m/s
V_{Flare}	63.29 m/s
V_{TD}	61.69 m/s
$V_A/V_{s,LND}$	1.23
$V_{Flare}/V_{s,LND}$	1.2
$V_{TD}/V_{s,LND}$	1.17
Vertical speed at touchdown	-0.91 m/s (-3 ft/s)
Total landing duration (from 1500 ft)	156 s
Landing duration	23 s
Total Fuel used (from 1500 ft)	64.9 kg
Total NO _x emissions	2.52 kg
Total CO ₂ emissions	205.03 kg
Total H ₂ O emissions	81.05 kg

Table 4.18 Main output data concerning the **JPAD** landing analysis of the A220-300.

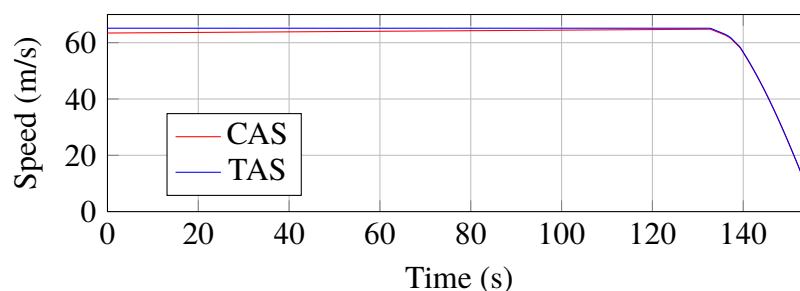


Figure 4.28 A220-300 landing speeds time histories - **JPAD**

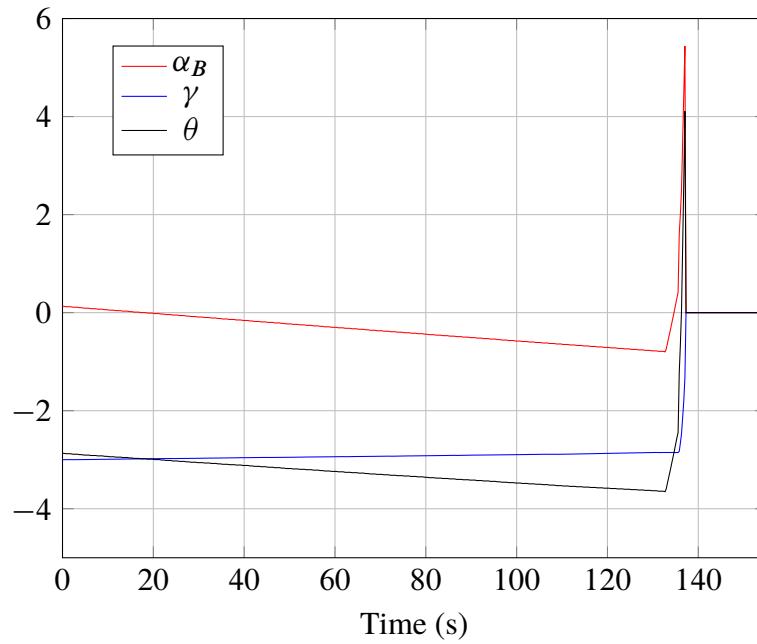


Figure 4.29 A220-300 landing angles time histories - JPAD

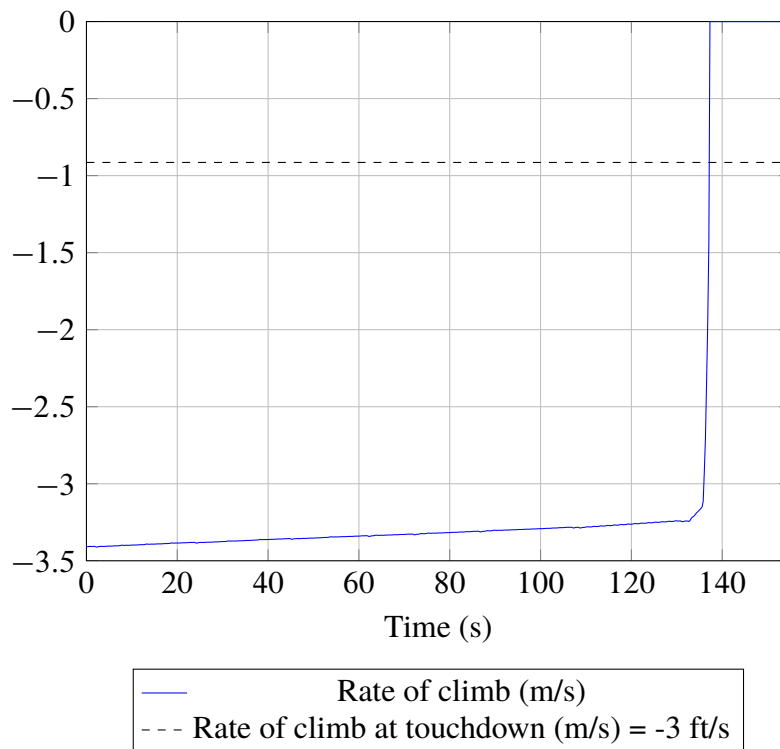


Figure 4.30 A220-300 landing rate of descent time histories - JPAD

The following two analyses concern the design mission simulation and the Payload-Range chart creation. Since the objective of the iterative loop implemented inside the JPAD analysis module is to match a target design range (see Figure 3.5), the mission profile analysis is needed to evaluate the amount of fuel needed to cover that required distance as well as to check if the related take-off weight becomes greater than the MTOW. In this case the allowed payload will be lower than the design payload making impossible to match the design range imposed by TLARs.

As can be seen from Table 4.19, the allowed passengers number is equal to the design passengers number of 135 specified by the TLARs and the total fuel used for the mission provides for a take-off weight equal to the MTOW as expected from a design mission. Furthermore, the estimated total amount of fuel complies with the maximum fuel tank capacity proving the feasibility of the mission.

It must be noted that, due to the complete analysis iterative process shown in Figure 3.5, the calculated design mission fuel is equal to the design fuel mass coming from the weights analysis (see Table 4.8) which is lower than the maximum fuel mass. Beside the overall mission information, Table 4.19 provides also for a summary of the main simulation output concerning each sub-phase. In addition, Figure 4.31 to Figure 4.39 show some of the most relevant simulation output charts.

Table 4.19 Main output data concerning the JPAD design mission analysis of the A220-300.

Output data	Value
Overall mission	
Mission distance	3100 nm
Total mission distance (+ alternate)	3300 nm
Block time	428 min
Total time (+ alternate and holding)	502 min
Initial aircraft mass	66910 kg
Final aircraft mass	51084 kg
Total mission fuel mass (+ alternate, holding and reserve)	16660 kg
Block fuel mass	13795 kg
Total NO _x emissions	293 kg
Total CO ₂ emissions	49632 kg
Total H ₂ O emissions	19616 kg
Design passengers number	135
Allowed passengers number	135
Take-off	
Distance	0.8 nm
Time	0.58 min
Fuel	49.00 kg
NO _x emissions	1.14 kg
CO ₂ emissions	166.76 kg
H ₂ O emissions	61.23 kg
Climb	
Distance	112 nm
Time	17 min
Fuel	963 kg
NO _x emissions	18.43 kg
CO ₂ emissions	2625.00 kg
H ₂ O emissions	1038.00 kg

Continuation of Table 4.19

Output data	Value
Cruise	
Distance	2887 nm
Time	388 min
Fuel	12513 kg
NO _x emissions	214 kg
CO ₂ emissions	39566 kg
H ₂ O emissions	15641 kg
First descent	
Distance	96 nm
Time	20 min
Fuel	210 kg
NO _x emissions	2.36 kg
CO ₂ emissions	663.17 kg
H ₂ O emissions	262.16 kg
Second climb	
Distance	19 nm
Time	4 min
Fuel	324 kg
NO _x emissions	8.21 kg
CO ₂ emissions	1024.16 kg
H ₂ O emissions	404.87 kg
Alternate cruise	
Distance	135 nm
Time	30 min
Fuel	703 kg
NO _x emissions	16.62 kg
CO ₂ emissions	2224.00 kg
H ₂ O emissions	879.16 kg
Second descent	
Distance	46 nm
Time	11 min
Fuel	128 kg
NO _x emissions	1.70 kg
CO ₂ emissions	403.32 kg
H ₂ O emissions	159.44 kg

Continuation of Table 4.19

Output data	Value
Holding	
Distance	0 nm
Time	30 min
Fuel	875 kg
NO _x emissions	29.13 kg
CO ₂ emissions	2768.16 kg
H ₂ O emissions	1094.31 kg
Approach and Landing	
Distance	5.1 nm
Time	2.56 min
Fuel	60.49 kg
NO _x emissions	1.29 kg
CO ₂ emissions	191.27 kg
H ₂ O emissions	75.61 kg

End of Table 4.19

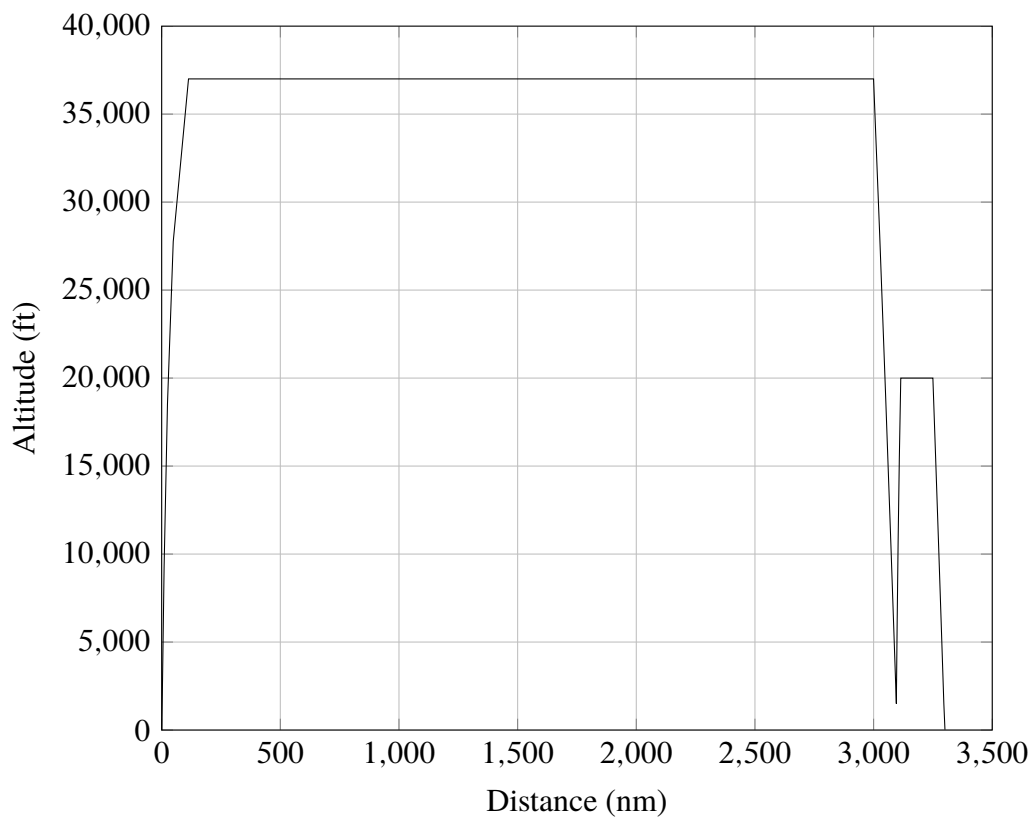


Figure 4.31 A220-300 design mission range profile - JPAD

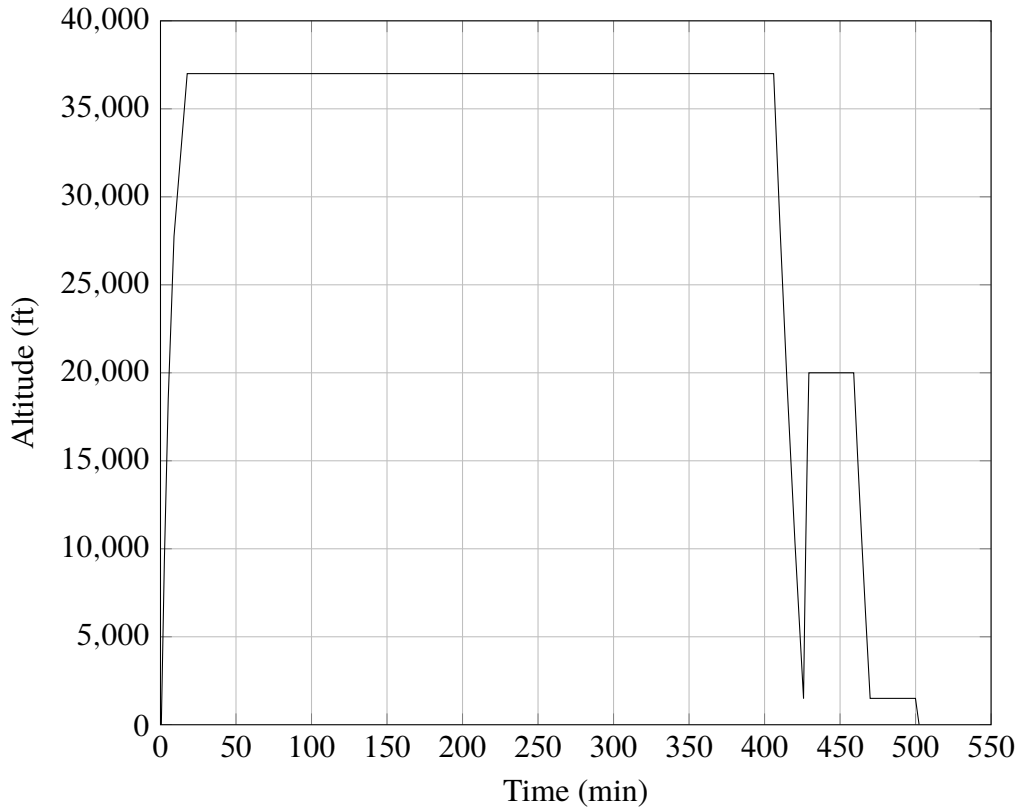


Figure 4.32 A220-300 design mission time profile - JPAD

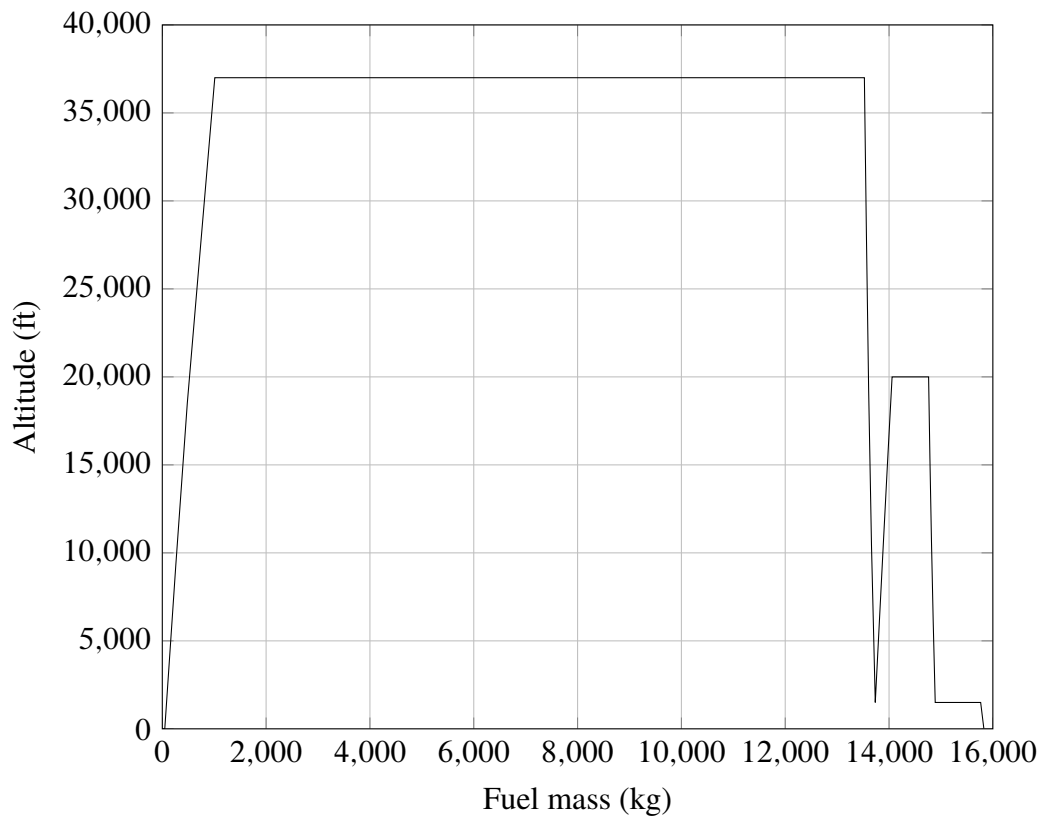


Figure 4.33 A220-300 design mission fuel burnt profile - JPAD

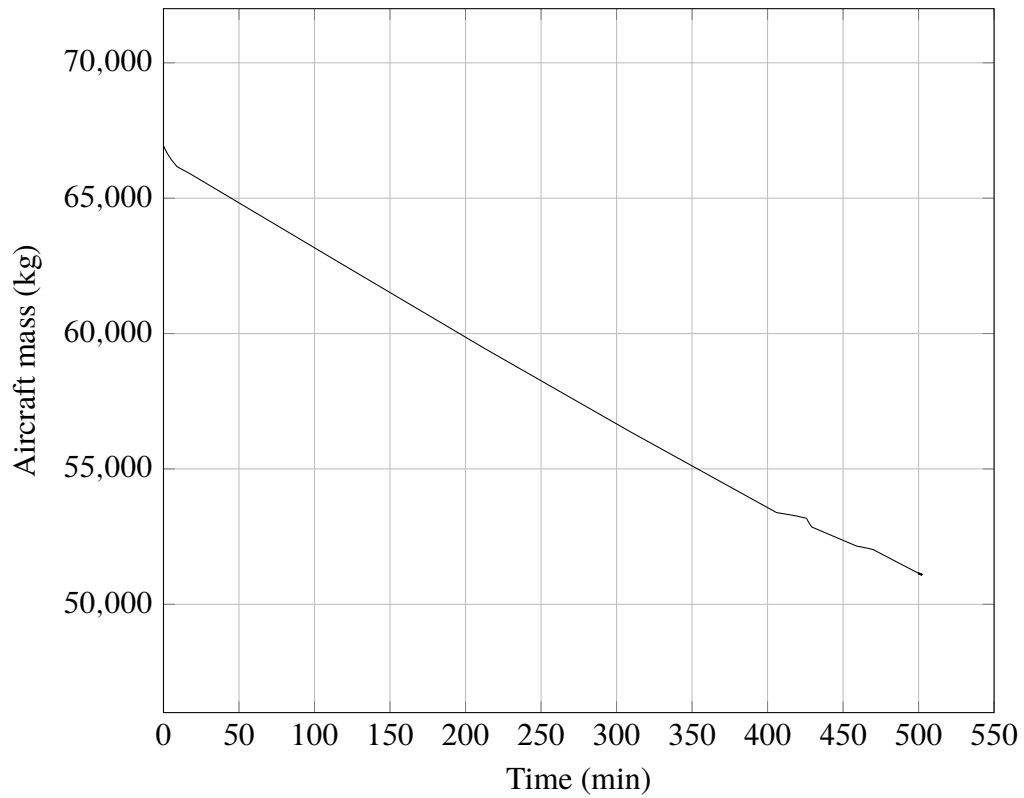


Figure 4.34 A220-300 aircraft mass evolution during the design mission - JPAD

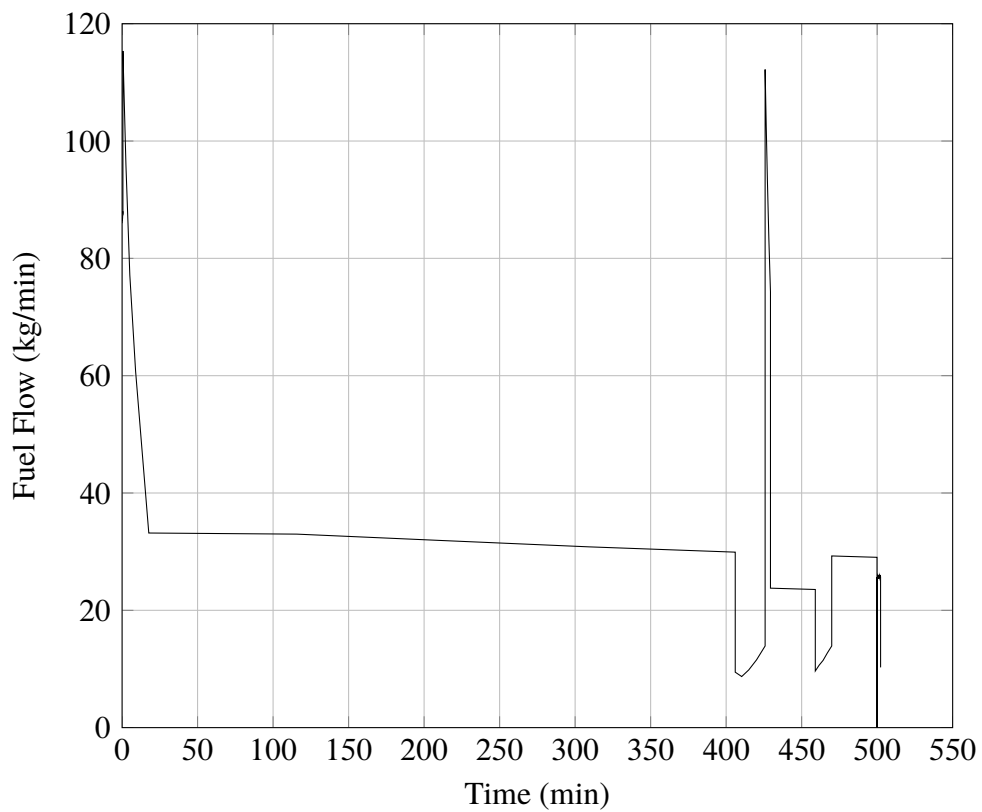


Figure 4.35 A220-300 Fuel flow evolution during the design mission - JPAD

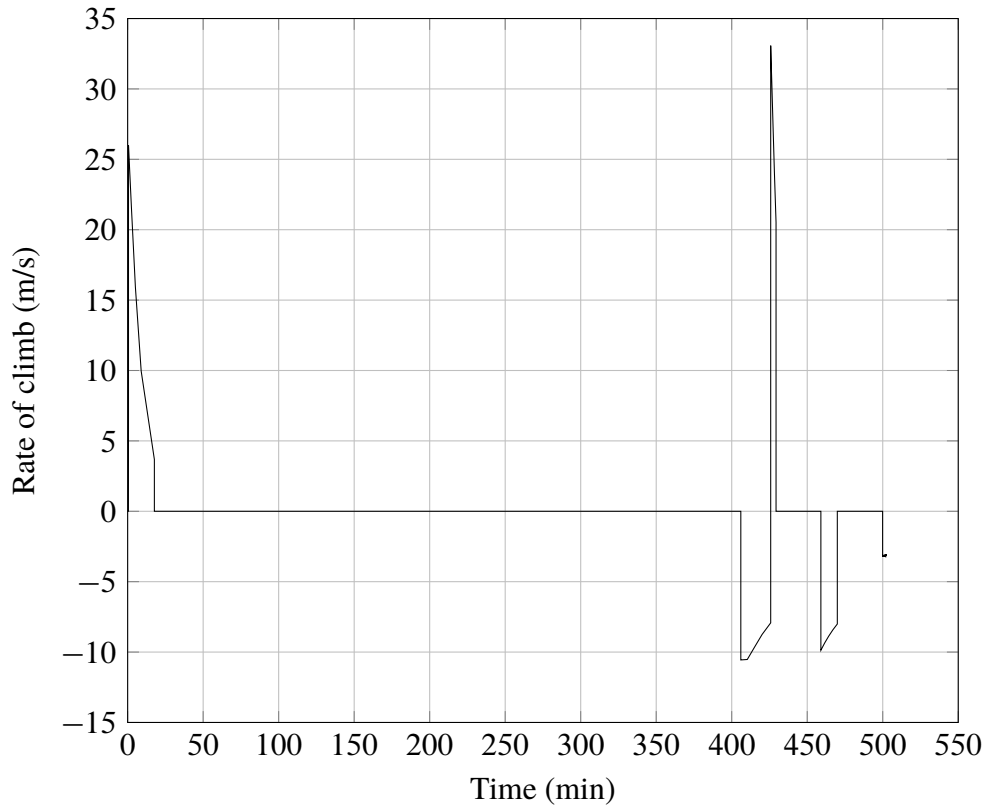


Figure 4.36 A220-300 rate of climb evolution during the design mission - JPAD

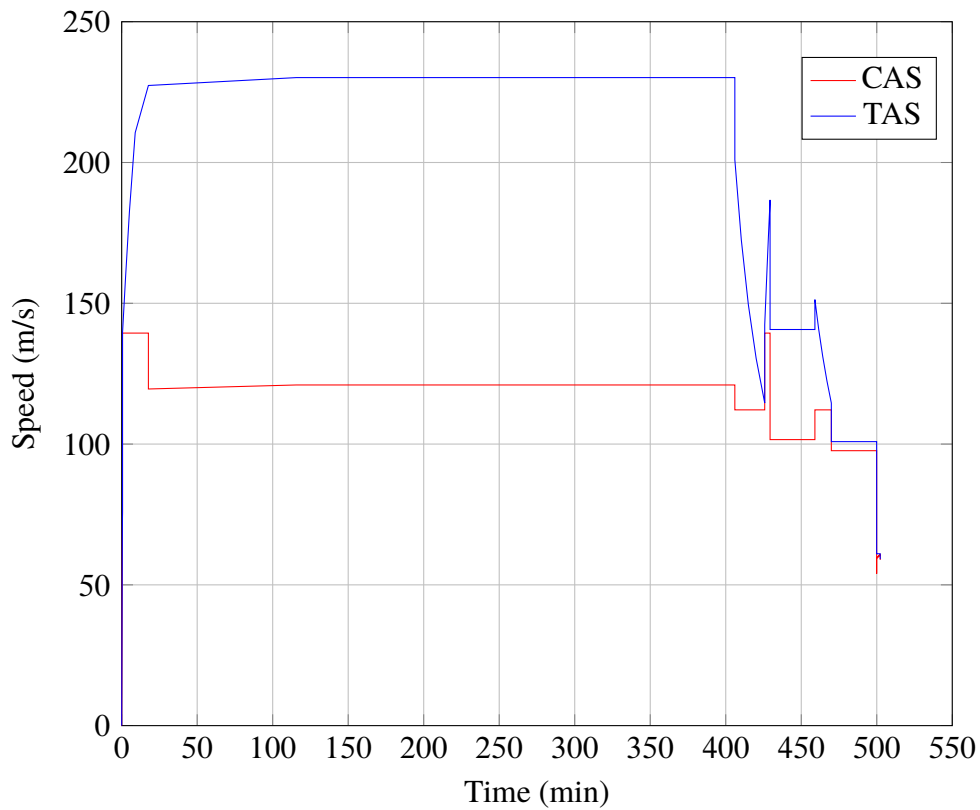


Figure 4.37 A220-300 TAS and CAS evolution during the design mission - JPAD

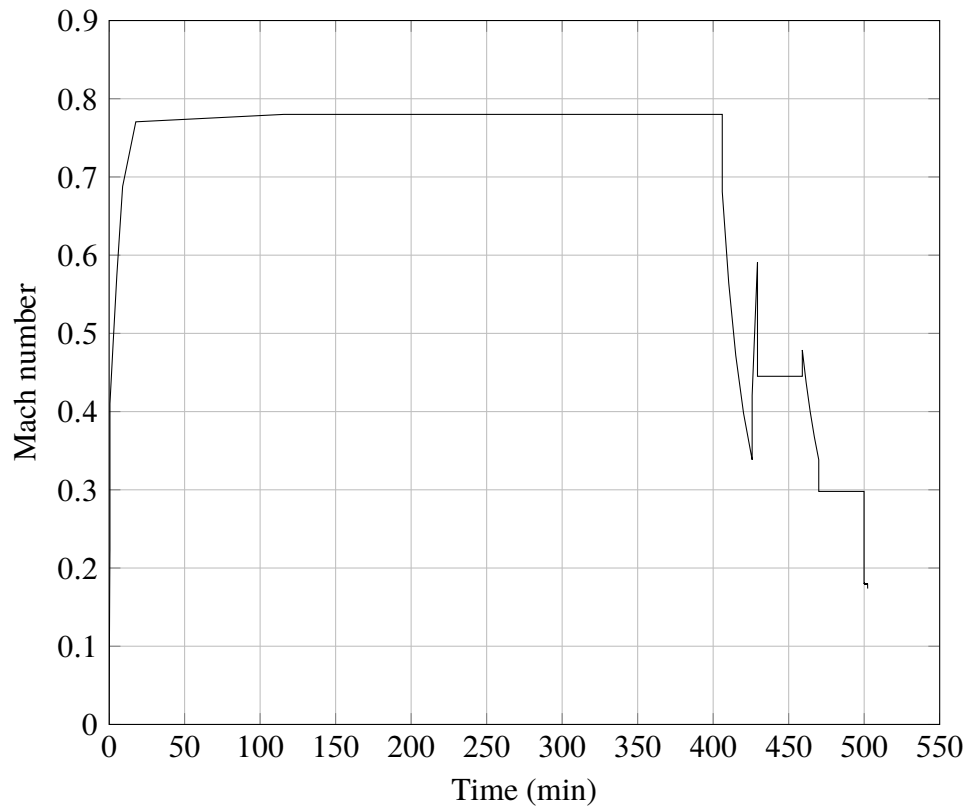


Figure 4.38 A220-300 Mach number evolution during the design mission - JPAD

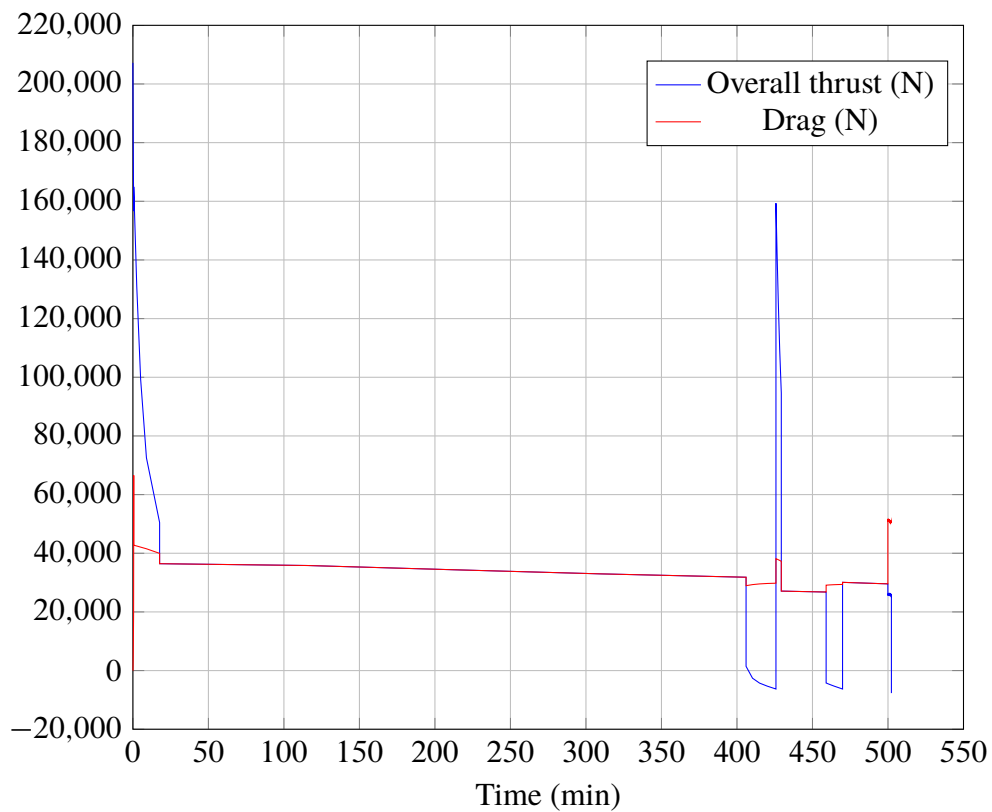


Figure 4.39 A220-300 thrust and drag evolution during the design mission - JPAD

Finally, Figure 4.40 shows the calculated Payload-Range chart compared to the one reported in [116] showing the good level of accuracy reached by the JPAD performance module. The main differences between the two charts are related to the little gap between the values of MZFW, OEW and max fuel mass of the A220-300 and the values estimated using JPAD (see Table 4.8). Moreover, Table 4.20 reported a numerical overview of the data concerning all main Payload-Range chart points.

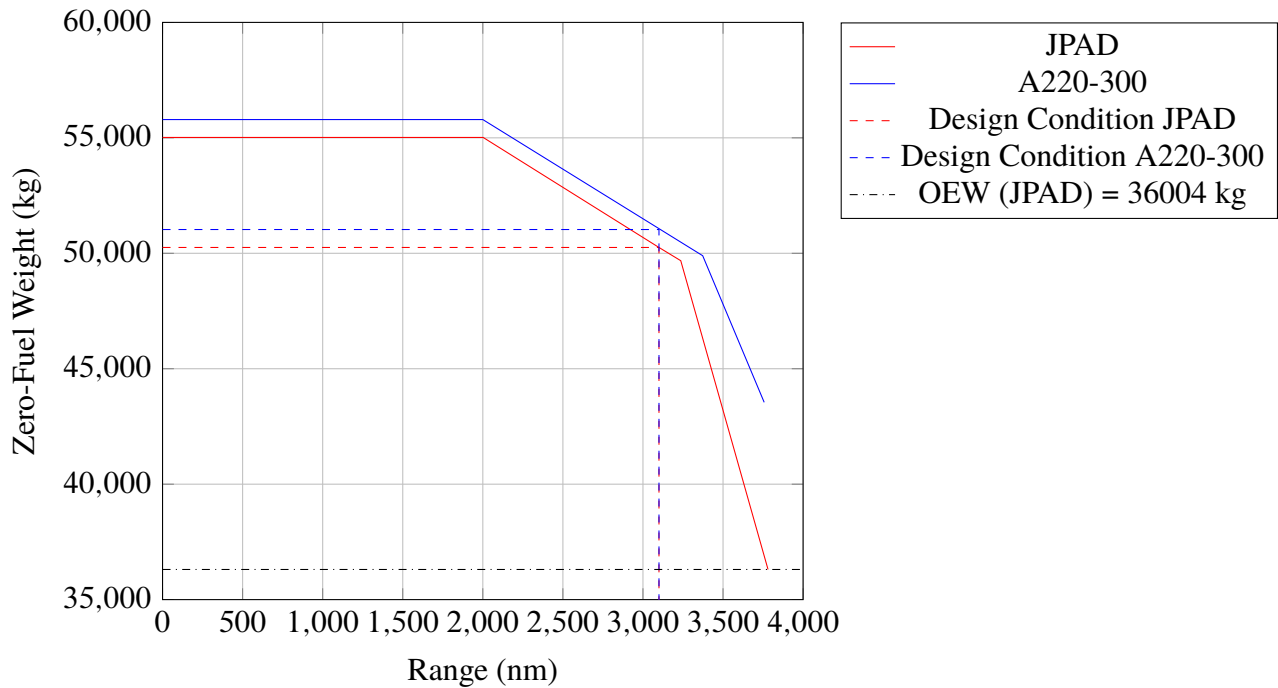


Figure 4.40 Payload-Range chart calculated with JPAD compared with the A220-300 Payload-Range chart [116].

	Harmonic Range	Design Range	Max Fuel	Zero Payload
Range	2002 nm	3100 nm	3236 nm	3781 nm
Aircraft mass	66911 kg	66911 kg	66911 kg	53539 kg
Payload mass	18711 kg	13946 kg	13946 kg	0 kg
Fuel mass	11894 kg	16660 kg	17233 kg	17233 kg

Table 4.20 Main output data concerning the JPAD Payload-Range analysis of the A220-300.

The last discipline to be analyzed is related to aircraft operating costs. Starting from weights data calculated with JPAD reported in Table 4.8 and performance analysis results in terms of block fuel and block time coming from design mission simulation, a complete DOC analysis has been performed. Furthermore, all economic assumptions listed in Table 4.11 have been used as additional input data to carry out this task.

A complete overview of each DOC contribution is shown in Table 4.21 providing also information about both total and cash DOC, while Figure 4.41 provide a visual representation of the total DOC breakdown.

	\$/flight	\$/h	\$/nm	¢/seat-nm
Depreciation	12744	1686	4.111	3.045
Interests	12234	1619	3.946	2.923
Insurance	983	130	0.317	0.235
Capital DOC	25960	3435	8.374	6.203
Cockpit crew	5441	720	1.755	1.300
Cabin crew	2720	360	0.878	0.650
Crew DOC	8161	1080	2.633	1.950
Fuel DOC	8867	1173	2.86	2.119
Landing charges	401	53	0.130	0.096
Navigation charges	1129	149	0.364	0.027
Ground handling charges	1436	190	0.463	0.343
Charges DOC	2967	393	0.957	0.709
Airframe maintenance charges	3193	422	1.030	0.763
Engines maintenance charges	5958	788	1.922	1.424
Maintenance DOC	9242	1223	2.981	2.208
Cash DOC	29237	3869	9.431	6.986
Total DOC	55198	7305	17.806	13.190

Table 4.21 Main output data concerning the JPAD DOC analysis of the A220-300 related to the design mission of 3100 nm.

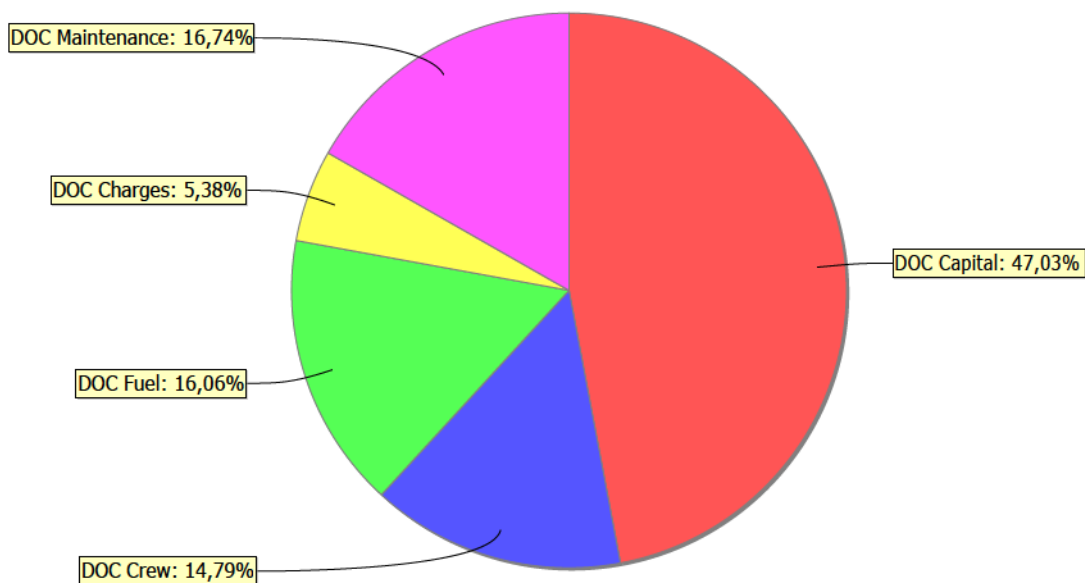


Figure 4.41 JPAD total DOC breakdown of the A220-300 parametric model.

The case study presented in this section has shown a possible application of the **JPAD** software concerning modern transport regional jets, highlighting software capabilities and the level of accuracy of the implemented analysis modules.

Furthermore, the **JPAD** A200-300 model presented in this section has been approved by the **ADORNO** project consortium to be used as reference 2014 conventional regional under-wing-mounted engines aircraft model. As for the **ADORNO** project, the A220-300 **JPAD** model will be used as reference state of the art regional jet to make all comparisons needed to investigate the research question object of this thesis work.

4.2 **TLARs** and key design aspects of innovative regional turbo-prop aircraft

As described at the beginning of this thesis work, to investigate the impact, in terms of performance, that innovative high-capacity turboprop aircraft configurations can have on the current regional aircraft scenario, as well as to assess which high-capacity turboprop configuration could be the one that maximizes potential performance advantages with respect to the state of the art of current regional jet aircraft, a set of **TLARs** suitable for modern regional transport applications, and in line with the main aircraft manufacturer market forecast, must be defined. This will be the starting point in the definition of several innovative turboprop aircraft concepts to be further analyzed and optimized via a dedicated **MDAO** process carried out using the **JPAD** software.

To design a turboprop that could be competitive with respect to regional jets, several aspects must be considered with respect to current turboprop aircraft:

- the maximum seats capacity must be increased.
- the **SFC**.
- the cabin comfort and perceived noise must be improved.
- the maximum cruise speed, cruise aerodynamic efficiency as well as the design range must be increased.

Those considerations, according also to the market forecast reported in the introduction of this thesis as well as research activities carried out during the first two loops of design of the **IRON** project, have led to the definition of the set of **TLARs** summarized in Table 4.22 [1].

As discussed in [1], large turbo-propeller aircraft (with about 70 seats) have a maximum take-off weight of about 23-28 tonnes with an empty weight slightly higher than 50% of the maximum take-off weight (about 13-17 tonnes). Turboprop aircraft have a straight tapered high-wing configuration with a surface of about 60-70 m² and a span of approximately 27-30 meters, which means an aspect ratio in the range 11-12.

A T-tail configuration is adopted, with ratio between tails and wing surfaces close to 0.20. Also, the fuselage length and fuselage fineness ratio are comparable for each aircraft, between 10 and 12.

The high-wing configuration with under-wing-mounted engines installation represents the state of the art for existing large turboprop aircraft. The main reason behind this layout is to have an

Performance requirements	
Passenger capacity	130 pax (108 kg each) at 32" seat pitch
Design range plus reserves	1600 nm + 100 nm alternate at 15 kft, 30 min holding at 1500 ft and 5% fuel reserve
Cruise Mach number and altitude	0.64 ÷ 0.68 at 30 kft, ISA condition and 97% MTOW
Time to climb	from 1500 ft to 25000ft \leq 16' at MTOW, ISA conditions
TOFL	\leq 1400m at MTOW, SL and ISA conditions
LFL	\leq 1400m at MTOW, SL and ISA conditions
Aerodynamic requirements	
Cruise efficiency	17
$C_{L_{max}}$ Landing	3.0
$C_{L_{max}}$ Take-Off	2.4
$C_{L_{max}}$ Clean	1.6

Table 4.22 TLARs for an innovative high-capacity turboprop aircraft [1]

easy cabin access and a better engine clearance due to a large propeller diameter. Furthermore, the under-wing-mounted engines configuration provides for a lighter wing structure (engine mass loading relief) and for a contained center of gravity excursion. Thus, a lower horizontal tail download is needed to trim the aircraft at the most forward center of gravity position. However, such a configuration could be not suitable for future high-capacity turboprop configuration with increased passenger capacity (130-150 seats).

Increasing the number of passengers means to increase the aircraft weight as well. Thus, a larger wing area to keep similar ground performance is needed. To avoid a large decay of the aerodynamic efficiency, the wing aspect ratio should be kept in the range of 11-12 which means to increase the wingspan affecting, this way, landing gears size and position. A larger wheel track is required to ensure ground stability while an increased maximum take-off weight demands for a heavier landing gear structure. For high-wing configurations, two landing gears installations are possible: nacelle-mounted (as illustrated in the left picture of Figure 4.42) or fuselage-mounted with pods (right picture of Figure 4.42).



Figure 4.42 Possible landing gear installation for high-wing turboprop aircraft [1].

These two solutions may provide several issues if used for new high-capacity turboprop aircraft. The nacelle-mounted landing gear will require for a very long and heavy leg which may be difficult to be retracted inside the nacelle, while the fuselage mounted landing gear could require very large and heavy pods to ensure the required wheel track. Moreover, due to a longer fuselage, both these layouts



Figure 4.43 Large propeller low-wing installation issues [1].

require longer landing gear legs length to achieve a reasonable value of the take-off and landing rotation angle. Unless new technological improvements concerning the landing gears design, both above-mentioned solutions could be unfeasible for high-capacity turboprop aircraft.

A low-wing configuration could solve this issue. However, as shown in Figure 4.43, the need for a very large propeller diameter (about 12-14 ft) makes impossible to reach the required engine clearance from the ground. Thus, a low-wing configuration with under-wing-mounted engines installation results to be unfeasible.

For this reason, innovative high-capacity turboprop configurations should be characterized by rear-mounted engines installation. This can lead to a more efficient wing, thanks to a large laminar flow extension, together with a lower cabin noise level (engines will be installed far from the cabin). Conversely, a rear-engines installation will lead to a wing weight increment since no engine mass relief can be used to reduce the wing loading.

Such a configuration must be carefully investigated to have a reliable prediction of aircraft tail aerodynamics, taking also into account for engines installation and the influence of the propeller in the horizontal tail sizing. This topic, together with aerodynamics and longitudinal stability effects linked to a three-lifting surfaces configuration, has been widely investigated in the thesis work by Vincenzo Cusati [107] within the framework of the **IRON** project.

Furthermore, this configuration can lead to a very large center of gravity excursion which can also affect aircraft performance. This could lead to a very big horizontal tail, needed to trim the aircraft at the most afterward center of gravity positions, resulting in a reduction of maximum lift capabilities. On the other hand, at the most forward center of gravity position, the longitudinal static stability margin could be very high providing for a very large download on the tail to trim the aircraft. Thus, the cruise aerodynamic efficiency will decrease affecting the fuel burned as well as aircraft **DOC**.

One possible solution could be to limit the center of gravity excursion, with the impossibility to operate the aircraft at low passengers number, complying with typical aircraft missions.

Similar considerations have already been outlined within the **IRON** project as described in [10]. However, although the limitation, the center of gravity excursion is still wider than a traditional turboprop configuration. Thus, the effect of the trim drag at the most forward center of gravity position will surely reduce the aircraft aerodynamic efficiency.

Another solution, coming from the second design loop of the **IRON** project, could be to add a third lifting surface to extend the design space and to cope with both cruise efficiency and maximum lift capabilities. However, as discussed Chapter 1, major concerns related to this configuration must be addressed to the downwash caused by the third lifting surface which affects not only the wing, causing to define a specific twist angle law along the wingspan, but the horizontal tail as well, providing for a large negative induced angle of attack.

4.3 High-capacity turboprop models definition and their MDAO

In this section, making use of the experience gained during the design activities of the first two loops of the **IRON** project and taking parts from the work reported in [1], developed by the author of this thesis together with the **DAF** research group of the University of Naples Federico II, three high-capacity turboprop aircraft configurations will be selected and described starting from the considerations made in the previous section and from the results of the feasibility study performed by NASA [20].

Here the rear-mounted engines configuration has been identified as the most promising layout followed by the upper-wing engines configuration with low-wing. However, requiring for large propeller diameters (12 up to 14 ft) the latter has been discarded due to both propeller and nacelle sizes not compatible with the low-wing configuration. At its place a conventional high-wing configuration with under-wing engines installation has been considered, assuming that main landing gears can be installed in fuselage mounted pods.

To cope with the above-mentioned large propeller diameter, the T-Tail layout, classified as the worst among all optima configurations presented in the NASA work [20], requires pylons with a non-negligible span, making these latter comparable to a horizontal tail. Thus, this configuration has been discarded since the first stage of this research activity. Despite all design issues encountered during the second loop of the **IRON** project, a three-lifting surfaces configuration has been selected to replace the T-Tail layout according to the promising results shown at the end of Chapter 1.

Before proceeding with the **MDAO** process, it is worth to illustrate all technological and geometrical assumptions as well as configuration effects that have been taken into account for each high-capacity turboprop under investigation. Those deal with both aerodynamics (in terms of drag, lift capabilities and downwash on the horizontal tail plane) and components weights.

General assumptions have been made for all configurations concerning the following items. An overall quantitative summary is provided in Table 4.23.

- Fuselage length and maximum diameter have been kept constant.
- Horizontal tail sweep at leading edge have been assumed to be 5° greater than wing sweep angle at leading edge. Only for the three-lifting surfaces configuration, both horizontal tail and canard sweep angles at leading edge have been kept constant and equal to a value of 10° . This to avoid a very large number of configurations to be analyzed.
- Horizontal tail and canard aspect ratios have been kept constant, with a specific value for each configuration.

- Center of gravity positions of some of the major on-board systems have been modified to provide for a better center of gravity excursion (especially in case of rear-mounted engines). All positions have been calculated using the **JPAD** standard on-board systems layout defined in Chapter 3; however, calibration factors have been used to change the following component positions.
 - Air conditioning and anti-icing system group, which has been moved from 25% to 30% of the wing **MAC**.
 - Electrical system group, which has been moved from 25% of the wing root chord to 42% of the fuselage length (half cabin).
 - Furnishings and equipments group, which has been moved from 50% of the fuselage cylinder trunk length to 37% of fuselage length.
 - Operating items group, which has been moved from 50% of the fuselage cylinder trunk length to 21% of fuselage length (close to the front galley).
- Considering all aircraft configurations as “More Electric Aircraft” [132], the mass group related hydraulic and pneumatic systems have been neglected, together with its influence on the overall center of gravity position, using dedicated calibration factors provided by the **JPAD** software.

High-wing configuration with wing-mounted engines

Starting with the high-wing configuration with wing-mounted engines, the horizontal tail-plane position has been fixed according to vertical tail tip chord position with a fixed incidence angle equal to 0.0 degrees. Furthermore, the horizontal tail aspect ratio has been fixed to 5.0 with the possibility to scale the span and the planform area.

Engines positions have been linked to the wing kink station assuming the natural laminar flow to be active only on the outer wing panel (about 50% of the wingspan). Since the effect of the natural laminar flow on the overall wing, coming from the analyses carried out during the **IRON** project, has been estimated as a reduction of -20 drag counts for each affected profile, the effect considered for this aircraft configuration has been fixed at -10 drag counts. However, the nacelle-wing interference effects provided by this configuration, provides for an average increment of the overall drag coefficient of about 10 drag counts.

Landing gears have been assumed to be mounted in fuselage pods. Their position has been linked to wing position assuming that wing and landing gears attachments are applied to the same fuselage frame. Furthermore, landing gears pods provide an increment in parasite drag which has been estimated as an increment of about 15 drag counts in addition to the excrescences drag contribution calculated by the **JPAD** aerodynamics module.

According to Torenbeek’s book [25], wing mass have been reduced by 5% due the mass-relief effect on the wing loading provided by wing-mounted engines.

To take into account the landing gears installed in fuselage pods, a further reduction of 5% of the wing mass has been considered. However, an increment of 2% has been considered to take into account for wing spoilers. Concerning the fuselage, Torenbeek [25] suggests to increase the estimated mass by 8% due to pressurization effects and by 7% due to landing gears pods.

Effects concerning wing and fuselage weights, as well as nacelle-wing interference, have already been implemented inside the **JPAD** software. However, for sake of clarity, they have been reported in Table 4.23 as well.

Low-wing configuration with rear-mounted engines

This unconventional configuration provides for engines installed at the horizontal tail-plane tip. The horizontal tail is fuselage-mounted, and it has been assumed to have a variable pitch angle. In particular, a value of -2° has been assumed for the cruise phase, while a value of -4° has been used for both take-off and landing. The horizontal tail-plane aspect ratio has been fixed at 4.40 for structural considerations regarding the engine installation.

Landing gears have been assumed to be wing-mounted, thus their position has been linked to the wing assuming a value of 60% of the **MAC**. Beside the wing weight increment due to spoilers installation and the fuselage weight increment due to pressurization, still present on this configuration, the following effects (derived from Torenbeek's book [25]) have been considered: +4% of fuselage weight due to rear engine installation; +65% of horizontal tail mass based on preliminary evaluation of combined aerodynamic loading and engine inertial contribution made during the design activities of the **IRON** project. Unlike the wing, the horizontal tail usually works with negative aerodynamic loads, thus the engine mass does not provide load relief effects. Thanks to the rear engine installation, the whole wing has been supposed to work in laminar flow conditions, reducing the wing parasite drag of about 20 drag counts.

In terms of horizontal tail lift capabilities, the tail-tip installation of both engines (assumed to be counter-rotating) provides also for a beneficial effect in terms of $C_{L\alpha}$ estimated as an average increment +10%. Moreover, as explained in [133], the tail-tip installation not only provides for the best lift curve slope but allows also to reduce nacelle-tail interferences as well as to provide for a negative (stable) pitching moment coefficient derivatives.

Three-lifting surfaces configuration

This configuration as well as the rear mounted provides for rear-engines installation at the horizontal tail-plane tip. Similar to the previous case, the horizontal tail has supposed to have a variable pitch angle according to the specific flight phase (same values assumed for the rear mounted configuration). Like the previous solution, the tail aspect ratio has been kept constant at 4.40 due to structural reasons linked to engines installation and its mass has been increased of 65% due to the same structural considerations made for the rear mounted solution. Same assumptions have also been made concerning main landing gear position, fuselage mass increment due to tail-mounted engines and pressurization, wing mass increment related to spoilers installation, and laminar flow effects on the wing. However, due to the installation of a new lifting surface on the fuselage, its mass has been further increased by 5% according to the preliminary design activities carried out during the second loop of the **IRON** project.

Thanks to the introduction of a third lifting surface, a fraction of fuel mass has been assumed to be stored in a canard fuel tank. Its storable fuel mass is linked to the estimated capacity which has been calculated assuming standard spar positions (20% and 55% of the local chord) and using the volume equation proposed by Torenbeek [25]. Thus, it has been possible to reduce the center of gravity excursion limiting longitudinal stability and aerodynamics issues.

Since **JPAD** is capable to model also a canard in the same way as for a normal wing, this effect has been easily simulated by considering an additional fuel tank also for this lifting surface. This effect has been modeled inside **JPAD** using the fuselage mass calibration factor of the weights analysis module.

In terms of aerodynamics and longitudinal static stability, the third lifting surface provides for a beneficial effect on the maximum lift coefficient as well as for a large downwash on the horizontal tail-plane.

From **CFD-RANS** analyses carried out during the second design loop of the **IRON** project, the overall downwash gradient acting on the horizontal tail-plane (caused by both wing and canard) can be assumed equal to a constant value of 0.53.

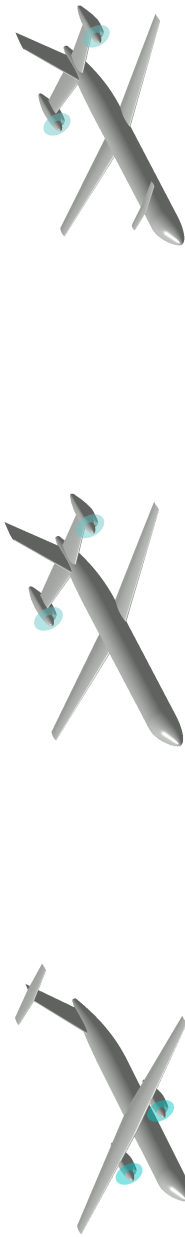
While the first effect can be taken into account inside **JPAD** by simply considering a new lifting surface contribution (see [92]), to implement the second effect in the overall multi-disciplinary workflow a user-defined downwash gradient has been assigned in all aerodynamic and stability input files disabling the automatic calculation of this latter.

The **MDAO** process

Starting from the set of **TLARs** described in Table 4.22, a sensitivity analysis has been carried out for each of the considered aircraft configurations by varying the following geometrical design parameters.

- Wing, in terms of span, area, sweep angle at leading edge and longitudinal position;
- Horizontal tail, only in terms of area (being the span calculated from the fixed value of the aspect ratio) and longitudinal position. However, the longitudinal position is fixed for the high-wing configuration with wing-mounted engines being the latter linked to the wing position. The sweep angle at leading edge is calculated from the wing for the first two configurations (5 degrees more than the wing), while for the three-lifting surfaces configuration, it has been kept constant and equal to a value of 10°.
- Canard planform, in terms of area, sweep angle at leading edge and longitudinal position. As for the horizontal tail, for the three-lifting surfaces configuration, this angle has been kept constant and equal to a value of 10°.

Each solution of this analysis has involved all aircraft design disciplines following the **JPAD** complete analysis cycle illustrated in Figure 3.5. The resulting cloud of solution points has been used to build a response surface (one per configuration) used as starting point for the optimization process, as shown in the flowchart of Figure 3.39. Each optimization process has involved two algorithms: the genetic algorithm ε -NSGAI [22] and the particle swarm optimization algorithm OMOPSO [23].



	Weight	Drag	Lift, Stability	Weight	Drag	Lift, Stability	Weight	Drag	Lift, Stability
Laminar Flow	—	-10dcs	—	—	-20dcs	—	—	-20dcs	—
Fuselage pressurization	+8% Fuselage	—	—	+8% Fuselage	—	—	+8% Fuselage	—	—
Fuselage landing gears and pods	+7% Fuselage -5% Wing	+15dcs	—	—	—	—	—	—	—
Wing spoilers installation	+2% Wing	—	—	+2% Wing	—	—	+2% Wing	—	—
Under-wing engines	-5% Wing	+10dcs	—	—	—	—	—	—	—
Rear-mounted engines	—	—	—	+4% Fuselage +65% Hor. tail	—	+10% $C_{L\alpha H}$	+4% Fuselage +65% Hor. tail	—	+10% $C_{L\alpha H}$
Canard installation	—	—	—	—	—	—	+5% Fuselage	—	$\left. \frac{d\epsilon}{d\alpha} \right _H = 0.53$

Table 4.23 Assumptions and main configuration effects on weights, aerodynamics and longitudinal static stability concerning all high-capacity turboprop configuration under investigation. All drag contributions are measured in drag counts (dcs) and have been modeled inside JPAD using dedicated drag coefficient calibration factors.

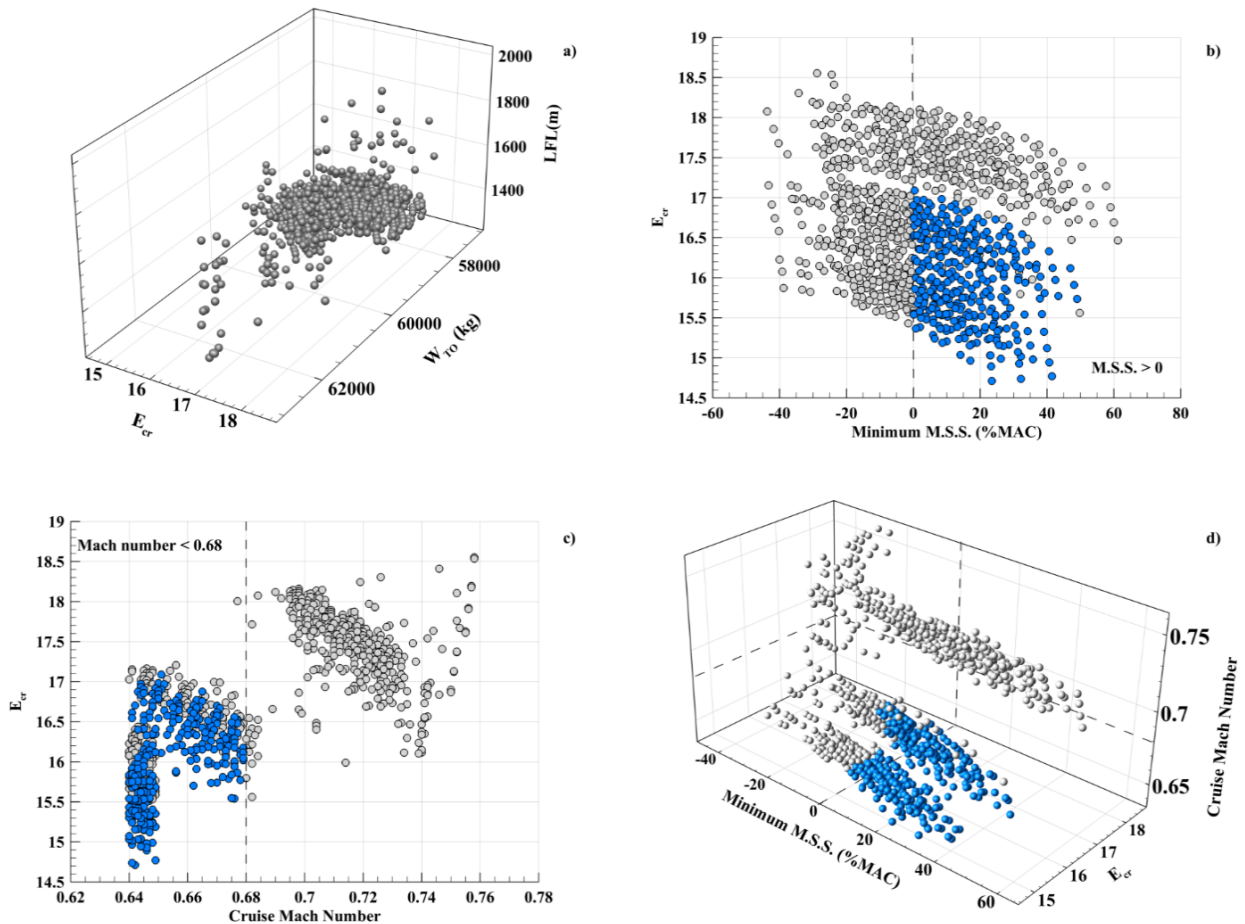


Figure 4.44 MDAO of the high-wing with wing-mounted engines configuration. Constraints on the minimum SSM and cruise Mach number: a) Example of response surface b) Limitation in the plane E_{cr} versus SSM c) Limitation in the plane E_{cr} versus cruise Mach number d) Solutions verifying both constraints 3D view [1].

At the end of the process, charts of all possible combinations of Pareto fronts as well as the complete set of the optima design variables and objectives have been produced and collected.

Form the analysis of results, obtained at the end of the optimization process for each configuration, a manual selection of each optimum high-capacity turboprop configuration has been made. However, before analyzing and comparing those optima configurations, a more detailed description of the MDAO problem under investigation must be provided. As shown in [1], Figure 4.44a illustrates an example of a response surface, represented as a cloud of points, generated for the wing-mounted engines configuration. In this example the LFL is plotted against both the MTOW and the cruise efficiency.

In addition to the design variables listed before, the multidisciplinary optimization has been carried out by imposing the following constraints:

- the minimum SSM (with respect to the max aft. center of gravity position) must be at least greater than zero.
- the maximum cruise Mach number must not exceed 0.68 to take into account for propeller operative limitation in terms of compressibility issues.

- the difference between the maximum afterward center of gravity position and the main landing gear position must be larger than 5% of the **MAC** to avoid rotation issues on the ground.
- the amount of fuel needed to cover the mission must not lead to a reduction in payload.
- the amount of fuel needed to cover the mission must comply with the maximum fuel mass estimated by the **JPAD** weights manager.

According to the imposed constraints, the number of points that satisfy all constraints at the same time is a subpart of the overall response surface as shown in Figure 4.44b and Figure 4.44c. Here the 3D cloud of points is represented in two-dimensional planes: cruise efficiency versus the minimum **SSM** and cruise efficiency versus cruise Mach number. Highlighted circles represent all solutions which comply with assigned constraints. Finally, in Figure 4.44d, solution points compliant with the assumed constraints are highlighted within the whole generated cloud of points. The same set of constraints has been applied also for the rear mounted and three-lifting surfaces configurations.

The optimization process has been mainly focused on aircraft mission performance. Effects of aerodynamics, weight and balance are implicitly included within selected objective functions. In particular, the followings objectives have been considered:

- **MTOW**, to be minimized;
- **TOFL** and **LFL**, to be both minimized ;
- **Time to climb** (from SL to an initial cruise altitude of about 25000ft), to be minimized;
- **Mission block fuel** (and so the amount of pollutant emissions at given engine database), to be minimized.

In these case studies, **DOC** have not been assigned as an objective function because, to comply with the imposed constraints (in particular the cruise speed limitation), their variability has resulted to be very small among all the three considered aircraft configurations.

To summarize, Table 4.24 gathers all the information needed to fully define each of the **MDAO** problems under investigation. Depending on the number of design variables and the related values range, 972 combinations of aircraft parametric models have been analyzed dealing with the high-wing configuration with wing-mounted engines installation, while 6075 and 34020 combinations have been analyzed for the low-wing configuration with rear-mounted engines and the three-lifting surfaces, respectively.

As previously described, each aircraft model coming from design parameters combinations shown in Table 4.24, have been analyzed following the flowchart illustrated in Figure 3.5. However, within the fuel mass iterative loop, a second nested iteration has been carried out to make both the **TOFL** and the cruise Mach number to comply with assigned **TLARs**. In particular, all engines reference static thrusts have been scaled with a step of $\pm 2.5\%$. As explained at the end of Chapter 3, the thrust scaling provides also for new values of engines dry masses and lengths, as well as their related nacelle dimensions. A visual representation of this process is provided in Figure 4.45.

Both the fuel mass loop and performance loop have been limited to a maximum number of iterations equal to 50. All aircraft configurations which have exceed this limitation have been assumed to be unfeasible and a penalty has been added their related objectives during the optimization process.

	Minimum:
Objectives	$f_1 = \text{MTOW}$ $f_2 = \text{TOFL}$ $f_3 = \text{LFL}$ $f_4 = \text{Time to climb}$ $f_5 = \text{Block fuel}$
	with respect to:
Constraints	$\text{SSM} > 0.0\%$ $M_{cr} < 0.68$ $\ X_{LG} - X_{CG_{maxaft}}\ \geq 5\% \text{MAC}$ Estimated TOW < MTOW Estimated mission fuel \leq maximum fuel mass
	by varying:
Design variables (High-wing - Wing-mounted engines)	$b_w \text{ (m)} \in [32.0 \div 35.5]$ with 4 values $X_{LEw} \text{ (m)} \in [13.0 \div 16.0]$ with 9 values $S_w \text{ (m}^2\text{)} \in [94.6 \div 115.7]$ with 3 values $\Lambda_{LEw} \text{ (deg)} \in [2.5 \div 10.0]$ with 3 values $S_h \text{ (m}^2\text{)} \in [16.8 \div 25.2]$ with 3 values
Total number of analyzed aircraft	972
Design variables (Low-wing - Rear-mounted engines)	$b_w \text{ (m)} \in [32.0 \div 35.5]$ with 5 values $X_{LEw} \text{ (m)} \in [18.0 \div 22.0]$ with 9 values $S_w \text{ (m}^2\text{)} \in [82.3 \div 100.6]$ with 3 values $\Lambda_{LEw} \text{ (deg)} \in [2.5 \div 10.0]$ with 3 values $S_h \text{ (m}^2\text{)} \in [31.1 \div 46.5]$ with 3 values $X_{LEh} \text{ (m)} \in [30.0 \div 32.0]$ with 5 values
Total number of analyzed aircraft	6075
Design variables (Three-lifting surfaces)	$b_w \text{ (m)} \in [32.0 \div 35.5]$ with 4 values $X_{LEw} \text{ (m)} \in [19.0 \div 22.0]$ with 7 values $S_w \text{ (m}^2\text{)} \in [82.3 \div 100.6]$ with 3 values $\Lambda_{LEw} \text{ (deg)} \in [2.5 \div 10.0]$ with 3 values $S_h \text{ (m}^2\text{)} \in [31.1 \div 46.5]$ with 3 values $X_{LEh} \text{ (m)} \in [30.0 \div 32.0]$ with 5 values $S_c \text{ (m}^2\text{)} \in [9.3 \div 13.9]$ with 3 values $X_{LEc} \text{ (m)} \in [5.0 \div 8.0]$ with 3 values
Total number of analyzed aircraft	34020

Table 4.24 MDAO problem definition for all high-capacity turboprop configurations.

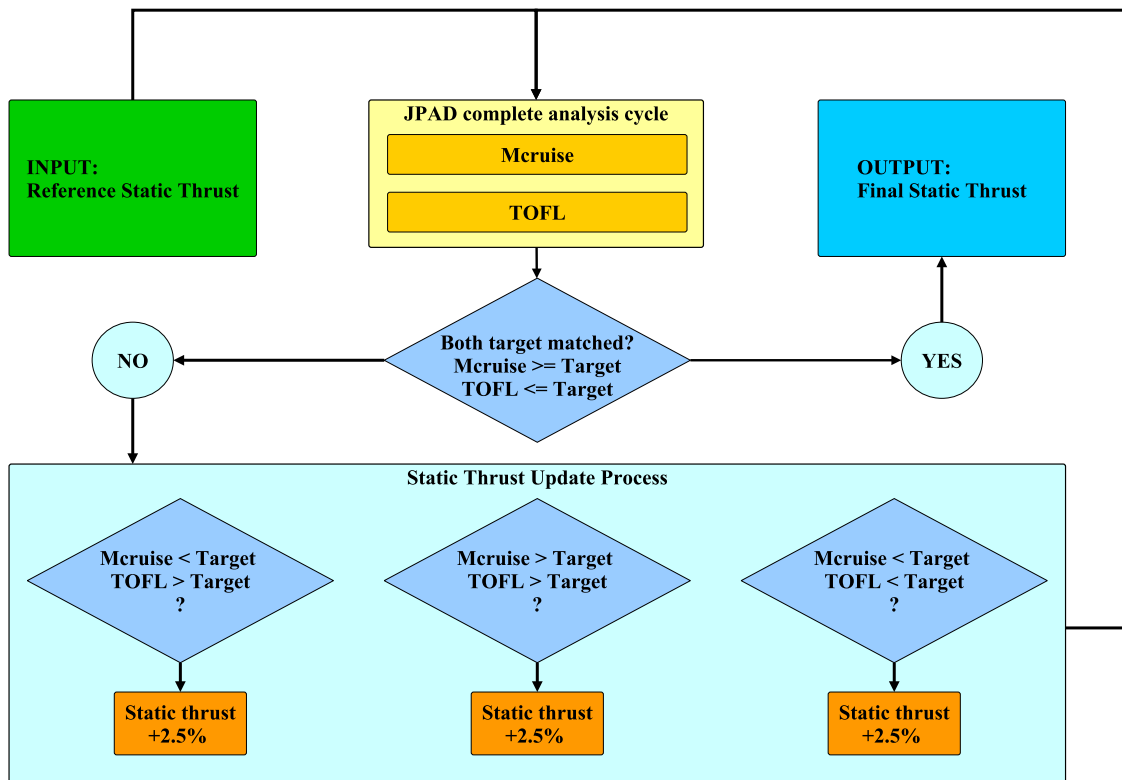


Figure 4.45 Static thrust update process for the MDAO of each high-capacity turboprop configuration.

4.4 Analysis of results

This final section will be dedicated to the analysis of results coming from the MDAO process carried out for the three high-capacity turboprop configurations described in the previous section and core of the work, developed by the author and the DAF group, reported in [1]. For each case an optimum solution will be selected and a comparison among all optima aircraft will be done to assess which configuration provides for the best results in terms of performance. This gives also an answer to the second part of the research question object of this thesis.

However, to have a fully understanding of possible benefits deriving from the adoption of innovative high-capacity turboprop configurations with respect to the state of the art of currently available regional jets, a comparison with the reference regional turbofan, assumed as the Airbus A220-300, will be performed.

Results suitable for this comparison will be taken from the JPAD A220-300 parametric model, described and validated at the beginning of this chapter, considering a new mission range equal to 1600 nm to cope with the TLARs defined in Table 4.22. The comparison will be done both in terms of mission-related quantities, like block fuel and block time, both in terms of capital and cash DOC.

MDAO results

To carry out a complete performance analysis inside JPAD for each high-capacity turboprop aircraft model involved in the MDAO process, the high by-pass ratio turbofan engine database used for the multi-disciplinary analysis cycle of the parametric model concerning the Airbus A220-300 cannot be used anymore.

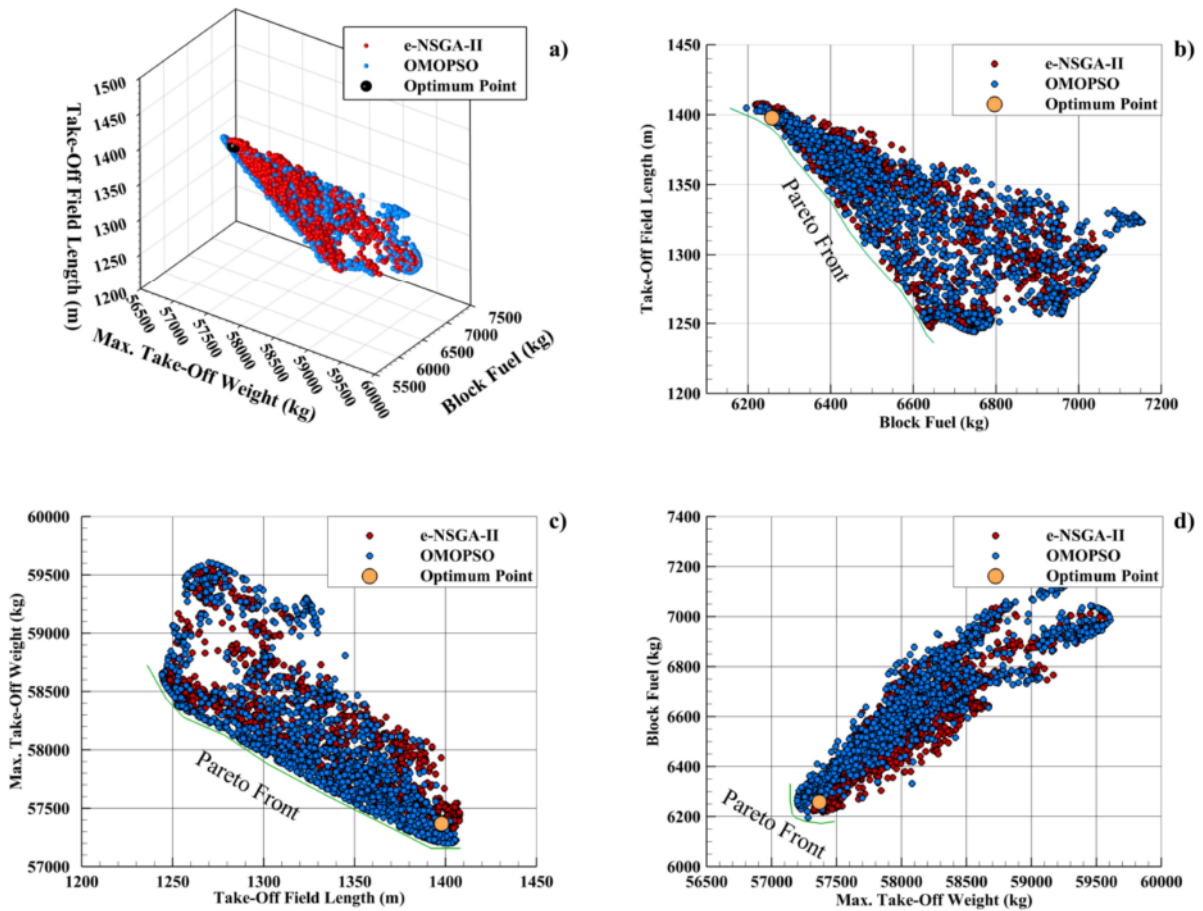


Figure 4.46 High wing with wing-mounted engines configuration. Pareto fronts and the “optimum” point [1].

To overcome this issue, a dedicated turboprop engine database has been generated by modifying a preexisting dataset, created by the DAF group to simulate the behavior of a PW-127 (suitable for turboprop models similar to the ATR-72), making use of the experience gained by the author of this thesis during the first two loops of design activities of the IRON project.

In terms of optimization, as reported in [1], a total of 5000 iterations and a population size of 500 elements have been applied for both ϵ -NSGAI [22] and OMOPSO [23] algorithms used to carry out the multi-objective optimization process inside JPAD.

For the first case study (high-wing configuration with wing-mounted engines) a number of 1483 and 1234 optima solutions have been found by the ϵ -NSGAI algorithm and the OMOPSO algorithm, respectively. The two sets of solutions are compared in Figure 4.46, where the green line represents the Pareto front. By looking at Pareto fronts in two-dimensional planes (see Figure 4.46) several optima solutions could be selected according to a specific objective. It must be remembered that, for a multi-objective optimization, it is a designer’s choice to prefer a solution over another. In this case, the “optimum” solution has been identified to be the one that minimizes the mission block fuel complying, at the same time, with ground performance and the time to climb reported in Table 4.22. The selected point is highlighted with a black sphere in Figure 4.46a and an orange circle in Figure 4.46b to Figure 4.46d. This point belongs to the set of solutions coming from ϵ -NSGAI algorithm, however both optimization algorithms provided very similar results.

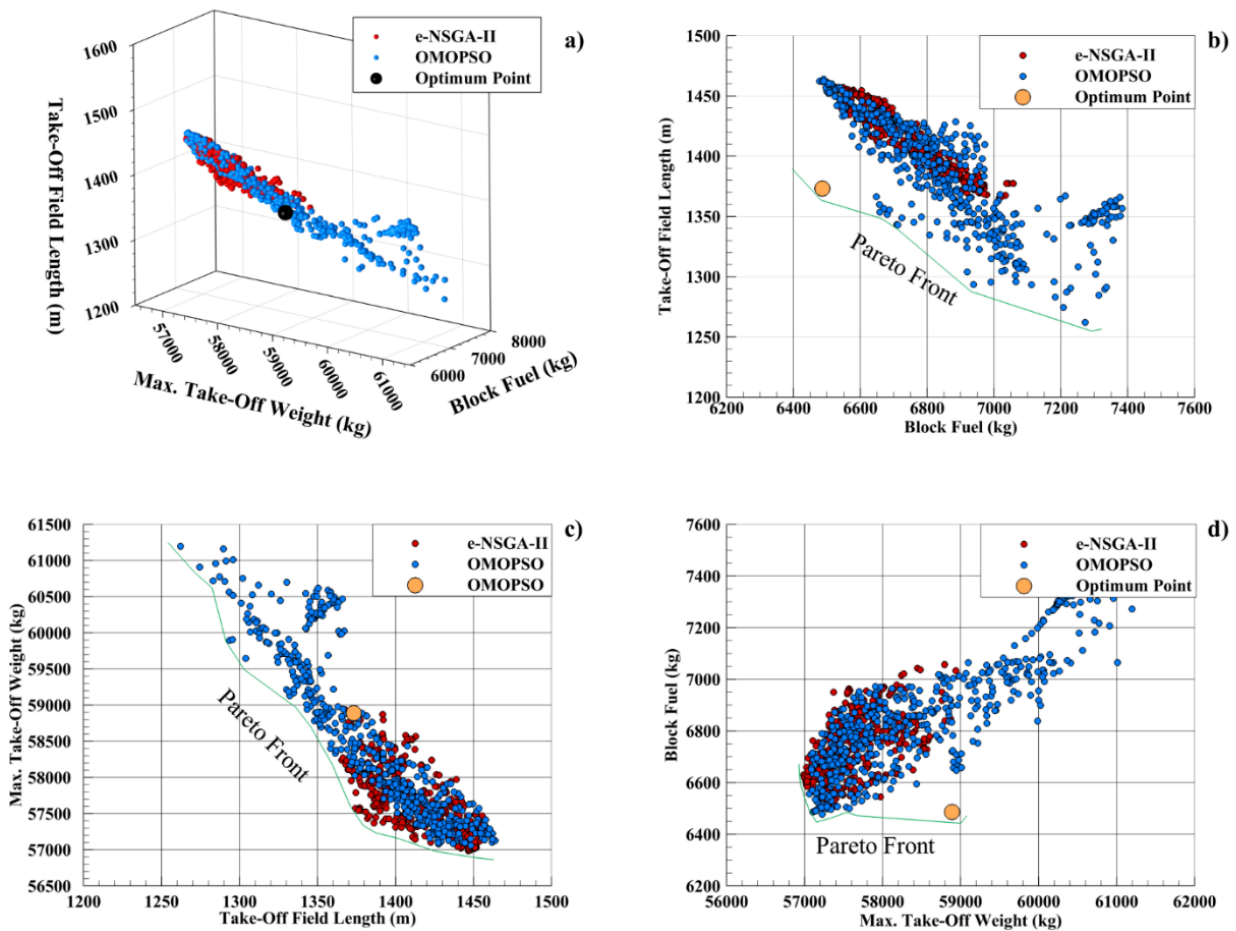


Figure 4.47 Low wing with rear-mounted engines configuration. Pareto fronts and the “optimum” point [1].

The same exercise has been conducted for the rear mounted engines configuration. In this case, starting from a response surface made of 6075 points, genetic algorithm and particle swarm have found 525 and 517 solutions respectively. The reduced number of possible solutions, despite the larger number of possible combinations, highlights that for this configuration the design space (according to assigned constraints and TLARs) is quite reduced. Several possible solutions among with the designer can decide which one is the “optimum” are available in this case too. In the same way of the previous configuration the optimum solution has been identified to be the aircraft that minimizes the block fuel providing for a TOFL and a LFL lower than 1400 m together with a time to climb lower than 16 minutes. This point has been selected among the solutions produced by the particle swarm algorithm (OMOPSO). In Figure 4.47a the “optimum” is highlighted with a black sphere, while from Figure 4.47b to Figure 4.47d it has been highlighted as an orange circle.

Finally, for the last investigated configuration (the three-lifting surfaces) 869 and 436 solutions have been found by applying the ε -NSGAI and OMOPSO algorithms, respectively, starting from a response surface made of 34020 points. This highlights the heavy limitation to the design space imposed by both assigned constraints and TLARs. To select the “optimum” configuration same considerations about the block fuel have driven the selection process. The selected candidate is highlighted in Figure 4.48a with a black sphere, while in two-dimensional Pareto fronts from Figure 4.48b to Figure 4.48d is highlighted with an orange circle.

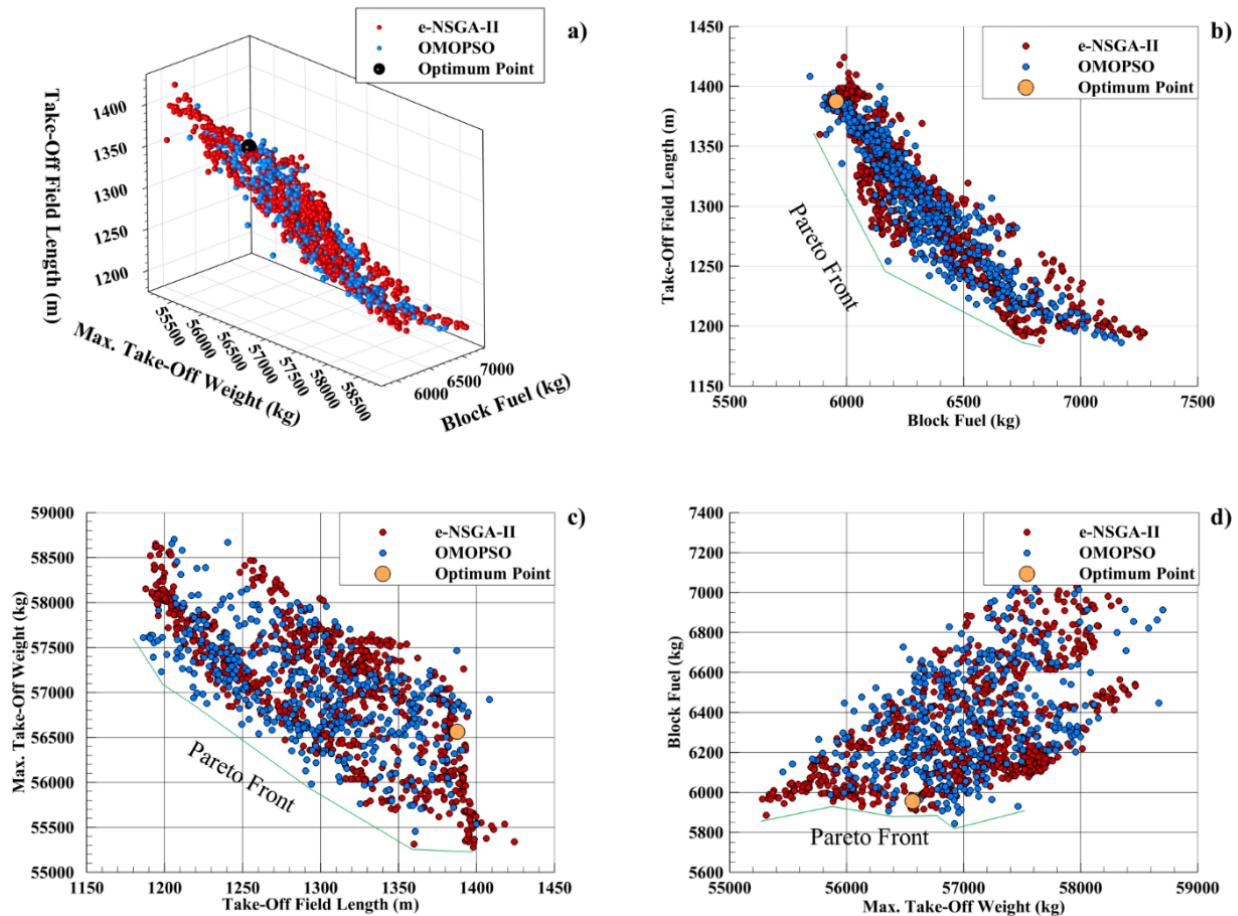


Figure 4.48 Three-lifting surfaces configuration. Pareto fronts and the “optimum” point [1].

Geometry of all optima solutions are compared in Figure 4.49. In addition, their main geometrical characteristics are summarized in Table 4.25. Both the high-wing configuration with wing-mounted engines and the low-wing configuration with rear-mounted engines are characterized by a wing area of about 105 m^2 and a wing aspect ratio of about 12.0, while the three-lifting surfaces aircraft has a reduced wing area (about 100 m^2) thanks to the additional lift contribution provided by the canard.

The two configurations with rear-mounted engines present a very large horizontal tail area (over 40% of the wing area) due to the very large center of gravity excursion, as reported in Table 4.25. Nevertheless, the three-lifting surfaces configuration presents a higher cruise efficiency thanks to the positive effect of the forward lifting surface (the canard) on the global trim drag contribution. It is worth to notice that the total aircraft wetted area (parasite drag) is slightly higher for the three-lifting surfaces compared with the simple rear-mounted engine configuration.

All three optima configurations are stable with respect to the most afterward center of gravity position with a reduced SSM, as shown in Table 4.25. This latter, according to considerations reported in [1], is acceptable and compliant with an improved flight control system which is foreseen for an entry in service 2035.

In terms of DOC, economic assumptions reported in Table 2.8 have been used changing only the fuel price according to the most recent value reported in Table 4.11.

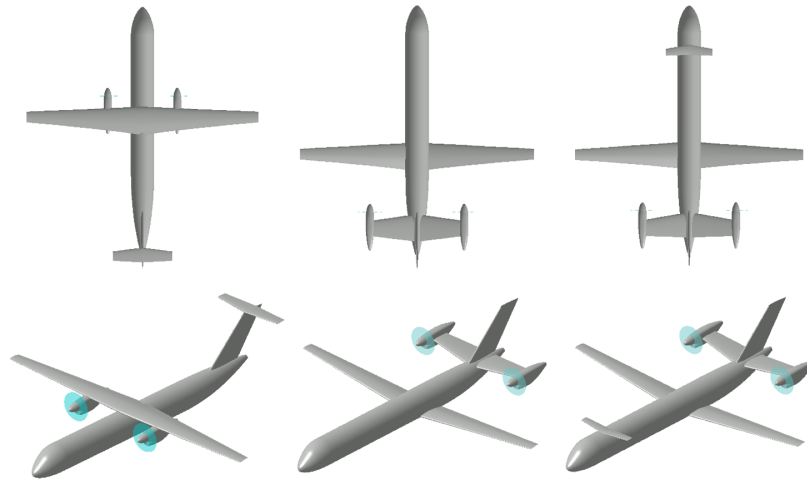


Figure 4.49 Final solution for each aircraft configuration [1].

	Wing-mounted engines	Rear-mounted engines	Three-lifting surfaces
$S_W(m^2)$	104.4	104.6	101.2
$S_H(m^2)$	16.83	46.5	44.82
$S_V(m^2)$	25.0	25.0	25.0
$S_C(m^2)$	—	—	9.37
AR_W	12.07	12.04	12.02
AR_H	5.00	4.40	4.40
AR_V	1.37	1.37	1.37
AR_C	—	—	5.57
l_B (m)	38.04	38.04	38.04
d_B (m)	3.535	3.535	3.535
Single engine static thrust (lbf)	23603	26054	23027
Single engine dry mass (kg)	3367	4122	3297
MTOW (kg)	57419	58794	56640
OEW (kg)	35665	36820	34593
Design Payload (kg)	14040	14040	14040
Max forward X_{CG} (%MAC)	22.7%	8.5%	-21.2%
Max afterward X_{CG} (%MAC)	50.6%	53.9%	23.2%
Operative X_{CG} (%MAC)	43.2%	12.8%	-14.41%
Initial cruise efficiency	16.7	16.6	17.6
Maximum cruise efficiency	18.4	17.8	18.8
SSM (%MAC)	3.64	1.16	1.95
$C_{L_{max,Clean}}$	1.63	1.57	1.79
$C_{L_{max,TO}}$	2.39	2.30	2.52
$C_{L_{max,LND}}$	2.97	2.86	3.10
TOFL (m)	1396	1380	1380
LFL (m)	1339	1384	1336
Time to Climb (min)	15.0	13.0	15.7
Cruise Mach Number	0.64	0.67	0.66
Block time - 1600 nm (min)	239	234	237
Block fuel - 1600 nm (kg)	6259	6479	5958
Total DOC ($\text{\$/seat-nm}$) - 1600 nm	13.02	12.95	12.83
Cash DOC ($\text{\$/seat-nm}$) - 1600 nm	7.68	7.70	7.54

Table 4.25 Multi-disciplinary analysis cycle results of all optima aircraft configurations.

	Wing-mounted engines	Rear-mounted engines	Three-lifting surfaces	Ref. Regional Jet
TOW (kg)	57419 (-3.11%)	58794 (-0.79%)	56640 (-4.42%)	59260
Cruise Mach Number	0.64 (-17.95%)	0.67 (-14.10%)	0.66 (-15.38%)	0.78
Initial cruise efficiency	16.7 (0.0%)	16.6 (-0.60%)	17.6 (+5.38%)	16.7
Relative cruise SFC	-19.22%	-17.02%	-18.56%	—
Utilization (hr/year)	3353 (-0.60%)	3346 (-0.39%)	3350 (-0.51%)	3333
Block Time (min)	239 (+6.22%)	234 (+4.00%)	237 (+5.33%)	225
Block Fuel (kg)	6259 (-10.40%)	6479 (-7.24%)	5958 (-17.24%)	6985
Total DOC (€/seat-nm)	13.02 (-13.37%)	12.95 (-13.84%)	12.83 (-14.63%)	15.03
Cash DOC (€/seat-nm)	7.68 (-7.69%)	7.70 (-7.45%)	7.54 (-9.37%)	8.32

Table 4.26 Optimization results. Comparison between the three optima high-capacity turboprop configurations and the reference regional turbofan platform on a mission of 1600 nm. Percentages are calculated with respect to the reference regional jet aircraft.

Using main performance and **DOC** as rules of comparison between all the three optima high-capacity turboprop configurations, the three-lifting surfaces has proven to be the best solution in agreement with the results obtained from the second design loop of the **IRON** project. In fact, although with very similar values of ground performance among all investigated configurations, the three-lifting surfaces aircraft provides for the lowest value of the block fuel, thanks to the improved cruise aerodynamic efficiency, as well as for the lowest **MTOW**.

The reduced block fuel mass is also linked to the amount of pollutant emissions (at fixed engine database), thus the three-lifting surfaces has resulted to be the greenest of the three investigated configurations. Moreover, thanks to the lighter structure (lowest **OEW**) and the reduced amount of fuel needed for the design mission of 1600 nm, this aircraft platform has provided also for the lowest amounts of total **DOC** and cash **DOC**. Those are mainly influenced by the block fuel mass, the block time as well as by the aircraft utilization, expressed in terms of block hours per year and calculated as proposed in the book by Kundu [127].

Comparisons with the reference regional jet

Finally, a comparison between the three chosen optima configurations and the reference regional jet platform is presented in Table 4.26 considering the design mission range of 1600 nm assumed in Table 4.22. The reference regional jet aircraft model is assumed to fly with a Mach number of 0.78 at the cruise altitude of 37000 ft, as described in the first section of this chapter. However, the payload mass has been modified to comply with the design payload of 14040 kg used for each high-capacity turboprop configuration. As can be seen from Table 4.22, all high-capacity turboprop configurations provides for a beneficial effect on the amount of block fuel related to the design mission of 1600 nm.

Focusing on each turboprop platform, the high-wing configuration with wing-mounted engines has a the biggest advantage in terms of mean cruise **SFC** (-19.22%) and provides for the second best reduction in **TOW** (-3.11%). However, the cruise aerodynamic efficiency shows no improvements, with respect to the reference regional jet, and the cruise Mach number is the lowest among all analyzed turboprop aircraft. Thus, this configuration is the worst in terms of block time providing for an additional little negative effect on the block fuel. From the combination of all these effects, this aircraft may be a good candidate to challenge a regional jet on this kind of missions with an overall

block fuel reduction of -10.40% and only 15 minutes of additional block time. In term of **DOC**, good results have been reached as well with a reduction of -13.37% in total **DOC** and -7.68% in cash **DOC**. However, despite the beneficial effect provided by the smaller block fuel mass, this aircraft is the worst in terms of both utilization and block time leading to the lowest reduction in total **DOC**. On the other hand, being the effect of the block fuel much more effective on the cash **DOC** rather than on the total **DOC**, this configuration provides for a slightly lower cash **DOC** value with respect to the one with low-wing and rear-engine installation.

Moving to the second high-capacity turboprop configuration, the latter has shown the lowest reduction in term of block fuel (-7.24%), with respect to the reference regional jet, since the beneficial effect provided by the smaller value of the mean cruise **SFC** (-17.02%), is mitigated by a very little reduction in **TOW** (.0.79%) and by a lower value of the cruise aerodynamic efficiency (-0.60%). On the other hand, the cruise Mach number has shown to be the greatest among all analyzed turboprop configurations, leading to the lowest increment in block time with respect to the reference regional jet. However, being this effect very limited, the related effect on the block fuel is also very limited. In terms of **DOC**, comparing this configuration with all other turboprop platforms, the lower block time provides for a better value of the utilization parameter which positively affects all costs contributions. Major drawbacks are provided by the increased amount of block fuel (and so of the fuel price) and by the **TOW** (the highest among all turboprop configurations) which influences maintenance costs. However, those effects are smaller than the one provided by the utilization, making this aircraft the second best solution in terms of total **DOC** reduction with respect to the reference regional jet. As for the previous case, the effect of the block fuel on the cash **DOC** is much more effective than on the total **DOC**, providing for the worst reduction of this value.

As stated before, the three-lifting surfaces has resulted to be the best turboprop configuration. This has been further confirmed by the comparison with the reference regional jet, from which this innovative high-capacity turboprop aircraft has highlighted the greatest reduction both in term of block fuel and **DOC**. In particular, this aircraft has provided for a mean cruise **SFC** reduction similar to the first configuration (-18.56% instead of -19.22%) together with the lowest value of the **TOW** and the highest value of the cruise aerodynamic efficiency (-4.42% and +5.38%, respectively, if compared to the reference regional jet). A cruise Mach number slightly lower than the second configuration has led to values of both block time and utilization intermediate between the first two analyzed aircraft. From the combination of all the above-mentioned positive effects together with the calculated values of the block time and the utilization parameter, the three-lifting surface configuration has experienced beneficial effects on all costs contributions.

4.5 Candidate's contribution to the applications chapter

This chapter has shown how the research problem has been investigated providing also an answer to the research question formulated at the beginning of this thesis. Although all activities described in this chapter have been performed by the author, the generation of the set of **TLARs** for the high-capacity turboprop as well as the definition of the set of assumptions reported in Table 4.23 has been carried out with the support of professor Fabrizio Nicolosi and Salvatore Corcione of the **DAF** research group.

Below the reader can find a summary of the activities performed by the author to answer the research question of this thesis.

- Multi-disciplinary analysis of the Airbus A220-300 parametric model using **JPAD**.
- Selection of the three high-capacity turboprop aircraft configurations to be used in the **MDAO** process.
- **MDAO** process of the three high-capacity turboprop configurations under investigation and comparison with the A220-300 analysis results.

List of publications involving the candidate and his contribution

- Nicolosi F., Corcione S., **Trifari V.**, Della Vecchia P., and De Marco A. «Design Guidelines for High Capacity Innovative Regional Turboprop Aircraft». In: *AIAA Scitech 2019 Forum*. American Institute of Aeronautics and Astronautics, 2019. DOI: 10.2514/6.2019-0256.
 - Candidate's contribution is related to the selection of the three high-capacity turboprop aircraft configurations to be used in the **MDAO** process as well as to the **MDAO** process carried out for each of the three high-capacity turboprop configurations under investigation.

Chapter **5**

CONCLUSIONS

After an in-depth market analysis, carried out in the first chapter of this thesis to investigate the current regional aircraft segment scenario, the following research question has been formulated: “What could be the impact, in terms of performance, that innovative high-capacity turboprop aircraft configurations can have on the current regional aircraft scenario?”.

Furthermore, to better investigate this topic, this question has been specialized in: “Which high-capacity turboprop configuration could be the one that maximizes potential performance advantages with respect to the state of the art of current regional jet aircraft?”

To fully answer those questions, the second chapter of this thesis has firstly shown all main outcomes related to the preliminary design activities carried out by the author, together with the **DAF** research group of the Department of Industrial Engineering of the University of Naples Federico II, during the first two loops of the European Clean Sky 2 project named **IRON**. As a result, a three-lifting surfaces high-capacity turboprop configuration has appeared to be a very promising solution for regional applications, reaching the Clean Sky 2 target block fuel reduction of -25% (with respect to a 2014 reference aircraft assumed as the Airbus A220-300) on both the design mission range of 1600 nm and the typical mission range of 400 nm (see Table 2.22 and Table 2.23).

In addition, as reported in Table 2.24 and Table 2.25, this configuration has provided also for both total and cash **DOC** reductions. However, at the end of the second loop of the **IRON** project, one main aspect could have been better investigated to further elaborate on this topic. This concerned the assessment of the reference regional jet used to make all the above-mentioned comparisons.

Parallel to the activities of the **IRON** project, the author of this thesis and other members of the **DAF** group have been involved in the development of a new multi-disciplinary analysis and optimization software for aircraft preliminary design applications named **JPAD**.

The third chapter of this thesis has been completely dedicated to the description of this software, highlighting its structure and capabilities as well as giving a comprehensive overview of the current state of the art related to the preliminary design and **MDAO** software scenario. Most of the results, mainly in terms of performance, generated for the **IRON** project have been calculated using **JPAD**.

Making use of the experience gained during the **IRON** project, as well as by using the **JPAD** software, the research question, object of this thesis, has been addressed in the fourth chapter. Firstly, to have a better term of comparison, with respect to the one used in the **IRON** project, a case study concerning the Airbus A220-330 has been presented. Here, the synergy between two European Clean Sky 2 projects has led to interesting outcomes. On one side the **IRON** project had allowed the development of **JPAD**; on the other side, the participation of the **DAF** group in the **ADORNO** project had allowed to increase the research group's knowledges concerning modern high by-pass ratio geared turbofan engines, leading to the definition of an improved engine database suitable for **JPAD** analyses. In particular, lower values of the cruise **SFC** have been obtained with an averaged reduction of about -6% with respect to the database used in the **IRON** project.

Once the reference aircraft has been validated, a set of **TLARs** suitable for modern regional transport applications have been assessed using the one coming from the **IRON** project as reference. Then, following the work presented by NASA in [20], three high-capacity turboprop configurations have been generated: a traditional high-wing layout with wing-mounted engines; an innovative low-wing configuration with engines mounted at the tip of the horizontal tail; and a three-lifting surfaces aircraft following the promising results of the **IRON** project. For each of those a complete **MDAO** process has been carried out using the **JPAD** software to select three optima solutions.

From the comparison between these optimized aircraft and the refined A220-300 **JPAD** model, the three-lifting surfaces has been confirmed to be the most promising candidate to challenge a regional jet on a design mission of 1600 nm providing for a block fuel reduction of -17.24% and only 13 minutes of additional block time. In addition, assuming all economic assumptions made for the **IRON** project and reported in Table 2.8, the three-lifting surface has also provided for a reduction in both total and cash **DOC** values of -14.63% and -9.37% respectively. Those results are in line with the outcomes of the second design loop of the **IRON** project. However, having refined the reference regional jet aircraft model, the expected reduction in block fuel resulted to be much lower, making impossible to reach the initial target value of -25%. On the other hand, from the refinement of the A220-300 economic assumptions (see Table 4.11), both the total and the cash **DOC** reductions have provided for much higher values than the ones calculated for the **IRON** project.

In conclusion, this thesis has shown that, under certain assumptions, the use of an innovative high-capacity turboprop configuration, rather than the state of the art of regional turbofan aircraft represented here by the Airbus A220-300, could allow to save up to 17.24% of the block fuel on a design mission of 1600 nm with an additional beneficial effect in terms of total and cash **DOC** values, estimated as -14.63% and -9.37% respectively. In addition, from the comparison of several possible high-capacity turboprop aircraft, selected to be compliant with an entry in service 2035, the three-lifting surfaces configuration has resulted to be the best both in terms of performance and **DOC**.

Future research works, which can be directly linked to the outcome of this thesis, could be addressed to the investigation of some detailed aspects of the final three-lifting surfaces configuration not considered in the scope of this thesis. One example may be related to structural and aeroelastic analyses of the horizontal tail with tip-mounted propellers; while another interesting aspect can be related to a detailed assessment of all on-board systems masses and center of gravity positions aimed at optimizing the center of gravity excursion of this kind of configuration.

Beside the answer to the initial research question, an added value provided by the author of this thesis has been the development, together with the **DAF** group, of the multi-disciplinary analysis and

optimization software, **JPAD**, as the result of a fruitful combination between Aerospace Engineering and Software Engineering.

In terms of software development, future activities will be addressed to the implementation of new analysis modules inside **JPAD** making use of the experience gained by the **DAF** group from ongoing research projects. In particular, a dedicated environmental noise calculator as well as an engine design suite could be integrated in the next few years following the development of the **ADORNO** project. Furthermore, due to the increasing interest toward the design of hybrid-electric aircraft, the development of **JPAD** will be surely oriented in this direction in order to have a mature, efficient and robust tool suitable for all incoming aircraft design challenges.

ACKNOWLEDGEMENTS

The research activities concerning the **IRON** project, reported in the second chapter of this thesis, have been performed in the framework of the REG GAM 2018 project which has received funding from the Clean Sky 2 Joint Undertaking under the European Union's Horizon 2020 research and innovation program under Grant Agreement n° 807089. The author is grateful to the partners of the **IRON** consortium for their contributions and feedback.

In addition, the author wants to thank also the engine manufacturer MTU, partner of the **ADORNO** project, for the support provided to the improvement of the engine database used in the case study of the Airbus A220-300 aircraft model shown in chapter 4. The **ADORNO** project has received funding from the Clean Sky 2 Joint Undertaking under the European Union's Horizon 2020 research and innovation program under Grant Agreement ENG ITD n° 821043.

REFERENCES

- [1] Nicolosi F., Corcione S., Trifari V., Della Vecchia P., and De Marco A. «Design Guidelines for High Capacity Innovative Regional Turboprop Aircraft». In: *AIAA Scitech 2019 Forum*. American Institute of Aeronautics and Astronautics, 2019. DOI: 10.2514/6.2019-0256.
- [2] Air Transport Action Group. *Climate Change*. 2020. URL: <https://www.atag.org/our-activities/climate-change.html>.
- [3] European Commision. *Clean Sky 2 Joint Undertaking Development Plan*. 2017. URL: <https://www.cleansky.eu/sites/default/files/inline-files/51.%20CS2DP%20December%202017.pdf>.
- [4] Embraer S.A. *Market Outlook 2019*. 2019. URL: <https://www.embraermarketoutlook2019.com>.
- [5] ATR Aircraft. *Turboprop market forecast 2018-2037*. 2018. URL: <http://www.atraircraft.com/turboprop-market-forecast.html>.
- [6] Cooper T., Smiley J., Porter C., and Precourt C. *Global fleet & MRO market forecast commentary 2018-2028*. 2018. URL: https://www.oliverwyman.com/content/dam/oliverwyman/v2/publications/2018/January/2018-2028_Global_Fleet_MRO_Market_Forecast_Commentary_Public_Final_web.pdf.
- [7] Airbus S.A.S. *Global Market Forecast 2018-2037*. 2018. URL: <https://www.airbus.com/aircraft/market/global-market-forecast.html>.
- [8] Bombardier Commercial Aircraft. *Market Forecast 2017-2036*. 2017. URL: <https://ir.bombardier.com/var/data/gallery/document/01/87/55/05/15/BCA-2017-2036-Market-Forecast-EN.pdf>.
- [9] European Commision. *Horizon 2020*. 2019. URL: <https://ec.europa.eu/programmes/horizon2020/en/area/transport>.
- [10] Nicolosi F., Corcione S., Della Vecchia P., Trifari V., and Ruocco M. «Aerodynamic design and analysis of an innovative regional turboprop configuration». In: *31st Congress of the International Council of the Aeronautical Sciences, ICAS 2018*. International Council of the Aeronautical Sciences, 2018. ISBN: 9783932182884.

- [11] Nicolosi F., Corcione S., Trifari V., Cusati V., Ruocco M., and Della Vecchia P. «Performance evaluation and DOC estimation of an innovative turboprop configuration». In: *2018 Aviation Technology, Integration, and Operations Conference*. American Institute of Aeronautics and Astronautics, 2018. DOI: <https://doi.org/10.2514/6.2018-3662>.
- [12] Nicolosi F., Corcione S., Della Vecchia P., Trifari V., Ruocco M., and De Marco A. «Design and aerodynamic analysis of a regional turboprop innovative configuration». In: *6th CEAS Air and Space Conference (CEAS 2017)*. Elsevier Procedia, 2017. ISBN: 9781510858794.
- [13] Drela M. *MSES - Software for high-lift multielement airfoil configurations*. 2019. URL: <https://tlo.mit.edu/technologies/mses-software-high-lift-multielement-airfoil-configurations>.
- [14] Perkins C.D. and Hage R. *Airplane Performance Stability and Control*. John Wiley and Sons Inc., 1949. ISBN: 9780471680468.
- [15] Sforza P. *Commercial Airplane Design Principles*. Elsevier, 2014. ISBN: 9780124199774.
- [16] Multhopp H. *Aerodynamic of the Fuselage*. Tech. rep. TM-1036. NACA, 1942.
- [17] Nicolosi F., Della Vecchia P., Ciliberti D., and Cusati V. «Fuselage Aerodynamic Prediction Methods». In: *Aerospace Science and Technology (Elsevier) AESCTE 55* (2016), pp. 322–343. DOI: <https://doi.org/10.1016/j.ast.2016.06.012>.
- [18] Roskam J. *Airplane Design: Preliminary Calculation of Aerodynamic, Thrust and Power Characteristics, Part VI*. DARCorporation, 1971. ISBN: 9781884885525.
- [19] Slingerland R. «Prediction of a tail downwash, ground effect and minimum unstick speed of jet transport aircraft». Doctoral thesis. Faculty of Aerospace Engineering, TU Delft, 2005. ISBN: 9090195513. URL: <http://resolver.tudelft.nl/uuid:6f647fd6-7cda-4351-b9e2-701b560055e1>.
- [20] Goldsmith I.M. *A Study to Define the Research and Technology Requirements for Advanced Turbo/Propfan Transport Aircraft*. Tech. rep. CR-166138. NASA, 1981. URL: <https://ntrs.nasa.gov/archive/nasa/casi.ntrs.nasa.gov/19820010328.pdf>.
- [21] Hadka D. *MOEA Framework, A Free and Open Source Java Framework for Multiobjective Optimization*. 2017. URL: <http://moeaframework.org/>.
- [22] Kollat J.B. and Reed P.M. «Comparison of Multi-Objective Evolutionary Algorithms for Long-Term Monitoring Design». In: *Advances in Water Resources* 26 (2006), pp. 792–807. DOI: [https://doi.org/10.1061/40792\(173\)359](https://doi.org/10.1061/40792(173)359).
- [23] Sierra M.R. and Coello Coello C.A. «Improving PSO-based multi-objective optimization using crowding, mutation and ϵ -dominance». In: *Evolutionary Multi-Criterion Optimization*. Springer, 2005. DOI: https://doi.org/10.1007/978-3-540-31880-4_35.
- [24] Jenkinson L.R., Simkin P., and Rhodes D. *Civil Jet Aircraft Design*. Butterworth-Heinemann, 1999. ISBN: 9780340741528.

- [25] Torenbeek E. *Synthesis of subsonic airplane design: an introduction to the preliminary design of subsonic general aviation and transport aircraft, with emphasis on layout, aerodynamic design, propulsion and performance*. Springer Netherlands, 1982. ISBN: 9789024727247. DOI: [10.1007/978-94-017-3202-4](https://doi.org/10.1007/978-94-017-3202-4).
- [26] Corcione S., Nicolosi F., and Della Vecchia P. «High Lift Aerodynamic characteristics of a Three Lifting Surfaces Turboprop Aircraft». In: *2019 Aviation Technology, Integration, and Operations Conference*. American Institute of Aeronautics and Astronautics, 2019. DOI: [10.2514/6.2019-2884](https://doi.org/10.2514/6.2019-2884).
- [27] Roskam J. *Airplane Flight Dynamics & Automatic Flight Controls*. DARcorporation, 1998. ISBN: 9781884885174.
- [28] Silverstein A. and Katzoff S. *Design charts for predicting downwash angles and wake characteristics behind plain and flapped wings*. Tech. rep. 648. NACA, 1939.
- [29] Silverstein A. *Downwash and wake behind plain and flapped wings*. Tech. rep. 651. NACA, 1939.
- [30] Fink R. *USAF Stability and Control DATCOM*. Tech. rep. AFWAL-TR-83-3048. Wright-Patterson Air Force Base, McDonnell Douglas Corporation, Ohio, 1978.
- [31] Phillips J.D. *Downwash in the plane of symmetry of an elliptically loaded wing*. Tech. rep. TP-2414. NASA, 1985.
- [32] Phillips J.D. *Approximate neutral point of a subsonic canard aircraft*. Tech. rep. TM-86694. NASA, 1985.
- [33] David W. Levy. «Prediction of Average Downwash Gradient for Canard Configurations». In: *30th Aerospace Sciences Meeting & Exhibit*. American Institute of Aeronautics and Astronautics, 1992. DOI: <https://doi.org/10.2514/6.1992-284>.
- [34] Kintscher M., Wiedemann M., Monner H., Heintze O., and T. Kühn. «Design of a smart leading edge device for low speed wind tunnel tests in the European project SADE». In: *International Journal of Structural Integrity* 2.4 (2011), pp. 383–405. DOI: [10.1108/17579861111183911](https://doi.org/10.1108/17579861111183911). URL: <https://doi.org/10.1108/17579861111183911>.
- [35] García-Mayoral R. and Jiménez J. «Drag reduction by riblets». In: *Philosophical transactions. Series A, Mathematical, physical, and engineering sciences* 369 (2011), pp. 1412–27. DOI: [10.1098/rsta.2010.0359](https://doi.org/10.1098/rsta.2010.0359).
- [36] Walsh M.J. «Riblets as a Viscous Drag Reduction Technique». In: *AIAA Journal* 21.4 (1983), pp. 485–486. DOI: [10.2514/3.60126](https://doi.org/10.2514/3.60126).
- [37] Mele B., Russo L., and Tognaccini R. «Drag bookkeeping on an aircraft with riblets and NLF control». In: *Aerospace Science and Technology* 98 (2020). DOI: [10.1016/j.ast.2020.105714](https://doi.org/10.1016/j.ast.2020.105714). URL: <https://doi.org/10.1016/j.ast.2020.105714>.
- [38] Barnwell R.W. and Hussaini M.Y. *Natural Laminar Flow and Laminar Flow Control*. Springer Science & Business Media, 2012. ISBN: 9781461277033.

- [39] Mele B. and Tognaccini R. «Numerical Simulation of Riblets on Airfoils and Wings». In: *50th AIAA Aerospace Sciences Meeting including the New Horizons Forum and Aerospace Exposition*. DOI: [10.2514/6.2012-861](https://doi.org/10.2514/6.2012-861).
- [40] Mele B., Tognaccini R., and Catalano P. «Performance Assessment of a Transonic Wing–Body Configuration with Riblets Installed». In: *Journal of Aircraft* 53.1 (2016), pp. 129–140. DOI: [10.2514/1.C033220](https://doi.org/10.2514/1.C033220).
- [41] Mele B. and Tognaccini R. «Slip Length–Based Boundary Condition for Modeling Drag Reduction Devices». In: *AIAA Journal* 56.9 (2018), pp. 3478–3490. DOI: [10.2514/1.J056589](https://doi.org/10.2514/1.J056589).
- [42] Trifari V., Ruocco M., Cusati V., Nicolosi F., and De Marco A. «Multi-disciplinary analysis and optimization Java tool for aircraft design». In: *31st Congress of the International Council of the Aeronautical Sciences, ICAS 2018*. International Council of the Aeronautical Sciences, 2018. ISBN: 9783932182884.
- [43] TXT Group. *Pacelab APD*. 2019. URL: <https://www.txtgroup.com/markets/solutions/pacelab-apd/>.
- [44] Stanford Aerospace Design Lab. *SUAVE*. 2019. URL: <http://suave.stanford.edu/>.
- [45] Filippone A. *Advanced Aircraft Flight Performance*. Cambridge University Press, 2012. ISBN: 9781107024007.
- [46] University of Manchester. *FLIGHT*. 2019. URL: <http://www.flight.mace.manchester.ac.uk/index.html>.
- [47] Nicolosi F. and Paduano G. «Development of a software for aircraft preliminary design and analysis». In: *3rd CEAS (Council of European Aerospace Societies) Congress*. 2011. ISBN: 9788896427187.
- [48] CFS Engineering. *CEASIOM*. 2019. URL: <https://www.ceasium.com/wp/>.
- [49] Zhang M., Rizzi A.W., Nicolosi F., and De Marco A. «Collaborative Aircraft Design Methodology using ADAS Linked to CEASIOM». In: *32nd AIAA Applied Aerodynamics Conference*. American Institute of Aeronautics and Astronautics, 2012. DOI: <https://doi.org/10.2514/6.2014-2012>.
- [50] Lissys Ltd. *Piano*. 2014. URL: <http://www.piano.aero/>.
- [51] Optimal Aircraft Design (OAD). *ADS - Aircraft Design Software*. 2016. URL: <http://www.pca2000.com/en/index.php>.
- [52] DARCorporation. *AAA - Advanced Aircraft Analysis*. 2019. URL: <https://www.darcorp.com/advanced-aircraft-analysis-software/>.
- [53] Raymer D. *RDS-win aircraft design software*. 2019. URL: <http://www.aircraftdesign.com/rds.shtml>.
- [54] Trifari V., Ruocco M., Cusati V., Nicolosi F., and De Marco A. «Java Framework for Parametric Aircraft Design – Ground Performance». In: *Aircraft Engineering and Aerospace Technology* 89.4 (2017), pp. 599–608. DOI: <http://dx.doi.org/10.1108/AEAT-11-2016-0209>.

- [55] Ciliberti D., Della Vecchia P., Nicolosi F., and De Marco A. «Aircraft directional stability and vertical tail design: A review of semi-empirical methods». In: *Progress in Aerospace Sciences* 95 (2017), pp. 140–172. DOI: <http://dx.doi.org/10.1016/j.paerosci.2017.11.001>.
- [56] Nicolosi F., Della Vecchia P., and Ciliberti D. «Aerodynamic interference issues in aircraft directional control». In: *Journal of Aerospace Engineering* 28.1 (2015). DOI: [https://doi.org/10.1061/\(ASCE\)AS.1943-5525.0000379](https://doi.org/10.1061/(ASCE)AS.1943-5525.0000379).
- [57] Nicolosi F., Della Vecchia P., Ciliberti D., and Cusati V. «Development of new preliminary design methodologies for regional turboprop aircraft by means of CFD analyses». In: *29th Congress of the International Council of the Aeronautical Sciences, ICAS 2014*. International Council of the Aeronautical Sciences, 2014. DOI: <https://doi.org/10.13140/2.1.5147.0721>.
- [58] Nicolosi F., Della Vecchia P., and Corcione S. «Design and aerodynamic analysis of a twin-engine commuter aircraft». In: *Aerospace Science and Technology* 40 (2015), pp. 1–16. DOI: <https://doi.org/10.1016/j.ast.2014.10.008>.
- [59] Nicolosi F., Corcione S., and Della Vecchia P. «Commuter aircraft aerodynamic characteristics through wind tunnel tests». In: *Aircraft Engineering and Aerospace Technology* 88.4 (2016), pp. 523–534. DOI: <https://doi.org/10.1108/AEAT-01-2015-0008>.
- [60] Nicolosi F., De Marco A., Della Vecchia P., and Sabetta V. «Roll performance assessment of a light aircraft: flight simulations and flight tests». In: *Aerospace Science and Technology* 76 (2018), pp. 471–483. DOI: <https://doi.org/10.1016/j.ast.2018.01.041>.
- [61] Coiro D. and Nicolosi F. «Design of Low-Speed Aircraft by Numerical and Experimental Techniques Developed at DPA». In: *Aircraft Design Journal* 4.1 (2001), pp. 1–18. DOI: [https://doi.org/10.1016/S1369-8869\(00\)00020-3](https://doi.org/10.1016/S1369-8869(00)00020-3).
- [62] Pascale L. and Nicolosi F. «Design and aerodynamic analysis of a light twin-engine propeller aircraft». In: *26th Congress of International Council of the Aeronautical Sciences, ICAS 2008*. International Council of the Aeronautical Sciences, 2008. ISBN: 0953399192.
- [63] Nicolosi F., Ciliberti D., Della Vecchia P., and Corcione S. «Wind tunnel testing of a generic regional turboprop aircraft modular model and development of improved design guidelines». In: *AIAA Aviation and Aeronautics Forum and Exposition*. American Institute of Aeronautics and Astronautics, 2018. DOI: <https://doi.org/10.2514/6.2018-2855>.
- [64] Della Vecchia P. and Nicolosi F. «Aerodynamic guidelines in the design and optimization of new regional turboprop aircraft». In: *Aerospace Science and Technology (AESCTE)* 38 (2014), pp. 88–104. DOI: <https://doi.org/10.1016/j.ast.2014.07.018>.
- [65] Coiro D., Nicolosi F., and Grasso F. «Design and Testing of Multi-Element Airfoil for Short-Takeoff-and-Landing Ultralight Aircraft». In: *Journal of Aircraft* 46.5 (2009), pp. 1795–1807. DOI: <https://doi.org/10.2514/1.43429>.
- [66] Della Vecchia P., Corcione S., Pecora R., Nicolosi F., Dimino I., and Concilio A. «Design and integration sensitivity of a morphing trailing edge on a reference airfoil: The effect on high-altitude long-endurance aircraft performance». In: *Journal of Intelligent Material Systems and Structures* 28.20 (2017), pp. 2933–2946. DOI: <https://doi.org/10.1177/1045389X17704521>.

- [67] Della Vecchia P. and Nicolosi F. «Aerodynamic guidelines in the design and optimization of new regional turboprop aircraft». In: *Aerospace Science and Technology* 38 (2014), pp. 88–104. DOI: <https://doi.org/10.1016/j.ast.2014.07.018>.
- [68] Oracle. *JavaFX: Getting Started with JavaFX*. 2014. URL: <https://docs.oracle.com/javase/8/javafx/get-started-tutorial/jfx-overview.htm#JFXST784>.
- [69] OPEN CASCADE SAS. *OPEN CASCADE*. 2018. URL: <https://www.opencascade.com/>.
- [70] Mohamed Fayad and Douglas C. Schmidt. «Object-oriented Application Frameworks». In: *Commun. ACM* 40.10 (1997), pp. 32–38. ISSN: 0001-0782. DOI: <http://doi.acm.org/10.1145/262793.262798>.
- [71] Ashwin U. «Object-Oriented Programming and its Concepts». In: *International Journal of Innovation and Applied Studies* 26.1 (2016), pp. 1–6. ISSN: 2028-9324. URL: <http://www.ijisr.issr-journals.org/abstract.php?article=IJISR-15-338-03>.
- [72] TIOBE. *TIOBE Index for March 2020*. 2020. URL: <https://www.tiobe.com/tiobe-index/>.
- [73] Nicolosi F., De Marco A., Attanasio L., and Della Vecchia P. «Development of a Java-Based Framework for Aircraft Preliminary Design and Optimization». In: *Journal of Aerospace Information Systems* 13.6 (2016), pp. 234–242. DOI: <https://doi.org/10.2514/1.I010404>.
- [74] Carmichael R. *USAF Digital Datcom*. 2013. URL: <http://www.pdas.com/datcom.html>.
- [75] Gluon. *Scene Builder*. 2019. URL: <https://gluonhq.com/products/scene-builder/>.
- [76] Apache Software Foundation. *Apache Groovy*. 2019. URL: <http://groovy-lang.org/>.
- [77] Kotlin Foundation. *Kotlin*. 2019. URL: <https://kotlinlang.org/>.
- [78] Gradle Inc. *Gradle User Manual*. 2019. URL: <https://docs.gradle.org/current/userguide/userguide.html>.
- [79] De Marco. A, Di Stasio M., Della Vecchia P., Trifari V., and Nicolosi F. «Automatic modeling of aircraft external geometries for preliminary design workflows». In: *Aerospace Science and Technology* (2020). DOI: [10.1016/j.ast.2019.105667](https://doi.org/10.1016/j.ast.2019.105667).
- [80] Gudmundsson S. *General Aviation Aircraft Design: Applied Methods and Procedures*. Elsevier Science, 2013. ISBN: 9780123973290.
- [81] Amadori K. «On Aircraft Conceptual Design. A Framework for Knowledge Based Engineering and Design Optimization». PhD. Department of Management and Engineering, Linköpings Universitet, SE-581 83 Linköping, Sweden: Linköping University Institute of Technology, May 2008. ISBN: 9789173938808.
- [82] Haimes R. and Drela M. «On the construction of aircraft conceptual geometry for high-fidelity analysis and design». In: *50th AIAA Aerospace sciences meeting including the new horizons forum and aerospace exposition*. 2012, p. 683.
- [83] Abbott I.H. and Von Doenhoff A.E. *Theory of Wing Sections*. Dover Publications, 1959. ISBN: 9780486605869.
- [84] Carichner G. and Nicolai L. *Fundamentals of aircraft and aircraft design*. AIAA, 2013. ISBN: 9781600867514. DOI: <https://doi.org/10.2514/4.867538>.

- [85] Raymer D. *Aircraft Design: A Conceptual Approach*. 5th ed. AIAA Education, 2012. ISBN: 9781600869112.
- [86] Sadraey M. *Aircraft design: A Systems Engineering Approach*. John Wiley & Sons Inc, 2012. ISBN: 9781119953401.
- [87] Howe D. *Aircraft conceptual design synthesis*. John Wiley & Sons Inc, 2000. ISBN: 9781860583018.
- [88] Torenbeek E. *Advanced Aircraft Design: Conceptual Design, Analysis and Optimization of Subsonic Civil*. John Wiley & Sons Inc, 2013. ISBN: 9781118568118.
- [89] Currey N.S. *Aircraft landing gear design : Principles and practices*. American Institute of Aeronautics and Astronautics, 1988. ISBN: 9780930403416.
- [90] Mecham M. «Airport Officials: Superjumbos Mean New Headaches». In: *Aviation Week and Space Technology* 141.21 (1994), pp. 76–80.
- [91] Horonjeff R. and McKelvey F.X. *Planning and Design of Airports*. McGraw-Hill, 1994. ISBN: 9780071446419.
- [92] Ruocco M. «High lift and stability issues for innovative transport aircraft configurations in aerodynamic design». PhD. Department of Industrial Engineering, University of Naples Federico II, Naples, Italy: University of Naples Federico II, 2020.
- [93] Hurt H.H. *Aerodynamics for Naval Aviators*. FAA Handbooks Series. Aviation Supplies & Academics, 1992. ISBN: 9781560271406.
- [94] Pierluigi Della Vecchia, Fabrizio Nicolosi, and Danilo Ciliberti. «Aircraft directional stability prediction method by CFD». In: *33rd AIAA Applied Aerodynamics Conference*. 2015. DOI: 10.2514/6.2015-2255. URL: <https://arc.aiaa.org/doi/abs/10.2514/6.2015-2255>.
- [95] Pinsker W.J.G. *The Landing Flare of Large Transport Aircraft*. Tech. rep. Reports and Memoranda No. 3602. Aerodynamics Dept., R.A.E., Bedford, 1967, p. 37. URL: <http://naca.central.cranfield.ac.uk/reports/arc/rm/3602.pdf>.
- [96] Young T.M. *Performance of the Jet Transport Airplane: Analysis Methods, Flight Operations, and Regulations*. Aerospace Series. Wiley, 2017. ISBN: 9781118384862.
- [97] Sadraey M. *Spoiler Design*. Tech. rep. Daniel Webster College. URL: <https://docplayer.net/25341921-Spoiler-design-mohamad-sadraey-daniel-webster-college.html>.
- [98] Jenkinson L.R. and Marchman J. *Aircraft Design Projects: For Engineering Students*. Elsevier, 2003. ISBN: 9780080498959.
- [99] De Baudus L. and Castaigns P. «Control your speed...in cruise». In: *Safety First* 21 (2016), pp. 7–21. URL: https://safetyfirst.airbus.com/app/themes/mh_newsdesk/pdf/safety_first_21.pdf.
- [100] Blake W. and Performance Training Group. *Jet transport performance methods*. Tech. rep. D6–1420. Boeing Company, Flight Operations Engineering, 2009.
- [101] Bérard A. and Isikveren A.T. «Conceptual Design Prediction of the Buffet Envelope of Transport Aircraft». In: *Journal of Aircraft* 46.5 (2009), pp. 1593–1606. DOI: 10.2514/1.41367. URL: <https://doi.org/10.2514/1.41367>.

- [102] Association of European Airlines (AEA). «AEA Requirements». In: 1989.
- [103] Air Transport Association of America. *Standard Method of Estimating Comparative Direct Operating Costs of Turbine Powered Transport Airplanes*. The Association, 1967. URL: <https://books.google.it/books?id=ZLCrnQEACAAJ>.
- [104] European Civil Aviation Conference (ECAC). «Recommendation ECAC/27-4, NO_x Emission Classification Scheme». In: *ECAC*. 2003.
- [105] Commission of the European Communities. *Amended Proposal COM 2002/683 of the European Parliament and the Council for a Directive on the Establishment of a Community Framework for Noise Classification for Civil Subsonic Aircraft of 29.11.2002*. Tech. rep. 683. 2002. URL: <http://ec.europa.eu/transparency/regdoc/rep/1/2002/EN/1-2002-683-EN-F1-1.Pdf>.
- [106] International Civil Aviation Organization (ICAO). «Aircraft Engine Emissions». In: *ICAO Annex 16 Environmental protection Volume II*. 2008,
- [107] Cusati V. «Design activities for innovative turboprop aircraft with minimum economic and environmental impact». PhD. Department of Industrial Engineering, University of Naples Federico II, Naples, Italy: University of Naples Federico II, 2020.
- [108] Prakasha P.S., Della Vecchia P., Ciampa P.D., Ciliberti D., Charbonnier D., Jungo A., Fioriti M., Boggero L., Mirzoyan A., Anisimov K., Zhang M., and Voskuijl M. «Model Based Collaborative Design & Optimization of Blended Wing Body Aircraft Configuration: AGILE EU Project». In: *Aviation Technology, Integration, and Operations Conference*. 2018. DOI: <https://doi.org/10.2514/6.2018-4006>.
- [109] Della Vecchia P., Stingo L., Nicolosi F., Cerino G., Ciampa P.D., Prakasha P.S., Fioriti M., Zhang M., Mirzoyan A., Aigner B., and Charbonnier D. «Advanced Turboprop Multidisciplinary optimization within AGILE project». In: vol. paper 2018-3205. AIAA Aviation 2018, Atlanta, US, June 1, 2018. URL: <https://www.agile-project.eu/cloud/index.php/s/SnVNVLJRPr699T4>. published.
- [110] Yang X.S. *Nature-inspired Metaheuristic Algorithms*. Luniver Press, 2010. ISBN: 9781905986286. URL: https://books.google.it/books?id=iVB%5C_ETlh4ogC.
- [111] Coello Coello C.A., Lamont G., and Van Veldhuisen D. «Pareto Epsilon Model». In: *Evolutionary algorithms for solving multi-objective problems*. Springer, 2007, pp. 17–18. ISBN: 9780387332543.
- [112] Mongillo M. «Choosing basis functions and shape parameters for radial basis function methods». In: *SIAM undergraduate research online* 4.190-209 (2011), pp. 2–6.
- [113] Hadka D. *Smile - Statistical Machine Intelligence and Learning Engine*. 2019. URL: <http://haifengl.github.io/smile/index.html>.
- [114] Coello Coello C.A., Lamont G., and Van Veldhuisen D. *Evolutionary algorithms for solving multi-objective problems*. Springer, 2007. ISBN: 9780387332543.
- [115] Kurzke J. *GasTurb*. 2019. URL: <http://www.gasturb.de/index.html>.

- [116] *Airport planning publication*. Tech. rep. BD500-3AB48-32000-00 issue 13. Airbus Canada Limited Partnership, 2019.
- [117] Airbus Canada Limited Partnership. *A220-300 Purpose built for efficiency*. 2019. URL: <https://www.airbus.com/aircraft/passenger-aircraft/a220-family/a220-300.html>.
- [118] Laneckij O. and Raschuk A. *The Plastic Airplane: a Review of the World's First Bombardier CS300 Airliner*. 2016. URL: https://en.cfts.org.ua/articles/the_plastic_airplane_a_review_of_the_worlds_first_bombardier_cs300 airliner.
- [119] *Type-Certificate Data Sheet for BD-500 (A220 Series)*. Tech. rep. EASA.IM.A.570. European Aviation Safety Agency (EASA), 2019.
- [120] *Type-Certificate Data Sheet for PW1500G Series Engines*. Tech. rep. EASA.IM.A.090. European Aviation Safety Agency (EASA), 2018.
- [121] Airbus Canada Limited Partnership. *Airbus family figures – Farnborough 2018 Edition*. 2018. URL: <https://www.airbus.com/content/dam/corporate-topics/publications/backgrounders/Airbus-Family-Figures-booklet.pdf>.
- [122] Pratt & Whitney. *PurePower PW1500G Engine*. 2018. URL: <https://newsroom.pw.utc.com/download/PW1500G.S16310.K.05.17.pdf>.
- [123] Nuic A., Poles D., and Mouillet V. «BADA: An advanced aircraft performance model for present and future ATM systems». In: *International Journal of Adaptive Control and Signal Processing* 24.10 (2010), pp. 850–866. DOI: 10.1002/acs.1176. URL: <https://onlinelibrary.wiley.com/doi/abs/10.1002/acs.1176>.
- [124] Schiktanz D. and Scholz D. *Survey of Experimental Data of Selected Supercritical Airfoils*. Tech. rep. Airport2030_TN_Supercritical_Airfoils. Aero – Aircraft Design, Systems Group Department of Automotive, and Aeronautical Engineering, Hamburg University of Applied Sciences, 2011. URL: https://www.fzt.haw-hamburg.de/pers/Scholz/Airport2030/Airport2030_TN_Supercritical_Airfoils_11-12-21.pdf.
- [125] Niță M. and Scholz D. *Estimating the Oswald Factor from Basic Aircraft Geometrical Parameters*. Deutsche Gesellschaft für Luft- und Raumfahrt - Lilienthal-Oberth e.V., 2012.
- [126] Phillips J.D. *The Aerodynamic Characteristics of Flaps*. Tech. rep. No. 2622. Ministry of Supply. Aeronautical Research Council Reports and Memoranda, 1947.
- [127] Kundu A.K. *Aircraft design*. Cambridge University Press, 2010. ISBN: 9780511844652. DOI: <https://doi.org/10.1017/CB09780511844652>.
- [128] International Air Transport Association (IATA). *Jet Fuel Price Monitor*. 2019. URL: <https://www.iata.org/en/publications/economics/fuel-monitor/>.
- [129] Airbus S.A.S. *Airbus 2018 Price List Press Release*. 2018. URL: <https://www.airbus.com/newsroom/press-releases/en/2018/01/airbus-2018-price-list-press-release.html>.
- [130] Schlangenstein M. and Layne R. *JetBlue Picks Pratt Over CFM for Engines Valued at \$1.03 Billion*. 2011. URL: <https://www.bloomberg.com/news/articles/2011-12-14/jetblue-to-buy-pratt-whitney-engines>.

- [131] *Aircraft recovery publication*. Tech. rep. BD500-3AB48-10400-00 issue 55. Bombardier Aerospace Commercial Aircraft, 2018.
- [132] Faleiro L., Herzog J., and Schievelbusch B. «Integrated Equipment Systems for a More Electric Aircraft – Hydraulics and Pneumatics». In: *24th Congress of the International Council of the Aeronautical Sciences, ICAS 2004*. International Council of the Aeronautical Sciences, 2004. ISBN: 0953399168.
- [133] Cusati V., Nicolosi F., Corcione S., Ciliberti D., and Della Vecchia P. «Longitudinal stability issues including propulsive effects on an innovative commercial propeller-driven aircraft». In: *2019 Aviation Technology, Integration, and Operations Conference*. American Institute of Aeronautics and Astronautics, 2019. DOI: [10.2514/6.2019-2882](https://doi.org/10.2514/6.2019-2882).